Molecular gas measurements of supermassive black hole masses in nearby galaxies



Pandora Dominiak

Balliol College

University of Oxford

A thesis submitted for the degree of

Doctor of Philosophy

Michaelmas 2025

Abstract

Cold molecular gas is the principal fuel reservoir for star formation in galaxies and, when organised in dynamically cold discs, provides a powerful tracer of the underlying gravitational potential. This thesis investigates how molecular gas can be exploited as a precise dynamical tracer in nearby galaxies, both to measure supermassive black hole (SMBH) masses and to constrain rotation-based galaxy scaling relations.

I start with presenting high-resolution Atacama Large Millimeter/submillimeter Array (ALMA) ^{12}CO(2–1) observations of the galaxies NGC 1684, NGC 0997 and NGC 1387, and ^{12}CO(3–2) observations of NGC 4751. Each galaxy has an extended regularly rotating molecular gas disc. I then forward model the CO data cubes in a Bayesian framework, using *Hubble Space Telescope* data to constrain the stellar contributions to the molecular gas kinematics, and infer SMBH masses for all four galaxies. The inferred masses span more than an order of magnitude in SMBH mass. I also explore the dominant sources of uncertainty in these measurements, including inclination degeneracies, stellar mass-to-light ratio assumptions and the impact of dust on the observed stellar distributions.

Next, I present high-resolution ALMA ^{12}CO(2–1) observations of four massive galaxies. Using the same methodology as before, I derive upper limits on the SMBH masses of NGC 0665 and NGC 5208 and a tentative SMBH mass (requiring further modelling) for NGC 0467. I was unable to place any constraint on the SMBH mass of NGC 7550. These galaxies provide practical guidance for future target selection and observational strategies.

I then construct a new local calibration of the CO Tully-Fisher relation (TFR) in the $W1$- and K_s-bands using the integrated CO line-widths of 71 galaxies. Due to the morphological diversity of the sample, I also construct separate late-type and early-type galaxy CO TFRs, finding that early-type galaxies are fainter at fixed rotation velocities.

Lastly, I analyse my SMBH mass measurements in the context of the $M_{BH} - \sigma_e$ relation. All SMBH masses derived in this thesis are consistent with the intrinsic scatter of established relations. I also construct a CO-only $M_{BH} - \sigma_e$ relation, outline the leading systematic biases of molecular gas SMBH work and conclude with directions for future work.

This thesis demonstrates the potential of molecular gas as a powerful and versatile dynamical tracer for advancing our understanding of SMBH growth and galaxy evolution across multiple physical scales.

Acknowledgements

First and foremost, I would like to thank my supervisor, Professor Martin Bureau, for placing his confidence in me when I first approached him about undertaking a DPhil. I am deeply grateful for the opportunity he gave me and for his guidance throughout these years. His commitment to scientific rigour and meticulous attention to detail have shaped both this thesis and my approach to research. I would also like to thank my collaborators, particularly the members of the WISDOM team, for their expertise, patience, and generosity in sharing their knowledge and code. I have learnt a great deal from working with them, and this thesis has benefited considerably from their contributions.

While this thesis represents the culmination of several years of research, much of what I will take away from my time at Oxford extends beyond the work presented here. I have been fortunate to study in an environment that places great value on intellectual curiosity, critical enquiry, and the careful examination of one's own ideas. These are lessons I hope to carry into my future work.

I am equally grateful for the people I have met during my time here. Their friendship, generosity, and companionship have made these years particularly rewarding. Although I cannot acknowledge everyone individually, I would like to express my thanks to all those who have been part of my time at Oxford. Three people, in particular, deserve special mention.

To Melika Gorgianeh, thank you for your kindness, warmth, and thoughtfulness throughout these years. Having pursued our DPhils alongside one another, under the guidance of the same supervisor, we have shared many of the same experiences, challenges, and uncertainties. I am very grateful to have shared this time with you.

To Aftab Mallick, whose friendship has meant a great deal to me, thank you for your generosity with your knowledge, for sharing your love of poetry and your faith, and for the example you have set in the way you conduct yourself. I am very grateful to have met you during my time at Oxford.

To Jeffrey Liu, who knows better than anyone what it has taken me to get here. There are more things for which I owe you thanks than I could reasonably recount, but I am particularly grateful for the home we have made together, and for the many days of shared work, discipline, and sacrifice that have helped bring this thesis to completion.

Finally, I would like to thank my parents. Long before I began studying physics, they instilled in me the values of perseverance, intellectual curiosity, and care in whatever I undertake. They also taught me the importance of finding enjoyment in life beyond one's work. I am deeply grateful for their love, encouragement, and the sacrifices they have made to give me the opportunities I have had. None of this would have been possible without them.

Declaration of Generative AI Use

I declare that my use of generative artificial intelligence (AI) tools in the preparation of this thesis has complied with the relevant University of Oxford, divisional and departmental guidance.

OpenAI's ChatGPT (GPT-5.1) was used in a limited capacity during the preparation of the Introduction, primarily to assist with refining the clarity, conciseness and readability of text, and to identify potentially relevant references for the general literature review. The structure and scientific content of the chapter were determined entirely by me. All suggested references were independently consulted and evaluated before inclusion in the thesis.

All scientific research, data analysis, interpretation of results and conclusions presented in this thesis are my own, except where contributions from collaborators are explicitly acknowledged. No generative AI tools were used for coding, data analysis or the production of figures.

Statement of Originality

I carried out the work presented in this thesis as a student at the Sub-department of Astrophysics, Department of Physics, University of Oxford, between Hilary Term 2021 and Michaelmas Term 2025 under the supervision of Prof. Martin Bureau. I hereby declare that no part of this thesis has been accepted or submitted in support of another degree, diploma or other qualification at the University of Oxford or at any other higher learning institutions. Except where otherwise stated or where reference is made to the work of others, the work in this thesis is entirely my own.

The work presented in Chapter 2 is based on the work published in Dominiak et al. (2024), Dominiak et al. (2025) and Dominiak et al. (2026a). As the first author of all three papers I carried out the ALMA data reduction, conducted the CO modelling and associated analysis of results and wrote the manuscript. The co-authors contributed to securing the data through previous proposals and provided comments. Dominiak et al. (2025) contains a section on JAM modelling of stellar kinematics in NGC 4751 which was entirely contributed by Prof. Michele Cappellari. Because the work is not my own, it has been entirely excluded from this thesis.

The work presented in Chapter 3 summarised in a paper undergoing internal team review and will submitted to a refereed journal in due course. As the first author of this draft I carried out the ALMA data reduction, conducted the CO modelling and associated analysis of results and wrote the manuscript. The co-authors contributed to securing the data through previous proposals.

The work presented in Chapter 4 is summarised in a paper that has been submitted to a refereed journal and is undergoing review. As the first author of this draft I carried out the ALMA ACA data reduction, conducted analysis of all the data and wrote the manuscript. The co-authors contributed to securing the data through previous proposals, supplied the high-resolution data cubes which were reduced as a part of previous work and provided comments.

Contents

List of Figures ix

List of Tables xii

1 Introduction 1
- 1.1 Galaxy formation and evolution . . . 1
  - 1.1.1 Galaxy formation . . . 2
  - 1.1.2 Role of SMBHs in galactic evolution . . . 4
  - 1.1.3 Molecular gas . . . 6
- 1.2 Measuring supermassive black hole masses . . . 8
  - 1.2.1 Stellar dynamics . . . 10
  - 1.2.2 Ionised gas dynamics . . . 12
  - 1.2.3 Maser dynamics . . . 13
  - 1.2.4 Reverberation mapping . . . 14
  - 1.2.5 Molecular gas dynamics . . . 16
- 1.3 Scaling relations . . . 18
  - 1.3.1 $M_{\rm BH} - \sigma_{\rm e}$ relation . . . 18
  - 1.3.2 Tully-Fisher relation . . . 21
- 1.4 This thesis . . . 23
  - 1.4.1 WISDOM Project . . . 23
  - 1.4.2 MASSIVE Survey . . . 25
  - 1.4.3 Structure of this thesis . . . 26

2 Supermassive Black Hole Masses 29
- 2.1 Introduction . . . 30
- 2.2 Dynamical Modelling . . . 31
  - 2.2.1 Simulating interferometric data . . . 31
  - 2.2.2 Fitting process . . . 37
- 2.3 NGC 1684 . . . 39
  - 2.3.1 Galaxy Properties . . . 39
  - 2.3.2 ALMA Observations . . . 40
  - 2.3.3 CO Modelling . . . 46

2.3.4 Discussion . . . 52
2.4 NGC 0997 . . . 54
2.4.1 Galaxy Properties . . . 55
2.4.2 ALMA Observations . . . 56
2.4.3 CO Modelling . . . 60
2.4.4 Discussion . . . 63
2.5 NGC 4751 . . . 65
2.5.1 Galaxy Properties . . . 65
2.5.2 ALMA Observations . . . 68
2.5.3 CO Modelling . . . 72
2.5.4 Discussion . . . 79
2.6 NGC 1387 . . . 90
2.6.1 Galaxy Properties . . . 90
2.6.2 ALMA Observations . . . 91
2.6.3 CO Modelling . . . 96
2.6.4 Discussion . . . 104
2.7 Conclusions . . . 108

3 Supermassive Black Hole Mass Upper Limits 112
3.1 Introduction . . . 113
3.2 NGC 0665 . . . 113
3.2.1 Galaxy Properties . . . 113
3.2.2 ALMA Observations . . . 114
3.2.3 CO Modelling . . . 119
3.3 NGC 5208 . . . 125
3.3.1 Galaxy Properties . . . 125
3.3.2 ALMA observations . . . 126
3.3.3 CO modelling . . . 129
3.4 NGC 0467 . . . 136
3.4.1 Galaxy Properties . . . 136
3.4.2 ALMA observations . . . 137
3.4.3 CO modelling . . . 141
3.5 NGC 7550 . . . 150
3.5.1 Galaxy Properties . . . 150
3.5.2 ALMA observations . . . 151
3.5.3 CO modelling . . . 156
3.6 Conclusions . . . 157

4 CO Tully-Fisher relation **160**
4.1 Introduction . . . 160
4.2 Data . . . 163
4.2.1 CO data . . . 163
4.2.2 Optical data . . . 169
4.2.3 Velocity widths . . . 169
4.2.4 Photometry . . . 172
4.2.5 Inclinations . . . 173
4.3 Results . . . 178
4.3.1 Data sub-samples . . . 178
4.3.2 Tully-Fisher relation . . . 179
4.3.3 Galaxy morphology . . . 181
4.4 Discussion . . . 187
4.4.1 Literature comparisons . . . 187
4.4.2 Galaxy morphology . . . 189
4.4.3 Scatter . . . 192
4.5 Conclusions . . . 193

5 Conclusions **195**
5.1 $M_{\rm BH} - \sigma_{\rm e}$ relation . . . 196
5.1.1 Our results . . . 196
5.1.2 Molecular gas $M_{\rm BH} - \sigma_{\rm e}$ relation . . . 196
5.1.3 MASSIVE Survey galaxies . . . 201
5.1.4 Systematic biases in SMBH mass measurements and their impact on $M_{\rm BH} - \sigma_{\rm e}$ relation . . . 203
5.2 Summary . . . 209
5.3 Future work . . . 210
5.3.1 Expanding the molecular gas SMBH mass sample . . . 211
5.3.2 CO Tully-Fisher relation . . . 218

Bibliography **223**

List of Figures

2.1 *HST* image of NGC 1684 overlaid with ^{12}CO(2–1) contours. 40
2.2 ^{12}CO(2–1) data products of NGC 1684 derived from ALMA observations. . 43
2.3 ^{12}CO(2–1) integrated spectrum of NGC 1684. 45
2.4 *HST* image of NGC 1684 overlaid with our best-fitting MGE model and mask. 48
2.5 Covariances between model parameters in the best-fitting model of NGC 1684. 50
2.6 PVD comparison between NGC 1684 data and models. 51
2.7 PVD comparison between NGC 1684 data and models with variable M/L. . 52
2.8 Cumulative mass function of NGC 1684. 54
2.9 *HST* image of NGC 0997 overlaid with ^{12}CO(2–1) contours. 55
2.10 ^{12}CO(2–1) data products of NGC 0997 derived from ALMA observations. . 58
2.11 ^{12}CO(2–1) integrated spectrum of NGC 0997. 59
2.12 *HST* image of NGC 0997 overlaid with our best-fitting MGE model and mask. 61
2.13 Covariances between model parameters in the best-fitting model of NGC 0997. 64
2.14 PVD comparison between NGC 0997 data and models. 65
2.15 Cumulative mass function of NGC 0997. 66
2.16 *HST* image of NGC 4751 overlaid with ^{12}CO(3–2) contours. 67
2.17 ^{12}CO(3–2) data products of NGC 4751 derived from ALMA observations. . 70
2.18 ^{12}CO(3–2) integrated spectrum of NGC 4751. 71
2.19 *HST* image of NGC 4751 overlaid with our best-fitting MGE model and mask. 74
2.20 Covariances between model parameters in the best-fitting model with constant M/L of NGC 4751. 76
2.21 PVD comparison between NGC 4751 data and models with constant M/L. 77
2.22 Covariances between model parameters in the best-fitting model with linear M/L of NGC 4751. 78
2.23 PVD comparison between NGC 4751 data and models with linear M/L. . . 79
2.24 Cumulative mass function of NGC 4751 for the model with a constant M/L. 80
2.25 Cumulative mass function of NGC 4751 for the model with a linear M/L. . 81
2.26 Central surface brightness profiles of MGE models for NGC 4751 86
2.27 *HST* image of NGC 1387 overlaid with ^{12}CO(2–1) contours. 91
2.28 NGC 1387 continuum image. 93
2.29 ^{12}CO(2–1) data products of NGC 1387 derived from ALMA observations. . 95
2.30 *HST* image of NGC 1387 overlaid with our best-fitting MGE model. 98

2.31 ^{12}CO(2–1) zeroth-moment map of the lower-resolution data cube of NGC 1387. 99
2.32 Covariance between inclination and M/L. 100
2.33 Covariances between model parameters in the best-fitting model of NGC 1387. 103
2.34 PVD comparison between NGC 1387 data and models. 104
2.35 Cumulative mass function of NGC 0997. 105

3.1 *HST* image of NGC 0665 overlaid with ^{12}CO(2–1) contours. 114
3.2 NGC 0665 continuum image. 116
3.3 ^{12}CO(2–1) data products of NGC 0665 derived from ALMA observations. . 118
3.4 ^{12}CO(2–1) integrated spectrum of NGC 0665. 118
3.5 *HST* image of NGC 0665 overlaid with our best-fitting MGE model. 119
3.6 Covariances between model parameters in the best-fitting model of NGC 0665. 122
3.7 PVD comparison between NGC 0665 data and models. 123
3.8 Cumulative mass function of NGC 0665. 125
3.9 *HST* image of NGC 5208 overlaid with ^{12}CO(2–1) contours. 126
3.10 NGC 5208 continuum image. 127
3.11 ^{12}CO(2–1) data products of NGC 5208 derived from ALMA observations. . 129
3.12 ^{12}CO(2–1) integrated spectrum of NGC 5208. 130
3.13 *HST* image of NGC 5208 overlaid with our best-fitting MGE model and mask. 131
3.14 Covariances between model parameters in the best-fitting model of NGC 5208. 133
3.15 PVD comparison between NGC 5208 data and models. 134
3.16 PVD comparison between NGC 5208 data and models with variable M/L. . 135
3.17 Cumulative mass function of NGC 5208. 136
3.18 *CFHT* image of NGC 0467 overlaid with ^{12}CO(2–1) contours. 137
3.19 NGC 0467 continuum image. 139
3.20 ^{12}CO(2–1) data products of NGC 0467 derived from ALMA observations. . 140
3.21 ^{12}CO(2–1) integrated spectrum of NGC 0467. 141
3.22 *CFHT* image of NGC 0467 overlaid with best-fitting MGE model and mask. 144
3.23 Covariances between model parameters in the best-fitting model of NGC 0467. 147
3.24 PVD comparison between NGC 0467 data and models. 148
3.25 Cumulative mass function of NGC 0467. 150
3.26 *HST* image of NGC 7550 overlaid with ^{12}CO(2–1) contours. 151
3.27 NGC 7550 continuum image. 153
3.28 ^{12}CO(2–1) data products of NGC 7550 derived from ALMA observations. . 155
3.29 ^{12}CO(2–1) integrated spectrum of NGC 7550. 155
3.30 *HST* image of NGC 7550 overlaid with our best-fitting MGE model and mask. 157

4.1 Example ^{12}CO(2–1) data products derived from 7-m ACA ALMA data. . . 170
4.2 Correlation between the total absolute $W1$-band and K_s-band magnitudes. . 173

4.3 Examples of unsharp-masked *HST* images and best-fitting ellipses from which dust inclination are estimated. 178
4.4 CO Tully-Fisher relations. 183
4.5 Morphological CO Tully-Fisher relations. 186

5.1 $M_{\rm BH} - \sigma_{\rm e}$ relation with SMBH masses from this thesis. 197
5.2 $M_{\rm BH} - \sigma_{\rm e}$ relation obtained using molecular gas measurements only. 200
5.3 $M_{\rm BH} - \sigma_{\rm e}$ relation with MASSIVE galaxies. 203
5.4 $M_{\rm BH} - \sigma_{\rm e}$ relation with SMBH masses derived using both stellar kinematics and molecular gas kinematics. 206
5.5 Cross comparison of SMBH masses derived using stellar kinematics and molecular gas kinematics. 208

List of Tables

1.1 Properties of the galaxies for which we determine SMBH masses. 27
1.2 ALMA observations used in SMBH mass determinations. 28

2.1 Parameters of the circular MGE PSFs for filters used. 34
2.2 Details of the *HST* images and parameters for their MGE luminosity conversion. 35
2.3 CO data cube properties for NGC 1684. 42
2.4 Parameters of the NGC 1684 detected continuum and its image. 46
2.5 Parameters of the deconvolved best-fitting MGE components for NGC 1684. 47
2.6 Best-fitting model parameters of NGC 1684 and associated uncertainties. . 49
2.7 CO data cube properties for NGC 0997. 56
2.8 Parameters of the NGC 0997 detected continuum and its image. 59
2.9 Parameters of the deconvolved best-fitting MGE components for NGC 0997. 60
2.10 Best-fitting model parameters of NGC 0997 and associated uncertainties. . 62
2.11 CO data cube properties for NGC 4751. 69
2.12 Parameters of the NGC 4751 detected cleaned continuum and its image. . . 72
2.13 Parameters of the deconvolved best-fitting MGE components for NGC 4751. 73
2.14 Best-fitting model parameters of NGC 4751 for the model with a constant M/L and associated uncertainties. 75
2.15 Best-fitting model parameters of NGC 4751 for the model with a linear M/L and associated uncertainties. 77
2.16 χ^2 of the NGC 4751 models. 80
2.17 Parameters of the deconvolved best-fitting dust-corrected MGE components for NGC 4751. 85
2.18 Best-fitting model parameters and associated uncertainties for alterative NGC 4751 models. 88
2.19 Parameters of the NGC 1387 detected cleaned continuum and its image. . . 93
2.20 CO data cube properties for NGC 1387. 94
2.21 Parameters of the deconvolved best-fitting MGE components for NGC 1387. 97
2.22 Best-fitting model parameters of NGC 1387 and associated uncertainties. . 102
2.23 Best-fitting parameters and associated uncertainties of models with different fixed MGE axial ratios for NGC 1387. 107

3.1 Parameters of the NGC 0665 detected cleaned continuum and its image. . . 115

3.2 CO data cube properties for NGC 0665. 117
3.3 Parameters of the deconvolved best-fitting MGE components for NGC 0665. 120
3.4 Best-fitting model parameters of NGC 0665 and associated uncertainties. . 121
3.5 Parameters of the NGC 5208 detected cleaned continuum and its image . . 127
3.6 CO data cube properties for NGC 5208. 128
3.7 Parameters of the deconvolved best-fitting MGE components for NGC 5208. 132
3.8 Best-fitting model parameters of NGC 5208 and associated uncertainties. . 132
3.9 Parameters of the NGC 0467 detected cleaned continuum and its image. . . 138
3.10 CO data cube properties for NGC 0467. 139
3.11 Parameters of the deconvolved best-fitting MGE components for NGC 0467. 144
3.12 Best-fitting model parameters of NGC 0467 and associated uncertainties. . 146
3.13 χ^2 of the NGC 0467 models. 149
3.14 Parameters of the NGC 7550 detected cleaned continuum and its image. . . 152
3.15 CO data cube properties for NGC 7550. 154
3.16 Parameters of the deconvolved best-fitting MGE components for NGC 7550. 156

4.1 CO data for the TFR galaxy sample. 165
4.2 Photometric data for the TFR galaxy sample. 174
4.3 Best-fitting parameters of the $W1$- and K_s-band CO TFRs. 182
4.4 Best-fitting TFR parameters of literature studies. 185

5.1 Molecular gas SMBH mass measurements. 198
5.2 SMBH mass measurements of galaxies of the MASSIVE Survey sample. . 202

To struggle and to understand – never this last without the other; such is the law.

— George Mallory's *Mont Blanc from the Col du Géant by the Eastern Buttress of Mont Maudit*

1 Introduction

Contents

1.1 Galaxy formation and evolution 1
1.1.1 Galaxy formation 2
1.1.2 Role of SMBHs in galactic evolution 4
1.1.3 Molecular gas 6
1.2 Measuring supermassive black hole masses 8
1.2.1 Stellar dynamics 10
1.2.2 Ionised gas dynamics 12
1.2.3 Maser dynamics 13
1.2.4 Reverberation mapping 14
1.2.5 Molecular gas dynamics 16
1.3 Scaling relations 18
1.3.1 $M_{\rm BH} - \sigma_{\rm e}$ relation 18
1.3.2 Tully-Fisher relation 21
1.4 This thesis 23
1.4.1 WISDOM Project 23
1.4.2 MASSIVE Survey 25
1.4.3 Structure of this thesis 26

1.1 Galaxy formation and evolution

Galaxies are some of the fundamental building blocks of our universe. They host stars, gas, dust and dark matter and provide the stage on which these components interact. In Lambda-Cold-Dark-Matter (ΛCDM) models, galaxies form and evolve within dark matter

haloes. They grow through processes of gravitational collapse, hierarchical merging and gas accretion. The observed morphological diversity of galaxies and their internal kinematics reflect differences in assembly histories. Therefore, the internal structure and dynamics of galaxies inform us about the physical processes that redistribute mass and angular momentum within them across the entire range of galactic scales.

1.1.1 Galaxy formation

According to the ΛCDM framework, galaxies form within dark matter haloes (e.g. White & Rees 1978; Blumenthal et al. 1984). Dark matter dominates the total gravitational mass of the Universe and the growth of locally overdense regions leads to the formation of dark matter haloes (e.g. Blumenthal et al. 1984). These haloes act as potential wells in which baryons can cool and condense (e.g. White & Frenk 1991; Springel et al. 2005). Therefore, galaxy formation can be viewed as the outcome of an interplay between halo assembly and the baryon cycle, which governs how gas is accreted, cools and is converted into stars (e.g. Somerville & Davé 2015; Naab & Ostriker 2017).

During halo assembly, baryons are accreted from the intergalactic medium and, depending on halo mass and redshift, can either be shock heated (hot accretion mode) or flow into the halo through cool filamentary streams without being shock heated (cold accretion mode; e.g. Birnboim & Dekel 2003; Kereš et al. 2005; Dekel & Birnboim 2006). These processes regulate the rate at which gas can reach the central regions of galaxies. When cooling times are short, heated gas can cool radiatively, losing thermal energy and settling toward the halo centres, thereby supplying the fuel required for both star formation and supermassive black hole (SMBH) growth (e.g. White & Frenk 1991; Benson et al. 2003; Somerville & Davé 2015). However, in sufficiently massive haloes the formation of stable virial shocks near the halo virial radii leads to the development of pressure-supported regions that inhibit efficient gas cooling (e.g. Birnboim & Dekel 2003; Croton et al. 2006; Dekel & Birnboim 2006). As a result, new cold gas accretion onto the galaxies is suppressed and galactic growth becomes increasingly dependent on mergers or slowly regulated cooling flows, often mediated by feedback processes (e.g. White & Frenk 1991; Fabian 2012; Somerville & Davé 2015).

In any given halo, if the accreted gas retains enough angular momentum to avoid rapid collapse, it settles into a rotationally supported disc (e.g. Fall & Efstathiou 1980; Mo et al. 1998). The size and mass surface density of the disc are determined by how the angular momentum is acquired during halo growth and how it is redistributed as the gas cools and collapses (e.g. Mo et al. 1998, 2010). Disc formation is therefore closely linked to the internal processes that can remove and/or redistribute low-angular momentum material, such as gravitational instabilities and feedback-driven outflows (e.g. Dekel & Silk 1986; Brook et al. 2011). On galactic scales, rotation provides the dominant support against gravity (Binney & Tremaine 2008). The resulting rotation curves reflect the distribution of mass in galaxies and give rise to empirical scaling relations such as the Tully-Fisher relation (e.g. Tully & Fisher 1977; Courteau et al. 2014; Lelli et al. 2016).

Within galactic discs, star formation occurs primarily in the cold molecular component of the interstellar medium (ISM; e.g. Bigiel et al. 2008; Kennicutt & Evans 2012; Krumholz 2014). The rate at which gas is converted into stars is regulated by local gravitational instabilities, turbulence and feedback from massive stars (e.g. Kennicutt 1998; Kennicutt & Evans 2012). This feedback injects energy and momentum into the surrounding gas, driving outflows and heating the ISM, which in turn reduces the star formation efficiency, particularly in low- and intermediate-mass haloes (e.g. Veilleux et al. 2005; Somerville & Davé 2015). Together, these processes regulate the baryon cycle and shape the relationship between stellar mass and halo mass across the galaxy population (e.g. Behroozi et al. 2013).

Galaxy structure is further shaped by mergers. Mergers can heat stellar discs, grow spheroids and redistribute angular momentum and orbital energy through violent relaxation (e.g. Lynden-Bell 1967; Barnes & Hernquist 1992). Gas-rich (wet) mergers can trigger central starbursts and build compact bulges, while gas-poor (dry) mergers tend to increase galaxy sizes and stellar envelopes without significant star formation. The latter is believed to be particularly important for the late-stage growth of massive early-type galaxies (ETGs; e.g. Hopkins et al. 2009; Naab et al. 2009).

Gas within galaxies can also lose angular momentum through gravitational torques arising from non-axisymmetric structures such as bars, spiral arms, galaxy interactions and other dynamical instabilities (e.g. Shlosman et al. 1989; Combes 2001; Hopkins

et al. 2016). These drive gas inflows over long timescales, contributing to the gradual growth of central stellar components, particularly in disc galaxies (e.g. Kormendy & Kennicutt 2004; Athanassoula 2005).

As a result of all these processes, present-day galaxies exhibit a wide range of dynamical structures. Late-type galaxies (LTGs) are typically dominated by ordered rotation, reflecting disc-dominated assembly histories (e.g. Courteau et al. 2007; Lelli et al. 2016), while ETGs span a continuum from rotation-dominated fast rotators to dispersion-dominated slow rotators (e.g. Emsellem et al. 2007, 2011; Cappellari 2016). This kinematic diversity reflects differences in assembly history, environment and the relative importance of dissipational and dissipationless growth. Therefore, the kinematic structure of a galaxy reflects how it formed and evolved, which in turn motivates the study of galactic dynamics as a way of understanding galactic evolution.

1.1.2 Role of SMBHs in galactic evolution

Observations over the last three decades have established that nearly every massive galaxy hosts a SMBH at its centre. Although SMBHs are massive, the region a SMBH influences dynamically typically subtends only the innermost tens of parsecs of its host galaxy, a negligible fraction of the overall galaxy extent. Despite this, SMBH masses are tightly correlated with several host galaxy properties, implying some coupling between SMBH growth and galaxy formation (e.g. Magorrian et al. 1998; Ferrarese & Ford 2005; Kormendy & Ho 2013; McConnell & Ma 2013). These correlations suggest that SMBHs co-evolve with their host galaxies, but the details of the self-regulating processes are still poorly understood (e.g Harrison et al. 2018; D'Onofrio et al. 2021).

Theoretical models broadly invoke two main regimes through which SMBHs can influence the evolution and properties of their host galaxies. In one class of models, SMBHs grow predominantly through slow gas accretion and observations of active galactic nuclei (AGNs) provide key evidence of this (e.g. Yu & Tremaine 2002; Marconi et al. 2004). As discussed in the context of galaxy evolution, gas within a galaxy must lose angular momentum to reach the nuclear regions. This gas can settle into a rotationally supported accretion disc, which can in turn deliver material farther inwards, feeding the SMBH and releasing the

gravitational energy that powers AGN activity (e.g. Fabian 2012; King & Pounds 2015). The accretion flow onto the SMBH releases energy both radiatively, in the form of photons and mechanically, through winds, jets and energetic particles (e.g. Fabian 2012; Kormendy & Ho 2013; Harrison 2017). This can impact the circumnuclear ISM by creating turbulence and shocks that heat cold star-forming gas or expel it entirely, thereby reducing or quenching (i.e. regulating) star formation (e.g. Alatalo et al. 2015). On larger spatial scales, AGN feedback can heat the surrounding halo gas, suppressing cooling flows and starving the galaxy of fresh fuel, thereby limiting further accretion and maintaining quiescence in massive systems (e.g. McNamara & Nulsen 2007; Fabian 2012; Voit et al. 2015). AGN feedback is thus commonly invoked to reproduce the observed suppression of star formation in high-mass galaxies (e.g. Strateva et al. 2001; Peng et al. 2010) and the bright-end break of the galaxy luminosity and stellar-mass functions (e.g. McNamara & Nulsen 2007).

In another class of models, galaxy interactions and mergers are thought to rapidly drive SMBH and host galaxy growth and their co-evolution. It has been established that SMBH masses and many host galaxy properties are correlated (see Section 1.3). The tightest of these correlations are generally those involving bulge properties, most notably the central stellar velocity dispersion (e.g Ferrarese & Merritt 2000), bulge stellar mass (e.g McConnell & Ma 2013) and bulge luminosity (e.g Marconi & Hunt 2003). As classical bulges and elliptical galaxies are thought to form efficiently through galaxy mergers and merger-driven violent relaxation, it is natural to associate the rapid assembly of bulges with rapid SMBH growth (e.g. Toomre & Toomre 1972; Hopkins et al. 2008). Galaxy mergers can efficiently drive gas into the central regions via strong gravitational torques, potentially triggering luminous AGN phases and episodes of rapid SMBH growth (e.g. Mihos & Hernquist 1996; Hopkins et al. 2006). Additionally, galaxy mergers can bring together the central SMBHs, allowing them to coalesce and increase the resulting SMBH mass independently of any gas supply (e.g. Volonteri et al. 2003). Nevertheless, the degree to which mergers dominate SMBH triggering remains debated, with modern observations suggesting that mergers are not the sole channel for AGN activity, particularly at moderate luminosities, even if they may be important for the most luminous quasar phases (e.g. Harrison et al. 2018; Ellison et al. 2019). This supports a hybrid view in which secular processes account for much of the

integrated SMBH mass growth, while mergers contribute episodically and may be especially influential for the most massive systems (Harrison et al. 2018).

As the central gravitational potentials of galaxies are shaped by their assembly histories and baryonic contents, constraining these quantities across multiple spatial scales is essential to test models of galaxy evolution (e.g. Ferrarese & Ford 2005; Kormendy & Ho 2013; Harrison et al. 2018). This, in turn, motivates the need for robust measurements of both SMBH masses and galaxy dynamics.

1.1.3 Molecular gas

Cold molecular gas is the ISM component most directly associated with star formation, as stars form within molecular clouds whose physical properties regulate the star formation efficiencies and gas depletion times at spatial scales of tens of parsecs (e.g. Bigiel et al. 2008; Kennicutt & Evans 2012; Krumholz 2014). As a result, molecular gas plays a central role in governing how galaxies convert baryons into stars and evolve over cosmic time. In nearby galaxies, the bulk of the molecular gas component is commonly traced through rotational transitions of carbon monoxide (CO), as molecular hydrogen (H_2) lacks a permanent dipole moment and is difficult to observe directly under typical cold ISM conditions (e.g. Bolatto et al. 2013; Carilli & Walter 2013).

Molecular gas forms where the ISM becomes sufficiently dense and shielded from dissociating ultraviolet radiation. Dust grains play a key role by catalysing the formation of molecular hydrogen and protecting it from destruction. Therefore, molecular gas exists readily in regions with sufficiently high metallicity and column density, where dust is present to efficiently shield the gas from dissociating ultraviolet radiation (e.g. Hollenbach & Salpeter 1971; Bolatto et al. 2013; Krumholz 2014). The amount of molecular gas present is set by a balance between formation and destruction processes that depends on local conditions such as gas mass density, radiation field strength and feedback (e.g. Krumholz et al. 2009; Glover & Clark 2012). However, once formed, molecular gas can persist over timescales comparable to the lifetime of galactic structures, making it a relatively stable and long-lived phase of the ISM rather than a transient by-product of star formation.

Importantly, molecular gas is present in a variety of galaxies. Although it is most abundant in star-forming disc galaxies, observations show that a significant fraction of ETGs also host molecular gas, including systems with little or no ongoing star formation (e.g. Young et al. 2011; Davis et al. 2011a; Alatalo et al. 2013). In these galaxies, the molecular component is often arranged in discs or rings and can remain dynamically regular even when star formation activity is weak (e.g. Davis et al. 2011a; Alatalo et al. 2013). This widespread presence of molecular gas across galaxies of different morphological types suggests that it is a common outcome of galaxy evolution rather than a feature unique to actively star-forming systems.

Nuclear molecular discs are observed in both early- and late-type galaxies, although the origin of the gas and the mechanisms that drive it to the centre can differ between galaxy populations. In LTGs, bars, spiral arms and other non-axisymmetric structures can exert gravitational torques on the ISM, removing angular momentum and driving gas inwards towards the central regions of the galaxy (e.g. Athanassoula 1992; Kormendy & Kennicutt 2004; Athanassoula 2005). Once this gas settles into the central potential, it can form a dynamically cold nuclear molecular disc and if sufficiently dense, this gas may also fuel central star formation and build a nuclear stellar disc over time (e.g. Bittner et al. 2020; Schultheis et al. 2025) In ETGs, the molecular gas that forms nuclear discs may instead originate from external accretion, minor mergers, or internally recycled stellar mass, before cooling and settling into an ordered rotating disc (e.g. Young et al. 2011; Davis et al. 2013a). These nuclear molecular discs are particularly useful for dynamical modelling because, when regular and rotationally supported, they provide dynamically cold tracers of the central gravitational potential.

In addition to its role in star formation, molecular gas is also dynamically important. Because it is cold, molecular gas typically has an intrinsic velocity dispersion that is small compared to those of stars and ionised gas (e.g. Davis et al. 2013a; Barth et al. 2016; Boizelle et al. 2019). When it is distributed in an ordered configuration, its motion is dominated by rotation rather than pressure support or non-gravitational forces (e.g. Kormendy & Ho 2013). Under these conditions molecular gas responds directly to the underlying gravitational potential, making it a useful tracer of galaxy mass. This is particularly valuable in regions

where other tracers may be affected by dust obscuration, complex excitation and/or disturbed kinematics (e.g. Ferrarese & Ford 2005; Bolatto et al. 2013; Kormendy & Ho 2013).

Although molecular gas is often dynamically cold and dominated by ordered rotation, this assumption is not universally valid. Feedback from AGN activity, radio jets and intense star formation can inject energy and momentum into the molecular ISM, generating turbulence, outflows and other non-circular motions that can cause the gas kinematics to depart from rotational equilibrium (e.g. Morganti et al. 2015; Leaman et al. 2019). Molecular gas is therefore most effective as a dynamical tracer when it is organised into regularly rotating discs with kinematics dominated by circular motion, conditions that must be verified observationally before dynamical modelling is undertaken.

Another strength of molecular gas is that it can trace physical processes across numerous spatial scales. Molecular gas can trace SMBH dynamics on tens-of-parsec scale, fuel star formation on sub-kiloparsec scale and trace galaxy dynamics on kiloparsec scale (when organised into extended discs; e.g. Leroy et al. 2008; Davis et al. 2011a, 2013a). As such, molecular gas provides a natural bridge between local processes in galaxy centres and the intermediate-scale dynamical structures of galaxies. In turn, this makes molecular gas a valuable tracer to link central and galaxy-scale dynamics, complementing other tracers that are typically sensitive to more restricted regions and/or physical conditions.

Taken together, these properties establish molecular gas as a key ingredient in galaxy evolution and a powerful probe of both baryonic processes and dynamical structures. Its prevalence across all galaxy types, relative dynamical simplicity when settled into regularly rotating discs and presence from central to galactic scales motivate its growing use in studies of galaxy dynamics and central mass distributions.

1.2 Measuring supermassive black hole masses

SMBH mass measurements rely on detecting a SMBH's gravitational imprint on a tracer in the immediate surrounding region. The data must resolve the spatial scales on which the SMBH contributes a measurable fraction of the total gravitational potential, above the competing influence of other mass components, primarily the stars. A standard way

of quantifying the region in which the SMBH potential dominates is through the sphere of influence (SoI; Peebles 1972), defined as

$$R_{\rm SoI} \equiv \frac{GM_{\rm BH}}{\sigma_{\rm e}^2} \quad , \tag{1.1}$$

where $M_{\rm BH}$ is the SMBH mass, $\sigma_{\rm e}$ is the luminosity-weighted stellar velocity dispersion measured within one effective radius $R_{\rm e}$ and G is the gravitational constant. An alternative and widely used definition is that of the radius of equivalence, where the enclosed stellar mass is equal to the SMBH mass. These two definitions are conceptually similar but not identical and the resulting radii can and do generally differ slightly depending on a galaxy's central stellar mass distribution and dynamics.

Some of the earliest robust dynamical SMBH measurements were made in the 1980s with the discovery of large dark objects in the centres of M31 (Dressler 1984; Dressler & Richstone 1988; Kormendy 1988) and M32 (Tonry 1984, 1987; Dressler & Richstone 1988), obtained using ground-based optical absorption-line spectroscopy. These early studies established the basic methodology behind dynamical SMBH mass detection, but they also highlighted the central difficulty of this emerging field: without spatially resolving the region where the SMBH dominates the potential, the inferred central mass is vulnerable to degeneracies with the stellar mass distribution.

The launch of the *Hubble Space Telescope* (*HST*) is widely regarded as the key milestone that enabled kinematics to be measured on substantially smaller physical scales, which not only enabled the confirmation of prior ground-based SMBH masses, but ushered in an era of demographic studies (e.g. Kormendy & Richstone 1995; Ferrarese & Ford 2005). The improved angular and thus spatial resolution of both photometry and spectroscopy led to major advances in stellar dynamical measurements and to this day a large fraction of SMBH mass measurements are based on stellar dynamics. Additionally, *HST* enabled the proliferation of ionised gas dynamical mass measurement, whose modelling is often simpler (in systems with regular nuclear discs) than that of stellar dynamics.

Another major methodological leap occurred when very long baseline interferometry (VLBI) was able to resolve H_2O megamaser emission in edge-on galactic circumnuclear discs, directly tracing the Keplerian rotation near the SMBHs at sub-parsec radii. When

present, maser discs remain among the most precise and physically transparent SMBH mass tracers. However, suitable systems are rare and masers primarily function as high-accuracy anchors; they cannot offer a way to obtain large, representative samples of SMBH masses.

A complementary approach to dynamical SMBH mass measurement is provided by reverberation mapping, which exploits time variability in AGNs rather than spatially resolving each SMBH SoI. Reverberation mapping has enabled SMBH masses to be measured for large samples of AGNs and it remains the primary route to study SMBH demographics beyond the local Universe (e.g. Shen 2013). However, as will be discussed later, reverberation mapping SMBH masses are ultimately tied to the spatially resolved dynamical measurements of nearby galaxies, through their dependence on SMBH – host galaxy correlations (e.g. Kormendy & Ho 2013).

More recently, the expansion of SMBH masses has been driven by high-resolution mm/sub-mm interferometry, particularly with the use of the Atacama Large Millimeter/sub-millimeter Array (ALMA), enabling SMBH mass measurements using cold molecular gas as a tracer. This development is particularly consequential because dynamically cold molecular discs are common in many nearby galaxies, thereby creating a clear pathway to methodologically uniform surveys of SMBH masses across galaxies of all morphological types. In the following subsections, we outline the principal techniques used to measure SMBH masses, highlighting their underlying assumptions, strengths and limitations.

1.2.1 Stellar dynamics

Stellar dynamical SMBH mass measurements are carried out by using the collisionless Boltzmann equation and its velocity moments (the Jeans equations) to model the stellar mass distribution and kinematics in the gravitational potential of a galaxy (e.g. Jeans 1915, 1922; Binney & Tremaine 2008). The SMBH mass is constrained by identifying the central mass required, in addition to the stellar contribution, to reproduce the observed line-of-sight velocity distributions (LOSVDs), including high-order LOSVD moments, derived from spectroscopic observations (e.g. Kormendy 1988; Dressler & Richstone 1988; Ferrarese & Ford 2005).

Modern stellar-dynamical methods largely rely on the adoption of three-integral (triaxial, axisymmetric, or spherical) models through Schwarzschild's orbit-superposition method,

for which one assumes a gravitational potential, numerically integrates a large number of representative stellar orbits and then assigns non-negative weights to each orbit such that their superposition reproduces the observed surface brightness and kinematics (e.g. Schwarzschild 1979; Schwarzschild 1993; Cretton et al. 1999; Gebhardt et al. 2000; Gebhardt et al. 2003; van den Bosch et al. 2008; McConnell et al. 2011). Complementary to orbit-superposition is Jeans modelling, which solves the axisymmetric or spherical Jeans equations under explicit assumptions about the anisotropy of the stellar velocity dispersion tensor, predicts the projected second moments and fits these directly to an observed moment map to constrain the SMBH mass (e.g. Cappellari 2008; Cappellari 2020; Simon et al. 2023).

The strength of stellar dynamical modelling is that it offers a ubiquitous probe of SMBH masses, as all galaxies host stars. However, the construction of robust dynamical models necessitates sophisticated modelling techniques and generally requires high signal-to-noise ratio (S/N) stellar kinematic data to measure the full shapes of the LOSVDs. Acquiring such data often demands large aperture telescopes and/or long integration times, as stellar absorption lines are faint, particularly in low surface brightness regions such as the centres of massive cored galaxies (e.g. Ferrarese & Ford 2005; Kormendy & Ho 2013). As models of stellar kinematics rely on the absorption lines of the integrated stellar population spectra, they are also strongly affected by dust extinction, frequently motivating observations in the near-infrared regime (e.g. Silge & Gebhardt 2003; Krajnović et al. 2009; Thater et al. 2019).

While dynamical models have historically often adopted an axisymmetric potential (e.g. Gebhardt et al. 2003), a non-negligible fraction ($\approx$ 12 per cent) of ETGs with stellar masses $M_* > 10^{10}$ $M_\odot$ are classified as weakly triaxial slow rotators (Emsellem et al. 2011). Triaxial models (e.g. van den Bosch et al. 2008; Pilawa et al. 2024) should be formally required for these systems, but early investigations have yielded varied results as to whether these triaxial model SMBH masses are consistent with those derived from axisymmetric models (e.g. van den Bosch & de Zeeuw 2010; Liepold et al. 2020; Pilawa et al. 2022; Quenneville et al. 2022). Furthermore, stellar dynamical models employing Schwarzschild's orbit-superposition method must describe the galaxy potential to large radii, necessitating the inclusion of a dark matter halo component, which can potentially increase the overall systematic uncertainties of the SMBH mass measurements (Gebhardt & Thomas 2009).

1.2.2 Ionised gas dynamics

Ionised gas provides a direct dynamical tracer of the enclosed mass under the condition that it is confined to a thin disc in (near-)circular rotation, such that the observed rotation curve is (nearly) equal to the circular velocity curve, defined in spherical symmetry as

$$v_{\rm c}^2(r) \equiv \frac{GM_{<r}(r)}{r} \quad , \tag{1.2}$$

where $v_{\rm c}(r)$ is the circular velocity at a given radius r and $M_{<r}(r)$ is the mass enclosed within that radius. In practice, the SMBH mass is obtained by fitting disc models to reproduce the rotation velocity of the nuclear disc. However, in the case of complex line profiles, the profiles can be fitted directly instead (Barth et al. 2001).

The first ionised gas SMBH mass measurement was published by Harms et al. (1994), who used *HST* Faint Object Spectrograph (FOS) spectroscopy of the compact ionised disc in M87 to probe the Keplerian motion around a central dark mass. Follow-up long-slit *HST* observations improved spatial sampling and modelling fidelity, obtaining the full rotation curve as opposed to a single spectrum, most notably the three-slit *HST* Faint Object Camera (FOC) spectroscopy of M87 by Macchetto et al. (1997). These measurements also incorporated important effects of the propagation of light through the telescope and spectrograph optics for the first time. Later, the Space Telescope Imaging Spectrograph (STIS) allowed for the complete mapping of the kinematic structure of the emission-line disc, as well as assessing the impact that the intrinsic velocity dispersion of the disc has on its dynamical support (Walsh et al. 2013).

Modelling ionised gas is conceptually straightforward, relying on the rotational velocities of a dynamically-cold thin disc, but it presents its own set of difficulties. In particular, the assumption of a dynamically-cold thin disc is seldom borne out by the data, as ionised gas is particularly susceptible to non-gravitational forces such as turbulence, shocks and radiation pressure. It is therefore no surprise that most galaxies do not fulfil this requirements for easy ionised gas modelling. A particularly important systematic effect of ionised gas modelling is thus that of pressure support (Neumayer 2010). Many nuclear ionised gas discs exhibit substantial intrinsic velocity dispersions, implying partial pressure support of

the discs. If neglected, ionised gas methods will yield systematically lower SMBH mass estimates than stellar kinematic methods (Kormendy & Ho 2013).

Whilst the ionised gas method has yielded a number of robust SMBH masses (e.g. Sarzi et al. 2001; Atkinson et al. 2005; Dalla Bontà et al. 2009), fewer than 20 per cent of nearby bulges have the regular velocity fields needed for dynamical modelling (Kormendy & Ho 2013). Nevertheless, the method has proven effective to infer large numbers of SMBH mass upper limits (e.g. Sarzi et al. 2001; Beifiori et al. 2009), which provide additional valuable information to constrain SMBH – host galaxy correlations (see Chapter 3).

1.2.3 Maser dynamics

VLBI maps of the 22-GHz emission from H_2O maser clouds reveal small but very bright spots in the sub-parsec circumnuclear discs surrounding some SMBHs, with nearly perfect Keplerian rotation. As the emitting radii are $\ll$ 1 pc and can be routinely spatially resolved with VLBI, maser emission probes some of the smallest spatial scales and hence provides some of the most precise dynamical SMBH masses available (e.g. Kormendy & Ho 2013).

Due to their excellent resolution of small physical scales, maser observations are currently considered the gold standard of SMBH mass determination. NGC 4258 was the first galaxy whose maser kinematics confirmed the presence of a central SMBH (of mass $\approx 10^7$ $M_\odot$; Miyoshi et al. 1995; Greenhill et al. 1995). Maser observations yield the velocities of only a few spots (occasionally a single one) along the major axis of each disc, effectively yielding one-dimensional kinematics (e.g. Herrnstein et al. 2005). The lack of two-dimensional kinematic information makes it difficult to assess the internal structure of the discs for warps and non-circular motions. In fact, even early studies indicated that the maser disc of NGC 4258 is significantly warped (Miyoshi et al. 1995; Neufeld & Maloney 1995) and subsequent modelling explicitly treated the warp as an intrinsic geometric property of the disc rather than a perturbation (e.g. Herrnstein et al. 2005; Humphreys et al. 2013). Such warps in well-mapped maser discs are relatively common (e.g. Greenhill et al. 2003; Gao et al. 2016; Zhao et al. 2018) and their accurate modelling is crucial to accurately determine SMBH masses.

However, despite yielding the tightest constraints on SMBH masses so far, only $\approx$ 3 per cent of local Seyfert 2 and low-ionisation nuclear emission region (LINER) galaxies

have masers that can be used to estimate SMBH masses (van den Bosch et al. 2016), all of which are relatively low-mass active galaxies with correspondingly low-mass SMBHs by construction. Of these, only $\approx 1/3$ show the classic high-velocity features indicating a thin accretion disc around a SMBH (e.g. Pesce et al. 2015; van den Bosch et al. 2016). Even with long-running dedicated programmes, the number of confirmed maser galaxies with robust SMBH masses is only 27 (Zhang et al. 2024).

1.2.4 Reverberation mapping

Reverberation mapping provides an indirect, yet powerful, method to estimate SMBH masses in AGNs, particularly at distances and redshifts for which spatially resolved dynamical measurements are not feasible. Unlike stellar, gas or maser dynamical techniques, reverberation mapping does not rely on spatially resolving each SMBH SoI. Instead, it exploits the time variability of the AGN continuum emission and its delayed response in the surrounding broad line region (BLR) gas (e.g. Blandford & McKee 1982; Peterson et al. 1991). As a result, reverberation mapping has become the primary technique to estimate SMBH masses in large samples of AGNs and it underpins much of our empirical understanding of SMBH growth across cosmic time (e.g. Peterson et al. 2004).

Direct reverberation mapping is based on the assumption that the BLR gas is photoionised by radiation originating in the accretion disc surrounding a SMBH. Variations in the ionising continuum propagate outward at the speed of light and induce corresponding variations of the emission-line fluxes from the BLR after a characteristic time delay. By monitoring the AGN continuum and emission-line light curves over time, one can measure this delay, which directly yields a characteristic BLR radius $R_{\rm BLR} = c\tau$, where τ is the measured lag (Peterson et al. 1991; Dietrich et al. 1993; Peterson et al. 2004). In parallel, the velocity scale of the BLR gas is inferred from the width of the broad emission lines, providing an estimate of the gas kinematics.

Under these assumptions, the SMBH mass can be estimated using

$$M_{\rm BH} = \frac{f R_{\rm BLR} \Delta V^2}{G} \quad , \tag{1.3}$$

where ΔV is the BLR emission-line width and f is a virial scaling factor that accounts for the unknown geometry, kinematics and inclination of the BLR. The first robust SMBH masses measured via reverberation mapping were of nearby Seyfert galaxies such as NGC 5548 (Peterson & Wandel 1999) and NGC 3783 (Onken & Peterson 2002). Many more studies have followed since (e.g. Wandel et al. 1999; Peterson et al. 2004; Bentz et al. 2010).

It is important to distinguish direct reverberation mapping from the broader use of reverberation mapping-calibrated mass estimators. Direct reverberation mapping requires long-term spectroscopic monitoring and is therefore observationally expensive, especially at high redshifts where cosmological time dilation lengthens the observed variability timescales. Consequently, many large AGN and quasar studies do not measure an individual BLR lag for each object. Instead, they use single-epoch virial mass estimators, in which $R_{\rm BLR}$ is inferred from an empirical BLR radius–luminosity relation calibrated using reverberation-mapped AGNs, and then combined with a BLR emission-line width measured from a single spectrum (e.g. Kaspi et al. 2000; Vestergaard & Peterson 2006; Bentz et al. 2013). These single-epoch masses are therefore not direct reverberation mapping measurements, but secondary mass estimates tied to the reverberation-mapped mass scale.

This distinction is particularly important for studies of SMBH demographics at high redshift. High-redshift quasars are often too distant for direct reverberation mapping to be practical, so their SMBH masses are commonly inferred using reverberation mapping-calibrated single-epoch relations. In some contexts, particularly for radio-selected AGN samples, radio luminosity or relations involving radio emission may also be used as statistical proxies for SMBH mass (e.g. Falcke et al. 2004; Merloni et al. 2006). Such approaches are valuable for studying large samples and cosmic evolution, but they are more indirect than direct reverberation mapping and inherit the scatter, calibration uncertainties and selection effects of the adopted scaling relation.

One major limitation common to both direct reverberation mapping and reverberation mapping-calibrated estimators comes from the calibration of f, which is typically obtained through simplified geometric modelling or by requiring that reverberation-mapped AGNs follow the same SMBH mass – host galaxy correlations as other galaxies with dynamical SMBH mass measurements (e.g. Woo et al. 2010). An f derived in such a manner

introduces an intrinsic systematic uncertainty, as any bias from the SMBH mass – host galaxy correlations of quiescent galaxies propagates directly into reverberation-based masses. Moreover, variations of BLR structure and inclination from object to object imply that individual reverberation-based masses can deviate significantly from the mean calibration (e.g. Collin et al. 2006). Another limitation in reverberation-based methods stems from this method being applicable only to actively accreting systems, so that reverberation-based masses are unlikely to be representative of those of the quiescent galaxy population.

Despite these limitations, direct reverberation mapping remains the fundamental method of measuring SMBH masses in AGN, while reverberation mapping-calibrated single-epoch and luminosity-based estimators provide the route to study large samples of galaxies beyond the local Universe, enabling statistical studies of SMBH growth and its cosmic evolution (e.g. Shen 2013). As such, reverberation mapping SMBH masses are best viewed as complementary to other dynamical SMBH mass measurements, the multiple approaches jointly defining the SMBH mass scale across cosmic time.

1.2.5 Molecular gas dynamics

In recent years, a new method of SMBH mass determination has emerged that utilises cold molecular gas as the kinematic tracer. Particularly, CO has come to dominate the field. Attempts at using other molecular gas tracers such as hot molecular hydrogen have proven difficult due to turbulence and excitation from accretion and jet heating (e.g. Scharwächter et al. 2013). In contrast, CO is typically dynamically cold with a low intrinsic velocity dispersion, such that its observed kinematics are generally dominated by ordered rotation rather than pressure support or non-gravitational forces, making it particularly well suited to dynamical modelling in galaxy centres.

CO can be detected in a wide variety of galaxies along the Hubble sequence, even those that are no longer star forming. A systematic study of the molecular gas content of 67 representative massive galaxies ($M_* \gtrsim 10^{11.5}$ $M_\odot$; for more details see Section 1.4.2) from the MASSIVE survey (Ma et al. 2014) reports a $\approx$ 25 per cent detection rate of CO line emission down to a molecular-to-stellar mass fraction of $\approx$ 0.1 per cent (Davis et al. 2019). Similarly, the ATLAS^{3D} volume-limited survey of local ETGs reports a CO detection rate

of ≈ 22 per cent (Young et al. 2011). Consequently, as long as a suitable molecular gas reservoir exists within the SoI of a SMBH and is kinematically undisturbed, CO dynamical modelling can be used in galaxies spanning a wide range of masses and morphological types.

CO observations (and the derived kinematics and dynamical masses) are unaffected by dust, which is another strength of the method. It is however worth noting that subsequent modelling steps still require the use of an optical or near-infrared image to quantify the stellar contribution of each galaxy and this can be affected by dust (see Section 2.5.4). In turn, this can affect the fraction of the total dynamical mass attributed to the stars and the SMBH (e.g. Boizelle et al. 2019, 2021; Cohn et al. 2021; Dominiak et al. 2025).

Like ionised gas SMBH mass measurements, molecular gas measurements are obtained by modelling the rotation of a circumnuclear disc in the combined gravitational potential of the stellar mass distribution and a central point mass. Interferometric observations of CO emission provide spatially resolved velocity fields and spectrally resolved line profiles, which are forward-modelled to account for beam smearing, channel averaging, spatial and velocity binning and the intrinsic surface-brightness distribution of the gas (e.g. Davis et al. 2013a,b). The SMBH mass is then constrained by identifying the additional central mass required to reproduce the inner rise of the rotation velocities once the stellar contribution is fixed.

NGC 4526 was the first galaxy for which molecular gas was used to infer a SMBH mass (Davis et al. 2013b). Using the Combined Array for Research in Millimetre Astronomy (CARMA), Davis et al. (2013b) obtained CO(2–1) measurements with a spatial resolution of 0.25 arcsec (20 pc), yielding a SMBH mass of $4.5^{+4.2}_{-0.3} \times 10^8$ $M_\odot$. This work showed that when a cold molecular disc is present and well resolved spatially, CO kinematics can deliver constraints competitive with traditional stellar and ionised gas methods. Since this initial measurement the molecular gas approach has expanded rapidly, fueled by advances in millimeter and sub-millimeter interferometry, most notably ALMA, which now routinely delivers the angular resolution and surface brightness sensitivity required to resolve circumnuclear molecular discs at sub-arcsecond scales. Since NGC 4526, 27 more SMBH masses have been measured using the molecular gas method (see Section 5.1.2).

1.3 Scaling relations

As discussed above, the physical processes that govern galactic evolution leave imprints on the structural and dynamical properties of galaxies. One way that such imprints are identified and quantified is through the use of scaling relations. They link disparate physical quantities, often measured on different spatial scales and provide insight into how different galactic components co-evolve. As the quantities that underpin scaling relations can be measured across large and diverse galaxy samples, they offer a powerful framework for testing models of galaxy evolution.

Among the many known galaxy scaling relations, those based on dynamics are particularly informative, as they connect (luminous) mass assembly to the underlying gravitational potential. This thesis focuses on two such relations. First is the relation between SMBH mass and central stellar velocity dispersion (e.g. Magorrian et al. 1998; Ferrarese & Merritt 2000; Gebhardt et al. 2000), which indicates that SMBH mass is closely linked to the depth of the central gravitational potential established during bulge formation, reflecting the coupled assembly histories of SMBHs and galaxy bulges (e.g. Hopkins et al. 2008; Kormendy & Ho 2013). Second is the Tully-Fisher relation (TFR; Tully & Fisher 1977), which connects galaxy rotation and thus total mass to the luminous mass, in turn linking galaxy rotation to the efficiency of baryon retention and star formation during disc assembly (e.g. McGaugh et al. 2000; Dutton et al. 2007). Together, these relations probe galaxy evolution on complementary spatial scales.

1.3.1 $M_{\rm BH} - \sigma_{\rm e}$ relation

Among the many SMBH – host correlations, the tightest and most widely used is that between SMBH mass ($M_{\rm BH}$) and stellar velocity dispersion measured within the half-light (effective) radius ($\sigma_{\rm e}$), commonly referred to as the $M_{\rm BH} - \sigma_{\rm e}$ relation (e.g. Ferrarese & Merritt 2000; Gebhardt et al. 2000; Gültekin et al. 2009). The $M_{\rm BH} - \sigma_{\rm e}$ relation represents the cornerstone of SMBH – host galaxy scaling relations because $\sigma_{\rm e}$ is a direct dynamical tracer of the central gravitational potential of a galaxy, rather than a quantity that depends on stellar populations (e.g. Ferrarese & Merritt 2000; Gebhardt et al. 2000; Tremaine et al. 2002; Kormendy & Ho 2013). In addition, the $M_{\rm BH} - \sigma_{\rm e}$ relation exhibits the smallest intrinsic

scatter among a variety of similar scaling relations, suggesting that it is more fundamental than others (e.g. Gültekin et al. 2009; Kormendy & Ho 2013). In practice, this makes the $M_{\rm BH} - \sigma_{\rm e}$ relation the default anchor for testing co-evolution models in which SMBH growth is regulated by bulges (e.g. Silk & Rees 1998; King 2003; Fabian 2012).

A key development in the field has been the steady growth and diversification of the SMBH mass sample. Nevertheless, the calibration of the $M_{\rm BH} - \sigma_{\rm e}$ relation can only be as robust as the underlying SMBH masses. Unlike many galaxy scaling relations that rely on homogeneous measurements, $M_{\rm BH} - \sigma_{\rm e}$ is built from a heterogeneous set of SMBH mass determinations, whose assumptions and systematics substantially differ, particularly across methods. Current $M_{\rm BH} - \sigma_{\rm e}$ studies include SMBH masses determined using the full range of methods discussed in Section 1.2 (e.g. van den Bosch 2016; Sahu et al. 2019). Moreover, these methods are not applied uniformly across the galaxy population. Stellar kinematic methods have mainly been used for ETGs, ionised gas is typically used for LTGs, masers are predominantly present in rather low-mass Seyfert 2 and LINER galaxies and reverberation mapping is by construction used exclusively for AGNs.

The number of galaxies that have SMBH mass measurements determined through multiple methods is very small. However, these comparisons already suggest that non-negligible method-dependent differences exist. The clearest example is that of NGC 4258, a galaxy with one of the most accurate maser-based determinations of a SMBH mass. Stellar dynamical modelling using an orbit superposition method recovers a SMBH mass $\approx$ 15 per cent lower than (but consistent with) the maser SMBH mass (Siopis et al. 2009). However, later stellar dynamical modelling using the Jeans anisotropic modelling method inferred a SMBH mass $\approx$ 25 per cent larger than the maser SMBH mass and $\approx$ 45 per cent larger than the previous stellar dynamical SMBH mass (Drehmer et al. 2015). Such results motivate cross-check studies and highlight the need for a homogeneous method of SMBH mass determination across the entire Hubble sequence.

The fact that SMBH mass measurements vary so starkly between modelling methods has consequences for our understanding of SMBH – host galaxy correlations in general. Firstly, we do not know what fraction of the observed scatter of a SMBH – host galaxy correlation is intrinsic or a consequence of the uncertainties of the SMBH mass measurements. This

is a particularly pressing issue, as the best-fitting slopes of the ETG and LTG $M_{\rm BH} - \sigma_{\rm e}$ relations differ significantly (e.g. Lauer et al. 2007; McConnell & Ma 2013), although as discussed above so do the methods of SMBH mass determination in galaxies of different morphological types. Such an offset may therefore reflect genuine underlying astrophysical differences, but also cross-calibration offsets between different methods of SMBH mass determination (e.g. Kormendy & Ho 2013).

In addition, the local SMBH mass sample may be affected by a selection bias associated with the requirement that the SMBH SoI must be spatially resolved for a reliable dynamical measurement. It has been argued that this angular resolution selection preferentially favours galaxies with unusually large $\sigma_{\rm e}$ at fixed stellar mass (e.g. Shankar et al. 2016; Shankar et al. 2019). This requirement also biases samples towards galaxies with high central surface brightnesses and compact stellar distributions since a sufficient signal-to-noise must be achieved within the small spatial region subtended by the sphere of influence. Low surface brightness galaxies are therefore disfavoured, as the exposure times to obtain adequate kinematics within the sphere of influence would be prohibitively long. This can lead to a biasing of the observed normalisation and potentially the inferred slope and scatter of the $M_{\rm BH} - \sigma_{\rm e}$ relation.

Due to sparser measurements, there are also significant uncertainties in the slopes, scatters and forms of the scaling relations towards the high-mass end (McConnell & Ma 2013). The high-mass end is dominated by a small number of giant elliptical and brightest cluster galaxies (BCGs), precisely where we expect galaxy assembly to become increasingly dominated by dry merging. As two galaxies undergo a dry merger, their SMBHs can coalesce, thereby increasing the SMBH mass in the merged galaxy substantially. However, the process of coalescence can scour the stars from the centre of the merged galaxy, thereby causing a deficit of central light and only a modest change of $\sigma_{\rm e}$. In the context of the $M_{\rm BH} - \sigma_{\rm e}$ relation, this can lead to an increased scatter or an upward offset/deviation compared to a single power-law extrapolation (e.g. Lauer et al. 2007; Kormendy & Ho 2013; Saglia et al. 2016). Several extreme measurements of $\sim 10^{10}$ $M_{\odot}$ (e.g. Thomas et al. 2016; Mehrgan et al. 2019) sit significantly above the best-fitting single power law. Recent work in fact argues that galaxies with depleted centres (known as core-Sérsic galaxies)

may lie on an entirely different $M_{\rm BH} - \sigma_{\rm e}$ relation, contributing to the apparent steepening or "break" at the massive end (Sahu et al. 2019).

Taken together, these considerations highlight the central importance of the $M_{\rm BH} - \sigma_{\rm e}$ relation and the limitations it has as a result of sample selection, measurement systematics and sparse coverage at the high-mass end. Addressing these issues requires expanding the sample of robust and homogeneously-determined SMBH mass measurements, particularly of massive ETGs.

1.3.2 Tully-Fisher relation

While the $M_{\rm BH} - \sigma_{\rm e}$ relation links SMBHs to the depths of the host galaxy central gravitational potentials, galaxy scaling relations based on rotation probe the gravitational potentials on much larger, galaxy-wide spatial scales. The TFR (Tully & Fisher 1977), which connects a galaxy's total luminosity to its rotational velocity, is one of the most fundamental empirical relations in extragalactic astronomy. By measuring the ordered rotation of a galaxy, we probe its global mass distribution, both luminous (stars, gas, dust, etc.) and dark (e.g. Zwaan et al. 1995; McGaugh & de Blok 1998; Courteau et al. 2014).

From the perspective of galactic evolution, the importance of the TFR lies in its remarkable tightness across a wide range of galaxy masses and environments, particularly when expressed in terms of stellar or baryonic mass (e.g. McGaugh et al. 2000; Lelli et al. 2016). At its core, the TFR links how fast a galaxy rotates to how much baryonic mass it contains, implying a close connection between the depth of the underlying gravitational potential and baryonic mass assembly (e.g. Mo et al. 1998; McGaugh et al. 2000). In turn, the depth of the potential well is dominated on galactic scales by dark matter, primarily the dark matter halo outside the central region (e.g. Mo et al. 1998; Courteau et al. 2014). The TFR therefore provides a direct observational constraint on how baryons populate dark matter haloes and how efficiently they cool, settle and form rotationally supported structures (e.g. Dutton et al. 2010). In a simple ΛCDM framework, dark matter haloes are characterised by a virial velocity that scales with halo mass, and departures from a tight baryonic TFR naturally arise from variations of cooling efficiency, feedback strength and angular momentum loss (e.g. Dutton et al. 2007). The observed small intrinsic scatter of the TFR therefore implies that feedback processes must

act in a self-regulating manner that limits star formation and gas accretion without strongly perturbing the ordered rotational structure of the galaxy (e.g. McGaugh et al. 2000; Lelli et al. 2016). As such, the TFR offers a complementary view to bulge-based relations: whereas the $M_{\rm BH} - \sigma_{\rm e}$ encodes information about processes acting on sub-kiloparsec scales in the central regions of galaxies, the TFR reflects the outcome of galaxy assembly over tens of kiloparsecs.

This distinction in physical scale naturally raises the question of whether SMBHs correlate only with the central gravitational potentials of galaxies traced by $\sigma_{\rm e}$, or whether they also retain information about the global potentials traced by galaxy rotation. Ferrarese (2002) explored the possible link between SMBH mass and dark matter halo mass and suggested that SMBH growth is regulated by the depth of the host halo. Similarly, Pizzella et al. (2005) presented evidence for a non-linear relation between SMBH and halo mass. However these were primarily studies showing a correlation between rotational velocity and σ, which in turn revealed a correlation with SMBH mass by relying on the $M_{\rm BH} - \sigma_{\rm e}$ relation itself. Subsequent studies argued that the apparent correlation between $M_{\rm BH}$ and global rotation is largely secondary, arising from covariances with bulge properties rather than a direct coupling to the halo, and therefore cannot be taken as evidence of SMBH – halo co-evolution (e.g. Kormendy et al. 2011; Smith et al. 2021a). Distinguishing between these possibilities remains an important test of SMBH – host galaxy co-evolution models.

As with the $M_{\rm BH} - \sigma_{\rm e}$ relation, a meaningful interpretation of the TFR requires that rotation velocities be measured using homogeneous kinematic tracers with well understood systematics. Comparisons across galaxy morphologies or redshifts become increasingly uncertain when different tracers are mixed, as each one probes a different spatial extent, excitation conditions and has a different susceptibility to non-circular motions (e.g. Courteau et al. 2014). Molecular gas, and more specifically CO, provides a particularly powerful solution to this problem. In addition to tracing dynamically cold circumnuclear discs suitable for SMBH mass measurements, CO emission can also trace ordered rotation on larger galactic scales. Most importantly, CO is detectable in galaxies spanning a wide range of morphological types, including ETGs where H I is often weak or dynamically disturbed (e.g. Rose et al. 2019; Dunne et al. 2021), and it can be observed out to high redshifts with modern millimetre and radio facilities (e.g. Carilli & Walter 2013; Topal et al.

2018; Novak et al. 2019; Decarli et al. 2022; Kaasinen et al. 2024). As such, CO offers a particularly powerful opportunity to probe the gravitational potentials of galaxies from nuclear to baryon-dominated intermediate scales, across all morphological types and across cosmic time (e.g. Davis et al. 2011a, 2015; Tiley et al. 2016b; Topal et al. 2018).

Taken together, the scaling relations discussed above provide complementary perspectives on the connection between different galactic components. The $M_{\rm BH} - \sigma_{\rm e}$ relation links SMBH mass to the depth of a galaxy's central gravitational potential primarily shaped by bulge formation, while the TFR connects galaxy rotation to the total mass established during galaxy assembly. Interpreting these relations in a consistent manner requires robust and homogeneous measurements of both SMBH masses and galaxy dynamics across a wide range of galaxy types and mass scales. These considerations motivate this thesis.

1.4 This thesis

The preceding subsections have highlighted several outstanding challenges to understand galaxy evolution through the lens of scaling relations. In particular, the use of heterogeneous dynamical tracers complicates their interpretation. The work presented in this thesis exploits the sensitivity and angular resolution of ALMA to obtain spatially resolved CO kinematics of a large sample of galaxies, enabling in many cases robust and homogeneous measurements of both the SMBH masses and galaxy rotation. The data presented in this thesis were obtained as part of two collaborative efforts, the WISDOM Project and the MASSIVE Survey, both of which are discussed below.

1.4.1 WISDOM Project

The most prominent systematic survey of molecular gas SMBH masses is the mm-Wave Interferometric Survey of Dark Object Masses (WISDOM) project. To date, the SMBH masses of 10 galaxies have been measured as part of the WISDOM project. After the success of NGC 4526, which used a standard χ^2 test to compare the one-dimensional outer envelope of the observed and simulated position-velocity diagrams (PVDs), the work of Onishi et al. (2017) and Davis et al. (2017) inferred the SMBH masses of NGC 3665 and NGC 4697,

respectively, by comparing the full data cubes using a Markov chain Monte Carlo (MCMC) method with Gibbs sampling to explore the space of all model parameters.

The WISDOM Project has inferred the SMBH masses of 6 more giant ETGs: NGC 4429 (Davis et al. 2018), NGC 0524 (Smith et al. 2019), NGC 0383 (North et al. 2019), NGC 7052 (Smith et al. 2021b), NGC 1574 and NGC 4261 (Ruffa et al. 2023). It has also inferred the SMBH mass of the dwarf ETG NGC 0404 (Davis et al. 2020) and the luminous infrared galaxy with an AGN Fairall 49 (Lelli et al. 2022). Since the first molecular gas SMBH mass measurements, the field has grown increasingly sophisticated in its modelling considerations. Davis et al. (2018) and North et al. (2019) highlighted that stellar mass-to-light ratio (M/L) gradients can be required to reproduce the circumnuclear CO kinematics, and that such gradients can be a key systematic in molecular gas SMBH mass measurements. Smith et al. (2019) proposed a novel technique in which the observed gas distribution itself is used to create the model data cube, as opposed to describing the molecular gas distribution with a parametric function. Such an approach allows to handle the complex molecular gas distributions that are occasionally revealed by ALMA, and it has been used in other papers since. Smith et al. (2019) and Ruffa et al. (2023) both inferred the presence of position angle warps, which can now also be effectively accounted for in the modelling. The WISDOM Project has also highlighted some of the key challenges in modelling molecular gas to infer SMBH masses. Davis et al. (2018), Smith et al. (2019) and Smith et al. (2021b) all revealed central holes in the molecular gas discs; these remain a problematic issue as their presence limits our ability to reliably probe gas within $R_{\rm SoI}$. In fact, Ruffa et al. (2023) showed that in the case of NGC 0612, the hole is so large as to prevent a robust SMBH mass determination entirely. In such cases, only upper limits on the SMBH masses can be derived.

More recently the work of Zhang et al. (2025a) and Zhang et al. (2025b) presented ultra high-resolution CO observations, enabling increased precision measurements of the SMBH masses in NGC 0383 and NGC 1574, respectively. In fact, Zhang et al. (2025a) spatially resolved the nuclear molecular gas disc down to $\approx 41,300$ Schwarzschild radii, better than any other molecular gas SMBH mass measurement to date. Such a resolution puts molecular gas measurements in the same range as that of the best maser observations (Zhang et al. 2024).

Parallel to the work carried out within the WISDOM Project, several other studies have demonstrated the feasibility of measuring SMBH masses using molecular gas dynamics and analogous techniques. To date, molecular gas-based SMBH mass measurements have been reported for an additional 13 ETGs (Barth et al. 2016; Boizelle et al. 2019; Nagai et al. 2019; Ruffa et al. 2019; Boizelle et al. 2021; Cohn et al. 2021; Kabasares et al. 2022; Nguyen et al. 2022; Dominiak et al. 2024; Kabasares et al. 2024), 2 compact relic (red nugget) galaxies (Cohn et al. 2023; Cohn et al. 2024) and 3 LTGs (e.g. Onishi et al. 2015; Nguyen et al. 2020; Nguyen et al. 2021). Together, these studies confirm that molecular gas provides a robust and broadly applicable dynamical tracer for SMBH mass measurements across a wide range of galaxy types and environments.

In addition to SMBH mass measurements, the WISDOM Project has pursued a parallel programme focussed on the spatially resolved properties of giant molecular clouds (GMCs) in ETGs, exploiting ALMA's exquisite angular resolution to characterise the molecular ISM on cloud scales. To date the GMC properties of 5 galaxies have been studied: NGC 4429 (Liu et al. 2021), NGC 5806 (Choi et al. 2023), NGC 0613 (Choi et al. 2024), NGC 5064 (Liu et al. 2025) and NGC 1387 (Liang et al. 2026). WISDOM has also addressed a variety of other issues in galaxy formation such as multiscale feedback cycles (North et al. 2021), the morphology of the molecular ISM in galaxy centres and its dependence on galaxy structure (Davis et al. 2022), the star formation efficiency of spheroids (Lu et al. 2022, 2025), the link between circumnuclear molecular gas reservoirs and AGN fuelling (Elford et al. 2023) and the beam-by-beam properties of molecular gas in ETGs (Williams et al. 2023).

1.4.2 MASSIVE Survey

The MASSIVE Survey is a volume-limited, multi-wavelength, photometric and spectroscopic survey of the most massive galaxies in the local universe (Ma et al. 2014). Massive ETGs are the modern-day remnants of the earliest major star-formation episodes in the history of our universe and are essential to understand cosmic evolution, galaxy formation, stellar populations and SMBH formation. The MASSIVE sample includes 116 candidate galaxies in the northern sky (Dec. $> -6°$) with distances $D < 108$ Mpc and absolute integrated K-band magnitudes $M_K < -25.3$, corresponding to stellar masses $M_* \gtrsim 10^{11.5}$ $M_\odot$. MASSIVE is

designed to address a wide range of issues in elliptical galaxy formation and to date has investigated the photometric (Goullaud et al. 2018) and stellar kinematic (Veale et al. 2017a; Veale et al. 2017b; Veale et al. 2018; Ene et al. 2018; Ene et al. 2019, 2020) properties of its sample galaxies, the break in the high-mass end of the TFR (Davis et al. 2015), the properties of hot and warm ionised gas (Goulding et al. 2016; Pandya et al. 2017) and the primary drivers of the variations of the global stellar initial mass function (IMF; Gu et al. 2022), all in the most massive ETGs. A systematic study of the molecular gas content of 67 representative MASSIVE galaxies reports a 25 per cent (17/67) detection rate of CO line emission down to a molecular-to-stellar mass fraction of ≈ 0.1 per cent (Davis et al. 2019).

Another primary goal of the MASSIVE survey is to detect and measure the dynamical masses of central SMBHs within these homogeneously selected sample galaxies. Thus far only 12 of the MASSIVE galaxies have had SMBH mass estimates derived from direct dynamical modelling published. Most of these measurements were obtained from spatially resolved stellar kinematics and axisymmetric Schwarzschild modelling: in two brightest cluster galaxies in rich clusters (NGC 4889, McConnell et al. 2011; NGC 3842, McConnell et al. 2012), two brightest galaxies in galaxy groups (NGC 1600, Thomas et al. 2016; NGC 7619, Rusli et al. 2013) and three Virgo cluster galaxies (M87, Gebhardt et al. 2011; NGC 4649, Shen & Gebhardt 2010; NGC 4472, Rusli et al. 2013). More recently, the MASSIVE team has relaxed the axisymmetric assumption and performed triaxial orbit-based modelling to obtain new SMBH masses for two fast-rotating MASSIVE ETGs (NGC 1453, Liepold et al. 2020 and Quenneville et al. 2022; NGC 2693, Pilawa et al. 2022) and one slow-rotating MASSIVE ETG (NGC 315, Pilawa et al. 2025). A new determination of the M87 SMBH mass based on the same triaxial orbit code, TriOS, is reported in Liepold et al. (2023). Additionally, three SMBH masses in MASSIVE galaxies have been determined from dynamical modelling of the CO kinematics (NGC 315, Boizelle et al. 2021; NGC 383, North et al. 2019; NGC 7052, Smith et al. 2021b).

1.4.3 Structure of this thesis

This thesis is comprised of three core chapters in addition to this introduction (Chapter 1) and conclusions (Chapter 5). Chapter 2 contains a detailed discussion of the methodology used

Table 1.1: Properties of the galaxies for which we determine SMBH masses.

Target	T-type	D	$\log\left(\frac{M_{H_2}}{M_\odot}\right)$	SFR	M_K	$\log\left(\frac{M_\star}{M_\odot}\right)$	σ_e	$\log\left(\frac{M_{BH}}{M_\odot}\right)$	R_{SoI}
		(Mpc)		($M_\odot$ yr^{-1})	(mag)		(km s^{-1})		(arcsec, pc)
(1)	(2)	(3)	(4)	(5)	(6)	(7)	(8)	(9)	(10)
NGC 1684	E3	62.8	9.20	0.34	−25.70	11.77	262	9.00	0.21, 63
NGC 0997	E0	90.4	9.26	0.47	−25.68	11.76	215	8.49	0.06, 28
NGC 4751	S0/E6	26.9	8.36	–	−22.11	10.72	335.4	9.65	1.18, 154
NGC 1387	SB0	19.3	8.33	0.08	−24.00	11.02	170.2	7.95	0.13, 12
NGC 0467	S0	75.8	8.77	–	−25.76	11.79	247	8.81	0.12, 46
NGC 0665	S0	62.3	9.18	0.29	−25.39	11.63	164	7.86	0.03, 12
NGC 5208	S0	105.0	9.49	0.58	−25.87	11.84	235	8.69	0.08, 38
NGC 7550	E-S0	72.7	8.85	0.86	−25.43	11.65	224	8.58	0.09, 33

Notes. Columns: (1) Target name. (2) Morphological type. (3) Distance. (4) Total molecular gas mass. (5) Total star-formation rate. (6) Extinction-corrected total absolute K-band magnitude. (7) Total stellar mass estimated using M_K. (8) Average luminosity-weighted stellar velocity dispersion within one effective radius. (9) SMBH mass derived from the $M_{BH} - \sigma_e$ relation of van den Bosch (2016) using σ_e. (10) Predicted SMBH sphere of influence radius calculated using σ_e and M_{BH}.

to determine SMBH masses using molecular gas methods. It then presents the measurements of SMBH masses in four galaxies. Two of these galaxies, NGC 1684 and NGC 0997, are MASSIVE Survey targets. The other two galaxies, NGC 4751 and NGC 1387, are WISDOM Project targets. The work presented in Chapter 2 is adapted from Dominiak et al. (2024), Dominiak et al. (2025) and Dominiak et al. (2026a). Chapter 3 presents as yet unpublished material on four more MASSIVE Survey galaxies whose data, for reasons that will be clear below, were not conducive to the inference of robust SMBH masses. For two of these targets we were instead able to obtain SMBH mass upper limits and for one we were able to obtain a tentative SMBH mass that requires follow-up study. The physical properties of the galaxies for which SMBH masses are modelled are listed in Table 1.1 and the details of their ALMA data are listed in Table 1.2. Chapter 4 presents as yet unpublished work on a new CO TFR calibration for the local Universe, based on a large sample of galaxies observed for the WISDOM Project. The conclusions presented in Chapter 5 explore the SMBH masses obtained in this thesis in the context of the $M_{BH} - \sigma_e$ relation and the impact of SMBH mass measurement systematics on the relation.

Table 1.2: ALMA observations used in SMBH mass determinations.

Target	Track	Date	Array	Baseline range	Time (s)	MRS (arcsec, kpc)	FoV (arcsec, kpc)
(1)	(2)	(3)	(4)	(5)	(6)	(7)	(8)
NGC 1684	uid_A002_Xb12f3b_X825a	31.03.2016	12-m	15 m – 453 m	484	6.8, 2.1	24.8, 7.5
	uid_A002_Xbb30f0_X1ae5	29.11.2016	12-m	15 m – 704 m	302	4.3, 1.3	24.8, 7.5
	uid_A002_Xc2f3fc_X248e	02.08.2017	12-m	54 m – 3.3 km	998	1.3, 0.4	24.8, 7.5
NGC 0997	uid_A002_Xb6e98e_X5d28	19.08.2016	12-m	15 m – 1.5 km	759	3.9, 1.7	24.9, 10.9
	uid_A002_Xbb154b_X1dbd	26.11.2016	12-m	15 m – 704 m	423	4.3, 1.9	24.9, 10.9
	uid_A002_Xbb154b_X1dbd	22.08.2017	12-m	21 m – 3.7 km	1361	1.5, 0.6	24.9, 10.9
NGC 4751	uid_A002_Xc067f7_X721	17.05.2017	12-m	15 m – 1.1 km	1361	2.2, 0.3	16.7, 2.2
NGC 1387	uid_A002_Xc44eb5_X2e5d	07.09.2017	12-m	41 m – 7.5 km	726	1.1, 0.1	24.4, 2.3
	uid_A002_Xba26cb_X492	04.11.2016	12-m	19 m – 1.1 km	242	3.1, 0.3	24.4, 2.3
	uid_A002_Xbbfdf3_X1224	21.12.2016	12-m	15 m – 492 m	242	5.9, 0.6	24.4, 2.3
	uid_A002_Xc2bb44_X2142	28.07.2017	7-m	9 m – 45 m	1028	28.4, 2.7	41.8, 3.9
NGC 0467	uid_A002_Xe230a1_X1d0a	13.10.2019	12-m	15 m – 784 m	544	5.9, 2.2	24.8, 9.1
	uid_A002_Xee1eb6_X33f9	18.07.2021	12-m	15 m – 3.7 km	2359	1.7, 0.6	24.8, 9.1
NGC 0665	uid_A002_Xb618c7_X1b51	31.07.2016	12-m	15 m – 1.1 km	1391	4.5, 1.4	24.8, 7.5
NGC 5208	uid_A002_Xb09eed_X103c8	21.03.2016	12-m	15 m – 460 m	635	6.2, 3.1	24.9, 12.7
NGC 7550	uid_A002_Xe1baa0_X1f3a	03.10.2019	12-m	15 m – 2.3 km	544	4.6, 1.6	24.8, 8.8
	uid_A002_Xeea188_X381c	24.07.2021	12-m	47 m – 5.2 km	2250	1.0, 0.4	24.8, 8.8
	uid_A002_Xee609c_X1f84	24.07.2021	12-m	15 m – 3.7 km	2250	1.3, 0.5	24.8, 8.8

Notes. Columns: (1) Target name. (2) Track ID. (3) Observations date. (4) ALMA array and type of antennae. (5) Minimum and maximum baseline lengths. (6) Total integration time on source. (7) Maximum recoverable scale (MRS), i.e. the largest angular scale structure that can be recovered with the given array configuration. (8) Field of view (FoV), i.e. the primary beam full-width at half-maximum.

This is what we were generated by nature and God in order to do. So what is this thing? When Pythagoras was asked, he said, 'to be an observer of the sky,' and he used to claim that he himself was an observer of nature, and it was for the sake of this that he had passed into his way of life. And they say that when someone asked Anaxagoras for what reason anyone might choose to come to be born and to live, he replied to the question by saying that it was 'to be an observer of the sky and the stars around it, as well as moon and sun,' since everything else at any rate is worth nothing.

— Aristotle's *Protrepticus*

2

Supermassive Black Hole Masses

Contents

2.1 Introduction 30
2.2 Dynamical Modelling 31
2.2.1 Simulating interferometric data 31
2.2.2 Fitting process 37
2.3 NGC 1684 39
2.3.1 Galaxy Properties 39
2.3.2 ALMA Observations 40
2.3.3 CO Modelling 46
2.3.4 Discussion 52
2.4 NGC 0997 54
2.4.1 Galaxy Properties 55
2.4.2 ALMA Observations 56
2.4.3 CO Modelling 60
2.4.4 Discussion 63
2.5 NGC 4751 65
2.5.1 Galaxy Properties 65
2.5.2 ALMA Observations 68
2.5.3 CO Modelling 72
2.5.4 Discussion 79
2.6 NGC 1387 90
2.6.1 Galaxy Properties 90
2.6.2 ALMA Observations 91
2.6.3 CO Modelling 96
2.6.4 Discussion 104
2.7 Conclusions 108

2.1 Introduction

Despite contributing very small fractions of the total galaxy masses and having very limited spatial extents, it is now recognised that central SMBHs have major impacts on the galaxies they lie within. Observational efforts over the last 30 years have indeed established that SMBH mass correlates with many host galaxy properties, suggesting co-evolution (e.g. Gebhardt et al. 2000; McConnell & Ma 2013; van den Bosch 2016). Nonetheless, the growth of both SMBHs and galaxies and their self-regulating relationship are poorly understood (e.g Harrison et al. 2018; D'Onofrio et al. 2021).

A key issue to better understand SMBH mass – host galaxy correlations is the accuracy of the SMBH masses. Whilst many easily-observed galactic properties can serve as indirect proxies of a SMBH's mass, an accurate measurement of the mass can only be obtained by directly probing and modelling the kinematics of the material orbiting the SMBH. Traditionally, integrated stellar populations (e.g. Cappellari et al. 2009; Krajnović et al. 2009; McConnell et al. 2012), ionised gas (e.g. van der Marel & van den Bosch 1998; Ferrarese et al. 1996) and masers (e.g. Kuo et al. 2011; Gao et al. 2016; Pesce et al. 2020) have been used as kinematic tracers.

Over the past decade, the unprecedented resolution and sensitivity of ALMA has also allowed to probe the kinematics of molecular gas within the SoI of SMBHs, thus leading to a new method of SMBH mass determination (Davis et al. 2013b). CO has proven itself to be an excellent kinematic tracer, present in the nuclear regions of both ETGs and LTGs and unattenuated by dust (Ruffa & Davis 2024).

In this chapter, we apply the CO dynamical modelling method to estimate the SMBH masses in four ETGs using high-resolution ALMA data. This chapter is structured as follows. In Section 2.2 we describe the general principles behind molecular gas dynamical modelling, including the process of creating of a model data cube and its fitting to the observed data. In Sections 2.3 and 2.4 we present the SMBH masses for NGC 1684 and NGC 0997, both MASSIVE Survey galaxies. In Section 2.5 and 2.6 we present the SMBH of NGC 4751 and NGC 1387, both WISDOM Project galaxies. In each of these sections we summarise the main properties of the targets, present the ALMA data and their reduction, outline the creation of

the properties of the continuum emission and the CO data cubes, and present and discuss the results of their dynamical modelling. We then briefly conclude our findings in Section 2.7

2.2 Dynamical Modelling

Dynamical modelling is carried out by fitting a model to the observed molecular gas distribution and kinematics. Each model data cube is created using the Python version of KINEMATIC MOLECULAR SIMULATION (KINMS[1]; Davis et al. 2013a). The KINMS method requires a circular velocity curve derived from the stellar light distribution. We create the stellar mass model using multi-Gaussian expansion (MGE) photometry (Cappellari 2002) and calculate the associated circular velocities using the JEANS ANISOTROPIC MODELLING Python package (JAMPY[2]; Cappellari 2020). We assume an axisymmetric, geometrically thin, circularly rotating gas disc with a spatially constant intrinsic dispersion $\sigma_{\rm gas}$ throughout, and we model instrumental effects during cube creation. Dark matter is neglected during modelling, as at the radii probed its contribution is expected to be small and largely degenerate with the stellar mass. We fit the full cube rather than moment maps to retain maximal information and avoid correlated errors associated with masking. The KINMS model is then compared in a Bayesian way to our data using the general Gibbs sampler with adaptive stepping GASTIMATOR[3]. We implement GASTIMATOR and KINMS using the Python wrapper KINMS_FITTER[4], which provides a simple interface between the two and an easily-accessible integrated library of surface brightness radial profiles. In this section we discuss the remaining details of model creation and of the fitting procedure.

2.2.1 Simulating interferometric data

In order to construct a model CO cube we need the following information: (i) a CO surface brightness model, (ii) a stellar light model, (iii) the corresponding circular velocity curve including a central point mass simulating the SMBH, and (iv) a realistic rendering of the interferometric response. Each step is discussed below.

[1] https://kinms.space
[2] https://pypi.org/project/jampy/
[3] https://github.com/TimothyADavis/GAStimator
[4] https://github.com/TimothyADavis/KinMS_fitter

Molecular gas distribution

In order to simulate a mock interferometric observation, we must first quantify the distribution of molecular gas in the galaxy. This can be done in one of two ways, both of which will be used for different targets throughout this thesis.

If the morphology of the molecular gas in the galaxy is relatively simple we can describe it using a parametric function. In general a thin (i.e. two-dimensional, 2D) exponential disc has been shown to be appropriate in ETGs (Davis et al. 2013a) and has been used in a number of works (e.g. Davis et al. 2017; Smith et al. 2019; Ruffa et al. 2023):

$$I(R) \propto e^{-R/R_0} \quad , \tag{2.1}$$

where R is the galactocentric radius and R_0 is the exponential scale length, the latter being a free parameter in the model. However, at the spatial resolutions achieved by ALMA central holes, depressions and/or complex features are often detected, thus making it necessary to employ more complex surface brightness profiles. A relatively common augmentation of the exponential disc model that we will use throughout (e.g. for NGC 1684, NGC 5208) is the addition of an inner truncation to capture the presence of a hole or depression in the gas:

$$I(R) \propto \begin{cases} 0 & R \leq R_{\rm hole} \\ e^{-R/R_0} & R > R_{\rm hole} \end{cases} , \tag{2.2}$$

where R is the galactocentric radius, R_0 is the exponential scale length and $R_{\rm hole}$ is the truncation radius, the latter two being free parameters of the model. However, as will be seen in Section 2.3, we have also experimented with other profiles when this is justified by the data, including central Gaussian tapers and intrinsic Gaussian profiles. In each case, the parameters that describe the analytic function become free parameters of the model.

However, when any combination of parametric functions fails to adequately reproduce the observed gas distribution there is an alternative way to simulate the molecular gas distribution. There is no intrinsic need to specify the distribution analytically, and in cases where the gas is particularly morphologically complex we can use the observed gas distribution as a component of our modelling instead. We implement this using the custom-made KinMS plugin SkySampler[5], described by Smith et al. (2019). First, we

[5] https://github.com/Mark-D-Smith/KinMS-skySampler

obtain the kinematics-independent distribution of the gas by integrating the point source model (i.e. the clean components yielded during the CASA cleaning process) of the gas distribution along the velocity axis. We choose to sample the clean components instead of the ALMA data cube itself, as mock data cube creation involves convolving the simulated data with a Gaussian beam to reproduce instrumental effects. If we were to sample the ALMA cube itself, which is already convolved with the beam, we would effectively be convolving and smearing the simulated cube twice. We then sample the distribution of gas with a large number of particles (of the order $\approx 10^6$). Assuming a certain position angle and inclination for the galaxy (both of which are usually free parameters of the KinMS model), the particle positions can then be deprojected into their intrinsic positions in the galaxy plane using the KinMS_fitter task `transformClouds`.

Whether the surface density profile is described using SkySampler or a parametric function, the molecular gas distribution must be scaled to match the data. Instead of specifying a central surface brightness, we instead scale the entire cube to match the overall integrated CO flux, leading to another free parameter of our model.

Lastly, we wish for our 2D molecular gas distribution to be transformed into a three-dimensional (3D) distribution and thus our model also takes into account the velocity dispersion of the molecular gas ($\sigma_{\rm gas}$), also another free parameter of our model. We assume this velocity dispersion to be spatially constant and small relative to the rotational velocities, as is typically observed in nearby, dynamically-cold molecular gas discs (often < 10 km s^{-1} e.g. Davis et al. 2017, Smith et al. 2019, North et al. 2019).

Stellar distribution

To infer the SMBH mass of each galaxy accurately, the stellar mass contribution must be quantified and accounted for by the model. The kinematics are in principle also affected by dark matter, but at the small radii probed here the dark matter contribution will be assumed to be negligible (it would in any case be largely degenerate with that of the stars). We parameterise the stellar light distribution using a multi-Gaussian expansion (MGE; Emsellem et al. 1994, Cappellari 2002) model of an optical image of the galaxy, which in the majority of cases is a *HST* image. Whilst the molecular gas itself is not affected by

Table 2.1: Parameters of the circular MGE PSFs for filters used.

Telescope	Instrument	Filter	G_k (arcsec)	σ_k
(1)	(2)	(3)	(4)	(5)
HST	ACS	F606W	0.385	0.0325
			0.489	0.0643
			0.126	0.2192
	WFC3	F110W	0.500	0.0494
			0.384	0.1055
			0.116	0.4009
			9.25×10^{-5}	1.1069
	WFC3	F160W	0.355	0.0494
			0.543	0.1206
			0.102	0.4117
CFHT	WIRCam	K_s-band	0.267	0.9820
			0.427	1.6560
			0.203	2.7213
			0.072	4.4024
			0.024	7.2564
			0.007	13.8925

Notes. Circular MGE components. (3) Filter. (4) Normalisation factor of Gaussian component (summing up to 1). (5) Standard deviation of Gaussian component.

dust, the *HST* images are. To this end we systematically choose the longest wavelength *HST* image available, to minimize dust extinction. In addition to this, we tend to mask the most obviously dust-obscured pixels in the images when possible.

The MGE model of the stellar light distribution is created using the `mge_fit_sectors` procedure of MgeFit[6] (Cappellari 2002). First, the MGE is parametrised as a sum of Gaussians, each with a central surface brightness I', a width σ' and an axial ratio q'. These Gaussians are then convolved with a point spread function (PSF) of the image filter in order to account for instrumental effects. Generic models of the *HST* filter PSFs were generated using TinyTim (Krist et al. 2011) and then parametrised by fitting a circular MGE model using the same MgeFit package as above. The results of the PSF parametrisation for the *HST* filters used in this thesis are listed in Table 2.1. The convolved Gaussians are then iteratively compared to the 2D projection of the stellar light distribution captured by the *HST* image until an adequate fit is made.

[6] https://pypi.org/project/mgefit/

Table 2.2: Details of the *HST* images used and parameters for the MGE luminosity conversion in the AB magnitude system.

Target	Instrument	Filter	Project code	PI	Exposure (s)	$M_{\odot,AB}$ (mag)	ZPT_{AB} (mag)	Extinction (mag)
(1)	(2)	(3)	(4)	(5)	(6)	(7)	(8)	(9)
NGC 0997	WFC3	F160W	15909	Boizelle	996	4.60	25.94	0.071
NGC 1684	WFC3	F110W	14219	Blakeslee	2496	4.52	26.82	0.051
NGC 4751	WFC3	F160W	15909	Boizelle	997	4.60	25.94	0.062
NGC 1387	WFC3	F160W	15909	Boizelle	1197	4.60	25.94	0.006
NGC 0665	WFC3	F110W	14219	Blakeslee	1997	4.52	26.82	0.078
NGC 5208	WFC3	F160W	15909	Boizelle	997	4.60	25.94	0.018
NGC 7550	ACS	F606W	14840	Bellini	696	4.72	26.49	0.338

Notes. (1) Target name. (2) *HST* instrument. (3) Filter. (4) Project code. (5) Principal investigator. (6) Exposure time. (7) Solar absolute magnitude. (8) Zero-point magnitude. (9) Galactic extinction. All images were obtained from the Mikulski Archive for Space Telescopes (MAST) in their calibrated and drizzled format.

Each best-fitting Gaussian is then converted into a corresponding peak surface brightness using standard MGE formalism (Cappellari 2002). This surface brightness is expressed in counts pixels^{-1} which can itself be converted to a surface brightness expressed in mag arcsec^{-2} in the corresponding photometric band, using standard photometric formulas. Finally, this surface brightness can then be converted into physical units of surface density ($L_\odot$ pc^{-2}) by adopting Solar luminosities from Willmer (2018) and calculating the zeropoints as in Sahu et al. (2019), all in the AB magnitude system (apart from NGC 0467 which has its surface density calculated in the Vega magnitude system; see Section 3.4.3 for details). We also adopt extinctions from the NASA/IPAC Extragalactic Database (Schlafly & Finkbeiner 2011) to correct for interstellar reddening. The details of the *HST* images used in this thesis, as well as all parameters necessary to convert our MGE Gaussians into physical units are listed in Table 2.2. The parameters of the best-fitting MGE Gaussians prior to convolution (from here on referred to as the deconvolved Gaussians) will be listed in their respective sections. In the case of NGC 0467 there is no *HST* image and thus we use a *Canada-France-Hawaii Telescope* (*CFHT*) image to parametrise the stellar light distribution. The details of the photometric conversion and treatment of the PSF are all discussed in the relevant Section 3.4.3.

Circular velocity curve

Given an inclination i, which is also a free parameter in most of our models, we can analytically deproject the 2D stellar light distribution into a 3D stellar luminosity density

distribution. The deprojection inferring the intrinsic density from the observed surface brightness is mathematically non unique (Gerhard & Binney 1996) and the degeneracy becomes particularly severe at low inclination (Rybicki 1987). Thus the MGE formalism provides one possible deprojection that is consistent with the observed surface brightness. However, this deprojection is only defined if $\cos^2 i < q'^2$ for all Gaussians, so that the flattest Gaussian of an MGE model dictates the minimum possible inclination for which an MGE model can be used in a dynamical model.

Our 3D light volume density distribution can itself be converted into a 3D stellar mass volume density distribution by multiplying each Gaussian component by a stellar M/L. For the near-infrared bands the use of a radially-constant M/L is typically an adequate approximation. Davis & McDermid (2017) found that when M/L gradients are explicitly allowed, they are generally mild in ETGs and do not significantly change the inferred central potential. As such, the M/L is another free parameter of the model. We can then take our stellar mass model, add to it an analytic Keplerian potential that simulates a central supermassive black hole mass, itself another free parameter in the model, and input this into the `mge_vcirc` routine of JamPy, to calculate the associated circular velocity curve.

In some models, where there is a clear need, we will instead use a radially linearly varying M/L. This is implemented by taking the circular velocity curve derived as above, assuming a M/L of unity (1 $M_\odot/L_\odot$) and scaling that curve by the square root of the variable M/L (as circular velocities are proportional to the square root of the enclosed masses). In such a case, the M/L intercept and M/L gradient are free parameters of our model as opposed to a singular constant M/L.

Simulated data cube

Given a molecular gas distribution, parameters orienting the molecular gas disc, and a circular velocity curve, KinMS can produce a simulated data cube. More specifically, KinMS produces a set of particles at given positions such that they replicate the specified molecular gas distribution. It then assigns each particle a velocity as expected given the circular velocity curve. For each particle, this velocity is then randomly augmented (an additional velocity component is added or subtracted) in order to reproduce the specified

velocity dispersion. The model data cube is then created by computing the line-of-sight projections of the particles, whilst taking into consideration some crucial free parameters of our model, such as the central position, systemic velocity, inclination and position angle (the latter two typically assumed to be radially constant). To replicate instrumental effects, this cube is then spatially convolved with the Gaussian synthesised beam. The model cube is then binned (spatially and spectrally) into pixels identical to those of the real data cube.

In general, every model will have the minimum parameters of a SMBH mass ($M_{\rm BH}$), spatially-constant stellar M/L, integrated flux and velocity dispersion ($\sigma_{\rm gas}$), and the "nuisance" disc parameters position angle, inclination (i), systemic velocity ($V_{\rm sys}$) and centre position (offsets in right ascension and in declination from the image phase centre). The particular information about the models used in each galaxy are contained in the relevant sections.

2.2.2 Fitting process

To identify the best-fitting model, we adopt a forward modelling approach whereby modelled data are compared against actual observations. Once a model data cube is generated as above, we compare it to the ALMA data cube using GAStimator[7], a Gibbs-style MCMC sampler with adaptive stepping which easily interfaces with KinMS through the Python wrapper KinMS_fitter. GAStimator explores the parameter space of all free model parameters by updating one parameter at a time while holding the remaining parameters fixed, a strategy reminiscent of Gibbs sampling. Because the conditional posterior distributions of the model parameters are not analytically known, direct Gibbs sampling is not possible. Instead, proposed parameter updates are evaluated using a Metropolis–Hastings acceptance criterion, whereby the likelihood of the resulting model is calculated and the proposed step is either accepted or rejected. For some of the parameters, we set reasonable priors (listed alongside the best-fitting model parameters in each section) to ensure that the fitting process converges in a finite time. Other parameters are allowed to vary across their entire possible range (for example, position angle varying over the full 360°). Typically, all priors are linearly uniform, except that of the SMBH mass which is logarithmically uniform because of its

[7] https://github.com/TimothyADavis/GAStimator

large dynamic range. However, in some cases (NGC 0997 and NGC 0665) we ultimately revert to a linear sampling (for explanation see Section 2.4.3).

Initially, the MCMC explores the parameter space in a manner such that the step size between each fit is adaptively scaled until the chain converges. Once the MCMC chain has converged, the maximum step size is fixed and the MCMC continues sampling the parameter space, to generate samples from the final posterior probability distribution. The initial burn-in phase to identify the convergent chain usually comprises ≈ 10 per cent of the total number of steps. Assuming the maximally ignorant priors above and constant Gaussian errors throughout the cube, the posterior probability distribution of a model is proportional to the log-likelihood function $\ln P \propto -0.5\chi^2$, where χ^2 is defined in the standard manner as the sum (over the mask defined by KinMS which contains all the pixels with flux 1.5 times the rms) of the differences between model and data squared normalised by the uncertainties squared. However, the formal Gaussian likelihood implicitly assumes that every pixel in the cube represents an independent constraint. In interferometric data this assumption is not strictly valid because the synthesised beam introduces correlations between neighbouring pixels, reducing the effective number of independent measurements. Consequently, the formal Gaussian likelihood effectively overestimates the number of independent constraints and, in the case of a large number of pixels, yields unrealistically small parameter uncertainties. The standard deviation of a χ^2 distribution is proportional to $\sqrt{2N}$, where N is the number of constraints. For a large N the standard deviation is non-trivial and sets the natural scale for statistically significant differences between models. Since χ^2 scales as σ^{-2}, multiplying the uncertainties by a factor of $(2N)^{0.25}$, where N is the number of constraints (i.e. the number of pixels within the same mask as defined above), rescales the likelihood by the factor of $\sqrt{2N}$. This effectively rescales the likelihood such that the differences between models take into account the statistical fluctuations of a model with N constraints, thereby mitigating the tendency of highly oversampled datasets to produce artificially tight confidence intervals. This approach was originally proposed by van den Bosch & van de Ven (2009) for use in least-squares fitting and adapted to the Bayesian framework by Mitzkus et al. (2017) and has been shown to yield uncertainties that are consistent with those found using a bootstrap approach (Smith et al. 2019).

Each of the free parameters of our model undergoes a process of marginalization as a part of the MCMC chain. The probability distributions of each parameter against the others are shown as 2D marginalizations in the form of corner plots in each respective section, where each data point represents the log-likelihood of a model. The coloured data points show models within $\Delta\chi^2 < \sqrt{2N}$ with the white data points being most likely and the blue data points least likely. The grey data points show all remaining models that do not fulfill the aforementioned condition. The posterior probability distributions of the individual parameters are also shown as 1D marginalizations (i.e. histograms). Chains are assumed to have converged when the histograms display a roughly Gaussian shape.

2.3 NGC 1684

The material in this section was originally published in the Monthly Notices of the Royal Astronomical Society, Volume 529, Pages 1597 – 1616.

2.3.1 Galaxy Properties

NGC 1684 is an E3 elliptical galaxy located at $04^{\rm h}52^{\rm m}31\overset{\rm s}{.}15$, $-03°06'21\overset{''}{.}8$ (J2000.0) in the constellation of Orion. We adopt the distance used in the MASSIVE survey, $D = 62.8 \pm 2.3$ Mpc, obtained through surface brightness fluctuation (Jensen et al. 2021). At this distance, 1 arcsec corresponds to ≈ 304 pc. NGC 1684 is in a group of 11 galaxies according to the Two Micron All Sky Survey (2MASS; Skrutskie et al. 2006) Redshift Survey (2MRS; Crook et al. 2007), of which it is the brightest. There is a much smaller elliptical galaxy-like object just $\approx$ 6 arcsec west of NGC 1684, most likely a low-mass galaxy in the process of being accreted (see Fig. 2.1).

Davis et al. (2015) estimated the inclination of the galaxy to be $42 \pm 5°$, but as neither dust lane nor interferometric observations of the source existed at the time, this was estimated using the axial ratio from the NASA/IPAC Extragalactic Database (NED). *HST* optical images reveal a prominent dust disc, with dust lanes to the north-west of the galaxy centre and an unobscured nucleus (Fig. 2.1). The dust disc has a semi-major axis of 24.5 arcsec and a semi-minor axis of 9.6 arcsec, yielding an inclination estimate of $\approx 67°$, clearly suggesting that the previous estimate was too low.

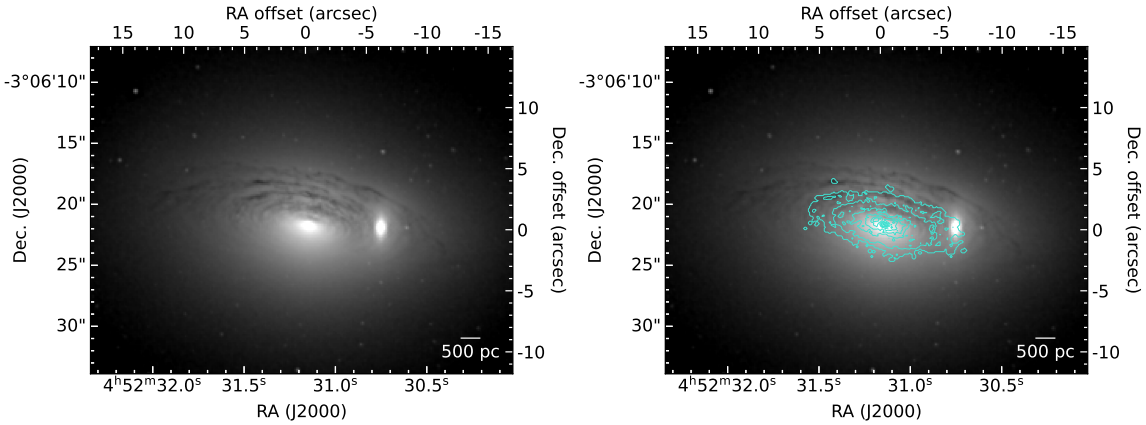


Figure 2.1: Unsharp-masked *HST* Wide Field Camera 3 (WFC3) F110W filter (J-band) image of NGC 1684 (left), overlaid with the ^{12}CO(2–1) integrated intensity contours (cyan) from our ALMA observations (right).

NGC 1684 hosts a significant molecular gas reservoir, with a total H_2 mass of $1.58^{+0.08}_{-0.07} \times 10^9$ $M_\odot$, and has a total star formation rate (SFR) of 0.34 ± 0.03 $M_\odot$ yr^{-1} derived from corrected 22 μm luminosities (Davis et al. 2015). It has an integrated absolute K-band magnitude of -25.70 (Quenneville et al. 2022) which results in a total stellar mass of 5.86×10^{11} $M_\odot$ (calculated using Eq. 2 of Cappellari 2013).

NGC 1684 does not have a direct SMBH mass measurement, but an estimate can be obtained using the $M_{\rm BH} - \sigma_{\rm e}$ relation of van den Bosch (2016). Assuming $\sigma_{\rm e} = 262$ km s^{-1} (Veale et al. 2018), a SMBH mass of $\approx 1.0 \times 10^9$ $M_\odot$ is expected. The $R_{\rm SoI}$ of a SMBH quantifies the spatial scale over which the gravitational potential of a SMBH is dominant, and using the typical definition of $R_{\rm SoI} \equiv GM_{\rm BH}/\sigma_{\rm e}^2$, we get a predicted $R_{\rm SoI} \approx 63$ pc (or $\approx$ 0.21 arcsec) for NGC 1684.

2.3.2 ALMA Observations

Observations of the ^{12}CO(2–1) emission line using the 12-m ALMA array were obtained as part of projects 2015.1.00187 (PI: Davis) and 2016.1.00683 (PI: Ma). The NGC 1684 data are comprised of three tracks taken on 31st March 2016, 29th November 2016 and 2nd August 2017, for a total of 30 minutes on source. Baselines span 15.1 m to 3.3 km, yielding an angular resolution of 0.1 arcsec, a maximum recoverable scale (MRS; the largest angular scale structure that can be reliably recovered by the interferometer) of 6.8 arcsec, and a field of view of 24.8 arcsec. The properties of the observations are listed in Table 1.2.

ALMA Band 6 was used for all observations. Each of the three tracks had a total of four spectral windows, one of which was centred on the redshifted frequency of the ^{12}CO(2–1) line (rest frequency $\nu_{\rm rest}$ = 230.5380 GHz) with a bandwidth of 1.875 GHz ($\approx$ 2440 km s^{-1}). For one track this spectral window was subdivided into 3840 channels of width $\approx$ 488 kHz ($\approx$ 0.64 km s^{-1}), while for the other two tracks this spectral window was subdivided into 1920 channels of width $\approx$ 977 kHz ($\approx$ 1.27 km s^{-1}). The remaining three spectral windows each had a bandwidth of 2 GHz ($\approx$ 2600 km s^{-1}) and were used to map the continuum. For one track these continuum spectral windows were subdivided into 128 channels of width $\approx$ 16 MHz ($\approx$ 20 km s^{-1}), while for the other two tracks these continuum spectral windows were subdivided into 240 channels of width $\approx$ 8 MHz ($\approx$ 10 km s^{-1}). For each track, bright quasars were used as bandpass, flux, phase and water vapour calibrators.

The data were calibrated using the standard ALMA pipeline and were concatenated using the default weighting, using the Common Astronomy Software Applications (CASA) package (McMullin et al. 2007).

Line emission

The continuum spectral windows and line-free channels of the line spectral window were linearly fit and the fit subtracted from the *uv*-plane data using the CASA `uvcontsub` task. The continuum-subtracted *uv* data were then imaged and cleaned in regions of source emission to a threshold equal to the root-mean-square (RMS) noise of the dirty channels (in regions free of line emission), using the cube mode of the CASA task `tclean` and Briggs weighting with a robust parameter of 0.5. We adopt a channel width of 10 km s^{-1}, the typical velocity resolution used in molecular gas determinations of SMBH masses. The resulting data cube has a synthesised beam of 0.21 arcsec $\times$ 0.14 arcsec (64 $\times$ 43 pc^2; sampled with $\approx$ 3 – 5 spaxels linearly) with a RMS noise of 0.53 mJy beam^{-1} channel^{-1}. Here and throughout the thesis the beam sizes are all full-widths at half-maxima (FWHM). All the properties of the resulting data cube are summarised in Table 2.3.

The zeroth (integrated-intensity), first (intensity-weighted mean line-of-sight velocity) and second (intensity-weighted line-of-sight velocity dispersion) moment maps of NGC 1684 are shown in Figs. 2.2, along with a kinematic major-axis PVD. The maps were created using the

Table 2.3: CO data cube properties for NGC 1684.

Image property	Value
Spatial extent (pix)	1024×1024
Spatial extent (arcsec)	51.2×51.2
Spatial extent (kpc)	15.6×15.6
Pixel scale (arcsec pix^{-1})	0.05
Pixel scale (pc pix^{-1})	15.2
Velocity range (km s^{-1})	3950 – 4850
Channel width (km s^{-1})	10
RMS noise (mJy beam^{-1} channel^{-1})	0.53
Number of constraints	194, 887
Synthesised beam (arcsec)	0.21×0.14
Synthesised beam (pc)	64×43

masked-moment technique (Dame 2011) implemented in the PYMAKEPLOTS package[8]. First, a copy of the CO data cube without primary-beam correction is boxcar-smoothed in the spatial and spectral dimensions, with a spatial kernel of 1.5 times the width of the synthesised beam and a spectral kernel of 4 times the channel width. A binary mask is then created by clipping the smoothed data cube at a threshold of five times the RMS noise of the line-free channels of the smoothed data cube. The moment maps and PVDs are then created by applying this mask to the unsmoothed primary beam-corrected (i.e. the original) data cube. All moment maps in this thesis are created in the same manner, using the same boxcar kernels with the same widths in both directions, unless stated otherwise. The PVD was constructed by summing pixels in each masked cube within a pseudo-slit 5 pixels wide oriented along the kinematic position angle of 258.°1, determined by our kinematic modelling results in Section 2.3.3.

In NGC 1684, we clearly detect a disc of molecular gas in regular rotation and coincident with (but smaller than) the dust disc (see Fig. 2.1), with a central hole of ≈ 0.35 arcsec in radius. Such holes are frequently detected in galaxies where the molecular gas has been sufficiently well spatially resolved, and may be due to a number of processes [e.g. shear and/or tidal disruption of gas clouds, Smith et al. 2021b, Liu et al. 2021; photodissociation by a hard radiation field due to an active galactic nucleus (AGN), Visser et al. 2009; thermal effects from an accretion disc reducing the fraction of gas emitting in the low-J transitions, Wada et al. 2018].

[8] https://github.com/TimothyADavis/pymakeplots

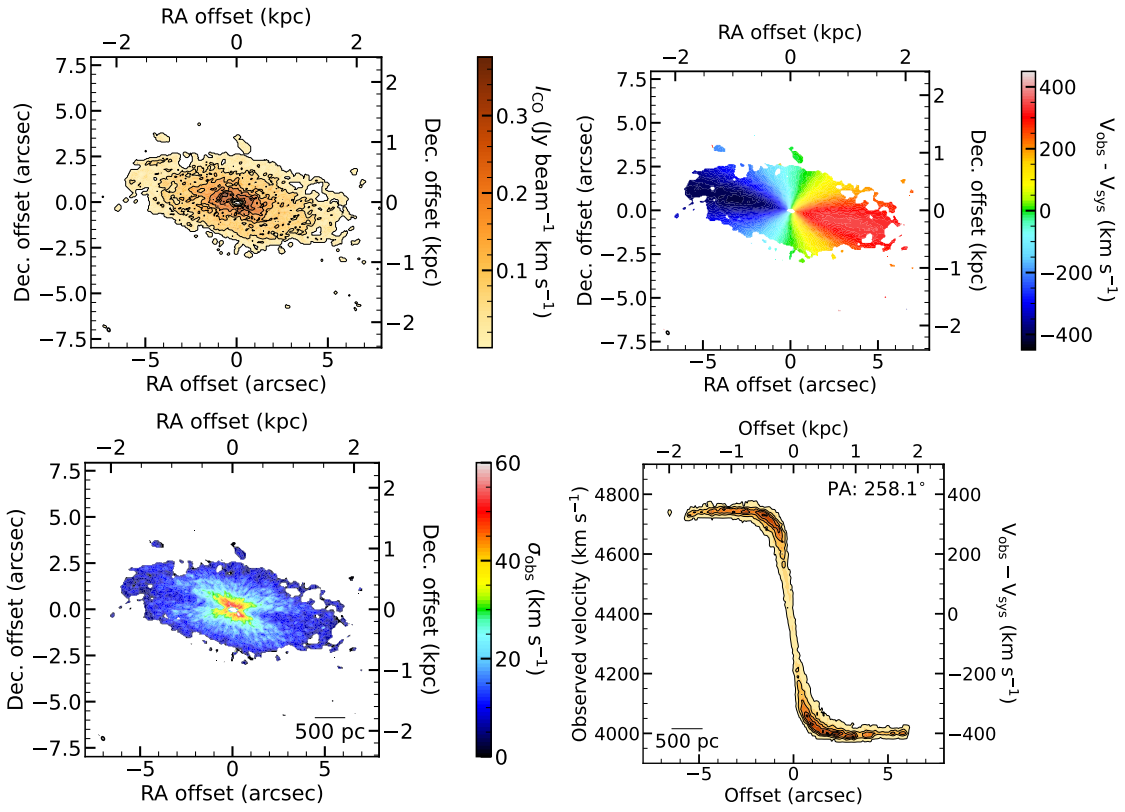


Figure 2.2: ^{12}CO(2–1) emission properties of NGC 1684 derived from our ALMA data. **Top-left:** Zeroth-moment (integrated-intensity) map. **Top-right:** First-moment (intensity-weighted mean line-of-sight velocity) map. The dashed black line shows the kinematic major axis. **Bottom-left:** Second-moment (intensity-weighted line-of-sight velocity dispersion) map. **Bottom-right:** Kinematic major-axis position-velocity diagram. The synthesised beam is shown in the bottom-left corner of each map as an open ellipse. A scale bar is shown in the bottom-left corner of the PVD. We note the presence of a small central hole in the molecular gas distribution. Likely as a result, there is no evidence of a central (Keplerian) rise of the rotation velocities at small radii.

For NGC 1684, the hole is slightly larger than the predicted radius of the SMBH sphere of influence, and thus does not allow for the innermost parts of the potential to be probed. Consequently, no Keplerian rise is present within R_{SoI}. SMBH mass measurements are still possible in such instances, as the presence of the SMBH will also enhance the gas rotation velocities at radii beyond the formal SMBH sphere of influence. However, the effect of the SMBH then becomes increasingly degenerate with that of the stars.

The second moment map exhibits the typical cross-shaped enhancement of the velocity dispersion centred on the nucleus, as expected in highly inclined discs (e.g. Barth et al. 2016, Davis et al. 2017, Smith et al. 2021a; also seen in Figs. 2.17 and 3.11). This feature arises from beam smearing of the steep central velocity gradient and should not be interpreted as

a genuine astrophysical feature. In the innermost regions of the disc, the circular velocity changes rapidly over spatial scales comparable to or smaller than the ALMA synthesised beam. Consequently, emission from gas spanning a broad range of line-of-sight velocities is convolved within a single resolution element, artificially broadening the observed line profiles and increasing the measured second moment. The resulting enhancement is anisotropic because the projected velocity gradients vary with position across the inclined rotating disc, producing the characteristic cross-shaped morphology seen in the velocity dispersion map. This interpretation is supported by our best-fitting model, which reproduces the observed feature despite assuming a spatially constant intrinsic gas velocity dispersion, confirming that this feature is a consequence of the instrumental beam and a high inclination of the galaxy rather than genuine local increases in molecular gas turbulence.

Figure 2.3 shows the integrated ^{12}CO(2–1) spectrum of NGC 1684 with the classic double-horn shape of a rotating disc. This spectrum is extracted from a 16 arcsec × 8 arcsec ($\approx 4860 \times 2430$ pc^2) region around the centre (that includes all detected emission), with an integrated line flux (measured within the mask defined above) of 99.9 ± 3.9 Jy km s^{-1}. Figure 2.3 also shows the integrated spectra of the ^{12}CO(2–1) (grey shading) and ^{12}CO(1–0) (black dashed line) lines obtained from the Institut de Radio Astronomie Millimétrique (IRAM) single-dish 30-m telescope observations reported by Davis et al. (2015). The 30-m telescope ^{12}CO(2–1) integrated intensity is smaller than that measured by ALMA, likely a consequence of flux omission due to the smaller primary beam ($\approx$ 11 arcsec) of the 30-m telescope, as well as potential pointing errors. The lopsided spectrum of NGC 1684 is a classic sign of the latter, suggesting the 30-m telescope was pointing slightly to the north-east of the galaxy centre. As we do not have ^{12}CO(1–0) observations ourselves, we adopt the total molecular gas masses (including contributions from heavy elements) estimated from the above ^{12}CO(1–0) 30-m telescope observations of Davis et al. (2015) in the standard manner [i.e. using Eq. 3 of Bolatto et al. 2013 and a standard CO-to-molecule conversion factor $\alpha_{\rm CO(1-0)} = 4.3$ M$_\odot$ pc^{-2} (K km s^{-1})$^{-1}$], yielding $(1.58 \pm 0.07) \times 10^9$ M$_\odot$ and a ^{12}CO(2–1)-to-^{12}CO(1–0) flux ratio of (expressed in Jy km s^{-1}) $R_{21} = 2.97$.

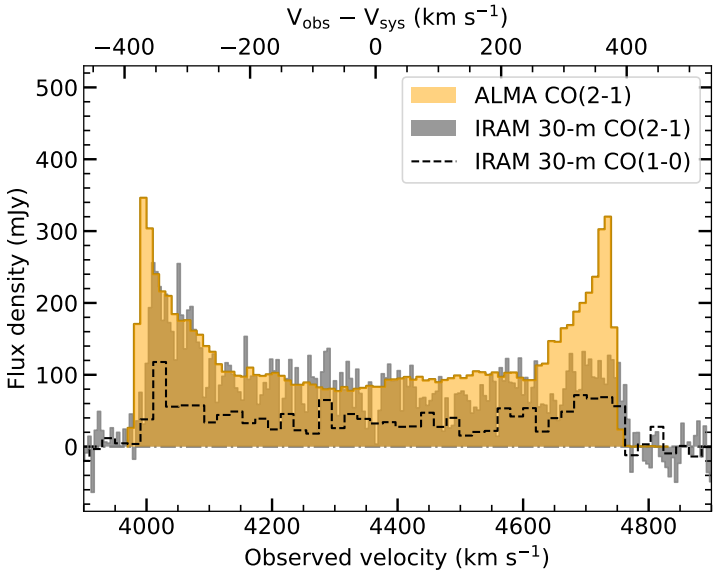


Figure 2.3: ^{12}CO(2–1) integrated spectrum of NGC 1684 derived from our ALMA data (orange shading), overlaid on the IRAM 30-m telescope ^{12}CO(2–1) (grey shading) and ^{12}CO(1–0) (black dashed line) observations of Davis et al. (2015). The ALMA aperture is a 16 arcsec × 8 arcsec ($\approx 4860 \times 2430$ pc^2) region centred on the galaxy centre, that includes all detected emission.

Continuum emission

An image of the 236.1 GHz (1.27 mm) continuum emission of NGC 1684 was created using the CASA task `tclean` in multifrequency synthesis mode and Briggs weighting with a robust parameter of 0.5. The line-free channels of the line spectral window were used as well as the continuum spectral windows. A small central source was detected and fitted with a Gaussian function using the CASA task `imfit`, revealing a spatially-resolved source with an integrated flux density of 22.9 ± 0.5 mJy. The synthesised beam of the continuum image is slightly smaller than that of the CO cube because the continuum image was created using multi-frequency synthesis, combining all continuum spectral windows and line-free channels across a much larger bandwidth than the CO cube. This provides denser sampling of the *uv*-plane and consequently a slightly smaller effective beam. All the properties of the NGC 1684 continuum image and the detected source are listed in Table 2.4.

Table 2.4: Parameters of the NGC 1684 continuum image and the detected continuum source.

Image property	Value
Image (pix)	512×512
Image (arcsec)	10.2×10.2
Image size (kpc)	3.10×3.10
Pixel scale (arcsec pix^{-1})	0.02
Pixel scale (pc pix^{-1})	6.08
RMS noise (mJy beam^{-1})	0.12
Synthesised beam (arcsec)	0.18×0.11
Synthesised beam (pc)	55×33
Source property	**Value**
Right ascension	$04^{h}52^{m}31\overset{s}{.}1410 \pm 0\overset{s}{.}0002$
Declination	$-03°06'21\overset{''}{.}624 \pm 0\overset{''}{.}002$
Integrated flux (mJy)	22.9 ± 0.5
Deconvolved size (marcsec)	$(267 \pm 9) \times (186 \pm 8)$
Deconvolved size (pc)	$(81 \pm 3) \times (57 \pm 2)$

2.3.3 CO Modelling

Model parameters

In the case of NGC 1684, we adopt a 2D axisymmetric exponential surface density profile with an inner truncation as defined in Equation 2.2. For completeness, we also considered alternative surface density profiles. We tried an exponential profile at large radii, truncated at an inner radius but extending inward as a half-Gaussian function. This model seemed more appropriate for NGC 1684 considering that it has some form of depression around the hole, but the fitting algorithm could not converge, most likely because the inner half-Gaussian parameters are not strongly constrained due to the limited spatial resolution of the observations. Other forms of extension inward from the truncation fared no better.

While NGC 1684 is not perfectly axisymmetric, with a slight isophotal twist at large radii, it is reasonable to assume axisymmetry for our purpose of constraining the SMBH mass using gas kinematics (that primarily depends on the mass enclosed within small radii). We parameterise the stellar light distribution of NGC 1684 using an MGE model of a *HST* Wide Field Camera 3 (WFC3) image in the F110W filter (J-band) (GO-14219, PI: Blakeslee) with a total exposure time of 2496 s. We convert this stellar light distribution into luminosities in the AB magnitude system by adopting a zero-point of 26.82 mag and a Solar absolute magnitude of 4.52 mag for the F110W filter (see Sahu et al. 2021 and Willmer

Table 2.5: Parameters of the deconvolved best-fitting MGE components of our model of NGC 1684.

$I'_{\odot}$ ($L_{\odot,F110W}$ pc^{-2}) (1)	σ' (arcsec) (2)	q' (3)
33295	0.214	0.572
14692	0.583	0.804
8160	1.125	0.813
3927	1.901	0.856
2057	3.740	0.750
737	9.255	0.666
76	28.087	0.550
147	28.087	0.900

Notes. Deconvolved MGE components. (1) Central surface brightness of Gaussian component. (2) Standard deviation of Gaussian component. (3) Axial ratio of Gaussian component.

2018, respectively). We also adopt galactic extinctions of 0.051 mag from NED (Schlafly & Finkbeiner 2011), to correct our images for interstellar reddening. The parameters of the deconvolved best-fitting MGE Gaussians are listed in physical units in Table 2.5 while the optical image overlaid with our best-fitting MGE model is illustrated in Fig. 2.4.

Results

As shown in Fig. 2.4, there is significant dust extinction to the north of the NGC 1684 nucleus. To reduce their impact, the dust lanes were masked in our MGE model, simultaneously masking the nearby galaxy neighbour. The resulting MGE model is clearly a good fit, especially in the very centre of the image, the region that matters most to constrain the SMBH mass.

The final MCMC chain had 300, 000 steps. It is clear that there is a large dark object present in the centre of NGC 1684, with a mass of $1.40^{+0.44}_{-0.39} \times 10^9$ $M_{\odot}$, where here and throughout this thesis the uncertainties are stated at the 3σ (99.7%) confidence level. The best-fitting M/L in the F110W filter is (2.50 ± 0.05) $M_{\odot}/L_{\odot,F110W}$. From Fig. 2.5, it is also clear that the well-known degeneracy between M_{BH} and M/L is present, equivalent to the conservation of (total) dynamical mass.

The quality of our fit is easiest to judge by overlaying models over the innermost part of the kinematic major-axis PVD. From left-to-right in Fig. 2.6, we thus overlay the best-fitting models with no SMBH, the best-fitting SMBH and an overly massive SMBH ($\approx$ 0.3 dex

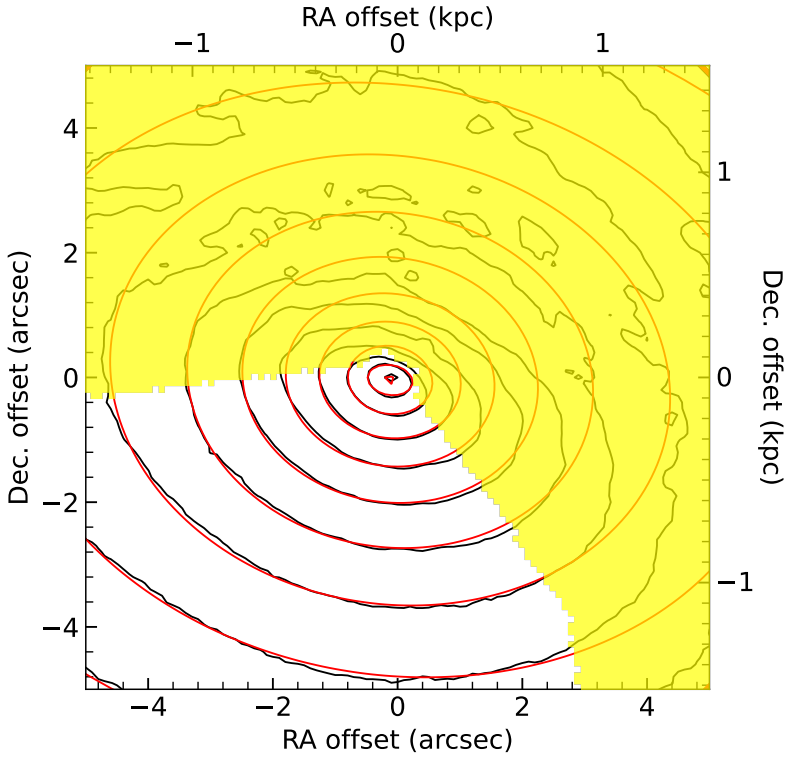


Figure 2.4: *HST* WFC3 F110W image of NGC 1684 (black contours), overlaid with our best-fitting MGE model (red contours). The northern and eastern sides of the image are masked (yellow shading), to exclude the foreground dust disc and contamination from a nearby galaxy.

more massive than the best fit), respectively, allowing all parameters other then the SMBH mass to vary. As expected for the best-fitting no SMBH model, a higher stellar M/L is derived to attempt to account for the high rotation velocities at small radii, but the model is nevertheless unable to fit those central velocities without greatly exceeding those relatively low velocities at larger radii. The compromise reached is thus unsatisfactory at both small and large radii (beyond the range shown in the figure). Again as expected, the best-fitting overly massive SMBH model yields a smaller M/L, but the fit is very poor at small radii, the model over-shooting even the highest velocities. The best-fitting SMBH model not only fits the data best, but the fit is very good at all radii and velocities, including those radii beyond the range shown in the figure.

So far, we have only considered models with a radially constant M/L, but in principle this need not be the case. A spatially variable M/L can exist as a result of stellar population variations and it is worth exploring. Crucially, the issue is whether a good fit to the data

Table 2.6: Best-fitting model parameters of NGC 1684 and associated uncertainties.

Parameter	Prior			Best fit	1σ uncertainty	3σ uncertainty
Mass model						
log(SMBH mass/$M_\odot$)	7	→	11	9.145	$-0.048, +0.047$	$-0.143, +0.118$
Stellar M/L_{F110W} ($M_\odot/L_{\odot,\mathrm{F110W}}$)	0.0	→	5.0	2.50	±0.02	±0.05
Molecular gas disc						
Inclination (°)	0.0	→	89.9	66.7	±0.3	$-0.8, +0.7$
Position angle (°)	0.0	→	359.9	258.1	±0.2	±0.5
Velocity dispersion (km s^{-1})	0.0	→	50.0	13.3	$-1.0, +1.1$	$-2.7, +2.9$
Scale length (arcsec)	0.0	→	5.0	2.33	$-0.09, +0.10$	$-0.24, +0.31$
R_{hole} (arcsec)	0.0	→	3.0	0.39	$-0.08, +0.07$	$-0.37, +0.17$
Nuisance parameters						
Centre RA offset (arcsec)	−3.2	→	3.2	0.33	±0.01	±0.03
Centre Dec. offset (arcsec)	−3.2	→	3.2	0.46	±0.01	±0.02
Systemic velocity (km s^{-1})	4200	→	4500	4364.3	$-1.0, +0.9$	$-2.5, +2.4$
Integrated intensity (Jy km s^{-1})	0.0	→	150.0	127.3	$-5.8, +5.7$	$-14.8, +15.8$

Note. The RA and Dec. offsets are measured with respect to the image phase centre, $04^{\mathrm{h}}52^{\mathrm{m}}31\overset{\mathrm{s}}{.}166$, $-03°06'22\overset{''}{.}11$ (J2000.0).

can then be obtained without a SMBH.

First, we consider a model with a linear M/L by taking the circular velocity curve of an MGE model with a M/L of unity and scaling that curve by the square root of M/L (since $v^2 \propto M$; for more details see Section 2.2.1). This adds one free parameter to our model. We ran the fit as before, allowing all parameters to vary. The best-fitting model has a M/L represented by $(M/L_{\mathrm{F110W}})\,/\left(\mathrm{M}_\odot/\mathrm{L}_{\odot,\mathrm{F110W}}\right) = 2.77 - 0.05\ (R/\mathrm{arcsec})$. As shown in the left panel of Fig. 2.7, the best-fitting no SMBH model with a linear M/L yields a marginally better fit at smaller radii than the best-fitting no SMBH model with a constant M/L, but a steep slope decreases the goodness of fit at larger radii and overall the fit is still very poor. Thus, a M/L linearly increasing inward cannot replace the presence of a central SMBH.

Second, we consider a model where the innermost Gaussian of the MGE parameterisation of the galaxy stellar mass has a different M/L than the other Gaussians. This effectively creates a model with a roughly Gaussian M/L at small radii that flattens out at larger radii. This adds one free parameter to our original model. We ran the fit as before, allowing all parameters to vary. The best-fitting model has a M/L_{F110W} of 5.22 $\mathrm{M}_\odot/\mathrm{L}_{\odot,\mathrm{F110W}}$ at the centre, 4.02 $\mathrm{M}_\odot/\mathrm{L}_{\odot,\mathrm{F110W}}$ at a radius of $0\overset{''}{.}5$ and 2.95 $\mathrm{M}_\odot/\mathrm{L}_{\odot,\mathrm{F110W}}$ at a radius of $1\overset{''}{.}0$, and the M/L flattens out at $\approx$ 2.6 $\mathrm{M}_\odot/\mathrm{L}_{\odot,\mathrm{F110W}}$ by a radius of $\approx 2\overset{''}{.}0$. As shown in the right

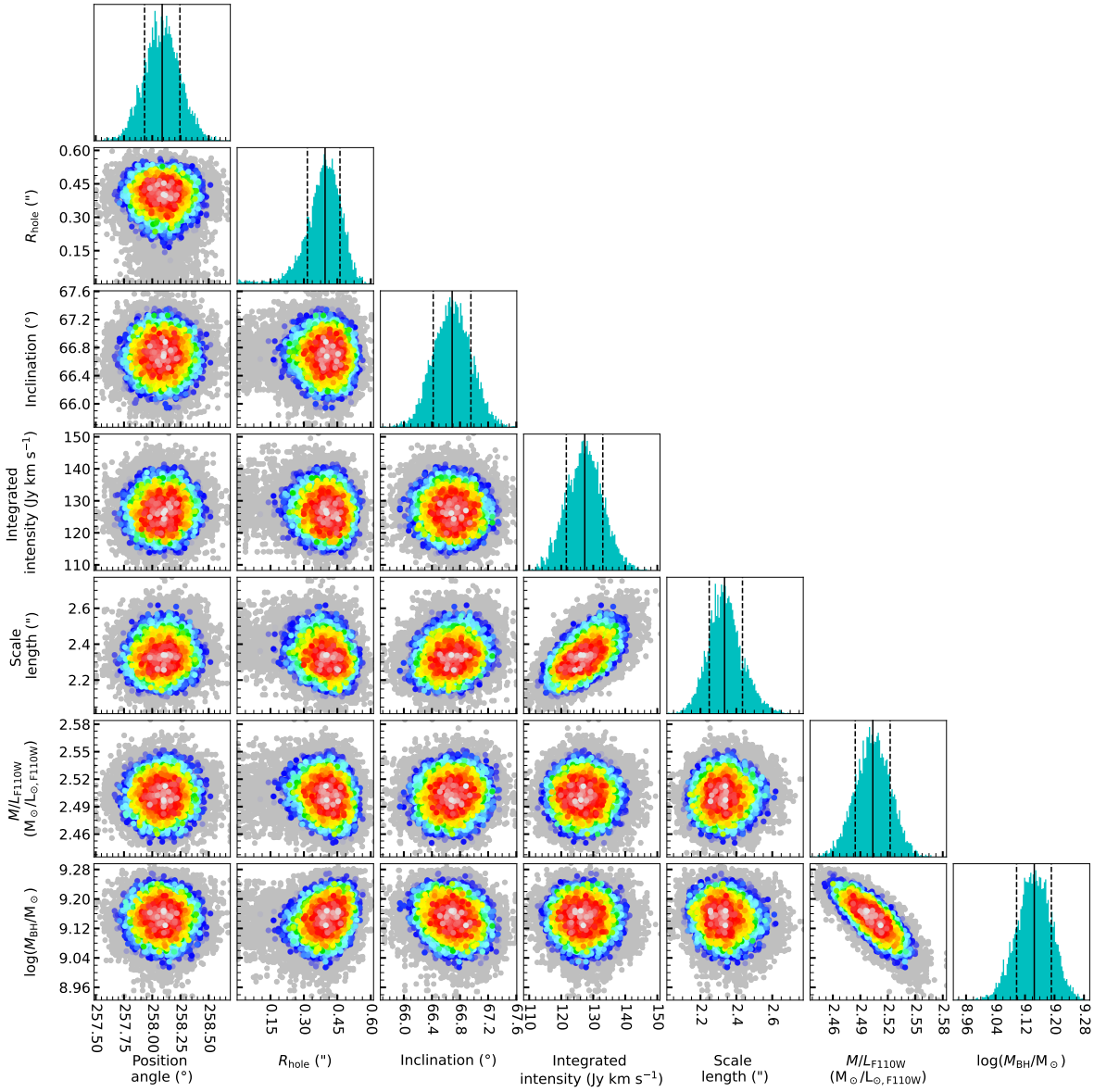


Figure 2.5: Corner plots of NGC 1684, showing the covariances between selected (primarily non-nuisance) model parameters. Each data point is a realisation of our model, colour-coded to show the relative log-likelihood of that realisation, with the white data points most likely and the blue data points least likely. Coloured points show models within $\Delta\chi^2 < \sqrt{2N}$ of the best-fitting model; grey data points show all remaining models. The histograms show the 1D marginalised posterior distribution of each model parameter, where the black solid line marks the median and the two black dashed lines the 68% confidence interval.

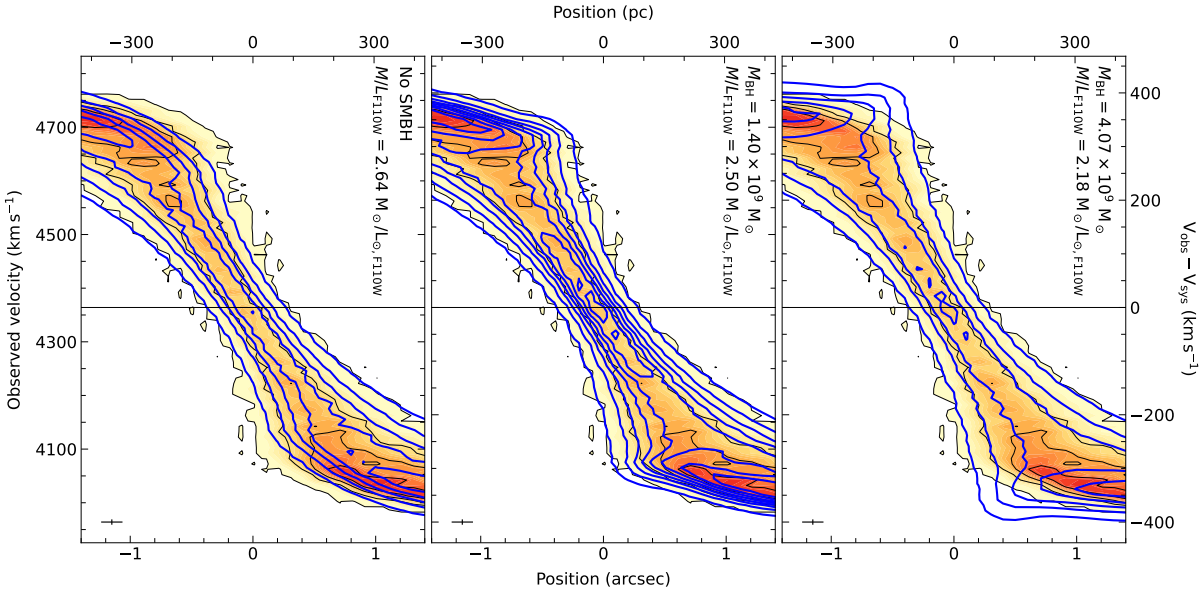


Figure 2.6: Innermost part (radii $\lesssim 1\farcs4$) of the observed kinematic major-axis PVD of NGC 1684 (orange scale with black contours), overlaid with the best-fitting no SMBH (left), free SMBH mass (centre) and overly-massive (by 0.3 dex) SMBH (right) model (blue contours), respectively. The SMBH mass and M/L of each model are listed in the top-right corner of each panel. An error bar is shown in the bottom-left corner of each panel showing the size of the synthesised beam along the kinematic major-axis and the channel width. The need for a central dark mass to fully account for the gas kinematics at all radii is clear.

panel of Fig. 2.7, this model does offer a good fit at both small and large radii, as a discrete increase of the M/L in the very centre effectively mimics a SMBH.

There is evidence suggesting that the centres of massive early-type galaxies have a non-standard IMF (e.g. La Barbera et al. 2016; van Dokkum et al. 2017), with a mismatch parameter (the ratio between a galaxy's M/L and the predicted M/L assuming a Milky Way-like IMF) sufficient to give credence to our best-fitting model with a Gaussian M/L but no SMBH. However, most of the evidence comes from modelling of stellar populations or strong gravitational lenses, neither of which necessarily considers the effects of a central SMBH. Using a molecular gas method similar to ours, Davis & McDermid (2017) instead inferred a range of both radially increasing and decreasing dynamically-determined M/L, implying both top- and bottom-heavy IMF variability between galaxies. Additionally, these gradients were significantly shallower than that of our best-fitting Gaussian M/L model. Thus, whilst a steep IMF gradient can technically explain the molecular gas kinematics of

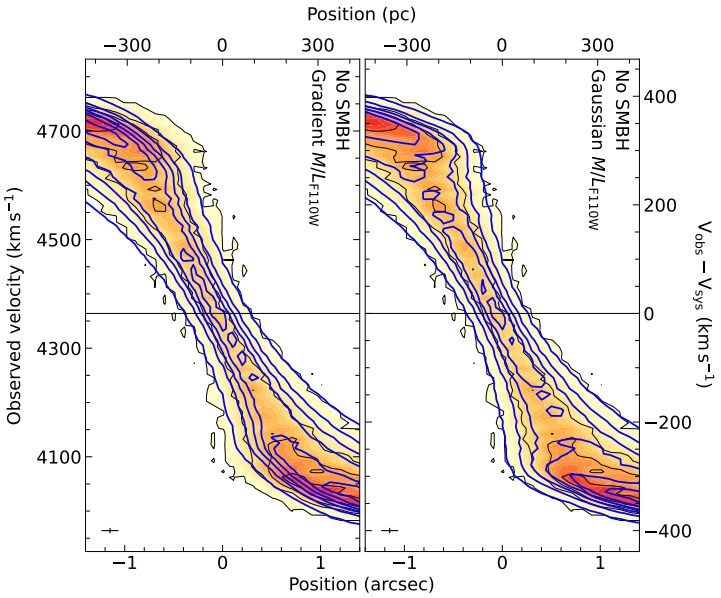


Figure 2.7: As Fig. 2.6, but for the best-fitting no SMBH with a linearly-varying M/L (left) and no SMBH with a Gaussian piecewise M/L (right) model, respectively.

NGC 1684 without a central SMBH, given the established nature of central SMBHs, we do not seriously consider the model with a Gaussian M/L but no SMBH.

In fact, when inferring M/L dynamically, an appropriate treatment of the dynamics *should* take into account the gravitational effects of the SMBH, even when considering a variable M/L. When considering models with a SMBH and a linear M/L, our best-fitting model has a gradient of ≈ 0. When considering models with a SMBH and a Gaussian M/L, a model with a central SMBH is strongly preferred over one without a SMBH. There is therefore no compelling reason to prefer a model with a variable M/L when accounting for the gravitational effects of the SMBH in NGC 1684.

2.3.4 Discussion

Aside from the fitting uncertainties reported in Table 2.6, SMBH mass measurements using molecular gas have several potential sources of systematic errors. Generally, the largest systematic error stems from the adopted distance. Indeed, as for all dynamical measurements, the SMBH mass scales linearly with distance, i.e. $M_{\rm BH} \propto D$, so any distance error impacts the inferred SMBH mass directly. It is generally accepted that the typical uncertainty on galaxy distances is $\approx 10\%$, consistent with the formal errors on the NGC 1684 distance measurement.

As is standard practice, we do not include the distance uncertainty in our final dynamical SMBH mass measurement, as our results can simply be scaled to any other adopted distance.

With the excellent angular resolutions of our ALMA data, the molecular gas disc of our target is revealed to have a central hole (see Section 2.3.2). This will also prove to be the case for many other of the targets in this thesis (NGC 0997, NGC1387, NGC 0665 and NGC 5208). The cumulative mass distribution of NGC 1684 shown in Fig. 2.8 shows that the synthesised beam size is much smaller than its hole, strongly suggesting the hole is resolved and real. This is supported by the posterior probability distributions shown in Fig. 2.5, even though the truncation radius is only loosely constrained. Using the standard definition of the SMBH sphere of influence (see Section 2.3.1) and our best-fitting SMBH mass, we derive $R_{\rm SoI} \approx 88$ pc (≈ 0.29 arcsec). Dynamical modelling determined that the best-fitting hole truncation radius is $R_{\rm hole} = 0.39^{+0.17}_{-0.37}$ arcsec, slightly larger than $R_{\rm SoI}$ (see Fig. 2.8). This is most likely the reason we do not see a Keplerian rise of the rotation velocities near the galaxy centre. Fortunately, this does not prevent us from achieving a good constraint on the SMBH mass, as the SMBH influence extends beyond $R_{\rm SoI}$. Instead we can look at the radius of equal mass contribution ($R_{\rm eq}$), defined as the radius where the enclosed stellar mass is equal to that of the SMBH. From Fig. 2.8, $R_{\rm eq} \approx 105$ pc (≈ 0.35 arcsec), which is only slightly smaller than the hole. This most likely explains the robust inferred SMBH mass, as the molecular gas detected at the hole is still significantly affected by the SMBH.

In fact, for a given data quality, the accuracy of the SMBH mass measurement should scale with the fraction of the enclosed mass due to the SMBH at the innermost radius probed. This radius is usually roughly the size of the synthesised beam ($R_{\rm beam}$), but when a hole is present it is really the truncation radius of the hole. In NGC 1684, $\approx 80\%$ of the enclosed mass at $R_{\rm beam}$ is due to the SMBH, which would have made a SMBH mass measurement trivial had it not been for the central hole. That fraction drops to $\approx 45\%$ at $R_{\rm hole}$, but fortunately this is still sufficient to provide a robust SMBH mass determination.

In our modelling, we have only considered the mass contributions of the stars and SMBH, and we have assumed dark matter and molecular gas to have negligible masses. As discussed in Section 2.3.1, NGC 1684 has a total molecular gas mass of $1.58^{+0.75}_{-0.71} \times 10^9$ $M_\odot$, which although significant is spread over the entire extent of the molecular gas disc (≈ 6 arcsec or

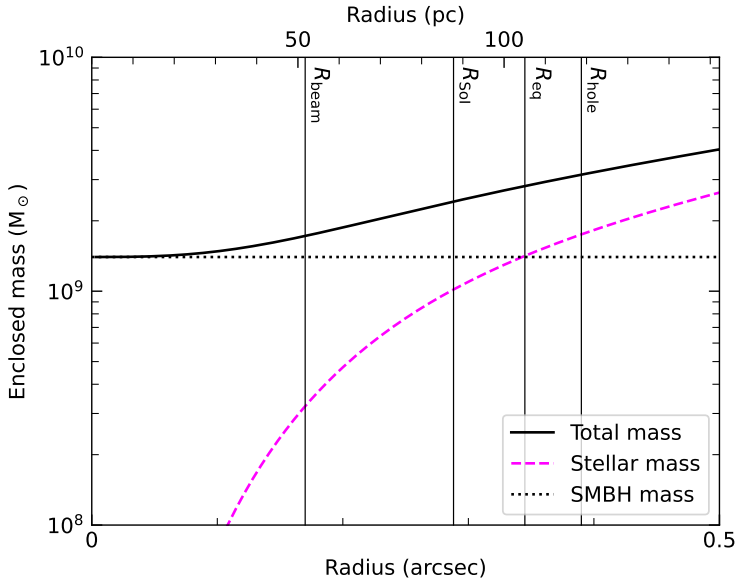


Figure 2.8: Cumulative mass function of NGC 1684, showing the relative contributions of the SMBH (black dotted line) and stars (magenta dashed line) to the total enclosed mass (solid black line). The four vertical black lines indicate the physical scales of the synthesised beam, the radius of the SMBH sphere of influence (assuming $\sigma_{\rm e}$ = 262 km s^{-1} and our best-fitting SMBH mass), the radius of equal mass contribution and our best-fitting hole truncation radius.

$\approx$ 1.8 kpc in radius). Considering in addition the central hole in the molecular gas, the mass contribution from molecular gas in the central region of the galaxy is negligible. In fact, by definition, it is formally nil at the innermost radii probed ($R_{\rm hole}$), and the cumulative mass function of molecular gas would not be visible in Fig. 2.8 even if it was plotted. Similarly, the spatial scales over which dark matter effects are significant are much greater than those considered here. In the very unlikely scenario that there is significant dark but diffuse matter in the central regions, the SMBH mass could be overestimated, but unless the distribution is significantly different from that of the stars, as mentioned earlier the dark matter is more likely to simply be assimilated with the stars and lead to a different M/L.

2.4 NGC 0997

The material in this section was originally published in the Monthly Notices of the Royal Astronomical Society, Volume 529, Pages 1597 – 1616.

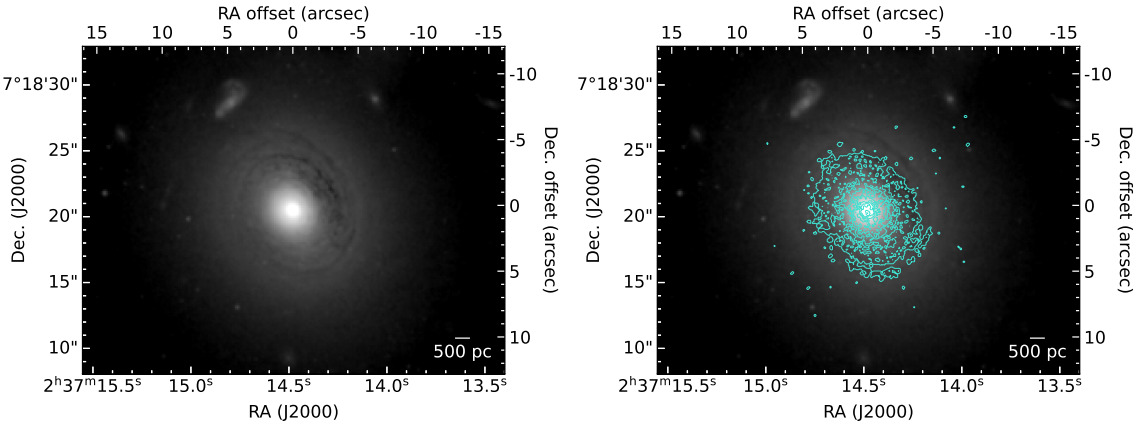


Figure 2.9: Unsharp-masked *HST* WFC3 F160W filter (H-band) image of NGC 0997 (top), overlaid with the ^{12}CO(2–1) integrated intensity contours (cyan) from our ALMA observations (bottom).

2.4.1 Galaxy Properties

NGC 0997 is an E0 elliptical located at $02^{\rm h}37^{\rm m}14\overset{\rm s}{.}50$, $+07°18'20\overset{''}{.}5$ (J2000.0) in the constellation of Cetus. We adopt the distance used in the MASSIVE survey, $D = 90.4$ Mpc (Ma et al. 2014). At this distance 1 arcsec corresponds to ≈ 438 pc. NGC 0997 is located in a group of three galaxies (according to 2MASS Redshift Survey; 2MRS, Crook et al. 2007), of which it is the brightest, and the galaxy distance was obtained by correcting for local peculiar velocities using group-corrected redshift distances (Ma et al. 2014).

HST optical images reveal a prominent dust disc, with dust lanes on all sides of the galactic centre and an unobscured nucleus (Fig. 2.9). There is a small and very faint galaxy-like object ≈ 9 arcsec north-north-east of NGC 0997. Slightly further out, ≈ 16 arcsec north of NGC 0997 (not visible in Fig. 2.9), there is another small object (PGC 200205) about which not much is known, but due to its apparent size it is most likely also a background galaxy.

Davis et al. (2015) estimated the inclination of the galaxy to be $34 \pm 5°$, consistent with the value presented in this thesis (Section 2.4.3). NGC 0997 hosts a molecular gas reservoir, with a total H_2 mass of $1.82^{+0.13}_{-0.12} \times 10^9$ M$_\odot$, and has a total SFR of 0.47 ± 0.04 M$_\odot$ yr^{-1}, determined as in NGC 1684. It has an integrated absolute K-band magnitude of -25.68 (Quenneville et al. 2022) which results in a total stellar mass of 5.74×10^{11} M$_\odot$, calculated as in Section 2.3.1.

NGC 0997 does not have a direct SMBH mass measurement. Assuming $\sigma_{\rm e} = 215$ km s^{-1} (Davis et al. 2019) and the $M_{\rm BH} - \sigma_{\rm e}$ relation of van den Bosch (2016), a SMBH mass of $\approx 3.0 \times 10^8$ M$_\odot$ is expected, yielding $R_{\rm SoI} \approx 28$ pc (≈ 0.06 arcsec).

Table 2.7: CO data cube properties for NGC 0997.

Image property	Value
Spatial extent (pix)	1024×1024
Spatial extent (arcsec)	51.2×51.2
Spatial extent (kpc)	22.4×22.4
Pixel scale (arcsec pix^{-1})	0.05
Pixel scale (pc pix^{-1})	21.9
Velocity range (km s^{-1})	6000 – 6700
Channel width (km s^{-1})	5
RMS noise (mJy beam^{-1} channel^{-1})	0.51
Number of constraints	145, 141
Synthesised beam (arcsec)	0.17×0.15
Synthesised beam (pc)	77×64

2.4.2 ALMA Observations

Observations of the ^{12}CO(2–1) emission line using the 12-m ALMA array were obtained as part of projects 2015.1.00187 (PI: Davis) and 2016.1.00683 (PI: Ma). The NGC 0997 data are also comprised of three tracks taken on 19th August 2016, 26th November 2016 and 22nd August 2017, for a total of 42 minutes on source. Baselines span 15.1 m to 3.7 km, yielding an angular resolution of 0.09 arcsec, a maximum recoverable scale of 4.3 arcsec, and a field of view of 24.9 arcsec. The properties of the observations are listed in Table 1.2.

ALMA Band 6 was used for all observations. Each of the three tracks had a total of four spectral windows, one of which was centred on the redshifted frequency of the ^{12}CO(2–1) line (rest frequency $\nu_{\rm rest}$ = 230.5380 GHz) with a bandwidth of 1.875 GHz ($\approx$ 2440 km s^{-1}) subdivided into either 3840 channels of width $\approx$ 488 kHz ($\approx$ 0.64 km s^{-1}) or 1920 channels of width $\approx$ 977 kHz ($\approx$ 1.27 km s^{-1}). The remaining three spectral windows each had a bandwidth of 2 GHz ($\approx$ 2600 km s^{-1}) and were used to map the continuum, with either 128 channels of width $\approx$ 16 MHz ($\approx$ 20 km s^{-1}) or 240 channels of width $\approx$ 8 MHz ($\approx$ 10 km s^{-1}). The data were calibrated using the CASA as before.

Line emission

The continuum spectral windows and line-free channels of the line spectral window were linearly fit and the fit subtracted from the *uv*-plane data using the CASA `uvcontsub` task. The continuum-subtracted *uv* data were then imaged and cleaned in regions of source emission to a threshold equal to the RMS noise of the dirty channels (in regions free of line emission),

using the cube mode of the CASA task `tclean` and Briggs weighting with a robust parameter of 0.5. We adopt a channel width of 5 km s^{-1}, smaller than typical, to aid SMBH mass detection (Davis 2014), but still much larger than the raw channel width of the observations. The resulting data cube has a synthesised beam of 0.17 arcsec × 0.15 arcsec (77 × 64 pc^2) with a RMS noise of 0.51 mJy $beam^{-1}$ $channel^{-1}$ for NGC 0997. All the properties of the resulting data cubes are summarised in Table 2.7.

The zeroth (integrated-intensity), first (intensity-weighted mean line-of-sight velocity) and second (intensity-weighted line-of-sight velocity dispersion) moment maps of NGC 0997 are shown in Figs. 2.10, along with a kinematic major-axis PVD, generated as in Section 2.3.2 using PYMAKEPLOTS, with a mask created by clipping the smoothed data cube at a threshold of 5 times the RMS noise of the line-free channels. The PVD was constructed as before, summing pixels in the cube within a pseudo-slit 5 pixels wide oriented along the kinematic position angle of 215°.2, determined by our kinematic modelling results in Section 2.4.3.

We detect a disc of molecular gas in regular rotation in NGC 0997, coincident with the dust disc and with a semi-annular central hole which extends to a maximal radius of ≈ 0.5 arcsec. Despite this, some molecular gas extends past the hole towards the centre of the galaxy. This asymmetric hole can be due to a number of reasons, e.g. photodissociation due to an AGN with asymmetric jets, asymmetric dust shielding or thermal effects and/or molecular gas not yet being fully settled.

For NGC 0997, the semi-annular hole poses a unique case. As the molecular gas on one side of the galaxy extends to its centre, a small enhancement of velocities can be seen on one side of the PVD at ≈ 0.2 arcsec, which is partly within the $R_{\rm SoI}$ determined using the best-fitting SMBH mass obtained in Section 2.4.3. However, the hole prevents this enhancement from being detected on the other side. In cases where there is no clear Keplerian rise within $R_{\rm SoI}$, it may not be possible to obtain a robust SMBH mass, but a SMBH mass upper limit can nevertheless usually be estimated.

Figure 2.11 shows the integrated ^{12}CO(2–1) spectrum of NGC 0997, with the classic double-horn shape of a rotating disc. This spectrum is extracted from a 16 arcsec × 16 arcsec (≈ 7000 × 7000 pc^2) region around the centre of NGC 0997, with an integrated line flux of 52.8 ± 1.5 Jy km s^{-1}. Figure 2.11 also shows the integrated spectrum of the ^{12}CO(2–1)

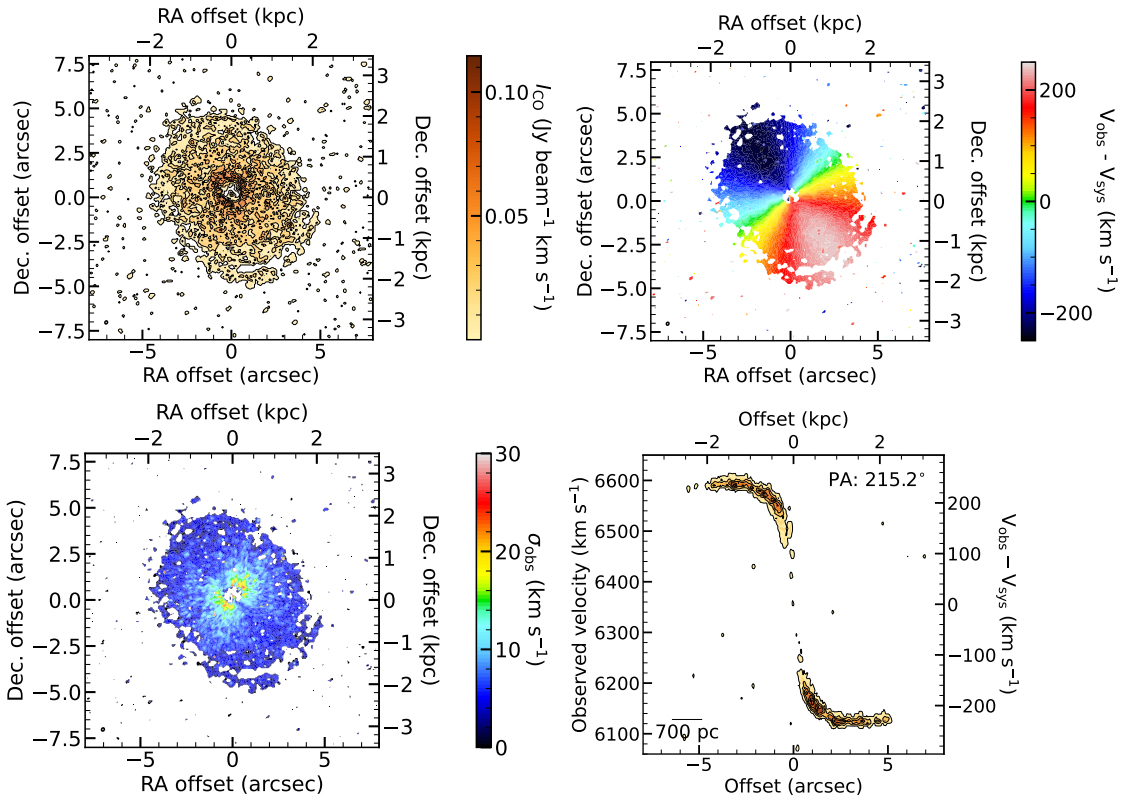


Figure 2.10: As Fig. 2.2 but for NGC 0997. We note the presence of a small, asymmetric central hole, as well as a faint secondary peak in the very centre of the molecular gas distribution. Likely as a result of the hole, there is no evidence of a central (Keplerian) rise of the rotation velocities at small radii. However, as a result of the secondary peak, we do see an asymmetric enhancement of velocities at the very centre.

(grey shading) and ^{12}CO(1–0) (black dashed line) lines obtained from the IRAM single-dish 30-m telescope observations reported by Davis et al. (2015). The 30-m telescope ^{12}CO(2–1) integrated intensity is smaller than that measured by ALMA, as in NGC 1684.

Continuum emission

An image of the 234.6 GHz (1.28 mm) continuum emission of NGC 0997 was created using the CASA task `tclean` in multi-frequency synthesis mode and Briggs weighting with a robust parameter of 0.5. The line-free channels of the line spectral window were used as well as the continuum spectral windows. A small spatially-resolved continuum source was detected, with an integrated flux density of 6.58 ± 0.08 mJy. All the properties of the NGC 0997 continuum image and the detected source are listed in Table 2.8.

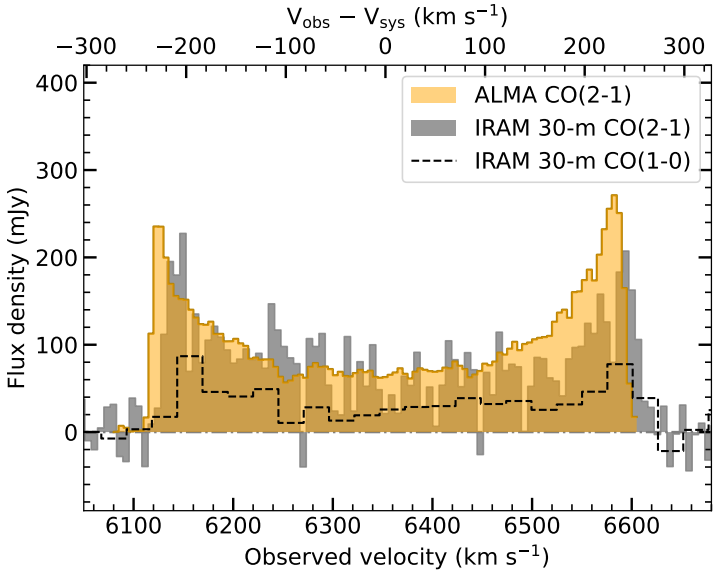


Figure 2.11: ^{12}CO(2–1) integrated spectrum of NGC 0997 derived from our ALMA data (orange shading), overlaid on the IRAM 30-m telescope ^{12}CO(2–1) (grey shading) and ^{12}CO(1–0) (black dashed line) observations of Davis et al. (2015). The ALMA aperture is a 16 arcsec × 16 arcsec ($\approx 7000 \times 7000$ pc^2) region centred on the galaxy centre, that includes all detected emission.

Table 2.8: Parameters of the NGC 0997 continuum image and the detected continuum source.

Image property	Value
Image size (pix)	1024×1024
Image size (arcsec)	51.2×51.2
Image size (kpc)	22.44×22.44
Pixel scale (arcsec pix^{-1})	0.05
Pixel scale (pc pix^{-1})	21.9
RMS noise (mJy beam^{-1})	0.04
Synthesised beam (arcsec)	0.15×0.12
Synthesised beam (pc)	66×53
Source property	**Value**
Right ascension	$02^{h}37^{m}14\overset{s}{.}47984 \pm 0\overset{s}{.}00007$
Declination	$+07°18'20\overset{''}{.}4706 \pm 0\overset{''}{.}0006$
Integrated flux (mJy)	6.58 ± 0.08
Deconvolved size (marcsec)	$(195 \pm 4) \times (114 \pm 3)$
Deconvolved size (pc)	$(85 \pm 2) \times (50 \pm 1)$

Table 2.9: Parameters of the deconvolved best-fitting MGE components of our model of NGC 0997.

$I'_{\odot}$ ($L_{\odot,F160W}$ pc^{-2}) (1)	σ' (arcsec) (2)	q' (3)
13772	0.056	0.941
25967	0.300	0.914
12176	0.731	0.935
6149	1.355	0.917
2937	2.310	0.922
1492	4.951	0.892
450	15.929	0.930

Notes. Deconvolved MGE components. (1) Central surface brightness of Gaussian component. (2) Standard deviation of Gaussian component. (3) Axial ratio of Gaussian component.

2.4.3 CO Modelling

Model parameters

In the case of NGC 0997, all fits using any combination of parametric functions failed to adequately reproduce the molecular gas disc. We therefore used the observed gas distribution instead, using SkySampler (see Section 2.2.1 for more details).

NGC 0997 appears axisymmetric at all radii. We parameterise the stellar light distribution of NGC 0997 using an MGE model of a *HST* WFC3 image in the F160W filter (H-band) (GO-15909, PI: Boizelle) with a total exposure time of 996 s. We convert this stellar light distribution into luminosities in the AB magnitude system by adopting a zero-point of 25.94 mag and a Solar absolute magnitude of 4.60 mag for the F160W filer (see Sahu et al. 2021 and Willmer 2018, respectively). We also adopt a galactic extinction of 0.071 mag for NGC 0997 from NED (Schlafly & Finkbeiner 2011), to correct the image for interstellar reddening. The parameters of the deconvolved best-fitting MGE Gaussians are listed in physical units it Table 2.9 while the optical image overlaid with our best-fitting MGE model is illustrated in Fig. 2.12.

Results

As shown Fig. 2.12, there is no significant dust extinction close to the centre of NGC 0997, so significant masking near the sphere of influence of the SMBH is not required. The resulting MGE model is clearly a good fit, especially in the innermost region most important to the SMBH mass determination.

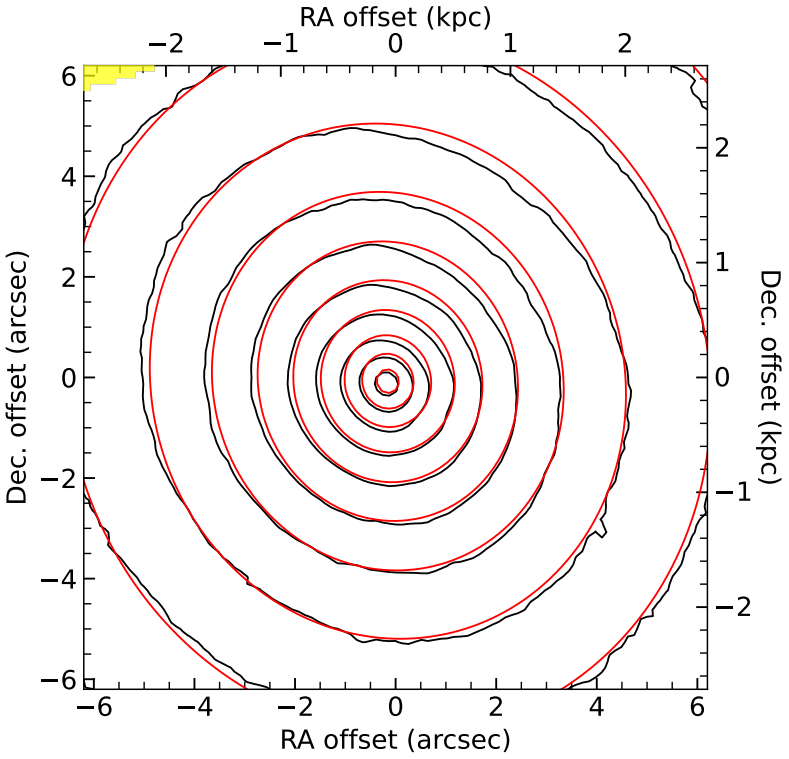


Figure 2.12: *HST* WFC3 F160W image of NGC 0997 (black contours), overlaid with our best-fitting MGE model (red contours). A small section of the north-western side of the image is masked, to exclude contamination from a nearby object.

When modelling the whole extent of the galaxy, the SMBH mass remained poorly constrained, most likely due to the relatively small flux within $R_{\rm SOI}$ compared to that within the whole galaxy. We thus conducted the modelling in two steps. For galaxy datasets for which constraining the inclination is problematic, it is common practice to fix the inclination at a previously determined value (e.g. North et al. 2019). First, we therefore modelled the entire galaxy to obtain a robust inclination, using the entire molecular gas disc. Second, we restricted the modelling to a 2 arcsec × 2 arcsec central area, fixing the inclination to that obtained in the previous step. The restriction of the modelling to a central area is also common practice (e.g. Ruffa et al. 2023), especially when using SkySampler, which is computationally expensive. When possible, it is preferable to include the outer regions of the molecular gas disc in the modelling to obtain the most accurate M/L for the entire disc. However, in practice, a SMBH mass can be determined from modelling the central area of the galaxy only, where the SMBH dominates, and the inclusion of the outer regions is not strictly necessary.

Table 2.10: Best-fitting model parameters of NGC 0997 and associated uncertainties.

Parameter	Prior			Best fit	1σ uncertainty	3σ uncertainty
Mass model						
SMBH mass (10^8 $M_\odot$)	0	→	100	9.55	$-3.81, +2.42$	$-9.15, +8.87$
Stellar M/L_{F160W} ($M_\odot/L_{\odot,\mathrm{F160W}}$)	0.0	→	5.0	1.52	±0.04	±0.11
Molecular gas disc						
Inclination (°)		(fixed)		34.3	–	–
Position angle (°)	0.0	→	359.9	215.2	±0.5	$-1.3, +1.4$
Velocity dispersion (km s^{-1})	0.0	→	50.0	10.2	1.1	$-2.7, +3.4$
Nuisance parameters						
Centre RA offset (arcsec)	−1.2	→	1.2	−0.01	±0.02	$-0.05, +0.04$
Centre Dec. offset (arcsec)	−1.2	→	1.2	−0.08	±0.02	±0.05
Systematic velocity (km s^{-1})	6100	→	6500	6357.2	$-1.6, +1.7$	$-4.1, +4.6$
$2'' \times 2''$ int. intensity (Jy km s^{-1})	0.0	→	50.0	9.4	$-0.5, +0.6$	$-1.5, +1.6$
$12'' \times 12''$ int. intensity (Jy km s^{-1})	0.0	→	50.0	44.2	$-2.1, +2.2$	$-5.5, +6.0$

Note. The RA and Dec. offsets are measured with respect to the image phase centre, $02^{\mathrm{h}}37^{\mathrm{m}}14\overset{\mathrm{s}}{.}485$, $+07°18'20\overset{''}{.}405$ (J2000.0).

The MCMC chain in the first stage modelling had 200,000 steps, yielding a best-fitting inclination $i = 34.3^{\circ+3.2}_{-2.6}$. Figure 2.13 reveals a very strong degeneracy between i and M/L, but this is to be expected given the small inclination. Indeed, for a dynamical mass measurement based on rotational velocities, the enclosed mass M_{tot} is related to the rotation velocity v_{rot} and thus the observed velocity v_{obs} as $M_{\mathrm{tot}} \propto v^2_{\mathrm{rot}}(R)R \propto v^2_{\mathrm{obs}}(R)R/\sin^2 i \propto \sin^{-2} i$, and $\sin i$ varies rapidly at small inclinations (see Smith et al. 2019 for further discussion).

Initial modelling suggested the presence of a central SMBH in agreement with that predicted from the $M_{\mathrm{BH}} - \sigma_{\mathrm{e}}$ relation, but we were unable to decisively exclude very low ($< 10^6$ $M_\odot$) SMBH masses. To treat this situation appropriately, we therefore chose to sample M_{BH} directly (i.e. linearly), as opposed to sampling $\log(M_{\mathrm{BH}}/M_\odot)$ (i.e. logarithmically) as done for NGC 1684. Indeed, when sampling the SMBH mass logarithmically, there is no natural lower boundary to the search, and $M_{\mathrm{BH}} = 0$ can never be probed. When the posterior distribution extends all the way to the lower search boundary, the choice of prior thus affects the final distribution and in turn any upper limit adopted. By sampling the SMBH mass lineary, this arbitrariness can be removed by employing the least informative prior possible and probing all the way to 0. The final second-stage MCMC chain had 200,000 steps. Figure 2.13 shows that there is a large dark object present in the centre of NGC 0997, with a mass ranging from 5.8×10^8 to 1.2×10^9 $M_\odot$ at the 1σ (68%) confidence level,

and from 4.0×10^7 to 1.8×10^9 $M_\odot$ at the 3σ (99.7%) confidence level, with a best fit of 9.55×10^8 $M_\odot$. The best-fitting M/L in the F160W filter is (1.52 ± 0.11) $M_\odot/L_{\odot,F160W}$.

Whilst the uncertainties on the SMBH mass of NGC 0997 are much larger than those of NGC 1684, and the SMBH mass posterior distribution superficially appears to extend all the way to 0, the lowest SMBH mass in the posterior distribution is actually 3×10^6 $M_\odot$, corresponding to a 4.3σ confidence interval. The presence of a SMBH is thus clearly necessary to reproduce the observed molecular gas distribution and kinematics. As before, the quality of the fit is easiest to judge by overlaying models over the innermost part of the kinematic major-axis PVD, so from left-to-right in Fig. 2.14 we overlay the best-fitting models with no SMBH, a free SMBH mass (equal to that of our best-fitting SMBH mass) and a fixed overly-massive SMBH (≈ 0.3 dex more massive than the best fit), respectively, allowing all parameters other then the SMBH mass to vary. As expected, the best-fitting no SMBH model has a marginally larger M/L but fails to accommodate the velocity enhancements within $R_{\rm SOI}$. Again as expected, the best-fitting model with an overly massive SMBH overshoots even the highest central velocities and yields a smaller M/L. Clearly, no satisfactory fit can be obtained with such a massive SMBH. The best-fitting SMBH model not only fits the data best and accounts very well for the central enhancements of velocities, but the fit is very good at all radii.

2.4.4 Discussion

As before, the largest source of systematic error in our measurements is from the adopted distance. Whilst no uncertainty is reported on the NGC 0997 distance measurement, we assume it to be $\approx 10\%$ and as standard we do not include it in our final SMBH uncertainties.

The central molecular hole of NGC 0997 is asymmetric and non-circular, with a maximal extent of $R_{\rm hole} \approx 0.5$ arcsec. The synthesised beam is again smaller than the hole, suggesting the hole is real. Using the standard definition of the SMBH sphere of influence and our best-fitting SMBH mass yields $R_{\rm SoI} \approx 89$ pc (≈ 0.20 arcsec). From the cumulative mass distribution of NGC 0997 shown in Fig. 2.15, $R_{\rm eq} \approx 110$ pc (≈ 0.25 arcsec). As discussed earlier, the PVD has an asymmetric enhancement of velocities at ≈ 0.2 arcsec, well within $R_{\rm eq}$ and approximately at $R_{\rm SoI}$. As such, this enhancement is likely the

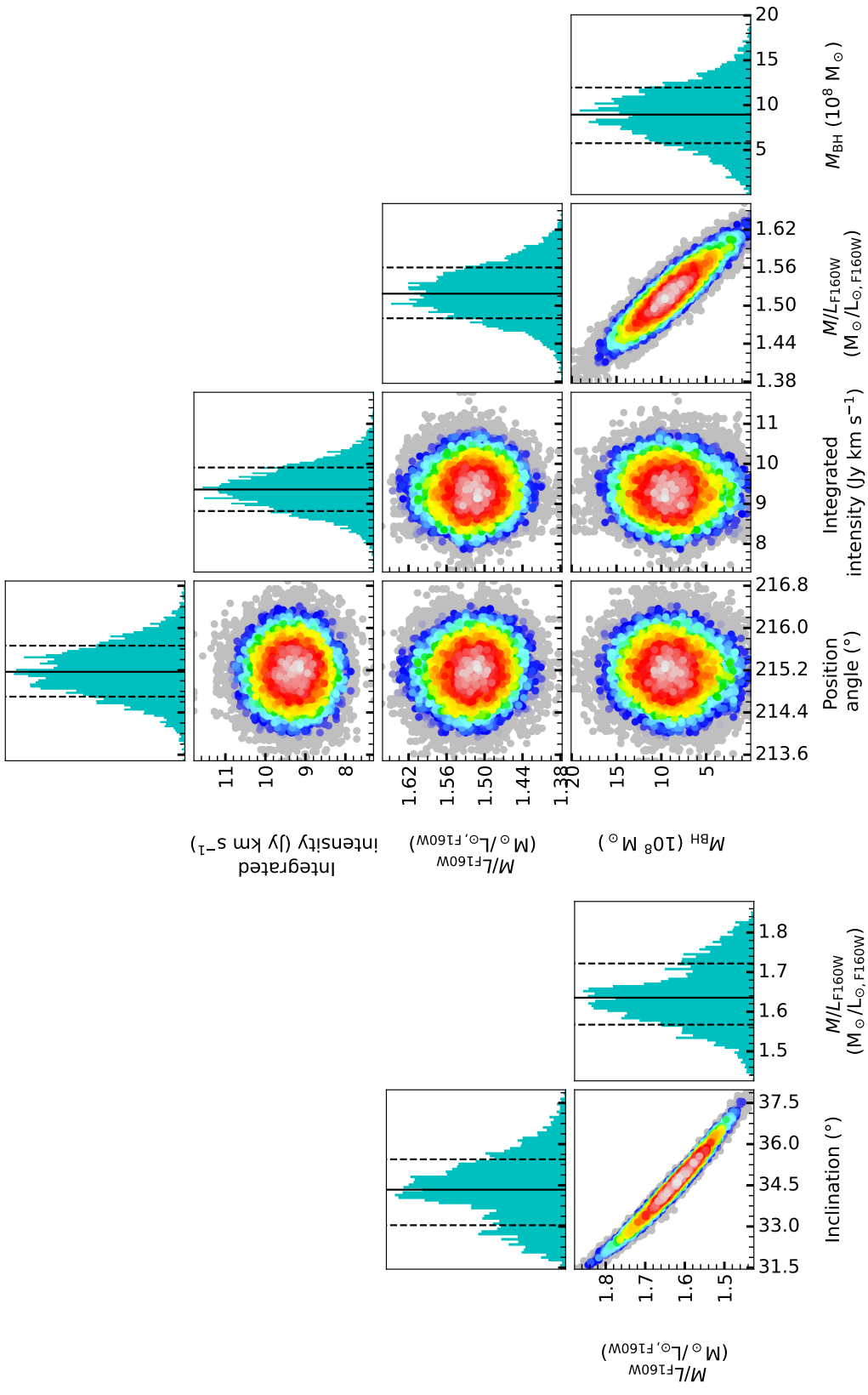


Figure 2.13: As Fig. 2.5, but for NGC 0997. **Left:** Results from first modelling step, showing the covariance between i and M/L. **Right:** Results from second modelling step, showing the covariances between all other non-nuisance parameters.

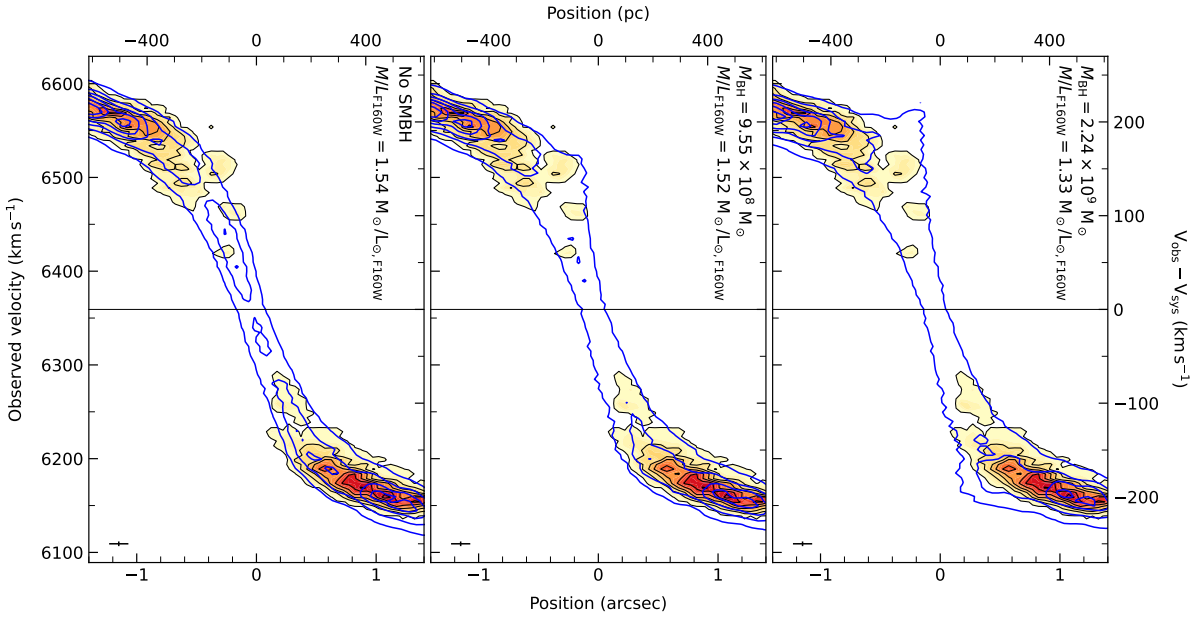


Figure 2.14: As Fig. 2.6, but for NGC 0997.

result of a SMBH and is the reason the SMBH mass can be constrained despite the otherwise depleted central molecular gas.

In NGC 0997, ≈ 74% of the mass enclosed at $R_{\rm beam}$ is due to the SMBH, which again would have made a SMBH mass measurement trivial if not for the central hole. This fraction however drops to ≈ 20% at the maximal extent of the hole, which probably explains why the 3σ confidence intervals are larger than expected.

As before, we consider the contributions from molecular gas to be negligible as NGC 0997 has a total molecular gas mass of $1.82^{+1.30}_{-1.21} \times 10^9$ M$_\odot$, spread over its entire molecular gas disc (≈ 5 arcsec or ≈ 2.2 kpc in radius). As before, we also consider dark matter effects negligible.

2.5 NGC 4751

The material in this section was originally published in the Monthly Notices of the Royal Astronomical Society, Volume 542, Pages 2039 – 2059.

2.5.1 Galaxy Properties

NGC 4751 is an ETG located at $12^{\rm h}52^{\rm m}50\overset{\rm s}{.}79$, $-42°39'35\overset{''}{.}7$ (J2000.0) in the constellation of Centaurus. We adopt a distance D = 26.9 Mpc, that was calculated using the galaxy

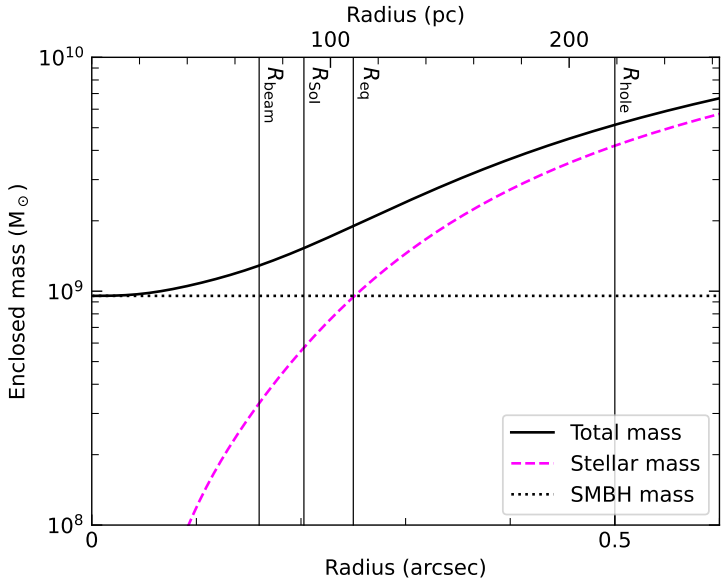


Figure 2.15: As Fig. 2.8, but for NGC 0997 (assuming $\sigma_e = 215$ km s^{-1} and our best-fitting SMBH mass). We note that $R_{hole} \approx 0.5$ arcsec refers to the visually-determined maximal extent of the asymmetric hole.

heliocentric velocity corrected for infall of the Local Group into the Virgo Cluster of galaxies and assuming a Hubble constant $H_0 = 72$ km s^{-1} Mpc^{-1} (Rusli et al. 2013). We choose the same distance and cosmology as Rusli et al. (2013), allowing us to perform a direct comparison of the SMBH mass measurements. At this distance, 1 arcsec corresponds to ≈ 130 pc.

NGC 4751 has a total absolute B-band magnitude of -19.71 and a total absolute V-band magnitude of -20.75 (Rusli et al. 2013). Based on 2MASS K_s-band images, it has a spheroid absolute magnitude of -21.53 ± 0.60 and a total absolute magnitude of -22.11 ± 0.20 (Sahu et al. 2019). Based on these and a 3.6 μm stellar M/L of 0.7 $M_\odot/L_{\odot,3.6\mu m}$ (Sahu et al. 2019), NGC 4751 has an estimated spheroid stellar mass $M_{\star,sph} = 3.09^{+2.53}_{-1.39} \times 10^{10}$ $M_\odot$ and an estimated total galaxy stellar mass $M_{\star,gal} = 5.25^{+1.67}_{-1.27} \times 10^{10}$ $M_\odot$ (Sahu et al. 2019).

HST optical images reveal a prominent nearly edge-on dust disc, ≈ 34 arcsec in diameter along its major axis, with dust lanes to the west of an unobscured nucleus (see Fig. 2.16). There is a small object ≈ 18 arcsec south of NGC 4751 that is most likely a foreground star (Fig. 2.16).

There is some disagreement as to whether NGC 4751 is an elliptical or a lenticular galaxy. Images of NGC 4751 suggest that it is comprised of two components, a relatively round central component with a steep radial surface brightness profile and an outer component that is flatter and has a shallower surface brightness profile. This is a defining characteristic of

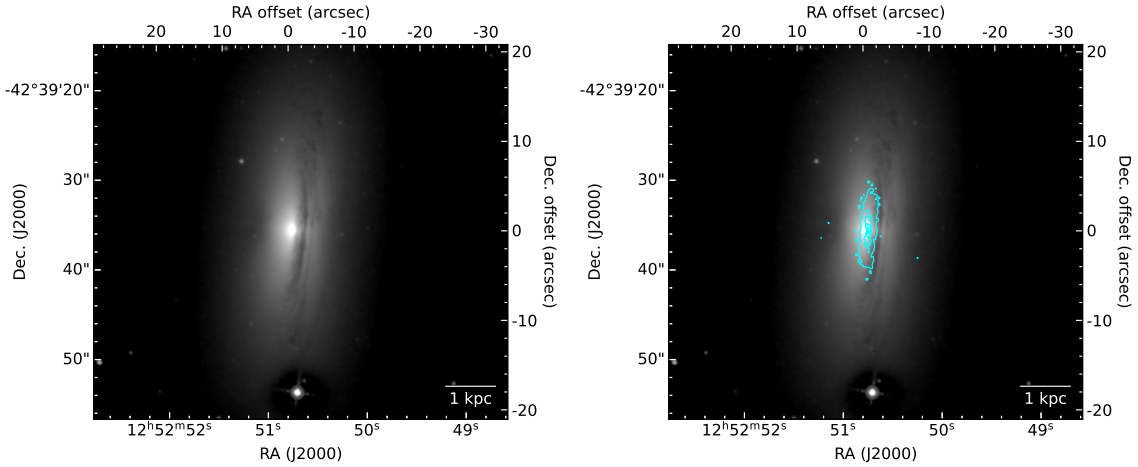


Figure 2.16: Unsharp-masked *HST* WFC3 F160W filter (H-band) image of NGC 4751 (top), overlaid with the ^{12}CO(3–2) integrated intensity contours (cyan) from our ALMA observations (bottom).

S0 galaxies, and if the central component is interpreted as a bulge and the outer component as a disc, the bulge-to-total luminosity ratio is $B/T = 0.55 \pm 0.05$ (Kormendy & Ho 2013). Thus, canonically-speaking, NGC 4751 should be classified as an S0 galaxy. However, some studies suggest that both cluster (Kormendy et al. 2009) and field (Huang et al. 2013) ellipticals are naturally divided into objects with cored stellar profiles that formed through dry (gas-poor) mergers and cuspy stellar profiles that formed through wet (gas-rich) mergers. Thus, Kormendy & Ho (2013) argued that NGC 4751 is really a highly-flattened extreme (E6) cuspy elliptical galaxy, whereby the central component is interpreted as resulting from a starburst event and the outer component is the consequence of the violent relaxation of pre-existing stars (Mihos & Hernquist 1994; Hopkins et al. 2009).

Integral-field spectroscopic data obtained using adaptive optics-assisted SINgle Faint Object Near-IR Investigation (SINFONI) observations on the Very Large Telescope were modelled using three-integral Schwarzschild models by Rusli et al. (2013) to infer a central SMBH mass $M_{\rm BH} = (1.4 \pm 0.1) \times 10^9$ M$_\odot$ and an R-band stellar $M/L_R = 12.2^{+0.6}_{-0.7}$ M$_\odot$/ L$_{\odot,R}$ (based on a model with dark matter present) or $M/L_R = 13.1^{+0.3}_{-0.4}$ M$_\odot$/ L$_{\odot,R}$ (based on a model without dark matter).

NGC 4751 has an effective radius $R_{\rm e} = 22.8$ arcsec, a central velocity dispersion $\sigma_0 = 357.6 \pm 17.7$ km s^{-1} (Campbell et al. 2014) and an effective stellar velocity dispersion $\sigma_{\rm e} = 355.4 \pm 13.6$ km s^{-1} (Rusli et al. 2013). Using the latter and the $M_{\rm BH} - \sigma_{\rm e}$ relation of

van den Bosch (2016), we expect a SMBH mass of $\approx 4.5{\times}10^9$ $M_\odot$, about three times larger than that inferred by Rusli et al. (2013). Calculating the sphere of influence as in previous sections and using the SMBH mass of Rusli et al. (2013) yields $R_{\rm SoI} \approx 48$ pc (≈ 0.37 arcsec), whereas the SMBH mass estimate from the $M_{\rm BH} - \sigma_{\rm e}$ relation yields $R_{\rm SoI} \approx 154$ pc (≈ 1.18 arcsec).

2.5.2 ALMA Observations

Observations of the ^{12}CO(3–2) emission line of NGC 4751 using the 12-m ALMA array in Band 7 were obtained as part of project 2016.1.01135.S (PI: Nagar). The data were collected with one track on 17th May 2017, for a total of 1361 s on source. The baselines ranged from 15 m to 1.1 km, yielding an angular resolution of 0.19 arcsec, a maximum recoverable scale of 2.2 arcsec (≈ 290 pc), and a field of view of 16.7 arcsec (≈ 2.2 kpc).

The relevant observations had four spectral windows, each with a bandwidth of 2.0 GHz (≈ 1735 km s^{-1}) subdivided into 128 channels of ≈ 16 MHz (≈ 13.5 km s^{-1}). Two of the spectral windows were centred on both sides of the redshifted frequency of the ^{12}CO(3–2) line (rest frequency $\nu_{\rm rest} = 345.796$ GHz), with a small gap in frequency between them. The remaining two spectral windows were used to map the continuum. The data were calibrated and imaged using CASA as before.

Line emission

Using the CASA task `tclean`, we interactively cleaned the continuum-subtracted *uv* data to a threshold equal to the RMS noise of the dirty channels in the cube (in regions without line emission). We imaged the data using the same CASA task, Briggs weighting with a robust parameter of 0.5 and a channel width of 30 km s^{-1}. We chose this channel width, roughly twice the native one, to improve the signal-to-noise ratio of the emission within the cube, in turn allowing us to adopt a higher angular and thus physical resolution, as required by our science goals. While the minimum SMBH mass detectable tends to increase with increasing channel width (Davis 2014), we expect the SMBH mass to be large enough (based on estimates from the $M_{\rm BH} - \sigma_{\rm e}$ relation) for this not to be an issue here. The resulting data cube has a synthesised beam of 0.20 arcsec $\times$ 0.18 arcsec ($\approx 26 \times 23$ pc^2), sampled

Table 2.11: CO data cube properties for NGC 4751.

Image property	Value
Spatial extent (pix)	800×800
Spatial extent (arcsec)	32.0×32.0
Spatial extent (kpc)	4.2×4.2
Pixel scale (arcsec pix^{-1})	0.04
Pixel scale (pc pix^{-1})	5.2
Velocity range (km s^{-1})	1300 – 2800
Channel width (km s^{-1})	30
RMS noise (mJy beam^{-1} channel^{-1})	0.44
Number of constraints	86, 091
Synthesised beam (arcsec)	0.20×0.18
Synthesised beam (pc)	26×23

with 0.04 arcsec spaxels, and a RMS noise of 0.44 mJy beam^{-1} channel^{-1}. The properties of our adopted data cube are summarised in Table 2.11.

The zeroth (integrated-intensity), first (intensity-weighted mean line-of-sight velocity) and second (intensity-weighted line-of-sight velocity dispersion) moment maps were created using a standard masked-moment technique (Dame 2011) implemented in the PYMAKEPLOTS package, clipped to a threshold of 5 times the RMS noise. A kinematic major-axis PVD is also created by taking a cut through the cube (with the same mask applied as in the moment maps) along a position angle of 354.°8. The resulting moment maps and PVD are shown in Fig. 2.17.

We detect a highly-inclined disc of molecular gas, ≈ 9 arcsec $\times$ 2 arcsec in projection, in regular rotation and coincident with but much smaller than the dust disc (see Fig. 2.16). The molecular gas of NGC 4751 appears to extends all the way to the centre, with no visible circumnuclear hole nor clear depression at the dynamically-determined centre of the galaxy (marked with a cyan cross in Fig. 2.17). There is however a small depression ≈ 0.2 arcsec north of the centre. The vast majority of existing molecular gas SMBH measurements used lower-J transitions, most commonly ^{12}CO(2–1). The lack of a central hole in our ^{12}CO(3–2) data could suggest that thermal effects in accretion discs reduce the fraction of gas emitting in the low-J transitions in the innermost regions. The PVD shows a rotation curve with a remarkably extended Keplerian rise in the centre.

Figure 2.18 shows the ^{12}CO(3–2) integrated spectrum of NGC 4751, extracted from a 12 arcsec $\times$ 12 arcsec ($\approx 1.6 \times 1.6$ kpc^2) region around the centre of the galaxy, using the primary beam-corrected cube with the same mask applied as for the moment maps and

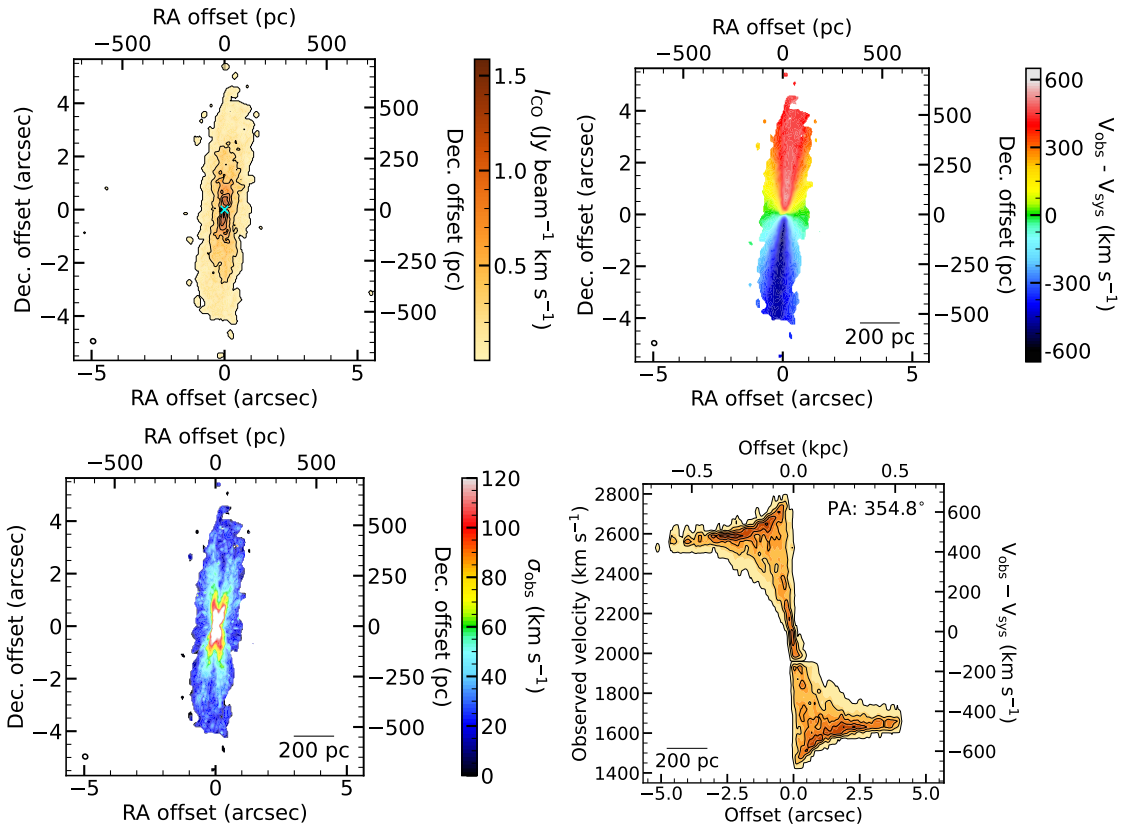


Figure 2.17: As Fig. 2.2 but for the ^{12}CO(3–2) line of NGC 4751. The cyan cross in the zeroth-moment map demarcates the dynamical centre of the galaxy

PVD. The spectrum exhibits the characteristic double-horn shape of a rotating disc. The integrated flux of our cube (measured within the mask defined above) is 80.5 ± 0.2 [stat] ± 8.1 [sys] Jy km s^{-1}, where the systematic uncertainty represents the 10 per cent absolute flux calibration accuracy (Andreani et al. 2016). The statistical uncertainty is calculated as in Liang et al. (2023), where for each line channel we calculate the integrated flux uncertainty within the 2D masked region and then propagate this uncertainty in the standard manner to the flux integrated over all channels. We assume no covariance between adjacent channels due to the large channel width. This number includes emission in the missing channels, which was interpolated linearly from the closest channels on either side. Assuming a ^{12}CO(3–2)/^{12}CO(1–0) line ratio of 0.31 (in brightness temperature units; Leroy et al. 2022) and a standard CO(1–0)-to-molecule conversion factor (with contribution from heavy elements included) $\alpha_{\mathrm{CO(1-0)}} = 4.35\ \mathrm{M_\odot\ pc^{-2}\ (K\ km\ s^{-1})^{-1}}$, we obtain a CO(3–2)-to-molecule conversion factor $\alpha_{\mathrm{CO(3-2)}} = 14.0\ \mathrm{M_\odot\ pc^{-2}\ (K\ km\ s^{-1})^{-1}}$, yielding a total molecular gas mass

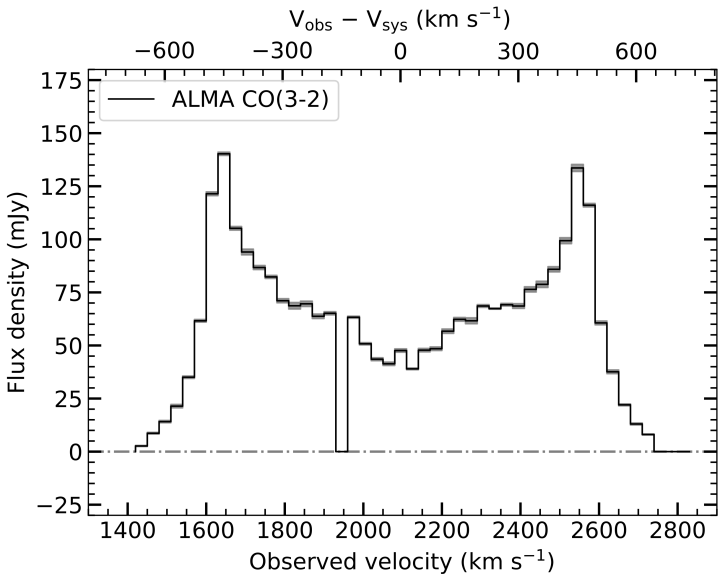


Figure 2.18: ^{12}CO(3–2) integrated spectrum of NGC 4751, with the characteristic double-horn shape of a rotating disc. Statistical uncertainties are shown as grey shading. The spectrum was extracted from a 12 arcsec × 12 arcsec (≈ 1.6 × 1.6 kpc^2) region centred on the galaxy centre, that includes all detected emission. The data were obtained in two spectral windows which do overlap, but the pipeline calibration process masked the end channels, likely due to bandpass calibration issues, hence the small gap at ≈ 1940 km s^{-1}.

of $(2.27 \pm 0.01[\text{stat}] \pm 0.22[\text{sys}]) \times 10^8$ M$_\odot$ over an inner region of ≈ 1 kpc in diameter.

Continuum emission

We imaged the continuum emission of NGC 4751 using the same continuum spectral windows and line-free channels of the line spectral windows that were used for continuum subtraction in the section above. We used the multi-frequency synthesis mode of the CASA task `tclean` and Briggs weighting with a robust parameter of 0.5, resulting in a continuum emission map with a central frequency of 343.548 GHz (0.87 mm) and a RMS noise of 0.09 mJy beam^{-1}. We cleaned this map to a threshold equal to 3 times the RMS noise and detected a small central source. Fitting this source with a 2D Gaussian function using the CASA task `imfit` reveals a spatially-resolved source with deconvolved full-widths at half-maximum (FWHM) of $(106 \pm 8) \times (75 \pm 9)$ marcsec^2 and an integrated flux density of 9.9 ± 0.2 mJy. The properties of the continuum emission are listed in Table 2.12.

Table 2.12: Parameters of the NGC 4751 continuum image and the detected cleaned continuum source.

Image property	Value
Image (pix)	800×800
Image (arcsec)	32×32
Image size (kpc)	4.2×4.2
Pixel scale (arcsec pix^{-1})	0.04
Pixel scale (pc pix^{-1})	5.2
RMS noise (mJy beam^{-1})	0.07
Synthesised beam (arcsec)	0.19×0.17
Synthesised beam (pc)	25×22
Source property	**Value**
Right ascension (J2000)	$12^{\rm h}52^{\rm m}50\overset{\rm s}{.}7444 \pm 0\overset{\rm s}{.}0001$
Declination (J2000)	$-42°39'35\overset{''}{.}546 \pm 0\overset{''}{.}001$
Integrated flux (mJy)	9.9 ± 0.2
Deconvolved size (mas)	$(106 \pm 8) \times (75 \pm 9)$
Deconvolved size (pc)	$(14 \pm 1) \times (10 \pm 1)$

2.5.3 CO Modelling

Model parameters

The simple morphology of NGC 4751 allows us reproduce the molecular gas distribution with an exponential surface density profile, parameterised as in Equation 2.1. This exponential surface brightness profile matches the NGC 4751 data well, and the choice of a centrally-concentrated profile has also been implemented in other works (e.g. Davis et al. 2013b; Ruffa et al. 2019). However it is worth noting that such a profile may not be generally appropriate for all ETGs. We also conducted tests where we allowed the exponential surface brightness profile to have a central hole, but the results of these tests suggest that there is no hole or that the hole is significantly smaller than our synthesised beam size.

Whilst no clear hole is visible in the moment maps, given the high inclination of the molecular gas disc it is of course very hard to rule out the presence of a hole of a size similar to or smaller than the synthesised beam. Indeed, at such a high inclination a small central hole would not be well resolved along the minor axis and emission along the minor axis of the galaxy might be beam-smeared and give the impression of a filled central hole. Nevertheless, due to the modelling results above, we proceed assuming no hole is present.

NGC 4751 appears axisymmetric at all radii. We parameterise the stellar light distribution using a MGE model of a *HST* WFC3 F160W filter (H-band) pipeline-drizzled image (GO-

Table 2.13: Parameters of the deconvolved best-fitting MGE components of our model of NGC 4751.

$\log I'_{\odot}$ ($L_{\odot,F160W}$ pc^{-2}) (1)	$\log \sigma'$ (arcsec) (2)	q' (3)
5.491	−0.815	0.647
4.851	−0.422	0.494
4.441	−0.238	0.990
4.150	0.171	0.750
4.099	0.177	0.319
4.002	0.524	0.517
3.511	0.934	0.397
2.913	1.411	0.420

Notes. Deconvolved MGE components. (1) Central surface brightness of Gaussian component. (2) Standard deviation of Gaussian component. (3) Axial ratio of Gaussian component.

15909, PI: Boizelle) with a total exposure time of 997 s, obtained from the Mikulski Archive for Space Telescopes (MAST). The surface brightnesses can be converted into luminosities using the AB magnitude system with a zero-point of 25.94 mag (Sahu et al. 2021) and a Solar absolute magnitude of 4.60 mag (Willmer 2018). Additionally, we adopt a galactic extinction of 0.062 mag from the NASA/IPAC Extragalactic Database (Schlafly & Finkbeiner 2011) to correct for interstellar reddening. The parameters of the deconvolved best-fitting MGE Gaussians are listed in physical units in Table 2.13 and the fit is shown in Fig. 2.19. As can be seen in Fig. 2.19, there is significant dust extinction to the west of the NGC 4751 nucleus. For our best-fitting model, we masked these dust lanes by hand, thus excluding the most obviously dust-obscured pixels, to minimise their impact on our final model. However, we explore the use of a more complex pixel-by-pixel colour correction of the dust in Section 2.5.4. The resulting MGE model provides a good fit, especially in the central regions the galaxy, which is crucial for determining an accurate SMBH mass.

In this case we also consider a M/L varying linearly with radius, in addition to the usual radially-constant M/L, as the $J-H$ colour map of NGC 4751 suggests an increase of the colour towards the centre of the galaxy that cannot be explained by an embedded dust disc (see Section 2.5.4 for more details). Thus, below we present two models that yielded equally good fits. One has a spatially-constant (free) M/L, the other has a radially linearly-varying M/L, modelled as described in Section 2.2.1 with two free model parameters ($M/L_{\mathrm{intercept}}$ and M/L_{gradient}).

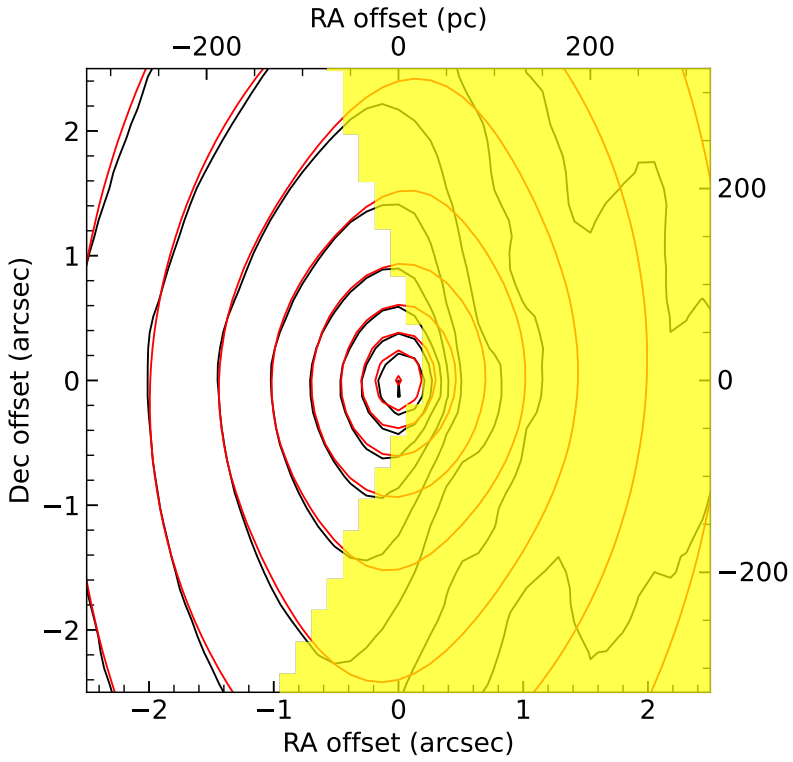


Figure 2.19: *HST* WFC3 F160W filter image of NGC 4751 (black contours), overlaid with our best-fitting MGE model (red contours). The western side of the image is masked (yellow shading), to exclude the most obviously dust-obscured pixels along the near side of the embedded disc.

Model with constant M/L

The final MCMC chain had 200,000 steps. It is clear that there is a massive dark object in the centre of NGC 4751, with a best-fitting mass of $3.43^{+0.45}_{-0.44} \times 10^9$ $M_\odot$ (3σ confidence level). The best-fitting M/L in the F160W filter is (2.68 ± 0.11) $M_\odot/L_{\odot,F160W}$. Figure 2.20 also shows a slight degeneracy between M_{BH} and M/L_{F160W}, equivalent to the conservation of (total) dynamical mass (see e.g. Smith et al. 2019 for more details).

The quality of our fit is easiest to judge by overlaying models over the kinematic major-axis PVD. From left to right in Fig. 2.21, we thus overlay the best-fitting model with no SMBH, a SMBH and an overly-massive SMBH (≈ 0.2 dex more massive than the best-fitting SMBH), respectively, allowing all parameters other then the SMBH mass to vary in the first and third case. As expected for the best-fitting no SMBH model, a higher stellar M/L is derived as the model attempts to account for the high rotation velocities at small radii without a SMBH. Nevertheless, the model is unable to reproduce those central velocities without

Table 2.14: Best-fitting molecular gas model with a constant M/L parameters and associated uncertainties.

Parameter	Prior			Best fit	1σ uncertainty	3σ uncertainty
Model with constant M/L						
Mass model						
$\log(M_{\rm BH}/{\rm M}_\odot)$	7	$\rightarrow$	11	9.535	$-0.021, +0.020$	$-0.059, +0.053$
Stellar $M/L_{\rm F160W}$ (${\rm M}_\odot/{\rm L}_{\odot,\rm F160W}$)	0.0	$\rightarrow$	5.0	2.68	±0.04	±0.11
Molecular gas disc						
Inclination (°)	0.0	$\rightarrow$	89.9	78.7	±0.1	$-0.5, +0.6$
Position angle (°)	0.0	$\rightarrow$	359.9	354.8	±0.1	$-0.3, +0.4$
Velocity dispersion (km s^{-1})	0.0	$\rightarrow$	50.0	15.1	±2.3	$-6.7, +6.5$
Scale length (arcsec)	0.0	$\rightarrow$	5.0	1.65	±0.06	$-0.15, +0.16$
Nuisance parameters						
Centre RA offset (arcsec)	-5.4	$\rightarrow$	5.4	0.03	±0.004	±0.01
Centre Dec. offset (arcsec)	-4.0	$\rightarrow$	4.0	0.31	±0.01	±0.02
Systemic velocity (km s^{-1})	1800	$\rightarrow$	2400	2094.5	±1.1	$-3.3, +2.9$
Integrated intensity (Jy km s^{-1})	0.0	$\rightarrow$	150.0	89.5	$-2.9, +2.8$	$-7.8, +7.5$

Note. The RA and Dec. offsets are measured with respect to the image phase centre, $12^{\rm h}52^{\rm m}50\overset{\rm s}{.}748$, $-42°39'35\overset{''}{.}880$ (J2000.0).

greatly exceeding the relatively low velocities at larger radii. The compromise reached is thus unsatisfactory at both small and large radii. Again as expected, the best-fitting overly-massive SMBH model yields a smaller M/L, but the fit is very poor at small radii, the model over-shooting even the highest velocities. The best-fitting SMBH model not only reproduces the data best, but the fit is very good at all radii and velocities.

Model with linearly-varying M/L

The final MCMC chain has 200,000 steps. The model has a best-fitting SMBH mass of $2.79^{+0.75}_{-0.57} \times 10^9$ ${\rm M}_\odot$ and a best-fitting M/L in the F160W filter represented by $(M/L_{\rm F160W})\,/\left({\rm M}_\odot/{\rm L}_{\odot,\rm F160W}\right) = 3.07^{+0.27}_{-0.35} - 0.09^{+0.08}_{-0.06}\,(R/{\rm arcsec})$. ETG M/L gradients have been explored in a number of previous works exploiting molecular gas dynamics (e.g. Davis & McDermid 2017; Davis et al. 2018; North et al. 2019). In these works, both positive and negative M/L gradients were detected and in most of these cases the gradients are mild, very much like our results (e.g. -0.37 ${\rm M}_\odot/{\rm L}_{\odot,\rm F160W}$ kpc^{-1} in NGC 524 compared to our -0.69 ${\rm M}_\odot/{\rm L}_{\odot,\rm F160W}$ kpc^{-1}; North et al. 2019).

Figure 2.22 again shows a negative correlation between the M/L intercept (i.e. the M/L in

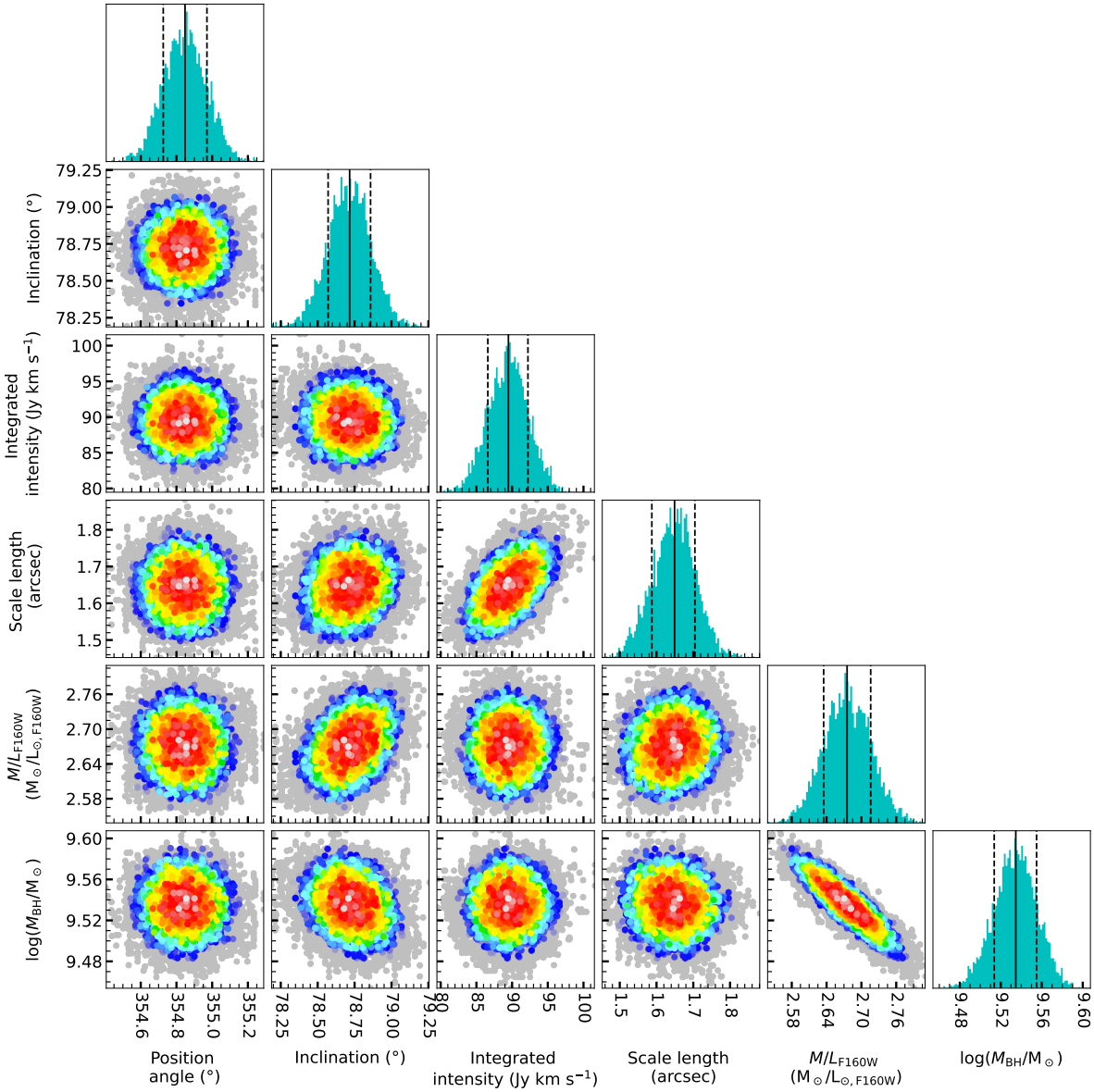


Figure 2.20: As Fig. 2.5, but for the best-fitting model with constant M/L for NGC 4751.

the centre of the galaxy) and the SMBH mass, which is again equivalent to the conservation of (total) dynamical mass. Consequently, there is also a positive correlation between SMBH mass and M/L gradient - as more mass is attributed to the SMBH, the M/L intercept decreases and thus the M/L gradient becomes less negative (to still fit the outer regions of the galaxy well).

As before, the quality of our best-fitting model is easiest to judge by overlaying it over the kinematic major-axis PVD. From left to right in Fig. 2.23, we overlay the best-fitting model with a radially linearly-varying M/L and no-SMBH, a SMBH and an overly-massive SMBH (≈ 0.2 dex more massive than the best-fitting SMBH), respectively, allowing all parameters

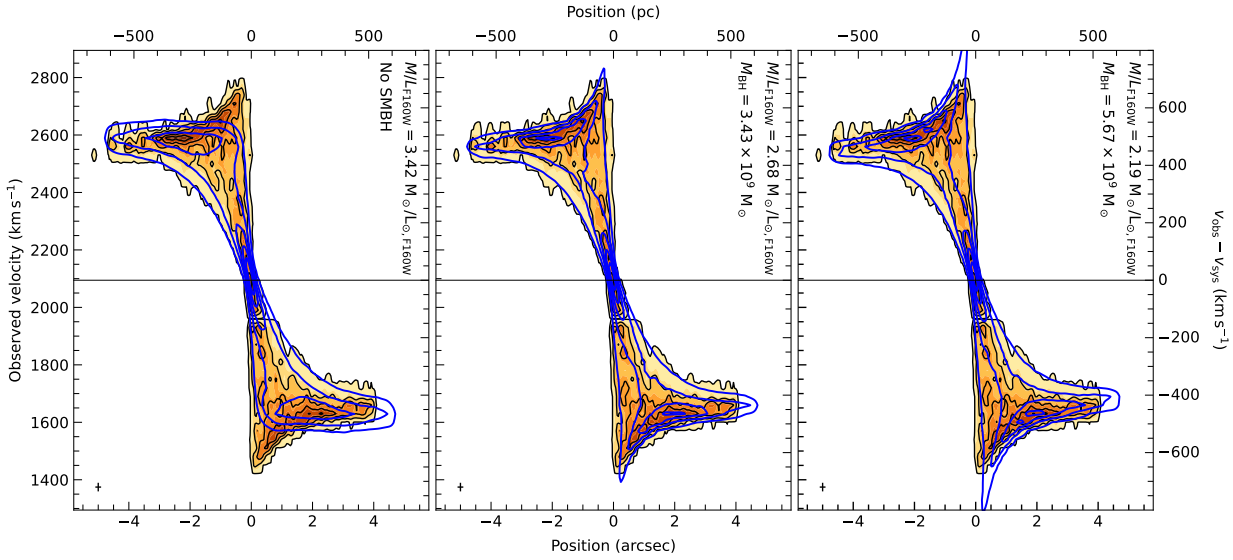


Figure 2.21: As Fig. 2.6, but for models with constant M/L for NGC 4751.

Table 2.15: Best-fitting molecular gas model with a linear M/L parameters and associated uncertainties.

Parameter	Prior			Best fit	1σ uncertainty	3σ uncertainty
Model with linearly-varying M/L						
Mass model						
$\log(M_{BH}/M_\odot)$	7	→	11	9.446	$-0.037, +0.039$	$-0.099, +0.103$
Stellar M/L_{F160W} intercept	0.0	→	5.0	3.07	$-0.13, +0.11$	$-0.35, +0.27$
Stellar M/L_{F160W} gradient	−2.0	→	2.0	−0.09	±0.03	$-0.06, +0.08$
Molecular gas disc						
Inclination (°)	0.0	→	89.9	78.6	$-0.2, +0.1$	$-0.5, +0.4$
Position angle (°)	0.0	→	359.9	354.8	±0.1	$-0.3, +0.4$
Velocity dispersion (km s^{-1})	0.0	→	50.0	14.8	±1.5	$-4.3, +4.4$
Scale length (arcsec)	0.0	→	5.0	1.65	±0.06	$-0.16, +0.15$
Nuisance parameters						
Centre RA offset (arcsec)	−5.4	→	5.4	0.03	±0.004	±0.01
Centre Dec. offset (arcsec)	−4.0	→	4.0	0.31	±0.01	±0.02
Systemic velocity (km s^{-1})	1800	→	2400	2094.3	$-1.1, +1.0$	$-4.4, +4.3$
Integrated intensity (Jy km s^{-1})	0.0	→	150.0	89.6	$-2.7, +2.8$	$-7.3, +7.8$

Notes. The RA and Dec. offsets are measured with respect to the image phase centre, $12^h52^m50\overset{s}{.}748$, $-42°39'35\overset{''}{.}880$ (J2000.0). The M/L and M/L intercept are expressed in units $M_\odot/L_{\odot,F160W}$ and the M/L gradient is expressed in units $M_\odot/L_{\odot,F160W}$ arcsec^{-1}.

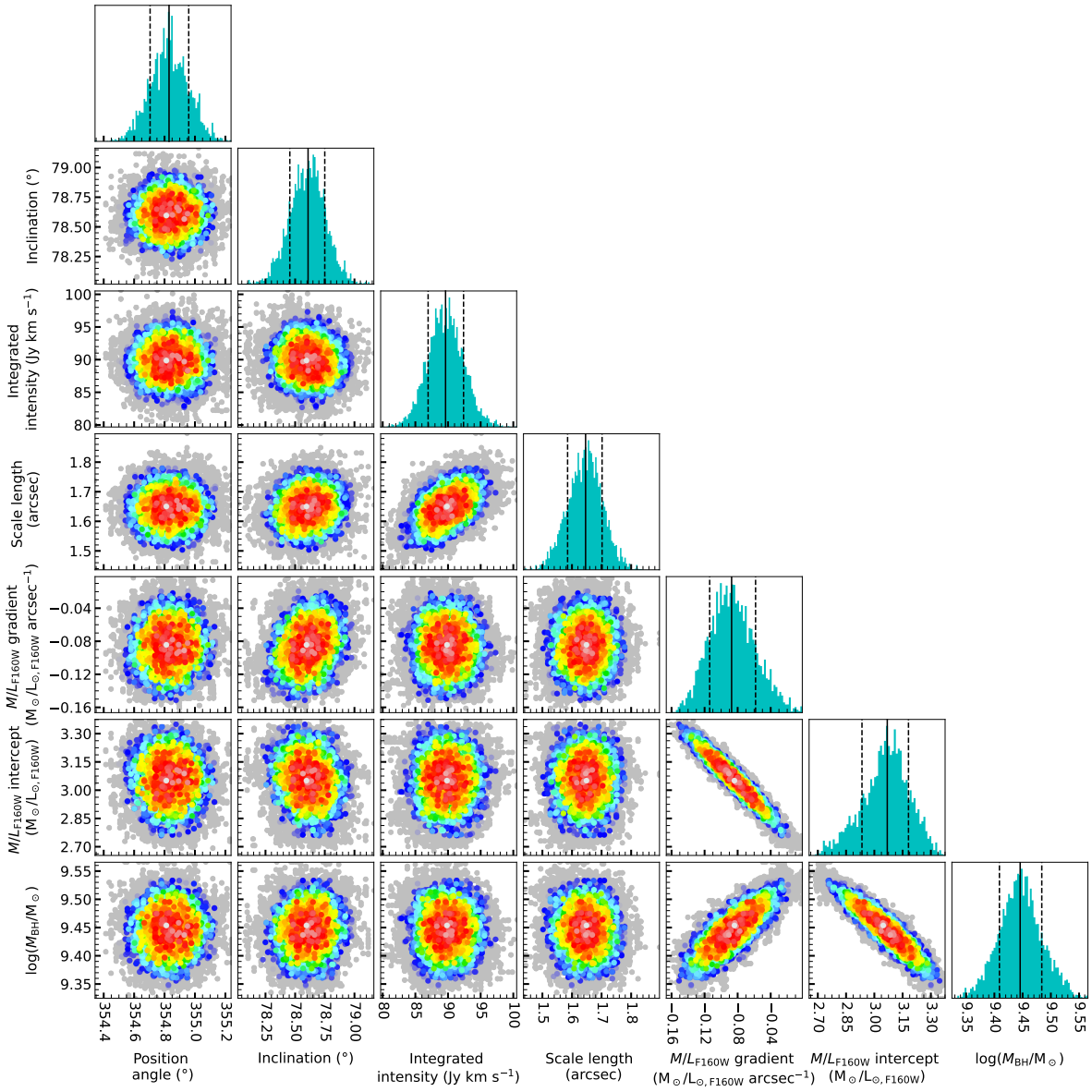


Figure 2.22: As Fig. 2.5, but for the best-fitting model with a linearly-varying M/L for NGC 4751.

other than the SMBH mass to vary in the first and third case. As expected, the best-fitting no SMBH model has a higher M/L intercept, to account for the high rotation velocities at small radii, and a more negative M/L gradient, to lower the overall M/L at larger radii. As before, the model fails to reproduce the extremely high central velocities without also exceeding the low velocities at large radii. The best-fitting overly-massive SMBH model yields a significantly smaller M/L intercept that contributes less dynamical mass to the stellar component. As expected, the M/L gradient is also now positive, as otherwise the low central M/L would lead to undershooting the velocities at large radii. Despite this, the

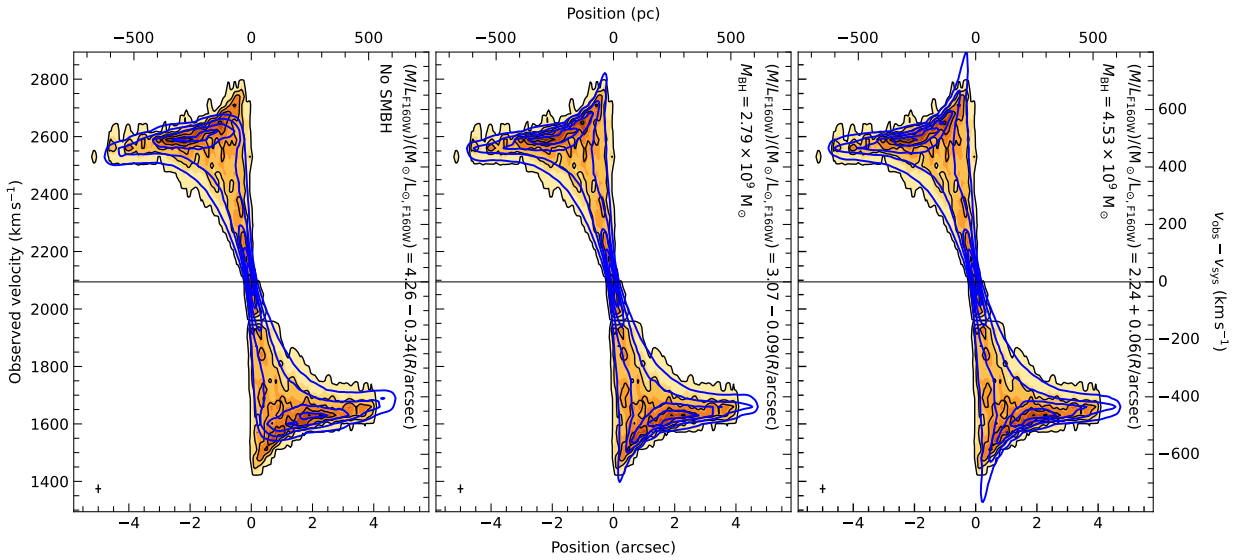


Figure 2.23: As Fig. 2.6, but for models with a linearly-varying M/L for NGC 4751.

overly-massive SMBH model is unable to reproduce the data satisfactorily. Once again, the best-fitting free SMBH model reproduces the data best, fitting well at all radii and velocities.

2.5.4 Discussion

Best-fitting molecular gas mass models

We presented molecular gas-based mass models with two different M/L radial profiles for NGC 4751. As shown in Figs. 2.21 and 2.23, the two models provide near-identical fits visually. Whilst the χ^2 statistic is primarily used to compare models against data, in a limited number of situations it can also be used to compare model against model. This is the case here, as the model with a constant M/L is nested within the model with a linearly-varying M/L (i.e. the model with a constant M/L is a particular case of the model with a linearly-varying M/L, where the M/L gradient is equal to 0). We can thus judge the relative goodness-of-fit of the two models more robustly by using the reduced χ^2 statistic χ^2_{red}. The best-fitting CO model with a constant M/L has $\chi^2_{\mathrm{red}} = 2.49$, while the best-fitting CO model with a radially linearly-varying M/L has $\chi^2_{\mathrm{red}} = 2.43$. As such, we can conclude that the model with a linearly-varying M/L is a marginally better fit (the additional M/L gradient variable would be expected to converge to 0 if the data strongly suggested a constant M/L). As the χ^2_{red} difference is small, however, we choose to also

Table 2.16: χ^2 of the models discussed.

Model (1)	$\chi^2_{\rm red}$ (2)	k (3)	BIC (4)
Best-fitting CO model with constant M/L	2.49	10	610
Best-fitting CO model with linearly-varying M/L	2.43	11	609

Notes. (1) Model. (2) Reduced χ^2 statistic. (3) Number of free parameters.(4) Bayesian information criterion.

report the Bayesian information criterion BIC $\equiv k \ln N - 2 \ln P$ to compare the models, where k is the number of free parameters of each model and N and $\ln P$ are as defined in Section 2.2.2. The BIC provides a heuristic approximation of the Bayes factor, which is the statistically-correct way to compare models. Indeed, the BIC not only allows for the comparison of non-nested models with different numbers of parameters, but it also penalises models with excessive dimensionality that could otherwise overfit the data. The BIC difference between the two best-fitting CO models presented in this paper is $\Delta_{\rm BIC} \approx 1$, and statistically-speaking it is not possible to formally prefer one model over the other (Kass & Raftery 1995). These results are summarised in Table 2.16.

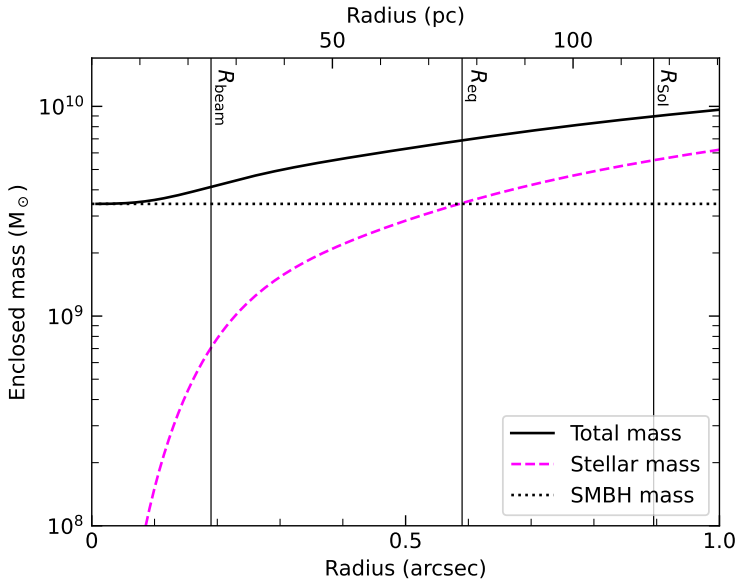


Figure 2.24: As Fig. 2.8, but for NGC 4751 for the model with constant M/L (assuming $\sigma_{\rm e}$ = 355.4 km s^{-1} and our best-fitting SMBH mass).

Figures 2.24 and 2.25 show the cumulative mass distribution of NGC 4751 for the molecular gas kinematic model with a constant M/L and the model with a radially linearly-varying M/L, respectively. Using the standard definition of a SMBH SoI and the best-fitting

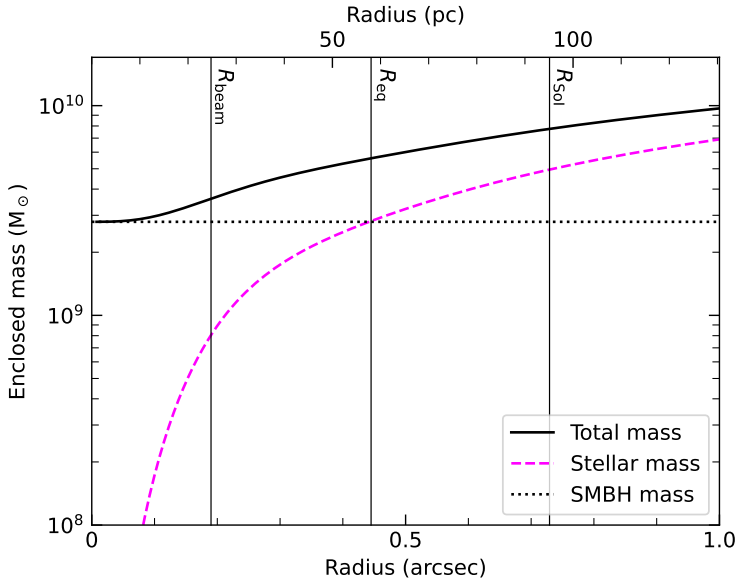


Figure 2.25: As Fig. 2.8, but for NGC 4751 for the model with a linearly-varying M/L (assuming $\sigma_{\rm e} = 355.4$ km s^{-1} and our best-fitting SMBH mass).

SMBH mass for the constant M/L model yields $R_{\rm SoI} \approx 116$ pc (≈ 0.89 arcsec), whereas the best-fitting SMBH mass for the linear M/L model yields $R_{\rm SoI} \approx 95$ pc (≈ 0.73 arcsec). Both of these are significantly larger than the size of the synthesised beam ($R_{\rm beam}$). One can also assess the impact of a SMBH by considering the radius at which the enclosed stellar mass is equal to that of the SMBH. Figure 2.24 shows this radius of equal mass contribution to be $R_{\rm eq} \approx 77$ pc (≈ 0.59 arcsec), smaller than the usual $R_{\rm SoI}$ but still significantly larger than $R_{\rm beam}$. Figure 2.25 shows the radius of equal mass contribution to be $R_{\rm eq} \approx 59$ pc (≈ 0.45 arcsec), also smaller than the usual $R_{\rm SoI}$, but still more than twice $R_{\rm beam}$. In fact, in both models the SMBH dominates the potential so significantly that at the innermost radius probed ($R_{\rm beam}$) ≈ 82 per cent of the enclosed mass is due to the SMBH in the constant M/L model and ≈ 76 per cent in the linear M/L model, making the SMBH mass determination trivial in both models.

The quality of a SMBH measurement can also be assessed in terms of how well resolved the SMBH SoI is and the proximity of the dynamical tracer to the SMBH. In the region dominated by the SMBH, Zhang et al. (2024) derived a simple relation between the highest circular velocity measured $v_{\rm c}$ and the innermost radius probed $R_{\rm min}$, where $R_{\rm min}$ can be normalised by respectively the Schwarzschild radius ($R_{\rm Schw} \equiv 2GM_{\rm BH}/c^2$, where c is the

speed of light), $R_{\rm SoI}$ and $R_{\rm eq}$. The resulting relations allow to compare the spatial resolutions of different datasets and the sizes of the regions probed in a $M_{\rm BH}$-independent manner. Our observations of NGC 4751 detect a maximum line-of-sight velocity $v_{\rm obs} \approx 687$ km s^{-1} (see e.g. Fig. 2.21). Deprojecting this velocity using $v_{\rm c} = v_{\rm obs}/\sin i$, where $i = 78.^{\circ}7$ (Table 2.14), the highest circular velocity probed is ≈ 700 km s^{-1}. This is the second highest circular velocity ever probed by a molecular gas measurement, rivaled only by the high-resolution measurement of NGC 0383 (Zhang et al. 2025a). While some of the high central velocities must originate from the dense central stellar component of the galaxy (see Fig. 2.16), our molecular gas data with a spatial resolution of ≈ 24 pc (0.19 arcsec) allow us to probe remarkably close to the SMBH: down to $R_{\rm min}/R_{\rm Schw} \approx 83,000$, $R_{\rm min}/R_{\rm SoI} \approx 0.23$ and $R_{\rm min}/R_{\rm eq} \approx 0.33$ for the model with a constant M/L, and $R_{\rm min}/R_{\rm Schw} \approx 101,000$, $R_{\rm min}/R_{\rm SoI} \approx 0.28$ and $R_{\rm min}/R_{\rm eq} \approx 0.46$ for the model with a radially linearly-varying M/L.

Molecular gas-derived SMBH mass uncertainties

Aside from the fitting uncertainties listed in Tables 2.14 and 2.15, which are fundamentally statistical in nature, our molecular gas measurements are subject to several potential sources of systematic error. The first of these is the distance. For all dynamical mass measurements, $M_{\rm BH} \propto D$, so the adopted distance affects the SMBH mass linearly. Conversely, the inferred SMBH mass can be re-scaled for any adopted distance. As standard, the distance uncertainties are neither quoted nor propagated into our SMBH mass measurement, but these are typically about 20 – 30 per cent when flow models are applied to relatively nearby galaxies ($D < 50$ Mpc; Lelli et al. 2016).

In our modelling we have only considered the mass contributions of the SMBH and stars, and have assumed the dark matter and molecular gas to have negligible masses. The spatial scales over which dark matter effects are significant are much greater than those considered in this paper and those where the SMBH dominates the potential. In the very unlikely scenario that there is significant diffuse dark matter in the central regions, its contribution to the circular velocity is expected to increase with radius similarly to that of the stars, whereas the contribution of the SMBH declines in a Keplerian fashion (see e.g. Fig. 7 of Lelli et al. 2022). Thus, the dark matter contribution is most strongly degenerate

with that of the stars, which would lead to a different best-fitting M/L without strongly affecting the SMBH mass. Furthermore, Rusli et al. (2013) considered models of NGC 4751 with and without dark matter, and there was no significant difference in the SMBH masses inferred, with only a minor impact on the M/L (see Section 2.5.1). Similarly, as discussed in Section 2.5.2, NGC 4751 has an extended molecular gas distribution with a total mass of $(2.27 \pm 0.01) \times 10^8$ $M_\odot$, which if plotted would not even be visible in Figs. 2.24 and 2.25 (as the total mass is only reached at the outer edge of the disc). The contribution of molecular gas is thus negligible compared to those of the SMBH and stars.

Another source of uncertainties of the model parameters reported in this work comes from the modelling assumptions made. Our modelling involves some trade-offs between allowing more model complexity, which should lead to more accurately reproduce the data, and introducing simplifying assumptions, to ensure model convergence and a reasonable computational time. Our models clearly include many simplifying assumptions, such as a constant position angle and inclination angle, but these assumptions are well substantiated by the data themselves (see Fig. 2.17). Our exploration of different M/L radial profiles appears in this case to be a useful test of how variations of an important model assumption affect the model outcomes, and the differences between the best-fitting $M_{\rm BH}$ and M/L of the two models are a reflection of systematic errors.

In addition to the two models presented in this paper, we tested alternative models to better quantify potential systematic errors. In the previous sections, we used an exponential surface brightness profile to parameterise the molecular gas distribution. An alternative and more appropriate, but often more computationally costly, way of representing the molecular gas distribution is to simply use the molecular gas distribution itself as a model input. This can be done through the use of either the zeroth-moment map or the clean components generated during the cleaning process. We chose to create such a model using the latter method and SkySampler (Smith et al. 2019). This yields a best-fitting SMBH mass $M_{\rm BH} = 2.94^{+0.36}_{-0.35} \times 10^9$ $M_\odot$ and a best-fitting F160W filter $M/L_{F160W} = (2.78 \pm 0.11)$ $M_\odot/L_{\odot,\rm F160W}$, representing a 17 per cent decrease of the SMBH mass and a 4 per cent increase of the M/L compared to the exponential disc model with a constant M/L.

A potential source of systematic errors arises from the choice of MGE model. Typically, we use the the MgeFit procedure to parameterise the stellar light distribution, but this is not the only method available to us. Davidson et al. (2024) present an alternative MGE model based on a 2D parametric galaxy fit obtained using the algorithm GALFIT. In addition to using a different algorithm, Davidson et al. (2024) utilise a different PSF. These differences can have a significant impact on the innermost Gaussian of the MGE, particularly in cuspy galaxies like NGC 4751, which can in turn impact modelling outcomes. To test these effects, we performed a fit using the Davidson et al. (2024) MGE (their Table 5; with uniform PA), yielding a best-fitting SMBH mass $M_{\rm BH} = 2.79^{+0.59}_{-0.61} \times 10^9$ $\rm M_\odot$ and a best-fitting F160W filter $M/L_{F160W} = 2.42^{+0.13}_{-0.11}$ $\rm M_\odot/L_{\odot,F160W}$, representing a 19 per cent decrease of the SMBH mass and a 10 per cent decrease of the M/L compared to those of the model with the MGE components from Table 2.13.

Another likely major source of systematic errors arises from noticeable dust extinction in the NGC 4751 *HST* image (Fig. 2.16). While care was taken to choose an image in the reddest filter possible (to minimise dust extinction) and we masked the most obviously dust-obscured pixels, a more thorough treatment of dust involves creating a dust-corrected MGE model. We now attempt this below.

We perform the dust correction using a WFC3 F110W filter (J-band) image in addition to the previously used F160W filter (H-band) image. We first re-drizzle the F110W filter image to match the pixels in the F160W filter image. Having converted both images to units of magnitude in the Vega system, we calculate the observed $J-H$ colour of every pixel $(J-H)_{\rm obs}$. Given that the inner region of the galaxy is reddened by the embedded dust disc, we can only confidently estimate the intrinsic $J-H$ colour on the outskirts of the image, beyond the large-scale dusty circumnuclear disc. We measure $(J-H)_{\rm int} = 0.8$ mag and assume this number throughout. We then calculate the colour excess of every pixel $E(J-H) \equiv (J-H)_{\rm obs} - (J-H)_{\rm int}$ and create an extinction map A_H by dividing the colour excess map by the ratio of the total extinctions obtained using the standard Galactic extinction curve with $R_V = 3.1$ (Fitzpatrick 1999), where R_V is the total-to-selective extinction ratio:

$$A_H = \frac{E(J-H)}{\left(\frac{A_J}{A_V}\frac{A_V}{A_H} - 1\right)} \quad . \tag{2.3}$$

Table 2.17: Parameters of the deconvolved best-fitting dust-corrected MGE components for NGC 4751.

Extinction-corrected			Nuker-corrected		
$\log I'_{\odot}$ ($L_{\odot,F160W}$ pc^{-2}) (1)	$\log \sigma'$ (arcsec) (2)	q' (3)	$\log I'_{\odot}$ ($L_{\odot,F160W}$ pc^{-2}) (1)	$\log \sigma'$ (arcsec) (2)	q' (3)
5.488	−0.935	0.951	5.577	−0.922	0.990
5.007	−0.590	0.405	5.028	−0.363	0.623
4.771	−0.446	0.790	4.183	−0.140	0.841
4.506	−0.272	0.990	4.518	0.043	0.351
4.033	0.088	0.990	4.212	0.235	0.708
4.255	0.103	0.327	3.991	0.466	0.556
3.928	0.328	0.441	3.631	0.787	0.456
4.017	0.534	0.512	2.702	1.255	0.334
3.526	0.935	0.401	3.029	1.255	0.778
2.923	1.412	0.416	–		

Notes. "Deconvolved" MGE Gaussian components. (1) Central surface brightness. (2) Standard deviation. (3) Axial ratio.

We then correct our F160W filter image in the usual manner using this extinction map. Inspection of this extinction-corrected F160W filter image shows that whilst the effects of dust have been significantly alleviated, the most prominent dust lane close to the central region of the galaxy remains, suggesting that the dust in that region is (close to being) optically thick. We thus proceed to create two different MGE models, based on how we choose to treat this remaining dust.

In the first case, we simply use the same hand-drawn mask used in our original MGE model (see Fig. 2.19), to exclude the near side of the dusty disc that most affects the galaxy surface brightness. We then create a new MGE, using the same procedure as always, which we refer to as the "extinction-corrected MGE", whose "deconvolved" Gaussian components are listed in Table 2.17. The minor-axis surface brightness profile of this extinction-corrected MGE is shown in Fig. 2.26 alongside that of the original MGE. This demonstrates that our dust correction strongly enhanced the central regions of the galaxy, especially the maximum (i.e. central) surface brightness. This extinction-corrected MGE model leads to a best-fitting SMBH mass $M_{BH} = 3.21^{+0.49}_{-0.43} \times 10^9$ $M_{\odot}$ and a best-fitting F160W filter $M/L_{F160W} = (2.42 \pm 0.10)$ $M_{\odot}/L_{\odot,F160W}$, representing a 7 per cent decrease of the SMBH mass and a 11 per cent decrease of the M/L compared to our exponential disc model with a constant M/L.

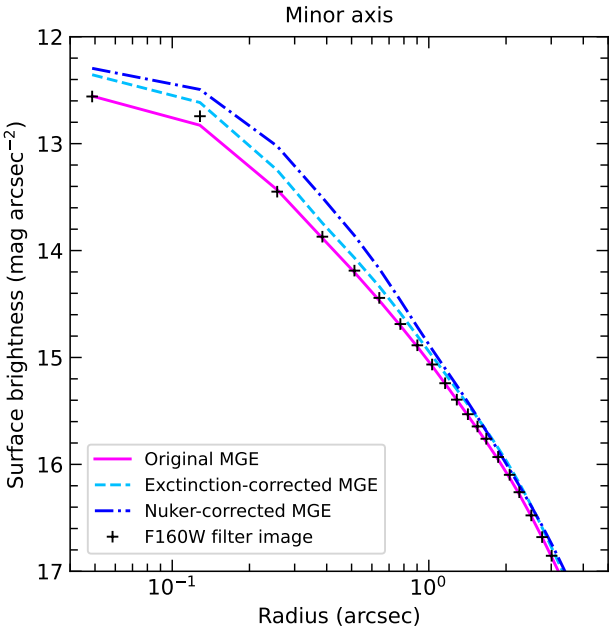


Figure 2.26: Central surface brightness profiles as a function of elliptical radius along the far side of the minor axis. Included are the profiles of the F160W filter image (black crosses), the original MGE (magenta line), the extinction-corrected MGE (cyan line) and the Nuker-corrected MGE (blue line).

In the second case, given that the standard extinction correction is insufficient to correct the dustiest portions of the image, we perform an additional correction in the following manner. Firstly, we identify the dustiest pixels of our original F160W filter image by creating a "dust mask", selecting all pixels with $(J-H)_{\rm obs} > 0.9$ mag. Having determined the outer position angle and axis ratio of the galaxy, we calculate the elliptical radius of every pixel in the dust-masked image to obtain a radial surface brightness profile which we fit with a 1D Nuker model (Lauer et al. 1995). The Nuker model is a double-power law with a break radius $r_{\rm b}$, that represents the transition between the inner and outer slopes γ and β, a surface brightness at the transition break radius $I_{\rm b}$ and a transition sharpness α. Nuker profiles are commonly used to describe the central surface brightness profiles of nearby galaxies observed with *HST*. Their ability to represent both cuspy and core-like nuclear profiles makes them particularly suitable for interpolating the central light distribution across the dust-obscured region of galaxies like NGC 4751. We perform the fit to the data using the `scipy.optimize.curve_fit` routine and obtain $r_{\rm b} = 0.45$ arcsec, $I_{\rm b} = 13.3$ mag arcsec^{-2}, $\alpha = 1.48$, $\beta = 1.60$ and $\gamma = 0.00$. We note that this and subsequent fits represent the

observed, and not intrinsic, Nuker parameters. We then repeat these dust-masking and profile-fitting steps with the extinction-corrected F160W filter image used for the previous fit, whilst keeping the break radius fixed to $r_b = 0.45$ arcsec. This yields $I_b = 13.2$ mag arcsec^{-2}, $\alpha = 1.26$, $\beta = 1.67$ and $\gamma = 0.01$. Finally, we replace the surface brightnesses of the dust-masked pixels in the extinction-corrected image with those predicted by the best-fitting Nuker model, and proceed with a MGE as before, which we refer to as the "Nuker-corrected MGE", whose "deconvolved" Gaussian components are listed in Table 2.17. As before, the minor-axis surface brightness profile is shown in Fig. 2.26 alongside the other models. This Nuker-corrected MGE leads to a best-fitting SMBH mass $M_{BH} = 3.65^{+0.39}_{-0.37} \times 10^9$ M$_\odot$ and a best-fitting F160W filter $M/L_{F160W} = 1.88^{+0.08}_{-0.07}$ M$_\odot$/L$_{\odot,F160W}$, representing a 6 per cent increase of the SMBH mass and a 30 per cent decrease of the M/L compared to the exponential disc model with a constant M/L.

It is worth highlighting that there are other, more involved dust-correction methods that we could implement, such as an embedded screen dust model. However, following the embedded screen model of Viaene et al. (2017) and Boizelle et al. (2019) results in less than 10 per cent higher dust correction along the major axis, in large part due to our use of a near-infrared image. As this does not change the best-fitting dynamical modelling parameters significantly more than the spread of the two MGE models above, we do not attempt this more detailed dust correction here.

For all four alternative models, we also carried out analogous tests using a radially linearly-varying M/L. The results of all the tests are listed in Table 2.18.

Considering all these tests, it is clear that the systematic variations of the SMBH mass are similar to the statistical uncertainties reported in Table 2.14, with $M_{BH} = 3.43^{+0.45}_{-0.44}[\text{stat}, 3\sigma]^{+0.22}_{-0.64}[\text{sys}] \times 10^9$ M$_\odot$ for the model with a constant M/L, where the first uncertainties are statistical and the second systematic. However, this is less clear when considering the M/L. Dust impacts the M/L significantly, with $M/L_{F160W} = 2.68 \pm 0.11[\text{stat}, 3\sigma]^{+0.10}_{-0.80}[\text{sys}]$ M$_\odot$/L$_{\odot,F160W}$ for the model with a constant M/L. For the radially linearly-varying M/L case, the variations of the SMBH mass are also similar to the statistical uncertainties, with $M_{BH} = 2.79^{+0.75}_{-0.57}[\text{stat}, 3\sigma]^{+0.75}_{-0.45}[\text{syst}] \times 10^9$ M$_\odot$. And again dust has a significant impact on the M/L, with $(M/L_{F160W})\,/\left(\text{M}_\odot/\text{L}_{\odot,F160W}\right) =$

Table 2.18: Best-fitting molecular gas model parameters and associated uncertainties, for the models explored in Section 2.5.4.

Parameter	SkySampler		Davidson et al. (2024)		Extinction-corrected		Nuker-corrected	
	Best fit	3σ	Best fit	3σ	Best fit	3σ	Best fit	3σ
Models with a constant M/L								
$\log(M_{\rm BH}/{\rm M}_\odot)$	9.47	$-0.06, +0.05$	9.45	$-0.11, +0.08$	9.51	±0.06	9.56	$-0.05, +0.04$
$M/L_{\rm F160W}$	2.78	±0.11	2.42	$-0.11, +0.13$	2.42	±0.10	1.88	$-0.07, +0.08$
Models with a radially linearly-varying M/L								
$\log(M_{\rm BH}/{\rm M}_\odot)$	9.39	$-0.09, +0.10$	9.37	$-0.14, +0.13$	9.43	$-0.09, +0.08$	9.55	$-0.08, +0.06$
$M/L_{\rm F160W}$ int.	3.15	$-0.38, +0.27$	2.60	$-0.27, +0.21$	2.71	$-0.22, +0.23$	1.93	$-0.21, +0.25$
$M/L_{\rm F160W}$ grad.	-0.10	$-0.07, +0.10$	-0.04	$-0.05, +0.07$	-0.07	$-0.06, +0.05$	-0.01	$-0.06, +0.05$

Note. The M/L and M/L intercept are expressed in units ${\rm M}_\odot/{\rm L}_{\odot,{\rm F160W}}$ and the M/L gradient is expressed in units ${\rm M}_\odot/{\rm L}_{\odot,{\rm F160W}}$ arcsec^{-1}.

$3.07^{+0.27}_{-0.35}[\text{stat, } 3\sigma]^{+0.08}_{-1.14}[\text{sys}] - 0.09^{+0.08}_{-0.06}[\text{stat, } 3\sigma]^{+0.08}_{-0.01}[\text{sys}]$ (R/arcsec). It is worth noting that the Nuker-corrected MGE model with a linearly-varying M/L yields a gradient remarkably close to zero, suggesting that much of the M/L gradient in previous models is due to the embedded dust disc.

These tests indicate that our method of rescaling the statistical uncertainties to approximate the systematic uncertainties is appropriate in certain contexts, but not in others. It is clear that the choice of MGE model has a significant impact on the inferred M/L and that the dust extinction correction of optical images needs to be more systematically implemented in the field of molecular gas modelling. On the other hand, it is also clear that the inferred SMBH masses from this ALMA Cycle 4 dataset are largely unaffected by the MGE models and that even the simplest models yield robust SMBH masses. This is consistent with the general understanding that, as long as the kinematic tracers remain regular and probe deep within $R_{\rm SoI}$, and the data resolve this $R_{\rm SoI}$, the SMBH mass will be less susceptible to uncertainties in the galaxy's central stellar light distribution.

Comparison to stellar kinematic results

As discussed in Section 2.5.1, Rusli et al. (2013) used SINFONI data to infer a SMBH mass of $(1.4 \pm 0.1) \times 10^9$ M$_\odot$ at 1σ (68 per cent) confidence level, modelled using three-integral Schwarzschild models and assuming the same distance as us. The SMBH mass of Rusli et al. (2013) is not consistent with either of our molecular gas masses.

Using the same SINFONI data Dominiak et al. (2025) obtained an alternative SMBH mass estimate using the JAM method (Cappellari 2008; Cappellari 2020). Assuming the same *HST* WFC3 F160W filter MGE parametrisation used to model the molecular gas kinematics in this Section, the best-fitting parameters and their 1σ formal uncertainties are $M_{\rm BH} = (2.52 \pm 0.12) \times 10^9$ $M_\odot$ and $(M/L)_{\rm tot} = 3.759 \pm 0.094$ $M_\odot/L_{\odot,\rm F160W}$ for the model with a cylindrically-aligned velocity ellipsoid $\rm JAM_{cyl}$, and $M_{\rm BH} = (3.24 \pm 0.29) \times 10^9$ $M_\odot$ and $(M/L)_{\rm tot} = 4.22 \pm 0.16$ $M_\odot/L_{\odot,\rm F160W}$ for a model with a spherically-aligned velocity ellipsoid $\rm JAM_{sph}$. These best-fitting parameters are remarkably consistent with those obtained using molecular gas modelling. The SMBH mass of Rusli et al. (2013) is not consistent with Dominiak et al.'s JAM SMBH masses either. The best-fitting inclination for both JAM models is $i \approx 72°$, also close to that derived from the molecular gas kinematics.

Part of this disagreement may stem from a potential underestimation of uncertainties in the Rusli et al. (2013) determination. Examining their Fig. 11, it is clear that the $\Delta\chi^2$ line exhibits multiple minima. The primary minimum corresponds to the formal best-fitting solution, with a black hole mass of approximately 1.4×10^9 $M_\odot$, as reported in their paper. However, there is a secondary minimum at 1.8×10^9 $M_\odot$, lying outside the formal 3σ confidence interval. This secondary minimum likely arises from numerical noise, a common feature of the Schwarzschild (1979) dynamical modelling method. It is also the reason why the associated $\Delta\chi^2$ are sometimes smoothed before determining confidence intervals (see e.g. Gebhardt et al. 2003). The sharp global minimum may also be an artifact of numerical noise. Arguably, a more realistic uncertainty would encompass the region where the $\Delta\chi^2$ profile sharply rises. This would correspond to a black hole mass range of approximately $[1.1, 2.0] \times 10^9$ $M_\odot$ (3σ limits). If this were the true confidence interval of the Rusli et al. (2013) models, it would significantly reduce, although not eliminate, the tension between their result and ours.

As discussed in Section 2.5.1, the M/L_R derived by Rusli et al. (2013) is unusually high, with $M/L_R = 12.2^{+0.6}_{-0.7}$ $M_\odot/$ $L_{\odot,R}$ (based on a model with dark matter present) or $M/L_R = 13.1^{+0.3}_{-0.4}$ $M_\odot/$ $L_{\odot,R}$ (based on a model without dark matter). Such an M/L_R is inconsistent (approximately twice) that expected from similar targets (Ge et al. 2021a). Rusli et al. (2013) do not use an R-band image directly, but rather re-scale a F160W filter *HST* image to a ground based R-band image, to achieve the desired resolution in

the central parts of the optical image. Neither the re-scaling procedure nor the MGE parameterisation is described in the paper, rendering us unable to perform any substantive further analysis of this issue. However, it is worth nothing that the overly-large M/L_R may be contributing to the smaller SMBH mass of Rusli et al. (2013), given the conservation of (total) dynamical mass during modelling.

The Schwarzschild model of Rusli et al. (2013) is a far more computationally-expensive and involved method than JAM, so one would ostensibly expect it to yield more realistic results. In addition, Rusli et al. (2013) considered models with and without a contribution from dark matter which, as mentioned in Section 2.5.4, can be a source of uncertainty especially affecting the stellar mass component of models. However, the NGC 4751 SMBH mass and M/L_R of Rusli et al. (2013) appear to be almost entirely unaffected by the addition of dark matter. In fact, the angular resolution of the SINFONI data (i.e. the FWHM of the PSF) of NGC 4751 is 0.22 arcsec, whereas the diameter of the SoI (assuming the SMBH mass of Rusli et al. 2013) is 0.70 arcsec, suggesting that the SINFONI data have an angular resolution sufficient to resolve the SoI. We would then expect the SMBH mass to be robust and less susceptible to any bias. If it is indeed the case that Rusli et al.'s (2013) SMBH mass is incorrect, as the Dominiak et al. (2025) JAM and our molecular gas modelling results seem to suggest, it highlights the importance of cross-checks between methods of SMBH mass determination.

2.6 NGC 1387

The material in this section has been submitted to Monthly Notices of the Royal Astronomical Society.

2.6.1 Galaxy Properties

NGC 1387 is a barred lenticular SB0 galaxy located at $03^{\rm h}36^{\rm m}57\overset{\rm s}{.}06$, $-35°30'23\overset{''}{.}9$ (J2000.0) within the Fornax Cluster. It is located at an angular distance of $\approx$ 19 arcmin ($\approx$ 107 kpc) to the west of NGC 1399 (Napolitano et al. 2022), the central galaxy of the Fornax Cluster. We adopt a distance of 19.3 $\pm$ 0.8 Mpc, calculated using surface brightness fluctuations (Blakeslee et al. 2009). At this distance, 1 arcsec corresponds to $\approx$ 94 pc.

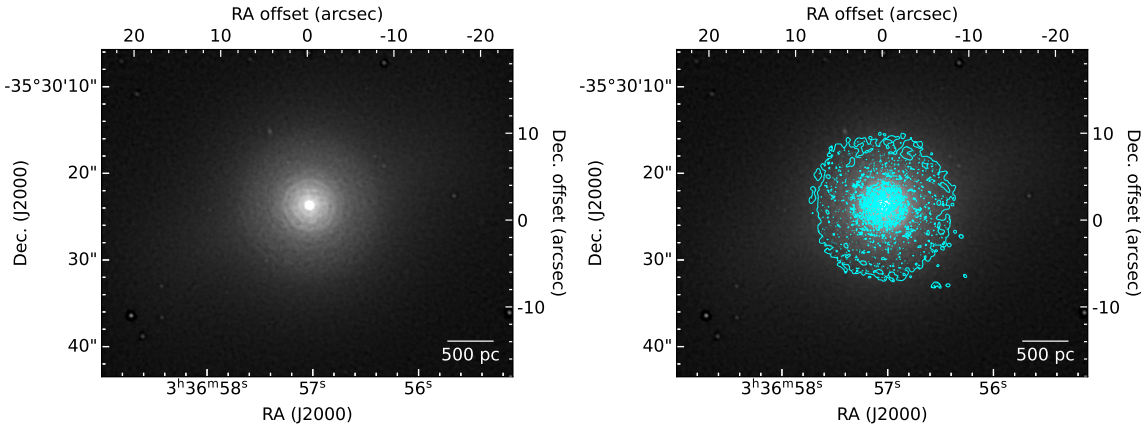


Figure 2.27: Unsharp-masked *HST* WFC3 F160W filter (*H*-band) image of NGC 1387 (left), overlaid with the ^{12}CO(2–1) integrated intensity contours (cyan) from our high-resolution ALMA data cube (right). Note that the unsharp masking has removed the smooth outer galaxy light and instead highlights the face-on nuclear disc and bar of the galaxy.

NGC 1387 has a total stellar mass of 4.70×10^{10} M$_\odot$, derived using an *i*-band absolute magnitude of −21.81 and a stellar M/L in the *i*-band $M/L_i = 1.31$ M$_\odot$/L$_{\odot,i}$ (Iodice et al. 2019). *HST* optical images reveal a prominent central bulge, a weak bar and a face-on dust disc extending ≈ 18 arcsec (≈ 1.7 kpc) in diameter along the major axis, with modest and flocculent dust (see Fig. 2.27).

NGC 1387 does not have an existing SMBH mass measurement in the literature, but an estimate can be obtained using the $M_{\rm BH} - \sigma_{\rm e}$ relation of van den Bosch (2016). Adopting $\sigma_{\rm e} = 170.2^{+12.2}_{-11.4}$ km s^{-1} (Wegner et al. 2003), a SMBH mass of $\approx 9^{+4}_{-3} \times 10^7$ M$_\odot$ is expected. We estimate the $R_{\rm SoI}$ in the usual manner to be $R_{\rm SoI} \approx 12$ pc (≈ 0.13 arcsec) for NGC 1387.

2.6.2 ALMA Observations

The ^{12}CO(2–1) emission line of NGC 1387 was observed with ALMA in Band 6 using both the 12-m array and the 7-m Atacama Compact Array (ACA) as a part of projects 2016.1.00437.S (PI: Davis) and 2016.2.00053.S (PI: Liu), respectively. The 12-m array data are comprised of three tracks taken on 2016 November 4, 2016 December 21 and 2017 September 7 for a total of 20 min on source. The baselines range from 15 m to 7.5 km, yielding a MRS of 5.9 arcsec (≈ 0.6 kpc). The FoV is 24.4 arcsec (≈ 2.3 kpc). The ACA data are comprised of one track taken on 2017 July 28 for a total of 17 min on source. The

baselines range from 9 to 45 m, yielding a MRS of 28.4 arcsec (≈ 2.7 kpc). The FoV is 41.8 arcsec (≈ 3.9 kpc). The properties of the observations are summarised in Table 1.2.

Each of the four observing tracks had a total of four spectral windows, one of which was centred on the redshifted frequency of the ^{12}CO(2–1) line (rest frequency $\nu_{\rm rest}$ = 230.5380 GHz). For the three 12-m array tracks, this spectral window had a bandwidth of 1.875 GHz (≈ 2440 km s^{-1}) subdivided into 3840 channels of width ≈ 488 kHz (≈ 0.64 km s^{-1}). For the ACA track this spectral window had a bandwidth of 2.0 GHz (≈ 2600 km s^{-1}) subdivided into 2048 channels of width ≈ 977 kHz (≈ 1.27 km s^{-1}). The remaining spectral windows for both the 12-m array and the ACA tracks had a bandwidth of 2.0 GHz (≈ 2600 km s^{-1}) subdivided into 128 channels of width ≈ 16 MHz (≈ 20 km s^{-1}). These were used to map the continuum emission.

The data were reduced using CASA version 4.7.2 (McMullin et al. 2007) and the standard ALMA pipeline. The following imaging steps were carried out using CASA version 6.4.3.

Continuum emission

An image of the continuum emission of NGC 1387 was created using the (u, v) components from all four tracks and cleaned with the CASA task `tclean`. The line-free channels of the line spectral windows as well as the continuum spectral windows were used, resulting in a central frequency of 239.4 GHz (1.25 mm). We adopted the multi-frequency synthesis mode, Briggs weighting with a robust parameter of 0.5 and cleaned the image to a threshold of 3 times the RMS noise of 0.03 mJy beam^{-1}. We detect a small central source of continuum emission with an integrated flux density of 1.23 ± 0.06 mJy and a peak intensity of 1.20 ± 0.03 mJy beam^{-1}. This continuum flux density is similar to, but inconsistent with, a previous measurement by Elford et al. (2023) of 1.00 ± 0.05 mJy. A Gaussian fit using the CASA task `imfit` confirms that the deconvolved source size is consistent with a point (i.e. an unresolved) source. The continuum image is shown in Fig. 2.28 and its properties and that of the detected source are summarised in Table 2.19.

Table 2.19: Properties of the NGC 1387 cleaned continuum image and the detected continuum source.

Image property	Value
Spatial extent (pix)	1000×1000
Spatial extent (arcsec)	20×20
Spatial extent (kpc)	1.9×1.9
Pixel scale (arcsec pix^{-1})	0.02
Pixel scale (pc pix^{-1})	1.9
RMS noise (mJy beam^{-1})	0.03
Synthesised beam (arcsec)	0.09×0.06
Synthesised beam (pc)	8×6
Source property	**Value**
Right ascension (J2000.0)	$03^{\rm h}36^{\rm m}57\overset{\rm s}{.}0335 \pm 0\overset{\rm s}{.}0001$
Declination (J2000.0)	$-35°30'23\overset{''}{.}682 \pm 0\overset{''}{.}001$
Integrated flux (mJy)	1.23 ± 0.06

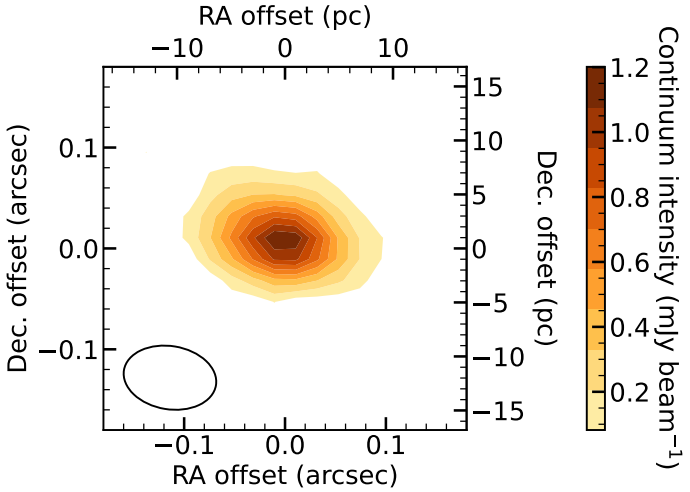


Figure 2.28: Central region (0.18 arcsec × 0.18 arcsec) of the NGC 1387 1.25 mm continuum image. Contours are evenly spaced between the peak intensity of 1.20 ± 0.03 mJy beam^{-1} and 3 times the RMS noise. The synthesised beam is shown in the bottom-left corner as a black open ellipse.

Line emission

The ^{12}CO(2–1) line was similarly imaged using the (u, v) components from all four tracks to create a data cube with high angular resolution. We fitted the same spectral windows used to image the continuum with a fit order of 0, and this fit was subtracted from the *uv*-plane data using the CASA task `uvcontsub`. These continuum-subtracted *uv* data were then imaged and cleaned using the cube mode of the CASA task `tclean`. The regions containing emission were cleaned to a threshold equal to 1.5 times the RMS noise of channels

Table 2.20: CO data cube properties for NGC 1387.

Data cube	Image property	Value
High-resolution	Spatial extent (pix)	1000×1000
	Spatial extent (arcsec)	30.0×30.0
	Spatial extent (kpc)	2.8×2.8
	Pixel scale (arcsec pix^{-1})	0.03
	Pixel scale (pc pix^{-1})	2.8
	Velocity range (km s^{-1})	1100 – 1400
	Channel width (km s^{-1})	10
	RMS noise (mJy beam^{-1} channel^{-1})	0.65
	Number of constraints	378, 450
	Synthesised beam (arcsec)	0.13×0.10
	Synthesised beam (pc)	12×10
Low-resolution	Spatial extent (pix)	300×300
	Spatial extent (arcsec)	30.0×30.0
	Spatial extent (kpc)	2.8×2.8
	Pixel scale (arcsec pix^{-1})	0.1
	Pixel scale (pc pix^{-1})	9.4
	Velocity range (km s^{-1})	1100 – 1400
	Channel width (km s^{-1})	10
	RMS noise (mJy beam^{-1} channel^{-1})	0.80
	Number of constraints	188, 777
	Synthesised beam (arcsec)	0.42×0.35
	Synthesised beam (pc)	39×33

free of any emission in the dirty (i.e. not yet cleaned) data cube. For the imaging we used a kinematic local-standard-of-rest velocity reference frame and Briggs weighting with a robust parameter of 0.8. The conventional robust parameter of 0.5 yielded very poor signal-to-noise ratios in regions of emission, whereas a parameter of 1.0 yielded a synthesised beam size that did not sufficiently sample the predicted SoI. A robust parameter of 0.8 represents a trade-off between the two. We adopted a channel width of 10 km s^{-1}, again selected to achieve angular (and thus spatial) and velocity resolutions effectively probing the predicted SMBH SoI while providing adequate sensitivity. The resulting data cube has a synthesised beam of 0.13 arcsec $\times$ 0.10 arcsec ($\approx 12 \times 10$ pc^2) with a RMS noise of 0.65 mJy beam^{-1} channel^{-1}. Its properties are summarised in Table 2.20.

We used the masked-moment technique of Dame (2011), implemented in the PYMAKEPLOTS package, to create the zeroth (integrated-intensity), first (intensity-weighted mean line-of-sight velocity) and second (intensity-weighted line-of-sight velocity dispersion) moment maps. The primary beam-uncorrected data cube was smoothed with a 3D Gaussian kernel whose FWHM in each spatial direction is equal to 3 times the FWHM of the major axis

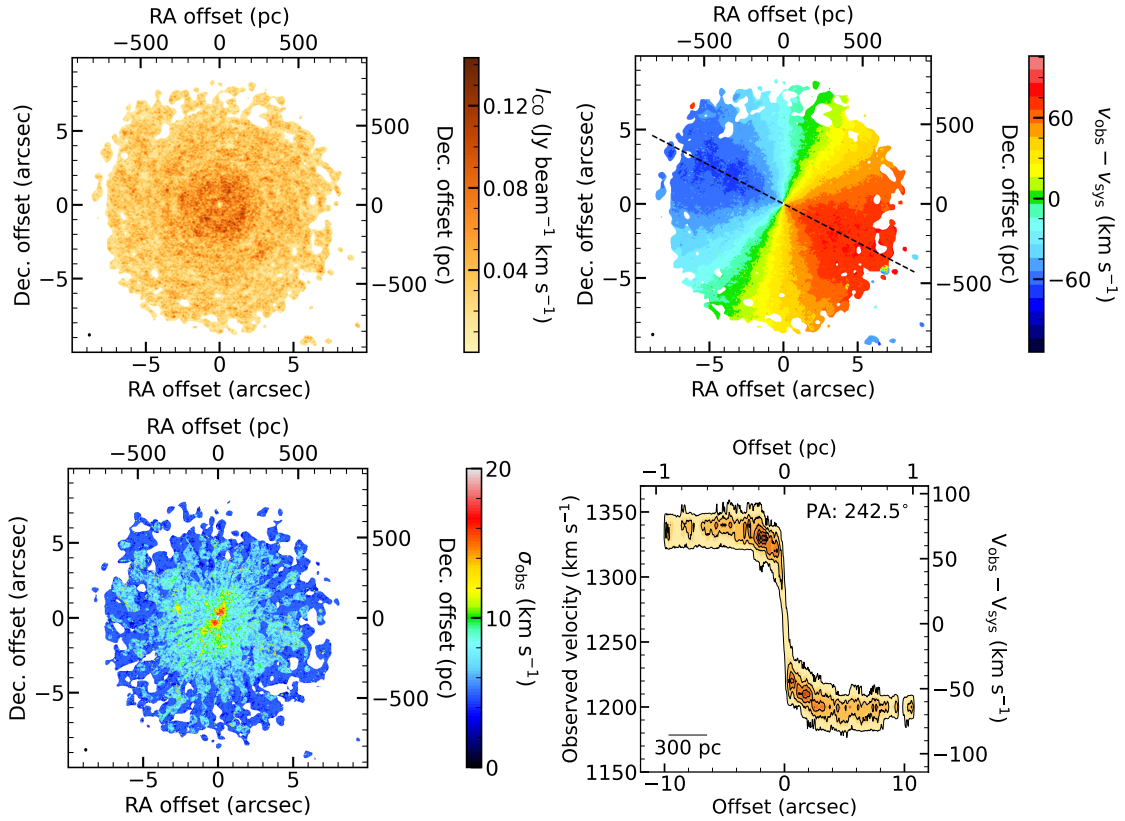


Figure 2.29: As Fig. 2.2, but for the ^{12}CO(2–1) line of NGC 1387. The dashed black line in the top-right panel shows the kinematic major axis.

of the synthesised beam, and whose FWHM in the velocity direction is equal to the channel width. All pixels above a clipping threshold equal to 2.5 times the RMS noise (measured in the unsmoothed primary beam-uncorrected data cube) were selected, creating a mask. This mask was then applied to the unsmoothed primary beam-corrected data cube to create the moment maps. The kinematic major-axis PVD was constructed by taking a 10-pixel wide cut through the masked data cube along a position angle PA of 242°.5 (determined using PaFit in Section 2.6.3). The resulting moment maps and PVD are shown in Fig. 2.29.

In NGC 1387 we detect a disc of flocculent, regularly-rotating molecular gas approximately 18 arcsec (≈ 1.7 kpc) in diameter, coincident with the central dust disc of the galaxy (see Fig. 2.27). We also detect a small central depression ≈ 0.2 arcsec (≈ 19 pc) in radius. This depression is similar in extent to the predicted R_{SoI}, and thus prevents the innermost parts of the gravitational potential from being probed robustly. This is likely the reason why no clear Keplerian rise of the velocities is present within R_{SoI}. A SMBH mass measurement is nevertheless still possible in NGC 1387, as the dynamical impact of the SMBH can be

traced up to ≈ 2 times the formal SoI given a robust stellar mass model (Davis 2014). The total flux of NGC 1387 was calculated to be 255 ± 3 Jy km s^{-1} in Liang et al. (2026), the companion paper to this work. This is the appropriate total flux to use in any follow-up studies, as it has been corrected using the procedure described in Jorsater & van Moorsel (1995) and represents the integrated flux at an infinite cleaning depth.

2.6.3 CO Modelling

Stellar potential

To accurately estimate the SMBH mass from the molecular gas kinematics, we need to quantify the stellar mass contribution to the kinematics. We thus parameterise the intrinsic (i.e. 'deconvolved') stellar light distribution using a MGE model (Emsellem et al. 1994; Cappellari 2002) of a *HST* WFC3 F160W filter (H-band) image. We selected the longest wavelength *HST* image available to minimise dust extinction. The surface brightnesses of the Gaussian components can then be converted to luminosity surface densities using the AB magnitude system with a Solar absolute magnitude of 4.60 mag (Willmer 2018) and a zero-point of 25.94 mag (Sahu et al. 2021). We adopt a Galactic extinction of 0.006 mag (Schlafly & Finkbeiner 2011) from the NASA/IPAC Extragalactic Database to correct for interstellar reddening.

Our MGE modelling relies on the assumption of axisymmetry. As can be seen in Fig. 2.30, NGC 1387 has a non-axisymmetric bar feature. MGE modelling can still be employed despite this, as the dominant disc is axisymmetric and the bar can be treated as a first-order perturbation of an otherwise axisymmetric system. In such a case, a standard procedure is to fit a single Gaussian axial ratio in the outer regions of the galaxy (far away from the bar) and to fix the axial ratios of all the Gaussians to this, even across the barred region (see Scott et al. 2009 for further details). Although this method may produce a poorer fit within the barred region, it provides a much better axisymmetric approximation of the gravitational potential of the disc, for use in our axisymmetric models. If we were to incorrectly interpret the bar as a nearly edge-on axisymmetric disc embedded into a spherical spheroid, and fit its detailed surface brightness, the deprojected intrinsic density would completely misrepresent the true density distribution. In any case, this approximation

Table 2.21: Parameters of the deconvolved best-fitting MGE components of our model of NGC 1387.

$\log\left(\frac{I'}{L_{\odot,F160W}\ pc^{-2}}\right)$ (1)	$\log\left(\frac{\sigma'}{arcsec}\right)$ (2)	q' (3)
5.068	−0.937	0.98
4.900	−0.579	0.98
4.617	−0.208	0.98
4.456	0.233	0.98
4.006	0.607	0.98
3.463	0.849	0.98
2.748	1.214	0.98
2.414	1.725	0.98

Notes. Deconvolved MGE components. (1) Central surface brightness of Gaussian component. (2) Standard deviation of Gaussian component. (3) Axial ratio of Gaussian component.

has little impact on our model, as the gas disc we model is limited to the central regions, where the influence of the bar is small. The roundness of the outer isophotes makes it difficult to constrain the (photometric) PA of the disc line of nodes, so we determine the (kinematic) PA from the molecular gas data using PaFit[9]. We then orient the MGE along this kinematic PA of 242.°5. For NGC 1387, we derive an axial ratio of 0.98 by inspecting the outer regions of the *HST* image and assuming an infinitely-thin disc. As all of our Gaussians have a fixed axial ratio $q' = 0.98$, the minimum inclination for which we are able to deproject is $i = 11.5°$, however this is sufficient for our purposes.

The parameters of the ('deconvolved') best-fitting Gaussians (i.e. those Gaussians best representing the 2D projection of the intrinsic 3D stellar light distribution, without instrumental effects) are listed in Table 2.21 in physical units. The fit is shown in Fig. 2.30 overlaid on the data. There is rather uniform dust extinction across the entire extent of the galaxy, so we have opted not to mask any part of the disc. The fit is superficially poor in the barred region of the galaxy (see the left panel of Fig. 2.30), but the resulting MGE model is clearly an excellent fit at small radii (see the right panel of Fig. 2.30), the most important region to constrain the SMBH mass, as well as the outermost radii unaffected by the bar.

Molecular gas distribution

To create the model data cube, KinMS also requires a model of the observed gas distribution. For this, we can use the observed but deconvolved molecular gas emission. We implement

[9] https://pypi.org/project/pafit/

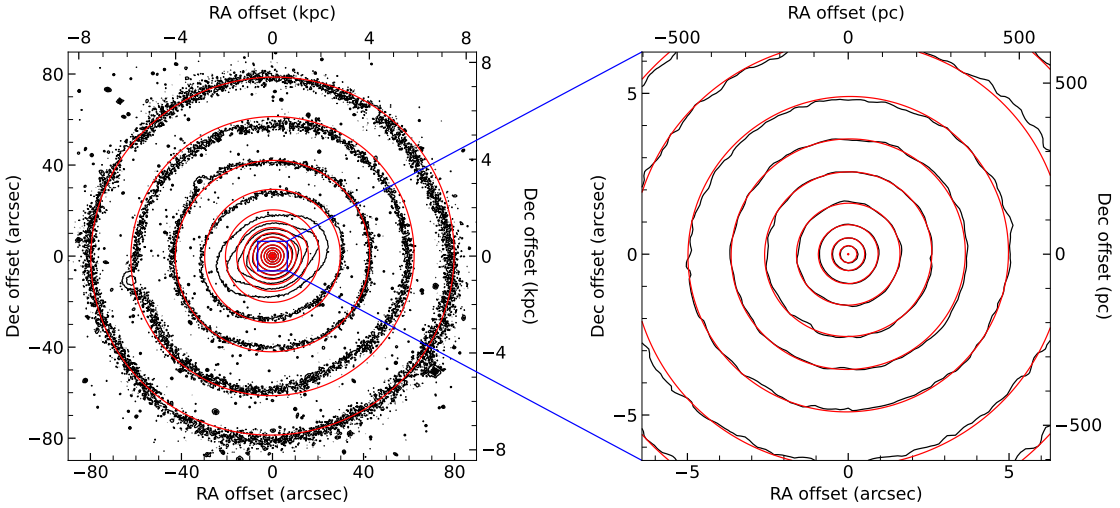


Figure 2.30: *HST* WFC3 F160W filter image of NGC 1387 (black contours), overlaid with our best-fitting MGE model (red contours). **Left:** Full extent of the galaxy showing the galaxy bulge, bar and extended stellar disc. **Right:** Central region only.

this using SkySampler. We sample the clean components of the gas distribution using 5×10^6 particles. Assuming a certain position angle and inclination of the galaxy, the particle positions generated by SkySampler can then be deprojected into their intrinsic positions in the galaxy plane using the KinMS_fitter task `transformClouds`.

Low-resolution cube and inclination prior

When using SkySampler, the inclination of the galaxy remained poorly constrained (±5° uncertainty), most likely due to the the face-on orientation of the galaxy and the sparsity of gas in the outer regions of the disc. As SkySampler models the gas distribution as an array of cloudlets rather than a cohesive and continuous disc, it effectively removes constraints that arise from the disc geometry. Instead, only the observed particle velocities are left, which are largely degenerate with the inclination. As such, SkySampler is known to struggle to constrain the inclination. Nevertheless, due to the flocculence of the molecular gas, using SkySampler is the only way we can reliably reproduce the surface brightness of NGC 1387 (an analytic surface brightness distribution would have too many parameters).

We overcome this problem by creating a second, lower-resolution data cube. The same continuum-subtracted *uv* data as for the high-resolution cube were imaged and cleaned in an analogous manner, but this time using Briggs weighting with a robust parameter of

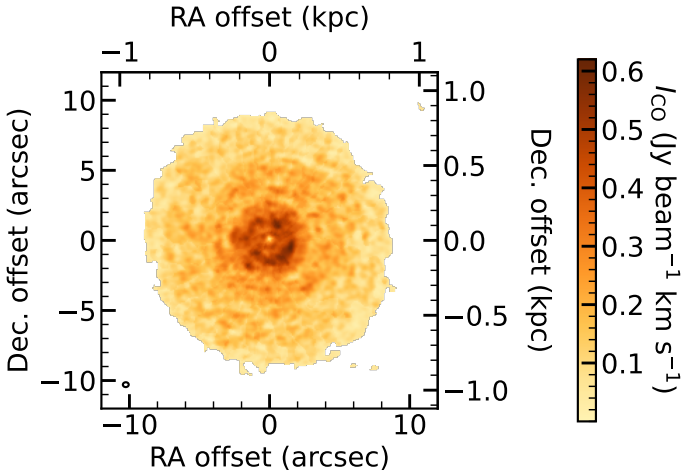


Figure 2.31: ^{12}CO(2–1) zeroth-moment (integrated-intensity) map of NGC 1387 derived from our ALMA lower-resolution data cube. The synthesised beam is shown in the bottom-left corner as an open ellipse.

2.0, corresponding to natural weighting and providing a decreased angular resolution but increased sensitivity. Additionally, we used the `uvtaper` option to apply a FWHM taper of 600 kilolambda (≈ 780 m), to further degrade the angular and thus spatial resolution (to ≈ 3 times that of our high-resolution data cube) and improve the sensitivity of the data cube. As with the high-resolution data cube, we adopt a channel width of 10 km s^{-1}. The resulting data cube has a synthesised beam of 0.42 arcsec × 0.35 arcsec (≈ 39 × 33 pc^2) with a RMS noise of 0.80 mJy beam^{-1} channel^{-1}, and its properties are also summarised in Table 2.20. Moment maps were again created, using the same method as described above, but in this case the Gaussian kernel's FWHM in each spatial direction was equal to the FWHM of the major axis of the synthesised beam. The mask was obtained by clipping the smoothed primary beam-uncorrected data cube to a threshold of 5 times its RMS noise. The resulting zeroth-moment map is shown in Fig. 2.31.

First, by degrading the angular resolution, we ensure higher signal-to-noise ratios in emission regions, particularly in the outer parts of the disc, making the determination of the boundaries of the molecular gas disc much easier. Second, due to the lower resolution, the molecular gas disc appears smoother and more regular, allowing to model it assuming an infinitely-thin axisymmetric disc with an exponential radial surface brightness profile. This eliminates the need to use SkySampler in this step, allowing us to use this lower-resolution cube to more reliably constrain the inclination prior to fitting the high-resolution cube. Due

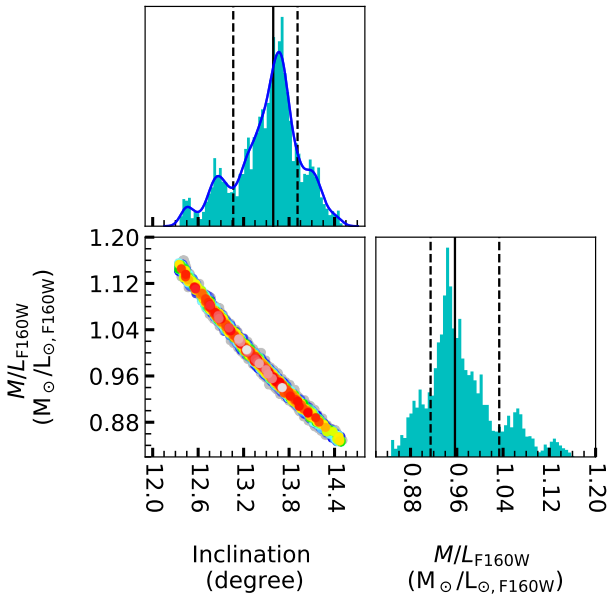


Figure 2.32: As Fig. 2.5, but for NGC 1387, showing the covariance between i and M/L from the first modelling step. The kernel density estimation of the inclination posterior probability distribution is shown as a solid blue line.

to the small central depression in both the higher- and the lower-resolution data cube, we also allowed for the possibility of an inner truncation in the radial surface brightness profile. The molecular gas distribution is thus parameterised by Eq. 2.2.

We thus create a KinMS model in the standard manner, using the stellar potential described in Section 2.6.3 and the molecular gas distribution described above. This model has a total of 11 free parameters: $M_{\rm BH}$, spatially-constant stellar M/L, molecular gas disc scale length (R_0), truncation radius ($R_{\rm hole}$), integrated flux density and spatially-constant velocity dispersion ($\sigma_{\rm gas}$), as well as the "nuisance" parameters describing the disc geometry position angle, inclination (i), systemic velocity ($V_{\rm sys}$) and centre position (offsets in right ascension and declination from the image phase centre). The priors of all the parameters are uniform, apart from that of the SMBH mass which is uniform in the logarithm due to its large dynamic range.

The MCMC chain in that first stage modelling had 200, 000 steps, yielding a best-fitting inclination $i = 13.6^{\circ+0.9}_{-1.2}$. Figure 2.32 reveals a very strong degeneracy between i and M/L, but this is to be expected given the small inclination. For a dynamical mass measurement based on rotational velocities, the enclosed mass $M_{\rm tot}$ is related to the rotation velocity $v_{\rm rot}$ and thus the observed velocity $v_{\rm obs}$ as $M_{\rm tot}(R) \propto v^2_{\rm rot}(R)R \propto v^2_{\rm obs}(R)R/\sin^2 i \propto \sin^{-2} i$, and $\sin i$ varies rapidly at small inclinations (see Smith et al. 2019 for further discussion of this

issue). Nevertheless, the MCMC chain of this initial stage of modelling converges without issue and the posterior probability distribution of the SMBH mass is Gaussian in shape, already strongly suggesting the presence of a central SMBH.

To model the high-resolution data cube with SkySampler, we adopt the posterior probability distribution of the inclination (obtained from our modelling of the low-resolution data cube without SkySampler) as a prior. As the inclination posterior probability distribution is comprised of a collection of discrete points, in practice we adopt a smooth approximation of that distribution as the prior. In other works that implement this method (e.g. Zhang et al. 2025a), this was achieved by fitting a parametric function to the posterior probability distribution, normally a Gaussian. However, in the case of NGC 1387, the inclination posterior probability distribution cannot be easily approximated using a parametric function, as it has an irregular shape with three smaller peaks around a central dominant one (see Fig. 2.32). We therefore instead choose to use a kernel density estimation (KDE), whereby the histogram is smoothed by placing a Gaussian kernel at each data point in the posterior distribution. The kernels are then summed to create a continuous function and normalized such that the area under the curve is equal to 1 to be used as the prior. To achieve this, we used the `neighbors.KernelDensity` task, part of the scikit-learn library, with a kernel width of 0.07, which provides sufficient smoothing of the histogram data but does not erase the overall shape of the posterior probability distribution. The kernel density estimation is overlaid on the inclination posterior probability distribution in Fig. 2.32.

Results

Our final results are generated by comparing the high-resolution data cube described in Section 2.6.2 to a KinMS model created using the stellar potential described in Section 2.6.3 and SkySampler, together with the inclination prior derived in Section 2.6.3. This model has a total of 7 free parameters: SMBH mass, spatially-constant stellar mass-to-light ratio, molecular gas disc integrated flux density and spatially-constant molecular gas velocity dispersion, and the nuisance parameters position angle, inclination and systemic velocity. We have opted to fix the centre position that of the detected continuum emission, as it is consistent with the kinematic centre determined in the previous modelling step (low-resolution data

Table 2.22: Best-fitting model parameters of NGC 1387 and associated uncertainties.

Parameter	Prior			Best fit	1σ uncertainty	3σ uncertainty
Mass model						
$\log(M_{\rm BH}/{\rm M}_\odot)$	7	$\rightarrow$	11	8.04	$-0.23, +0.18$	$-0.87, +0.41$
Stellar $M/L_{\rm F160W}$ (${\rm M}_\odot/{\rm L}_{\odot,\rm F160W}$)	0.0	$\rightarrow$	5.0	0.90	$-0.14, +0.16$	$-0.35, +0.44$
Molecular gas disc						
Velocity dispersion (km s^{-1})	0.0	$\rightarrow$	50.0	6.0	± 0.3	$-0.8, +0.9$
Integrated intensity (Jy km s^{-1})	0	$\rightarrow$	300	264	± 9	$-26, +25$
Nuisance parameters						
Inclination (degree)	11.5	$\rightarrow$	20.0	14.2	$-1.1, +1.3$	$-2.6, +4.1$
Position angle (degree)	0.0	$\rightarrow$	359.9	243.9	± 0.3	$-1.0, +0.9$
Systemic velocity (km s^{-1})	1100	$\rightarrow$	1400	1267.2	± 0.3	$-0.7, +0.8$

Note. The centre position is fixed to that of the unresolved continuum source, $03^{\rm h}36^{\rm m}57\overset{\rm s}{.}0335$, $-35°30'23\overset{''}{.}682$ (J2000.0).S

cube) and the reduction of the model dimensionality leads to a decrease of the computing time. Additionally, given the presence of the central depression in the molecular gas and the associated lack of constraints from the disc geometry, SkySampler struggled to accurately determine the kinematic centre. The SMBH mass prior is again uniform in the logarithm, the inclination prior is set by the previous low-resolution data cube modelling (see Section 2.6.3), and all remaining parameters again have uniform priors. The model parameters and their priors (i.e. search ranges), best-fitting values and 1σ (68.3 per cent) and 3σ (99.7 per cent) uncertainties are listed in Table 2.22.

The final MCMC chain in this second stage of our modelling had 150,000 steps. Figure 2.33 shows the posterior probability distribution of some of the non-nuisance model parameters. It unequivocally shows that there is a massive dark object at the centre of NGC 1387, with a best-fitting mass of $1.10^{+1.71}_{-0.95} \times 10^8$ ${\rm M}_\odot$. The best-fitting M/L in the F160W filter is $0.90^{+0.44}_{-0.35}$ ${\rm M}_\odot/{\rm L}_{\odot,\rm F160W}$. As expected due to the face on nature of the galaxy, Fig. 2.33 shows a very strong degeneracy between M/L and inclination and a weaker degeneracy between $M_{\rm BH}$ and inclination. Figure 2.33 also reveals a positive correlation between $M_{\rm BH}$ and M/L (see Smith et al. 2019), as the effects of inclination are sufficiently strong in this face-on system to overwhelm the usual degeneracy arising from the conservation of total dynamical mass.

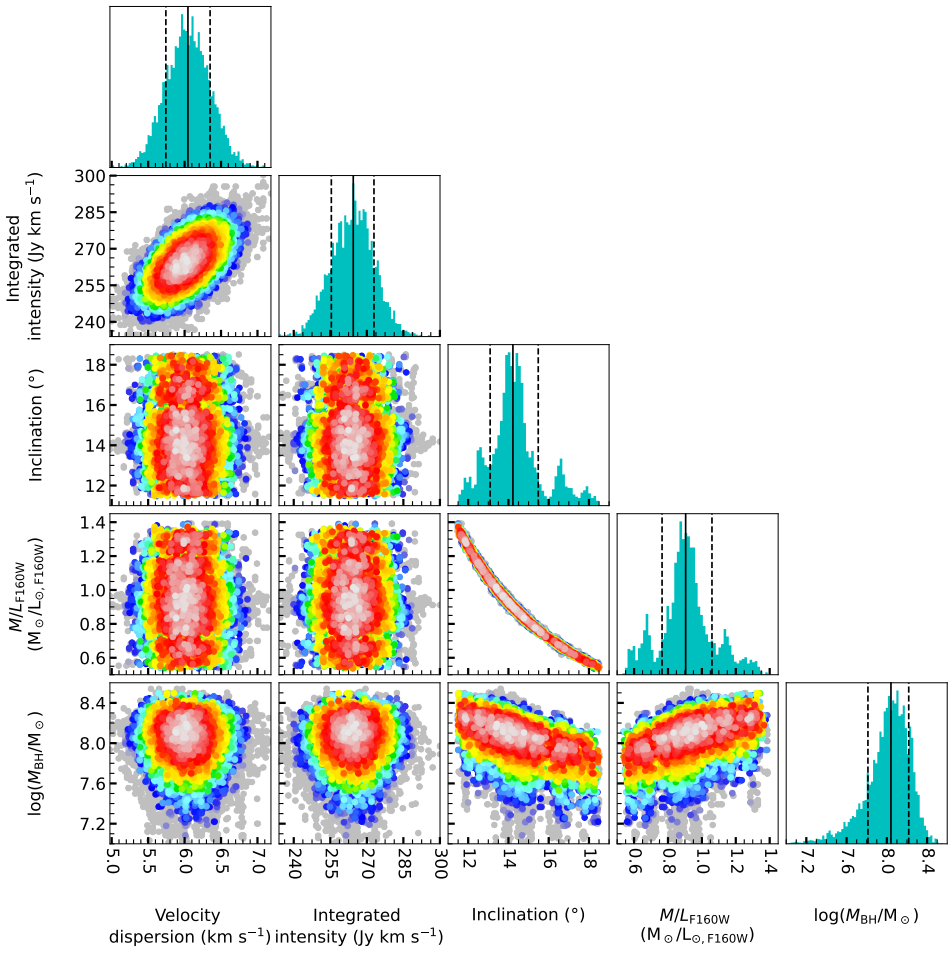


Figure 2.33: As Fig. 2.32, but for selected (primarily non-nuisance) model parameters from the second and final modelling step.

The quality of our best-fitting model can be judged by overlaying it over the kinematic major-axis PVD, as done in the central panel of Fig. 2.34. For comparison, we also generate and overlay two other models, one with no SMBH (left panel of Fig. 2.34) and one with an overly-massive SMBH (≈ 0.4 dex more massive than the best-fitting SMBH; right panel of Fig. 2.34), allowing all parameters other than the SMBH mass to vary. As expected, the model with no SMBH tries to compensate for the lack of a central SMBH by adopting a higher M/L to account for the high rotation velocities at small radii. However, the model with no SMBH is not able to fully account for the central velocities in an adequate manner and provides a poor fit in those central regions. Also due to the higher M/L, the the fit is noticeably poorer at larger radii. It would also be typically expected that the best-fitting model with an overly-massive SMBH would be forced towards a smaller M/L, however

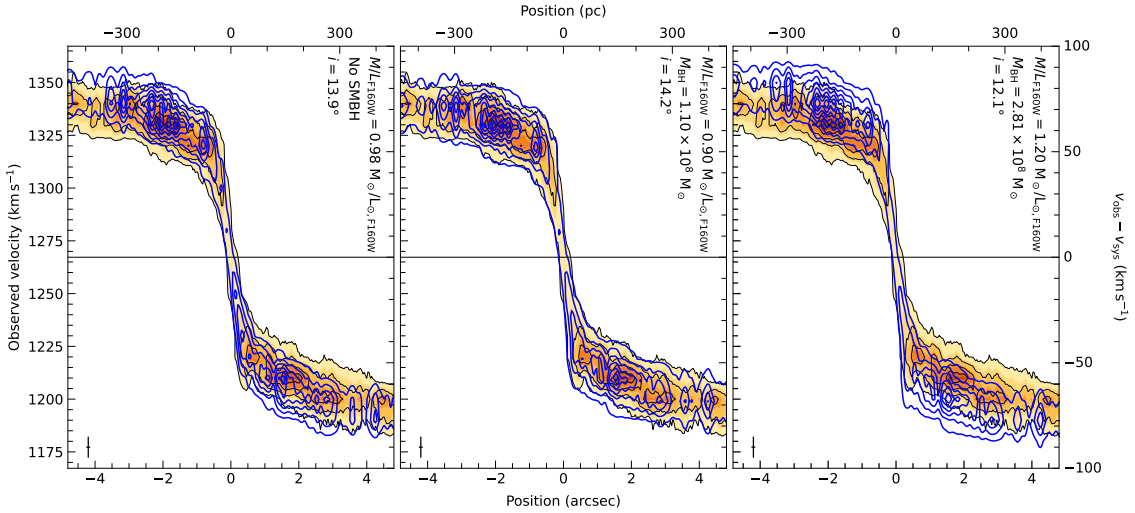


Figure 2.34: As Fig. 2.6, but for the inner part (radii $R \lesssim 5.0$ arcsec) of NGC 1387. In addition to the SMBH mass and M/L, the inclination of each model is also listed in the top-right corner of each panel.

in this case the effect is opposite. As shown by Fig. 2.33, a higher $M_{\rm BH}$ tends towards a lower inclination which in turn is correlated with a higher M/L. This is exactly what happens in the model with an overly-massive SMBH which drives the best-fitting inclination down to $i = 12.1°$ which in turn results in a higher M/L than that of our best-fitting model. However, due to the overly massive SMBH, the model over-shoots the central velocities despite the lower inclination, resulting again in a very poor fit.

2.6.4 Discussion

Best-fitting mass model

Figure 2.35 shows the cumulative mass distribution of NGC 1387. Using the standard approximation of a SMBH SoI and the best-fitting SMBH mass yields $R_{\rm SoI} \approx 16$ pc (≈ 0.17 arcsec). One can also assess the impact of a SMBH by considering the radius at which the enclosed stellar mass is equal to that of the SMBH. Figure 2.35 shows this radius of equal mass contribution to be $R_{\rm eq} \approx 19$ pc (≈ 0.20 arcsec), slightly larger than $R_{\rm SoI}$. Whilst our observations of NGC 1387 have a fairly high angular and thus spatial resolution, spatially resolving the SMBH SoI by a factor of two, the smallest scale probed is restricted by the presence of the central hole, which is greater than the size of the synthesised beam. We estimate the radius of this hole by eye to be ≈ 0.2 arcsec (≈ 19 pc) and have shown

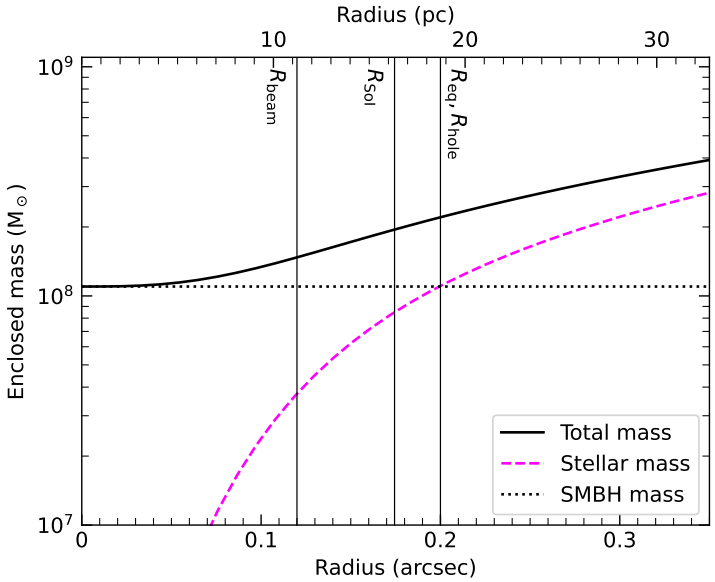


Figure 2.35: As Fig. 2.8, but for NGC 1387 (assuming $\sigma_e = 170.2$ km s^{-1} and our best-fitting SMBH mass). We list the approximate radius of the central hole (R_{hole}) which is in this case the same as the radius of equal mass contribution (R_{eq}).

it as such in Fig. 2.35. We have chosen not to report the truncation radius obtained from the modelling of the our lower-resolution data cube (see Section 2.6.3), as the synthesised beam of that data cube is larger than the hole and thus does not provide a reliable measure of the hole size. Nevertheless, since the innermost radius probed (the radius of the hole R_{hole}) is approximately the same as the radius of equal mass contribution, we can conclude that we do in fact measure the effects of the SMBH directly. At this innermost radius, $\approx$ 49 per cent of the enclosed mass is due to the SMBH.

Systematic uncertainties

As discussed in Section 2.2.2, we have rescaled our statistical uncertainties to approximately account for systematic uncertainties. However, these systematic uncertainties can also be quantified through the creation of models with alternative assumptions and the comparison of those models against our fiducial (i.e. best-fitting) model (the one presented in Section 2.6.3).

A major source of uncertainty is the dust present in the *HST* image used to create the MGE model. The issue of dust correction has increasingly been considered in the field of molecular-gas SMBH mass determinations (e.g Boizelle et al. 2019, 2021; Cohn et al. 2024; Dominiak et al. 2025) and in some cases it has been shown to affect the determined SMBH

mass by ≈ 30 per cent (Cohn et al. 2021) and the determined M/L also by ≈ 30 per cent (Dominiak et al. 2025). Due to the face-on nature of NGC 1387 and its rather uniform dust distribution, we are unable to manually mask the dust. We can instead deal with the effects of dust by performing a dust correction. For this we use a WFC3 F110W filter (J-band) image alongside the F160W filter (H-band) image. We first convert the images to units of magnitude in the Vega system and subtract the F160W filter image from the F110W filter image to calculate the observed $J - H$ colour of every pixel. We then examine the outskirts of this image, away from the dustiest regions, to estimate the intrinsic $J - H$ colour of the galaxy, $(J - H)_{\rm int} = 0.75$. Subtracting this from the observed colour map generates an excess colour map $E(J - H) = (J - H)_{\rm obs} - (J - H)_{\rm int}$ with a typical colour excess of 0.12 mag peaking at 0.22 mag. This is then converted into an H-band extinction A_H map by dividing it by the ratio of the total extinctions obtained from the standard Galactic extinction curve with a total-to-selective extinction ratio $R_V = 3.1$ (Fitzpatrick 1999), leading to an average A_H of 0.14 mag with a peak of 0.26 mag. This extinction map is then applied to the original F160W filter image to correct the dust. Lastly, this dust-corrected image is used to generate a new MGE model as in Section 2.6.3, and in turn a new dynamical model. This leads to a best-fitting SMBH mass of $1.91^{+1.64}_{-1.22} \times 10^8$ $\mathrm{M}_\odot$ and a best-fitting M/L of $0.86^{+0.28}_{-0.26}$ $\mathrm{M}_\odot/\mathrm{L}_{\odot,\mathrm{F160W}}$, representing a 74 per cent increase of the SMBH mass and a 5 per cent decrease of the M/L compared to our fiducial model. Despite this 74 per cent increase, the dust-corrected MGE model best-fitting SMBH mass is still consistent with our fiducial SMBH mass within the 3σ statistical uncertainties reported in Table 2.22, however this result highlights the significant effect that dust correction can have on SMBH mass determination and the importance of its consideration in further works.

Another source of potential systematic uncertainty is the assumed axial ratio of the MGE Gaussians. The presence of a bar and the subsequently poor fit of the MGE over it renders us unable to use standard statistical measures like χ^2 when determining the axial ratio. The adopted $q' = 0.98$ was determined by eye and as such is somewhat uncertain. To investigate the effect of our choice of fixed axial ratio on the final best-fitting parameters, we generated a series of best-fitting dynamical models whose MGE models had different fixed axial ratios in the range $0.94 \leq q' \leq 1.00$. The upper boundary of this range simply represents a perfectly

Table 2.23: Best-fitting parameters and associated uncertainties of models with different fixed MGE axial ratios for NGC 1387.

q'	$\log(M_{\rm BH}/{\rm M}_\odot)$		$M/L_{\rm F160W}$ ($\rm M_\odot/L_{\odot,F160W}$)	
	Best fit	3σ uncertainty	Best fit	3σ uncertainty
0.94	8.02	−0.84, +0.37	0.90	−0.36, +0.38
0.96	8.06	−0.85, +0.36	0.86	−0.24, +0.39
0.98	8.04	−0.87, +0.41	0.90	−0.35, +0.44
1.00	8.06	−0.94, +0.43	0.92	−0.33, +0.43

Note: The $q' = 0.98$ model is the fiducial best-fitting model adopted in this paper.

circular MGE, whilst the lower boundary represents the lowest q' that still yields a good fit by eye. In all these cases the MGE models were oriented along the same kinematic PA of 242.°5. The best-fitting parameters of these models are listed in Table 2.23. All the models are statistically consistent with one another and the differences between the SMBH masses and M/L of these models and those of our fiducial model are significantly smaller than the 3σ statistical uncertainties reported on our fiducial model.

An additional source of systematic uncertainty stems from our assumptions about the M/L radial profile. Whilst it is typically reasonable to assume that M/L is constant across galaxies, we can nevertheless create models with alternative M/L profiles to assess the effects this might have on the SMBH mass. In particular, there is a bright central ring of ionised-gas emission in NGC 1387, suggesting star-forming regions (Iodice et al. 2019). We thus tested a linearly-varying M/L radial profile. We implemented this by creating a circular velocity curve assuming $M/L = 1\ \rm M_\odot/L_{\odot,F160W}$, and then scaling these velocities by the square root of the M/L profile. Keeping all other parameters as before, a model with a radially linearly-varying M/L yields a best-fitting SMBH mass of $4.3^{+11.5}_{-4.2} \times 10^7\ \rm M_\odot$, a 61 per cent decrease compared to out fiducial model, but nevertheless consistent with it within the 3σ statistical uncertainties reported in Table 2.22. The best-fitting M/L is $(M/L_{\rm F160W})\,/\left(\rm M_\odot/L_{\odot,F160W}\right) = 0.83^{+0.28}_{-0.22} - 0.02^{+0.02}_{-0.02}\ (R/\rm arcsec)$, a decrease of 8 per cent in the very centre. Whilst this result is consistent with our fiducial model within even 1σ statistical uncertainties, it is somewhat unexpected, as due to conservation of total dynamical mass a smaller SMBH would imply a larger M/L whereas this M/L is smaller than that of our fiducial model. However, this result can be explained by the best-fit inclination of

$15.6^{\circ}{}^{+2.7}_{-2.2}$, an increase of 10 per cent compared to our fiducial model. Looking at Fig. 2.33 an inclination change of 10% should lead to a change in M/L consistent with the above result.

Aside from direct assumptions we make in our model, an important source of systematic error is the adopted galaxy distance. This is largely dependent on the distance-measurement method used, with numerical action methods presenting discrepancies of a factor of 2 (McQuinn et al. 2021), whilst Cepheid and tip of the red giant branch distance indicators can routinely yield uncertainties of < 5 per cent (Riess et al. 2024). The distance used in this paper was determined using surface brightness fluctuations, which typically yield distances accurate to ≈ 5 per cent (Cantiello & Blakeslee 2023), consistent with the stated uncertainties on the NGC 1387 distance measurement. As is standard practice, however, we do not include the distance uncertainty in our final uncertainty budget, as our fiducial mass can be trivially (linearly) scaled to any other adopted distance.

2.7 Conclusions

In this chapter we have presented the molecular gas dynamical measurements of the SMBH masses in four nearby galaxies: NGC 1684, NGC 0997, NGC 4751 and NGC 1387. In the case of NGC 4751 the modelling was performed using high resolution ALMA observations of the ^{12}CO(3–2) line, whereas the remaining three galaxies utilised high resolution ALMA observations of the ^{12}CO(2–1) line. The aim of this chapter was twofold. First, to obtain robust SMBH mass constraints in individual galaxies using molecular gas as a kinematic tracer, and second, to assess the practical strengths and limitations of this method across a small but diverse sample of early-type galaxies.

In Section 2.3 we found that NGC 1684 has a regularly rotating molecular gas disc with a spatial extent of $\approx$ 6 arcsec ($\approx$ 1.8 kpc) in radius and a central hole of radius $0.39^{+0.17}_{-0.37}$ arcsec, slightly larger than the expected SMBH sphere of influence, preventing us from detecting a clear Keplerian rise of the rotational velocities at small radii. Adopting a 2D axisymmetric exponential surface density profile with an inner truncation, an MGE model derived from a *HST* WFC3 F110W filter image, and assuming a constant mass-to-light ratio, we infer a SMBH mass of $1.40^{+0.44}_{-0.39} \times 10^9$ $M_{\odot}$ and a stellar F110W filter M/L of

(2.50 ± 0.05) $M_\odot/L_{\odot,F110W}$. We also explored alternative M/L profiles, however these did not exclude the possibility of a central SMBH.

In Section 2.4 we found that NGC 0997 also has a regularly rotating molecular has disc, with a spatial extent of $\approx$ 5 arcsec ($\approx$ 2.2 kpc) in radius and a partially-filled asymmetric central hole with a maximal radius of $\approx$ 0.5 arcsec, much larger than the expected SMBH sphere of influence, preventing us from detecting a Keplerian velocity rise. We modelled NGC 0997 using two steps. First, we modelled the entire galaxy in order to obtain a robust inclination using the entire molecular gas disc. Then in the second step we restricted the modelling to the central 2 arcsec $\times$ 2 arcsec area, fixing the inclination to that obtained in the previous step. In both steps we used SkySampler to model the cube using the observed gas distribution itself, an MGE model derived from a *HST* WFC3 F160W filter image, and assumed a constant M/L. In order to exclude models with very low SMBH masses we also sampled the the M_{BH} parameter space linearly, as opposed to the regular method of sampling the space logarithmically. With this linear SMBH mass sampling, we infer a SMBH mass in the range 4.0×10^7 to 1.8×10^9 $M_\odot$ and a stellar F160W filter M/L of (1.52 ± 0.11) $M_\odot/L_{\odot,F160W}$.

In Section 2.5 we found that NGC 4751 has a regularly-rotating molecular gas disc and a very strong circular velocity upturn in the central regions of the galaxy. In fact, our analysis of NGC 4751 contains the second highest circular velocity ever probed by a molecular gas measurement, rivaled only by the high-resolution measurement of NGC 0383 (Zhang et al. 2025a). We explored dynamical models with two different M/L radial profiles: constant and linearly varying. The excellent resolution of the sphere of influence in this galaxy allows us to infer a SMBH mass $M_{BH} = 3.43^{+0.45}_{-0.44}[\text{stat}, 3\sigma]^{+0.22}_{-0.64}[\text{sys}] \times 10^9$ $M_\odot$ and a stellar F160W filter M/L $M/L_{F160W} = 2.68 \pm 0.11[\text{stat}, 3\sigma]^{+0.10}_{-0.80}[\text{sys}]$ $M_\odot/L_{\odot,F160W}$ when assuming a constant M/L, and a SMBH mass $M_{BH} = 2.79^{+0.75}_{-0.57}[\text{stat}, 3\sigma]^{+0.75}_{-0.45}[\text{syst}] \times 10^9$ $M_\odot$ and a stellar F160W filter M/L (M/L_{F160W}) $/\left(M_\odot/L_{\odot,F160W}\right) = 3.07^{+0.27}_{-0.35}[\text{stat}, 3\sigma]^{+0.08}_{-1.14}[\text{sys}] - 0.09^{+0.08}_{-0.06}[\text{stat}, 3\sigma]^{+0.08}_{-0.01}[\text{sys}]$ (R/arcsec) when assuming a radially linearly-varying M/L. In this section we also explored sources of molecular gas-derived SMBH mass uncertainties, in particular modelling assumptions. In addition to exploring models with different mass-to-light ratio profiles, we also explored the effects of using the SkySampler tool which allows us to use the observed gas distribution itself instead of a parametric function when

modelling the molecular gas distribution. We also explored the effects that different MGE models can have on how the total dynamical mass is divided between stellar mass and the SMBH by the model. In addition to using an MGE model from literature, we also looked at two methods of image dust correction in the production of MGE models. The tests indicated that whilst our general approach of rescaling statistical uncertainties better approximates the systematic uncertainties, such rescaling is not appropriate in all contexts. In particular, the choice of MGE model had a significant impact on the inferred M/L and that the dust extinction correction of optical images needs to be more systematically implemented in the field of molecular gas modelling. On the other hand, it was also clear that SMBH masses are largely unaffected by the MGE models when the data is well-resolved and a Keplerian rise is as strong as that of NGC 4751. This is consistent with the general understanding that, as long as the kinematic tracers remain regular and probe deep within $R_{\rm SoI}$ the SMBH mass will be less susceptible to uncertainties in the galaxy's central stellar light distribution.

Lastly, in Section 2.6 we found that NGC 1387 has a face-on, regularly-rotating central molecular gas disc with a diameter of $\approx$ 18 arcsec ($\approx$ 1.7 kpc) and a central depression slightly larger than the SMBH sphere of influence. We modelled the galaxy in two steps as due to the flocculent and face-on nature of the molecular gas the inclination of the galaxy remained poorly constrained during initial modelling attempts. First, we created a data cube with a degraded resolution to ensure higher signal-to-noise in the outer regions of the galaxy and used an exponential radial surface brightness profile in the model. This allowed us to effectively constrain the inclination. We then used the posterior probability distribution of the inclination as a prior in the second step of modelling, where we used a high-resolution data cube and the SkySampler task to accurately reproduce the molecular gas distribution. We infer a SMBH mass of $1.10^{+1.71}_{-0.95} \times 10^8$ $M_\odot$ and a F160W filter stellar mass-to-light ratio of $0.90^{+0.44}_{-0.35}$ $M_\odot/L_{\odot,\rm F160W}$. Similarly to NGC 4751 we also attempt to quantify systematic uncertainties by exploring a range of alternative models with dust-corrected MGE models and linearly-varying M/L profiles. As in NGC 4751, our NGC 1387 results confirm that the choice of MGE model and an appropriate treatment of dust can have a significant impact on the determined SMBH mass.

Taken together, the four SMBH mass measurements presented in this chapter span more than an order of magnitude in black hole mass and illustrate both the capabilities and the limitations of molecular gas dynamical modelling. It is clear that molecular gas kinematics provide a powerful way of obtaining SMBH mass measurements, particularly in ETGs with dynamically cold central gas discs. At the same time, the work in this chapter highlights the need for careful target selections and for a future detailed treatment of the stellar component when modelling in order to obtain robust SMBH masses.

The truth is that he wanted to draw a little comfort from gazing at the stars. There were still one or two up there, at the zenith. As always, seeing them revived him; they were distant, they were omnipotent and at the same time they were docile to his calculations; just the contrary to humans, always too near, so weak and yet so quarrelsome.

— Giuseppe Tomasi di Lampedusa's *The Leopard*

3

Supermassive Black Hole Mass Upper Limits

Contents

3.1 Introduction 113
3.2 NGC 0665 113
3.2.1 Galaxy Properties 113
3.2.2 ALMA Observations 114
3.2.3 CO Modelling 119
3.3 NGC 5208 125
3.3.1 Galaxy Properties 125
3.3.2 ALMA observations 126
3.3.3 CO modelling 129
3.4 NGC 0467 136
3.4.1 Galaxy Properties 136
3.4.2 ALMA observations 137
3.4.3 CO modelling 141
3.5 NGC 7550 150
3.5.1 Galaxy Properties 150
3.5.2 ALMA observations 151
3.5.3 CO modelling 156
3.6 Conclusions 157

3.1 Introduction

This chapter presents dynamical models for galaxies in which we do not obtain robust SMBH masses, but in some of them we can instead place robust SMBH mass upper limits. Whilst upper limits are of course less desirable than precise measurements, they still serve a valuable role in constraining the allowed parameter space in black hole-galaxy scaling relations. In the high-mass regime, which is the focus of this Chapter, they rule out over-massive SMBHs that would otherwise steepen the relations. In fact, SMBH mass upper limits have been found to be be entirely consistent with the BH – size – luminosity relation of van den Bosch (2016). When viewed across a sample, upper limits can shrink the bounds of credible best-fit slopes, intercepts, and scatters just as effectively as a lower-quality detections (i.e. those with large uncertainties), provided they are incorporated with the correct likelihood for censored observations.

It is also important to report these upper limits as they identify the need for follow-up studies. Galaxies with an unresolved $R_{\rm SoI}$ where a modest improvement in resolution would allow for an upper limit to be converted into a measurement are worth pursuing in future studies. On the other hand, galaxies where the limiting factor is astrophysical and not instrumental (e.g. intrinsic non-circular motions that violate the modelling assumptions or the presence of large circumnuclear holes) are not worth the allocation of limited observing time.

Lastly, this chapter serves an additional expository role. For each galaxy, we present the ALMA CO observations, the associated photometric models used to describe the stellar mass distribution and the dynamical modelling that leads to the inferred SMBH mass upper limits. Together, these case studies illustrate both the strengths and the limitations of molecular gas SMBH mass measurements.

3.2 NGC 0665

3.2.1 Galaxy Properties

NGC 0665 is an S0 lenticular galaxy located at $01^{\rm h}44^{\rm m}56\overset{\rm s}{.}10$, $+10°25'22\overset{''}{.}9$ (J2000.0) in the constellation of Pisces. We adopt the distance used in the MASSIVE survey, $D = 62.3 \pm 2.4$ Mpc, obtained through surface brightness fluctuation (Jensen et al. 2021).

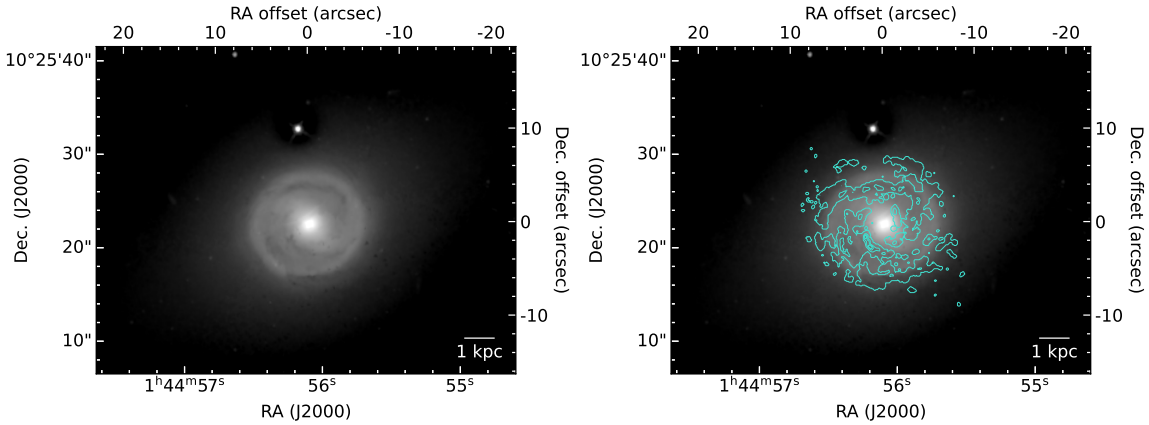


Figure 3.1: Unsharp-masked *HST* WFC3 F110W filter (J-band) image of NGC 0665 (left), overlaid with the ^{12}CO(2–1) integrated intensity contours (cyan) from our ALMA observation (right).

At this distance, 1 arcsec corresponds to ≈ 302 pc. NGC 0665 is located in a group of four galaxies (according to 2MRS; Crook et al. 2007), of which it is the brightest.

HST images reveal a dusty disc with spiral structures, and an unobscured nucleus (Fig. 3.1). There is a much smaller object ≈ 10 arcsec north of NGC 0665, most likely a background galaxy. NGC 0665 hosts a significant molecular gas reservoir, with a total H_2 mass of $1.51^{+0.11}_{-0.10} \times 10^9$ $M_\odot$ and a total SFR of 0.29 ± 0.03 $M_\odot$ yr^{-1} (Davis et al. 2015). This molecular gas in NGC 0665 is regularly rotating and its kinematic axis is well-aligned with its photometric axis (Ene et al. 2018). It has an integrated absolute K-band magnitude of −25.39 (Quenneville et al. 2023) corresponding to a total stellar mass of 4.28×10^{11} $M_\odot$ (calculated using Eq. 2 of Cappellari 2013).

NGC 0665 does not have a direct SMBH mass measurement, but an estimate can be obtained using the $M_{\rm BH} - \sigma_{\rm e}$ relation of van den Bosch (2016). Assuming $\sigma_{\rm e}$ = 164 km s^{-1} (Veale et al. 2018), a SMBH mass of ≈ 7.2×10^7 $M_\odot$ is expected, yielding $R_{\rm SoI}$ ≈ 12 pc (≈ 0.03 arcsec).

3.2.2 ALMA Observations

Observations of the ^{12}CO(2–1) emission line using the 12-m ALMA array in Band 6 were obtained for all four galaxies as part of projects 2015.1.00187 (PI: Davis). The properties of the observations are listed in Table 1.2. The NGC 0665 data are compromised of a single track taken on 2016 July 31, for a total of 23 minutes on source. Baselines span from 15.1 m

Table 3.1: Parameters of the NGC 0665 continuum image and the detected cleaned continuum source.

Image property	Value
Image (pix)	250×250
Image (arcsec)	20×20
Image size (kpc)	7.2×7.2
Pixel scale (arcsec pix^{-1})	0.08
Pixel scale (pc pix^{-1})	24.2
RMS noise (mJy beam^{-1})	0.03
Synthesised beam (arcsec)	0.27×0.25
Synthesised beam (pc)	24.7×22.1
Source property	**Value**
Right ascension (J2000)	$01^{\rm h}44^{\rm m}56\overset{\rm s}{.}0980 \pm 0\overset{\rm s}{.}0004$
Declination (J2000)	$+10°25'22\overset{''}{.}520 \pm 0\overset{''}{.}008$
Integrated flux (μJy)	495 ± 51

to 1.1 km, yielding an angular sensitivity of 0.29 arcsec, a maximum recoverable scale of 4.5 arcsec, and a field of view of 24.8 arcsec. The single track had four spectral windows. One window, centred on the redshifted ^{12}CO(2–1) frequency of 227.366186, was used to map the molecular gas with a bandwidth of 1.875 GHz ($\approx$ 2440 km s^{-1}) subdivided into 3840 channels of width 488 kHz ($\approx$ 0.64 km s^{-1}). The remaining three spectral windows were used to map the continuum. Two of these tracks each had a bandwidth of 2 GHz ($\approx$ 2600 km s^{-1}) subdivided into 128 channels of width 16 MHz ($\approx$ 20 km s^{-1}). The last remaining spectral window had a bandwidth of 1.875 GHz ($\approx$ 2440 km s^{-1}) subdivided into 240 channels of width 8 MHz ($\approx$ 10 km s^{-1}).

Continuum emission

An image of the NGC 0665 continuum was created in the standard manner and cleaned with the CASA task `tclean` with a central frequency of 235.3 GHz (1.27 mm). We adopted the multi-frequency synthesis mode with Briggs weighting with a robust parameter of 0.5. The continuum was cleaned to a threshold of 2 times the RMS noise of 0.03 mJy beam^{-1}. We detect a central source of continuum emission with an integrated flux density of 0.50 ± 0.05 mJy and a peak intensity of 0.46 ± 0.03 mJy beam^{-1}. Fitting the continuum using the CASA task `imfit` reveals that the source is unresolved and its deconvolved size is consistent with that of a point. The continuum image is shown in Fig. 3.2 and its properties are listed in Table 3.1.

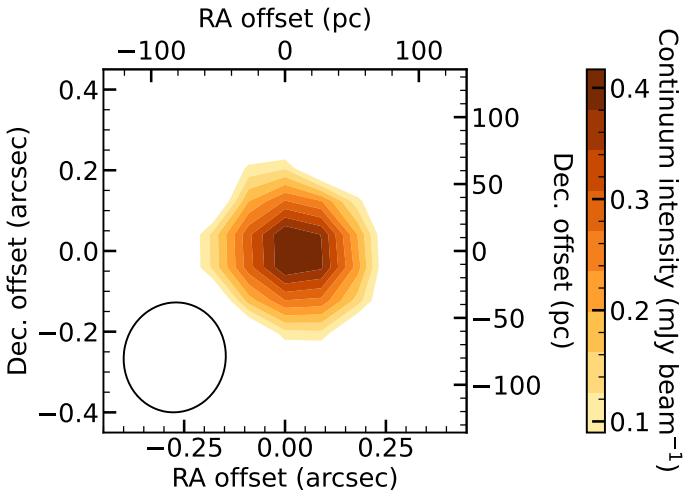


Figure 3.2: Central region (0.9 arcsec × 0.9 arcsec) of the NGC 0665 1.27 mm continuum image. Contours are evenly spaced between the peak intensity of 0.46 ± 0.03 mJy beam^{-1} and 3 times the RMS noise. The synthesised beam is shown in the bottom-left corner as a black open ellipse.

Line emission

We create the cube as usual, subtracting the continuum using the CASA task `uvcontsub` and the cleaning using the `tclean` task. The regions of emission were cleaned to a threshold of ≈ 1.2 mJy beam^{-1} channel^{-1} which is ≈ 2 times the RMS noise of the line-free channels of the dirty data cube. To image the line emission we chose a Briggs weighting with a robust parameter of 1.0, in order to recover more signal-to-noise in the loosely defined outer edges of the molecular gas disc. We also adopted a channel width of 10 km s^{-1}, the typical used in SMBH mass determinations. The resulting data cube has a synthesised beam of 0.33 arcsec × 0.29 arcsec (99 × 89 pc^2) with a RMS noise of 0.63 mJy beam^{-1} channel^{-1}, and its properties are summarised in Table 3.2.

The moment map mask was created in the usual manner by smoothing the data cube using a boxcar kernel whose spatial dimension is equal to 4 times the FWHM of the major axis of the synthesised beam and whose spectral dimension is equal to 1.5 times the velocity width, and then clipping the smoothed data cube to a threshold of 6 times the RMS. This mask was then applied to the unsmoothed primary beam-corrected data cube to create moment maps. We detect a disc of molecular gas about ≈ 8 arcsec in radius, coincident with and slightly larger than the dust disc (see Fig. 3.1). The gas is clumpy and sparse, arranged in a series of spiral structures, with no gas within the galactic center. It appears

Table 3.2: CO data cube properties for NGC 0665.

Image property	Value
Spatial extent (pix)	250×250
Spatial extent (arcsec)	20.0×20.0
Spatial extent (kpc)	7.2×7.2
Pixel scale (arcsec pix^{-1})	0.08
Pixel scale (pc pix^{-1})	24.2
Velocity range (km s^{-1})	5000 – 5800
Channel width (km s^{-1})	10
RMS noise (mJy beam^{-1} channel^{-1})	0.63
Number of constraints	69, 410
Synthesised beam (arcsec)	0.33×0.29
Synthesised beam (pc)	99×89

to be mostly regularly rotating. There are some highly localised areas of higher velocity dispersion gas ($\approx 40 - 60$ km s^{-1}) around the centre of the galaxy, however, the bulk of the gas is dynamically cold (< 30 km s^{-1}) throughout. Due to the complete lack of gas within a radius of ≈ 2 arcsec we are unable to probe $R_{\rm SoI}$. In such instances we are unable to obtain a robust SMBH mass, however an upper limit can be placed on the mass nonetheless. We also created a kinematic PVD by taking a 10-pixel wide cut through the masked data cube along a position angle of 117.°0. The resulting moment maps and PVD are shown in Fig. 3.3.

In Fig. 3.4 we can see the integrated ^{12}CO(2–1) spectrum of NGC 0665 with a double-peaked shape of a rotating disc and a mild asymmetry consistent with the observed gas distribution. This spectrum was extracted from a 18 arcsec $\times$ 18 arcsec ($\approx 6500 \times 6500$ pc^2) region around the centre with an integrated FWZI flux density of 41.4 ± 4.4 Jy km s^{-1}. Figure 3.4 also shows the integrated spectrum of the ^{12}CO(2–1) (grey shading) and ^{12}CO(1–0) (black dashed line) lines obtained from the IRAM single-dish 30-m telescope observations reported by Davis et al. (2015). In contrast to the ALMA data, the 30-m ^{12}CO(2–1) spectrum does not display a pronounced double horned profile. This is most likely because the single-dish primary beam of ≈ 11 arcsec cannot fully capture the total extent of the molecular gas disc (which is ≈ 18 arcsec across) and therefore its spectrum is dominated by the emission from the inner regions of the disc.

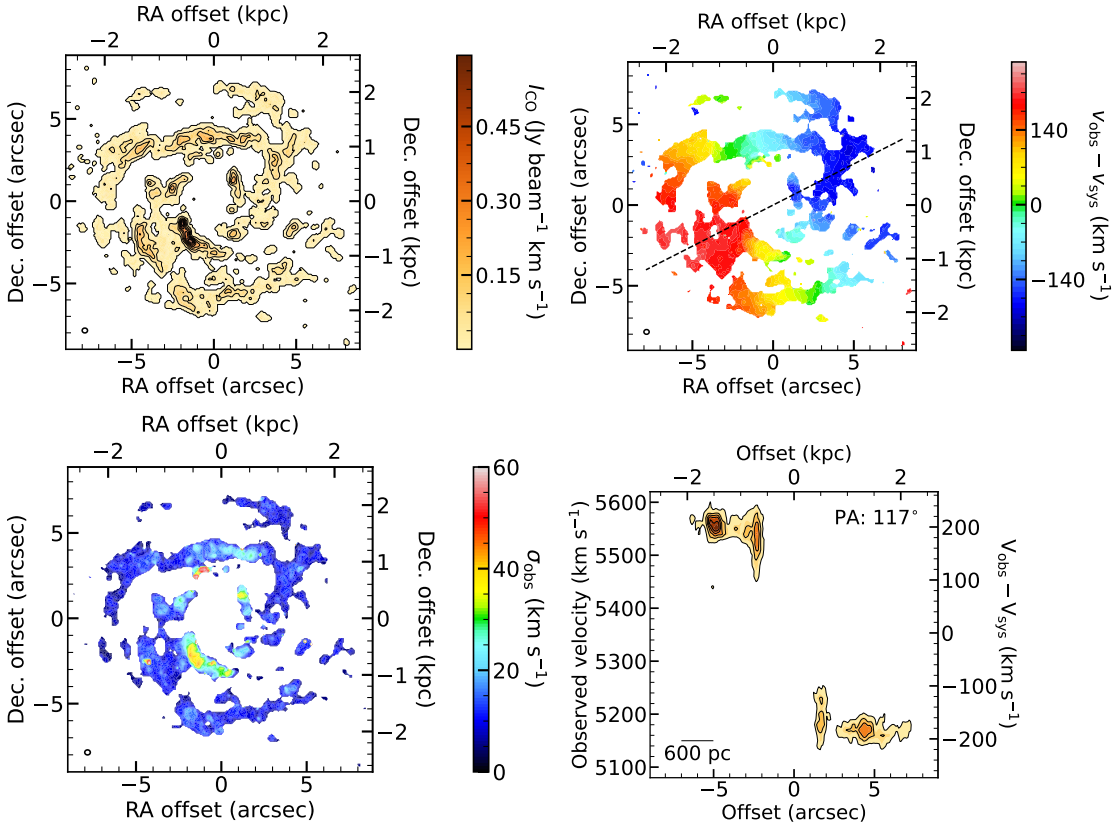


Figure 3.3: As Fig. 2.29 but for NGC 0665.

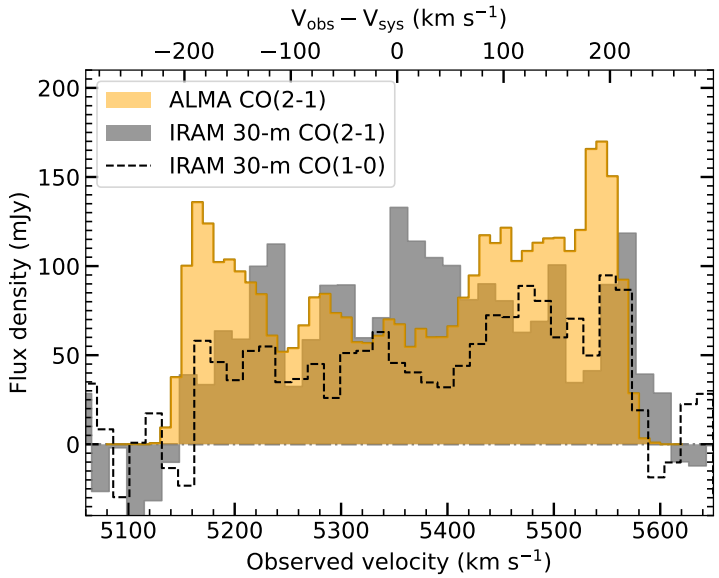


Figure 3.4: ^{12}CO(2–1) integrated spectrum of NGC 0665 derived from our ALMA data (orange shading), overlaid on the IRAM 30-m telescope ^{12}CO(2–1) (grey shading) and ^{12}CO(1–0) (black dashed line) observations of Davis et al. (2015). The ALMA aperture is a 18 arcsec × 18 arcsec ($\approx 6500 \times 6500$ pc^2) region centred on the galaxy centre, that includes all detected emission.

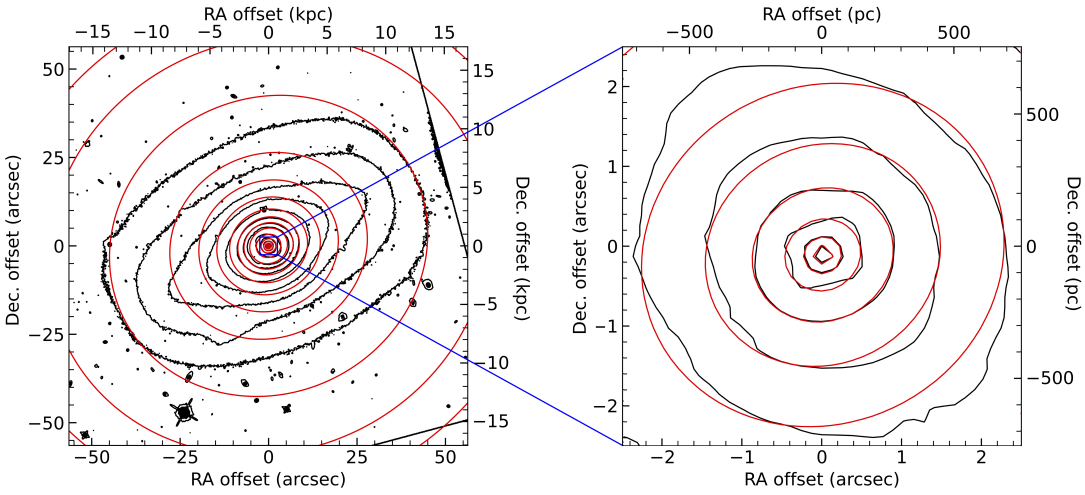


Figure 3.5: *HST* WFC3 F110W filter (J-band) image of NGC 0665 (black contours), overlaid with our best-fitting MGE model (red contours). **Left:** Full extent of the *HST* image showing the galaxy bulge and bar. **Right:** Central region only.

3.2.3 CO Modelling

Model parameters

As can be seen in Fig. 3.5, NGC 0665 has a prominent bar, which itself is not an axisymmetric feature. The standard procedure in such a case is to obtain the axial ratio of the Gaussians from the outer regions of the galaxy and to fix them to this constant value even over the barred region, as in NGC 1387 (Section 2.6.3; for further details see Scott et al. 2009). Whilst such a treatment will produce a superficially poorer fit within the region of the bar, the model will overall produce a better kinematic fit. However, NGC 0665 appears to be an extremely large elliptical and the *HST* image is neither large nor deep enough to image the outer regions of the galaxy outside of the bar. As such, we instead choose to use the innermost dust disc to constrain the axial ratio for our Gaussians, in this case $q' = 0.96$. As discussed in Section 2.6.3, the MGE luminosity surface density can only be analytically deprojected into a luminosity volume distribution if $\cos^2 i < q'^2$ and therefore the flattest Gaussian of an MGE model imposes a minimum inclination on the dynamical modelling. Our chosen axial ratio will allow us to deproject to a minimum inclination of $i \approx 16°$ which is sufficient for our purposes.

We obtain a stellar light distribution for NGC 0665 using an MGE model of a *HST*

Table 3.3: Parameters of the deconvolved best-fitting MGE components of our model of NGC 0665.

$I'_{\odot}$ ($L_{\odot,F110W}$ pc^{-2}) (1)	σ' (arcsec) (2)	q' (3)
69439	0.096	0.960
12444	0.410	0.960
8239	1.048	0.960
3464	3.598	0.960
543	6.582	0.960
313	11.544	0.960
121	50.379	0.960

Notes. Deconvolved MGE components. (1) Central surface brightness of Gaussian component. (2) Standard deviation of Gaussian component. (3) Axial ratio of Gaussian component.

WFC3 image in the F110W filter (J-band) (GO-14219, PI: Blakeslee) with a total exposure time of 1997 s. We convert this stellar light distribution into luminosities in the AB magnitude system by adopting a zero-point of 26.82 mag (Sahu et al. 2021), a Solar absolute magnitude of 4.52 mag for the F110W filter (Willmer 2018) and a galactic extinction of 0.078 mag from NED (Schlafly & Finkbeiner 2011).

Shown in Fig. 3.5 is the MGE model for NGC 0665. Despite providing a bad fit in the outer regions of the galaxy, it is clear that the fit in the centre of the galaxy, which matters the most in constraining the SMBH mass, is good. Given that the axial ratio was fixed to that of the inner parts of the galaxy, it is necessary for the kinematic position angle to align with the position angle of the MGE model. As such, we have fixed the position angle to 117.0°, which is in agreement with an independent determination of position angle through kinematic modelling (116.0 ± 3.2°; Ene et al. 2018).

Due to the sparse and complex molecular gas in NGC 0665, we model the gas distribution using SkySampler as described in Section 2.2.1. We sample the CASA clean components with 10^6 particles. Because of the sparsity, SkySampler struggled to accurately determine the kinematic centre from the disc geometry alone, thus we have opted to fix the central position to that of the continuum emission, similarly to NGC 1387.

Due to the face-on nature of the galaxy, as well as the complex molecular gas distribution, we also had difficulties in constraining the inclination. We therefore decided to supply our model with a Gaussian inclination prior centred on the best-fit inclination of $i = 34 \pm 5°$, obtained from Davis et al. (2015), with a standard distribution of $\sigma = 1.67$ which sets the

Table 3.4: Best-fitting model parameters of NGC 0665 and associated uncertainties.

Parameter	Prior			Best fit	1σ uncertainty	3σ uncertainty
Mass model						
SMBH mass (10^8 $M_\odot$)	0	→	80	13.8	< 26.6	< 60.8
Stellar M/L ($M_\odot/L_{\odot,\mathrm{F110W}}$)	0.0	→	5.0	1.93	−0.28, +0.43	−0.57, +1.45
Molecular gas disc						
Velocity dispersion (km s^{-1})	0.0	→	50.0	27.3	−2.2, +2.4	−5.7, +7.3
Integrated intensity (Jy km s^{-1})	0.0	→	50.0	33.7	−2.0, +2.1	−5.3, +5.8
Nuisance parameters						
Position angle (°)		(fixed)		117.0	–	–
Inclination (°)	20.0	→	55.0	36.6	−4.6, +4.3	−10.6, +10.2
Systematic velocity (km s^{-1})	5000	→	5800	5353.2	−2.0, +2.1	−5.8, +5.6

Note. The centre position is fixed to that of the unresolved continuum source, $01^h44^m56\overset{s}{.}0980$, $+10°25'22\overset{''}{.}520$ (J2000.0).

3σ probability at the reported errors. The Davis et al. (2015) estimate was obtained using ellipse fitting to dust structures, which has been shown to be a robust method of inclination estimation (Davis et al. 2011a) and is appropriate to use in the case of NGC 0665 as its molecular gas disc is clearly aligned with the dust (see Fig. 3.1). Additionally, this inclination estimate is in agreement with the best-fit inclination obtained through kinematic modelling when it is left as a free parameter. However, we note that the errors quoted on the Davis et al. (2015) inclination are not true statistical Gaussian uncertainties derived from a well-defined likelihood, but rather a visually-motivated inclination tolerance. Therefore, the use of such a prior is not strictly rigorous, but rather serves as a pragmatic way to regularise the parameter space around a plausible inclination and aid convergence.

Results

Initial modelling with the typical logarithmic sampling of the SMBH mass suggested that we cannot exclude models with very low mass black holes, however there was a slight preference for SMBH masses around $\log(M_{\mathrm{BH}}) \approx 9$ visible in the posterior distribution. Therefore, as in Section 2.4.3, we modelled the SMBH mass linearly such that $M_{\mathrm{BH}} = 0$ can be robustly probed. Our final MCMC chain had 200,000 steps. Figure 3.6 shows that we are unable to definitively confirm the presence of a central dark object, likely due to the large central hole. Since we have linearly sampled the SMBH mass, we have opted to list the "best-fitting" SMBH of 1.38×10^9 $M_\odot$ in Table 3.4, as there is a discernible, albeit

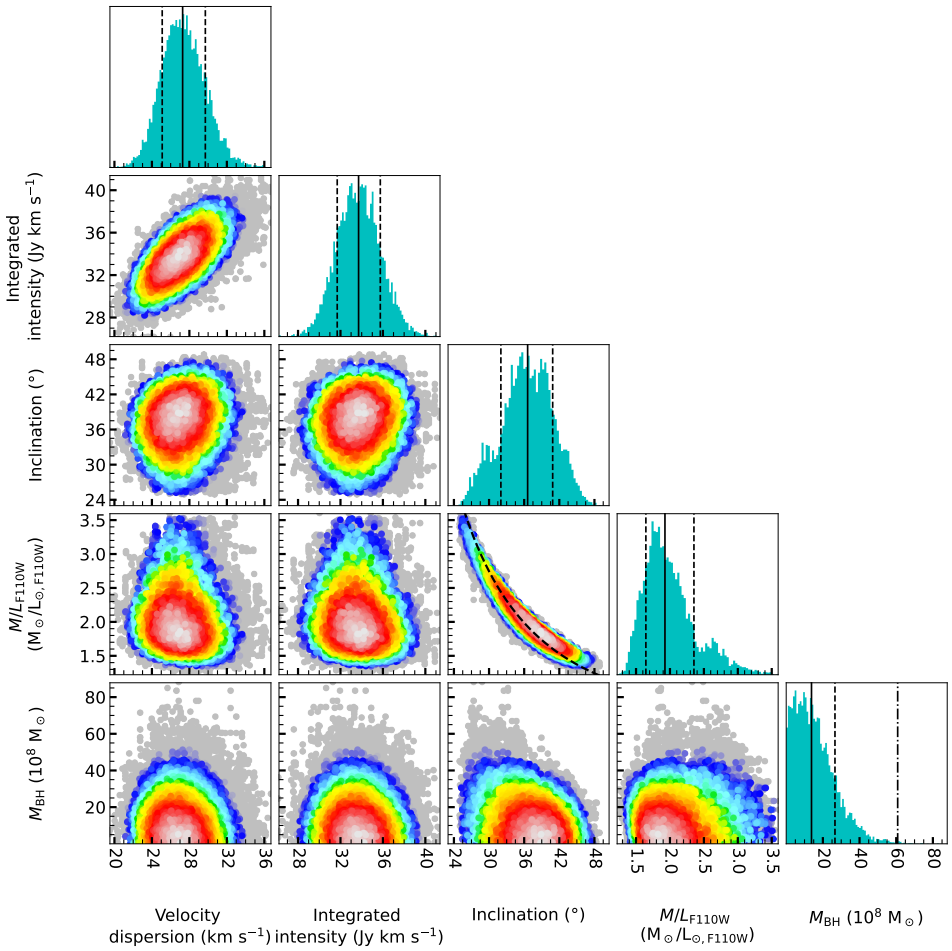


Figure 3.6: As Fig. 2.5, but for NGC 0665. The solid line over the 1D marginalised posterior distribution of the SMBH mass represents the median result, the dashed line represents the 68% confidence interval and the dot-dashed line represents the 99.7% confidence interval. Plotted over the 2D posterior distribution of inclination versus M/L is a dashed line showing the expected $M/L \propto 1/\sin^2 i$ relation between the two parameters.

small, peak in the SMBH mass posterior distribution. We do however stress that this does not constitute a robust SMBH determination, should only be understood as the median SMBH mass and instead the appropriate interpretation of our result is an upper limit on the SMBH of $< 2.7 \times 10^9$ M$_\odot$ at the 1σ (68 per cent) confidence level and $< 6.1 \times 10^9$ M$_\odot$ at the 3σ (99.7 per cent) confidence level. Whilst the 3σ uncertainties do not extend entirely to $M_{\rm BH} = 0$, and instead extend to 8.0×10^6 M$_\odot$, it is clear in Fig. 3.6 that the posterior distribution functionally extends to 0 and models with no SMBH mass are similarly preferred to those with a mass $\approx 10^9$ M$_\odot$. Consequently, we cannot definitively exclude models with no SMBH. The best-fitting M/L in the F110W filter is $1.93^{+1.45}_{-0.57}$ M$_\odot$/L$_{\odot,\rm F110W}$.

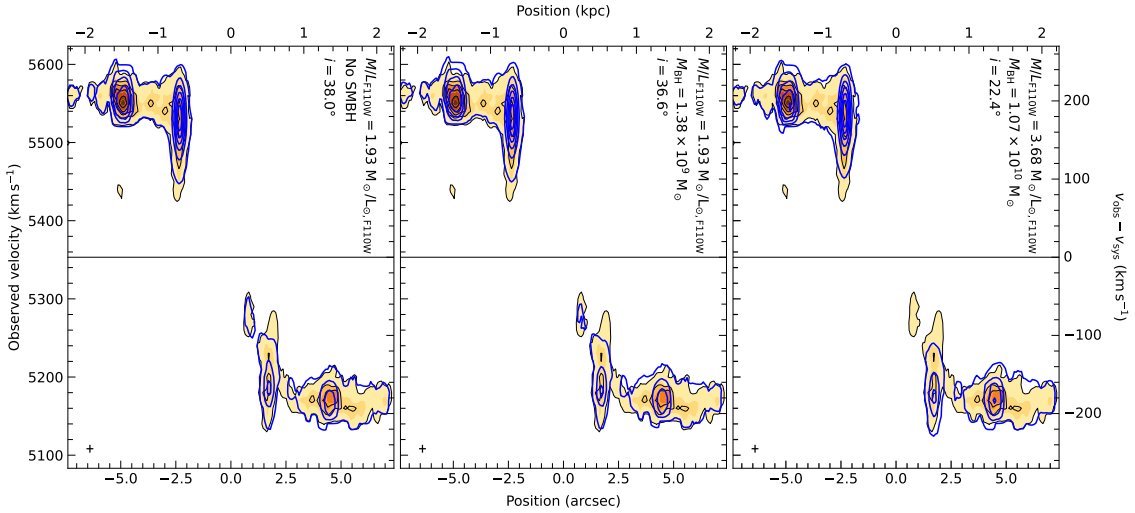


Figure 3.7: As Fig. 2.6, but for NGC 0665.

In Fig. 3.6 we can also see a very strong degeneracy between the inclination and M/L, which is to be expected given the galaxy's face-on nature. Plotted over the inclination versus M/L scatter plot is a dashed line showing the expected $M/L \propto 1/\sin^2 i$ relation between the two parameters. The corner plot highlights the effects that a poorly-constrained inclination has on modelling, as the majority of the large upper uncertainties on the M/L are clearly driven by the uncertainties at low inclination. Figure 3.6 also shows a mild anti-correlation between SMBH mass and M/L which represents the conservation of total dynamical mass and is to be expected.

In Fig. 3.7 we show the major-axis kinematic PVD overlaid with three models: a model with no SMBH, a model corresponding to the posterior median SMBH mass from our main fit, and a model with an over-massive SMBH (≈ 0.3 dex above the 3σ upper threshold). All other parameters for the models with no SMBH and an overly-massive SMBH mass were allowed to vary in the same manner as those for the main fit. Likewise, all fixed quantities remained the same, as did the inclination prior. We have chosen to plot the posterior-median (i.e. "best-fitting") SMBH mass in the middle panel of the Figure, rather than the 1σ or 3σ upper limit, as the SMBH mass is degenerate with M/L. Consequently, the best-fitting M/L reported from the main fit is not, in general, the best-fitting M/L for a model in which $M_{\rm BH}$ is fixed at its upper limit. As can be seen in the left and middle panels of the Figure, the models with no SMBH mass and the median SMBH mass are practically indistinguishable.

The innermost gas probed is sufficiently far away from the central SMBH hole that the gas is not meaningfully affected by the SMBH's presence or lack thereof, and is the reason why we cannot confirm the presence of a central SMBH. Looking at the right panel with the overly-massive SMBH, we can see that there is a slightly higher velocity in the innermost blue-shifted peak of the model PVD, which is also the emission closest to the centre of the galaxy and thus most affected by the presence of an over-massive SMBH. However, we do not see the typical large effect that the over-massive SMBH has on the model PVD, most likely due to the majority of the gas being so far away from its dynamical influence. The lack of the usual mismatch between model and observation is also possibly attributable to the fact that the model with an overly-massive SMBH prefers a significantly larger M/L and a very low best-fitting inclination (values listed in the Fig. 3.7). In this sense, this overly-massive SMBH model emulates the behaviour we see with NGC 1387 in Section 2.6.3, where the overly-massive SMBH drives the inclination down which in turn results in a higher M/L. However, even though the visual comparison of Fig. 3.7 is not striking, we must remember that a PVD samples only a one-dimensional slice through the data cube. While this provides good information about the central rotation curve, it necessarily discards all of the other available kinematic data. By contrast, the MCMC fitting procedure makes use of the entire 3D data cube and the posterior distributions represent models that are able to fit the entire geometry of the gas, not just a 1D slice. Looking at Fig. 3.6 we can see that not only is the overly-massive SMBH excluded when the entire cube is considered, but that both the overly large M/L and the very low inclination of the model are also excluded. Therefore, we must only treat plots like Fig. 3.7 as heuristics and visual aids, but ultimately base our conclusions on the robust cube-based modelling.

The cumulative mass distribution of NGC 0665, assuming the median SMBH mass, is shown in Fig. 3.8, where we can see that $R_{\mathrm{eq}} \approx 127$ pc (≈ 0.42 arcsec) and $R_{\mathrm{SoI}} \approx 221$ pc (≈ 0.73 arcsec), both of which are significantly smaller than the central hole in emission which extends to ≈ 510 pc (≈ 1.7 arcsec). At the edge of detectable emission only $\approx 12\%$ of the total mass enclosed is due to the SMBH. All of this is in agreement with our above findings that a SMBH mass estimate cannot be obtained for NGC 0665 given the quality of the data.

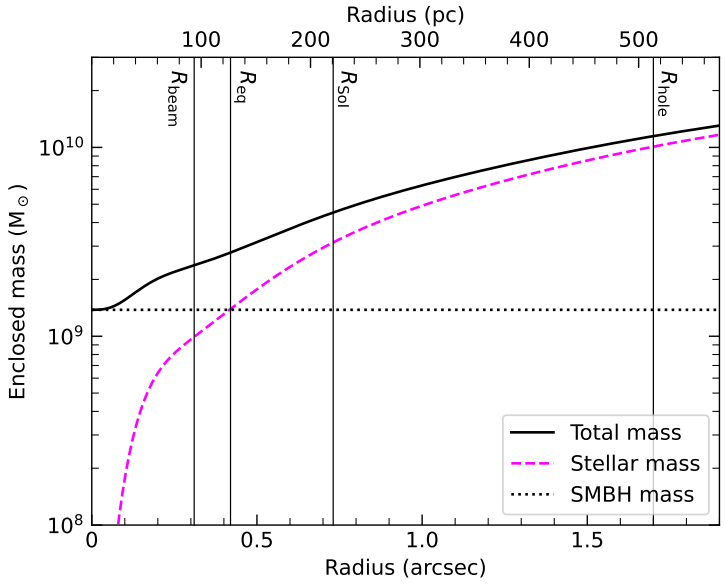


Figure 3.8: As Fig. 2.8, but for NGC 0665 (assuming $\sigma_e = 164$ km s^{-1} and our best-fitting SMBH mass).

3.3 NGC 5208

3.3.1 Galaxy Properties

NGC 5208 is an S0 lenticular galaxy located at $12^h32^m27\overset{s}{.}94$, $+07°18'59\overset{''}{.}2$ (J2000.0) in the constellation of Virgo. We adopt the distance used in the MASSIVE survey, $D = 105.0$ Mpc (Ma et al. 2014). At this distance, 1 arcsec corresponds to ≈ 509 pc. NGC 5208 is in a group of 3 galaxies (according to 2MRS; Crook et al. 2007), of which it is the brightest and its distance is obtained through surface brightness fluctuation (Jensen et al. 2021).

HST images reveal a dust disc, with prominent dust lanes to the west of the galaxy and an unobscured nucleus (Fig. 3.9). NGC 5208 hosts a significant molecular gas reservoir, with a total H_2 mass of $3.09^{+0.15}_{-0.14} \times 10^9$ M$_\odot$, and a SFR of 0.58 ± 0.05 M$_\odot$ yr^{-1} (Davis et al. 2015). It has an integrated absolute K-band magnitude of -25.87 (Quenneville et al. 2023) corresponding to a total stellar mass of 6.96×10^{11} M$_\odot$, calculated as before.

NGC 5208 does not have a direct SMBH mass measurement, but an estimate can be obtained using the $M_{BH} - \sigma_e$ relation of van den Bosch (2016). Assuming $\sigma_e = 235$ km s^{-1} (Davis et al. 2019) and the $M_{BH} - \sigma_e$ relation of van den Bosch (2016), a SMBH mass of $\approx 4.9 \times 10^8$ M$_\odot$ is expected, yielding $R_{SoI} \approx 38$ pc (≈ 0.08 arcsec).

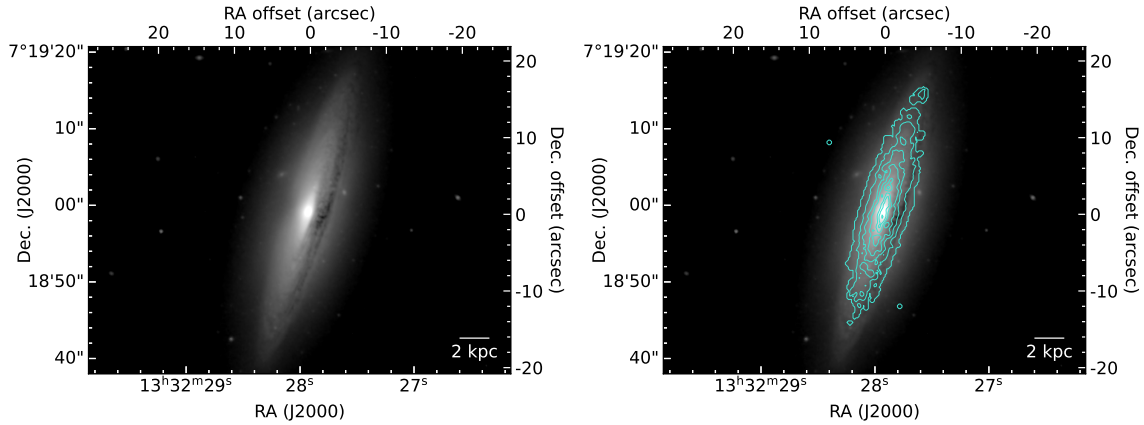


Figure 3.9: Unsharp-masked *HST* WFC3 F160W filter (*H*-band) image of NGC 5208 (left), overlaid with the ^{12}CO(2–1) integrated intensity contours (cyan) from our ALMA observations (right).

3.3.2 ALMA observations

Observations of the ^{12}CO(2–1) emission line using Band 6 of the 12-m ALMA array were obtained as part of project 2015.1.00187 (PI: Davis). The properties of the observations are listed in Table 1.2. The NGC 5208 data are also comprised of a single track and were taken on the 2016 March 21, for a total of 10 minutes on source. Baselines span from 15.3 m to 460 m, yielding an angular sensitivity of 0.7 arcsec, a maximum recoverable scale of 6.2 arcsec, and a field of view of 24.9 arcsec. The spectral setup for NGC 5208 is identical to that of NGC 0665 (see Section 3.2.2).

Continuum emission

We imaged the NGC 5208 continuum in the usual manner and cleaned it using the CASA task `tclean`. We adopted the multi-frequency synthesis mode with Briggs weighting with a robust parameter of 0.5. We cleaned the continuum to a threshold of 3 times the RMS noise of 0.06 mJy beam^{-1}. We detect a continuum source with a central frequency of 234.3 GHz (1.28 mm), an integrated flux density of 1.22 ± 0.09 mJy, and a peak intensity of 1.27 ± 0.05 mJy beam^{-1}. Fitting the continuum using the CASA task `imfit` reveals that the source's deconvolved size is consistent with that of a point (i.e. it is unresolved). The continuum image is shown in Fig. 3.10 and its properties are listed in Table 3.5.

Table 3.5: Parameters of the NGC 5208 continuum image and the detected cleaned continuum source.

Image property	Value
Image (pix)	256×256
Image (arcsec)	51.2×51.2
Image size (kpc)	26×26
Pixel scale (arcsec pix^{-1})	0.2
Pixel scale (pc pix^{-1})	101.8
RMS noise (mJy beam^{-1})	0.05
Synthesised beam (arcsec)	0.77×0.69
Synthesised beam (pc)	393×352
Source property	**Value**
Right ascension (J2000)	$13^{\rm h}32^{\rm m}27\overset{\rm s}{.}9224 \pm 0\overset{\rm s}{.}0010$
Declination (J2000)	$+07°18'59\overset{''}{.}120 \pm 0\overset{''}{.}011$
Integrated flux (mJy)	1.22 ± 0.09

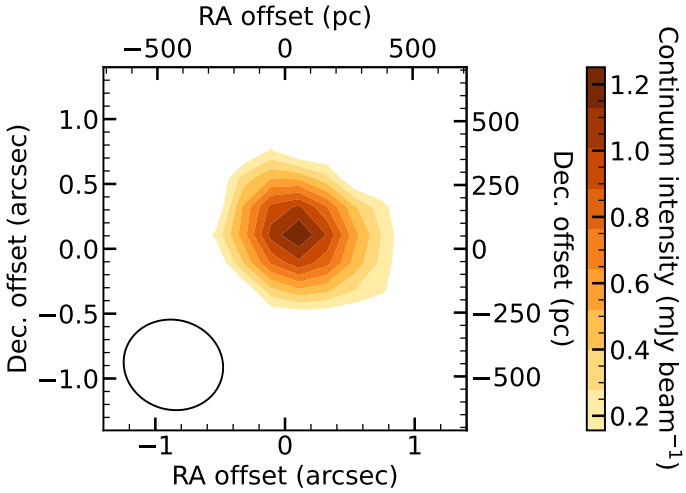


Figure 3.10: Central region (2.8 arcsec × 2.8 arcsec) of the NGC 5208 1.28 mm continuum image. Contours are evenly spaced between the peak intensity of 1.27 ± 0.05 mJy beam^{-1} and 3 times the RMS noise. The synthesised beam is shown in the bottom-left corner as a black open ellipse.

Line emission

We created the cube as usual using the CASA task `uvcontsub` to subtract the continuum and using the `tclean` task to clean the line emission to a threshold of 3 times the RMS noise of in the line-free channels of the dirty cube. For the imaging we adopt a Briggs weighing with a robust parameter of 0.5. Whilst a lower Briggs weighing might reduce our mean beam size by $\approx$ 0.1 arcsec in either direction, this still does not allow us to probe the centre of the galaxy in a way that would make a SMBH measurement possible. As such, the trade-off for signal-to-noise associated with a lower robust parameter is not

Table 3.6: CO data cube properties for NGC 5208.

Image property	Value
Spatial extent (pix)	256×256
Spatial extent (arcsec)	51.2×51.2
Spatial extent (kpc)	26×26
Pixel scale (arcsec pix^{-1})	0.20
Pixel scale (pc pix^{-1})	101.8
Velocity range (km s^{-1})	6150 – 7200
Channel width (km s^{-1})	10
RMS noise (mJy beam^{-1} channel^{-1})	1.05
Number of constraints	48, 123
Synthesised beam (arcsec)	0.84×0.75
Synthesised beam (pc)	428×382

worth it. We adopted the usual channel width of 10 km s^{-1}. The resulting data cube has a synthesised beam of 0.84 arcsec × 0.75 arcsec (428×382 pc^2) with a RMS noise of 0.64 mJy beam^{-1} channel^{-1}, and its properties are summarised in Table 3.6.

The moment map mask was created as before, using the usual boxcar kernel in both spatial and spectral dimensions and clipping the smoothed data cube to a threshold of 5 times the RMS. This mask is then applied to the unsmoothed primary beam-corrected data cube. The moment maps show a disc of molecular gas, about ≈ 26 arcsec across, in regular rotation and coincident with the dust disc (see Fig. 3.9). As can be seen in Fig. 3.11, the observed $\sigma_{\rm gas}$ is dynamically cold (< 30 km s^{-1}) along the outer edges, but rises to about ≈ 70 km s^{-1} in the centre, however this is likely dominated by beam smearing. We also detect a prominent depression in the molecular gas, about ≈ 3 arcsec in radius. This depression is ≈ 4 times larger than the beam size, suggesting that it's a real depression and not just a poorly resolved hole. Likewise, the depression is far larger than the predicted radius of the SMBH sphere of influence, and thus does not allow for the potential to be probed. Consequently no Keplerian rise is present within $R_{\rm SoI}$. As for NGC 0665, it is unlikely that we will be able to obtain a robust SMBH mass, but an upper limit can be placed nonetheless. We also created a kinematic PVD by taking a 5-pixel wide cut through the masked data cube along the dynamically-determined position angle of 344.°1. The resulting moment maps and PVD are shown in Fig. 3.11.

In Fig. 3.12 we can see the integrated ^{12}CO(2–1) spectrum of NGC 5208 with the classic well-defined double-horn shape of a rotating disc. This spectrum was extracted from a

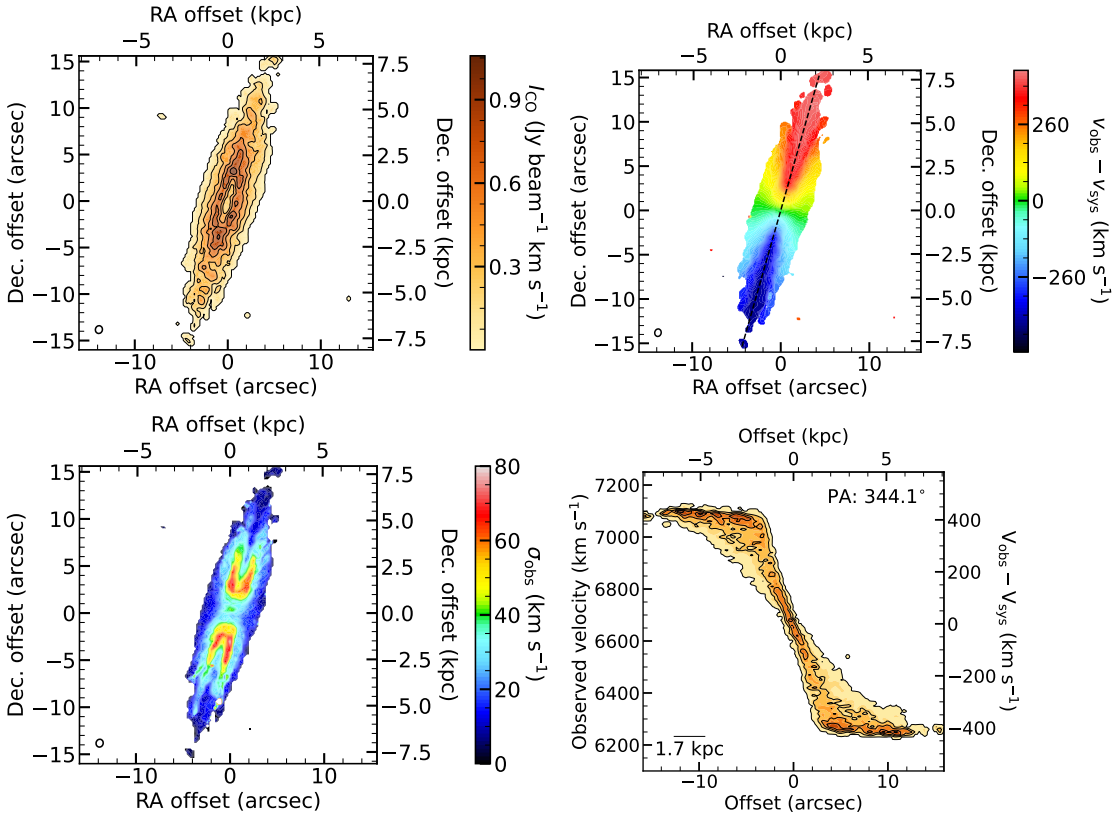


Figure 3.11: As Fig. 2.29 but for NGC 5208.

32 arcsec × 32 arcsec (≈ 16300 × 16300 pc^2) region around the centre with an integrated FWZI flux density of 60.7 ± 2.1 Jy km s^{-1}. Figure 3.12 also shows the integrated spectrum of the ^{12}CO(2–1) (grey shading) and ^{12}CO(1–0) (black dashed line) lines obtained from the IRAM single-dish 30-m telescope observations reported by Davis et al. (2015). As with NGC 0665, the 30-m ^{12}CO(2–1) spectrum does not display a pronounced double horned profile. Given the large extent of the galaxy, this is also most likely because the ≈ 11 arcsec primary beam cannot fully capture the total extent of the molecular gas disc. In contrast, the 30-m ^{12}CO(1–0) spectrum, with a primary beam of ≈ 22 arcsec, is able to capture some of the double horned profile of a rotating disc.

3.3.3 CO modelling

Model parameters

NGC 5208 has a simple and well-behaved molecular gas distribution. As such, we choose to model its gas distribution using a parametric function. Since the galaxy has a depression

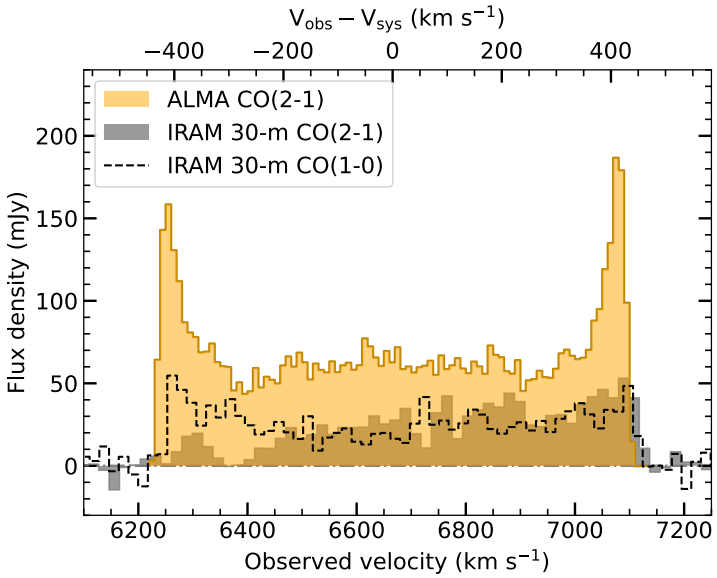


Figure 3.12: ^{12}CO(2–1) integrated spectrum of NGC 5208 derived from our ALMA data (orange shading), overlaid on the IRAM 30-m telescope ^{12}CO(2–1) (grey shading) and ^{12}CO(1–0) (black dashed line) observations of Davis et al. (2015). The ALMA aperture is a 32 arcsec × 32 arcsec ($\approx 16300 \times 16300$ pc^2) region centred on the galaxy centre, that includes all detected emission.

rather than an outright hole, we initially tested profiles which included a gradual decrease towards the centre. We tested an intrinsic Gaussian profile along the galaxy radius as well as an exponential profile which truncates and continues as a Gaussian function towards the centre. Neither model produced satisfactory results and converged fully, likely due to the large number of free model parameters. However in both cases it was clear that the best-fitting models preferred a very sparse gas distribution in the centre. Owing to this we decided to also test models with central cutoffs. Ultimately, the best fitting model was obtained with a 2D axisymmetric exponential surface density profile with an inner truncation at the edge of the central depression as described by Equation 2.2 in Section 2.2.1.

We obtain a stellar light distribution for NGC 5208 as usual, using an MGE model of a *HST* WFC3 image in the F160W filter (*H*-band) (GO-15909, PI: Boizelle) with a total exposure time of 997 s. We convert this stellar light distribution into luminosities in the AB magnitude system by adopting a zero-point of 25.94 mag (Sahu et al. 2021), a Solar absolute magnitude of 4.60 mag for the F110W filter (Willmer 2018) and a galactic extinction of 0.018 mag from NED (Schlafly & Finkbeiner 2011).

As shown in Fig. 3.13, there is significant dust extinction to the west of the NGC 5208 nucleus. To reduce their impact, the dust lanes were masked in our MGE model. The

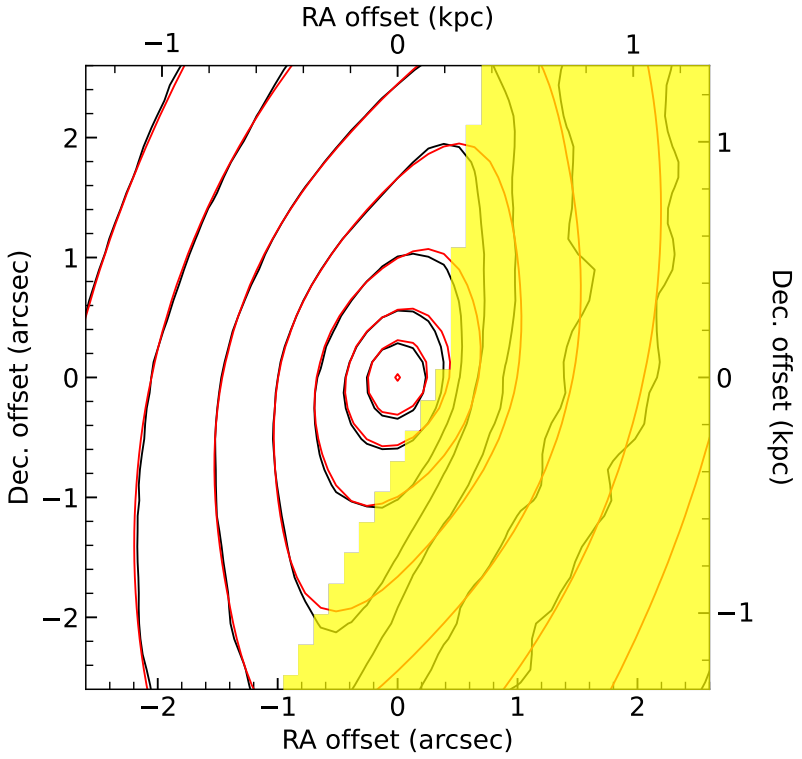


Figure 3.13: *HST* WFC3 F160W filter image of NGC 5208 (black contours), overlaid with our best-fitting MGE model (red contours). The western side of the image is masked (yellow shading), to exclude the most obviously dust-obscured pixels along the near side of the embedded disc.

resulting MGE model is clearly a good fit, especially in the very centre of the image, the region that matters most to constrain the SMBH mass.

Results

A constant M/L ratio failed to fit the galaxy well, especially in its central regions. Therefore, we allowed for the M/L ratio to vary linearly with galaxy radius (as defined in Section 2.2.1 as a part of our model. The final MCMC chain had a 300,000 steps. We are unable to confirm the presence of a central dark object nor constrain its mass, likely due to the extensive hole/depression in the centre of the galaxy and the subsequent lack of a Keplerian rise in the PVD. We are able to obtain an upper limit on the SMBH mass of $< 3.03 \times 10^9$ $M_\odot$ at the 3σ confidence level and a best-fitting M/L in the F160W filter represented by $(M/L_{\mathrm{F160W}})\,/\,(M_\odot/L_{\odot,\mathrm{F160W}}) = 1.42^{+0.08}_{-0.09} - 0.04^{+0.01}_{-0.01}\ (R/\mathrm{arcsec})$. Figure 3.14 shows the degeneracy between M/L intercept and M/L gradient, as is expected in models

Table 3.7: Parameters of the deconvolved best-fitting MGE components of our model of NGC 5208.

$I'_{\odot}$ ($L_{\odot,F160W}$ pc^{-2}) (1)	σ' (arcsec) (2)	q' (3)
46042	0.130	0.850
32102	0.333	0.652
7791	0.800	0.830
7771	1.683	0.255
5102	2.204	0.563
1775	5.198	0.460
509	6.850	0.573
1479	8.182	0.200
350	14.435	0.313
89	16.842	0.568
69	27.981	0.253
26	34.559	0.415

Notes. Deconvolved MGE components. (1) Central surface brightness of Gaussian component. (2) Standard deviation of Gaussian component. (3) Axial ratio of Gaussian component.

Table 3.8: Best-fitting model parameters of NGC 5208 and associated uncertainties.

Parameter	Prior			Best fit	1σ uncertainty	3σ uncertainty
Mass model						
$\log(M_{BH}/M_{\odot})$	5	→	11	–	–	< 9.482
Stellar M/L intercept	0.0	→	5.0	1.42	±0.03	−0.09, +0.08
Stellar M/L gradient	−1.0	→	1.0	0.04	±0.003	±0.01
Molecular gas disc						
Velocity dispersion (km s^{-1})	0.0	→	50.0	10.5	−1.2, 1.4	−3.3, +3.9
Scale length (arcsec)	0.0	→	7.0	5.05	−0.24, +0.26	−0.61, +0.73
R_{hole} (arcsec)	0.0	→	5.0	2.99	−0.15, +0.14	−0.46, +0.40
Integrated intensity (Jy km s^{-1})	0.0	→	150.0	64.7	±2.7	−6.9, +7.8
Nuisance parameters						
Centre RA offset (arcsec)	−12.5	→	12.5	−0.20	±0.02	−0.06, +0.07
Centre Dec offset (arcsec)	−12.5	→	12.5	−0.81	±0.04	±0.11
Inclination (°)	0.0	→	89.9	80.8	±0.2	±0.6
Position angle (°)	0.0	→	359.9	344.1	±0.2	±0.5
Systematic velocity (km s^{-1})	6200	→	7000	6665.9	±1.2	−3.5, +3.3

Notes. The RA and Dec. offsets are measured with respect to the image phase centre, $13^{h}32^{m}27.^{s}916$, $+07°18'59.''810$ (J2000.0). The M/L and M/L intercept are expressed in units $M_{\odot}/L_{\odot,F160W}$ and the M/L gradient is expressed in units $M_{\odot}/L_{\odot,F160W}$ arcsec^{-1}.

with a linearly-varying M/L.

As before, the quality of our fit is easiest to judge by overlaying models over the kinematic major-axis PVD. From left to right in Fig. 3.15 we overlay the best-fitting model with no SMBH, a SMBH at the 3σ upper threshold, and an overly-massive SMBH ($\approx$ 0.8 dex above the 3σ threshold), respectively, allowing all parameters other than the SMBH mass

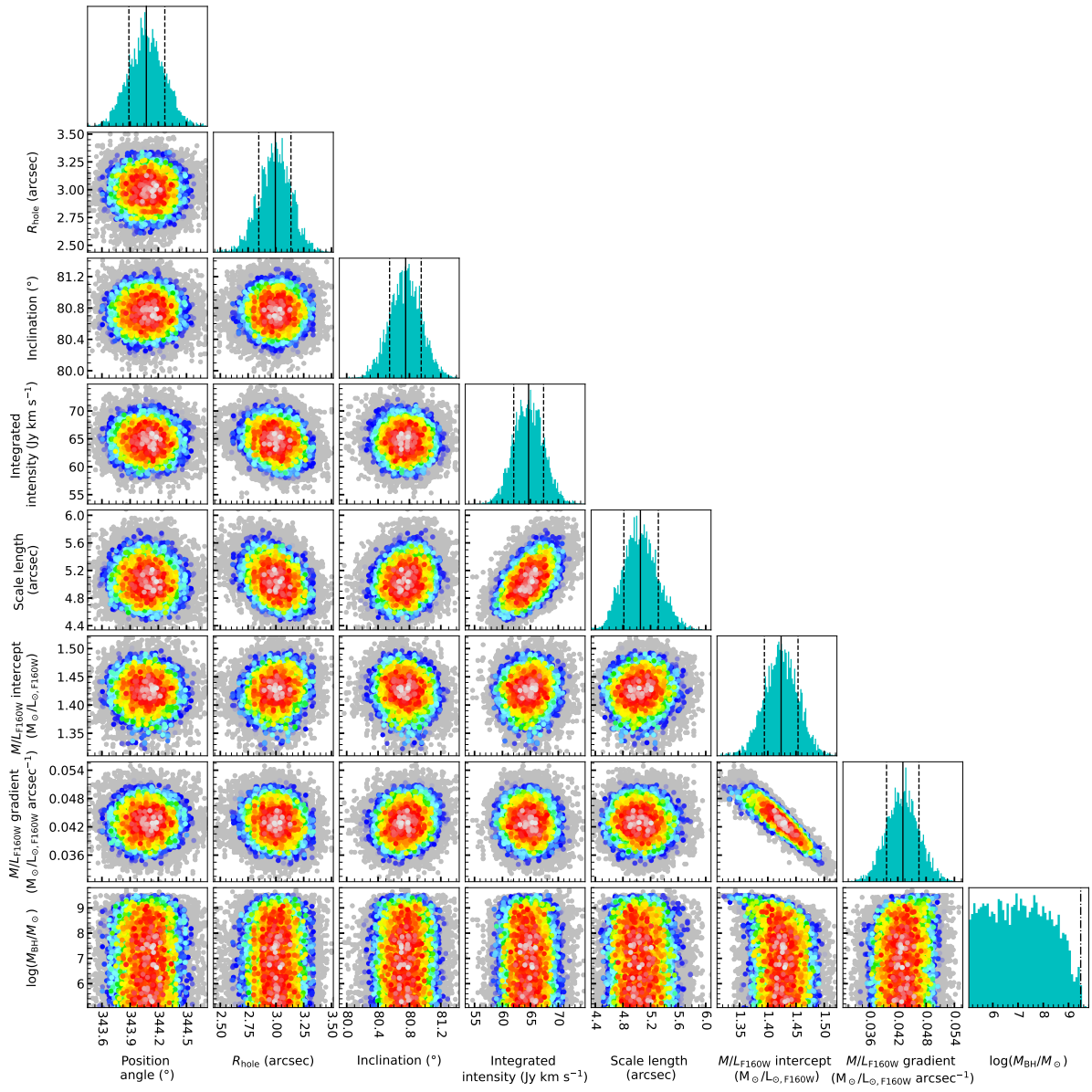


Figure 3.14: As Fig. 2.5, but for the best-fitting model for NGC 5208. The dot-dashed line over the 1D marginalised posterior distribution of the SMBH mass represents the 99.7% confidence interval.

to vary in the first and third case. Contrary to NGC 0665, none of the fit parameters in NGC 5208 appear to be strongly correlated with SMBH mass. Therefore, for the middle panel of Fig. 3.15 we create a model with the SMBH mass at the 3σ upper limit, as the posterior distribution in Fig. 3.14 suggests that the overall best-fitting M/L would also be the best-fitting M/L for a model in which $M_{\rm BH}$ is fixed at its upper limit. Of course, there does appear to be a mild anti-correlation between $M/L_{\rm intercept}$ and SMBH mass at the high-mass end, but not in a way that would significantly affect the model.

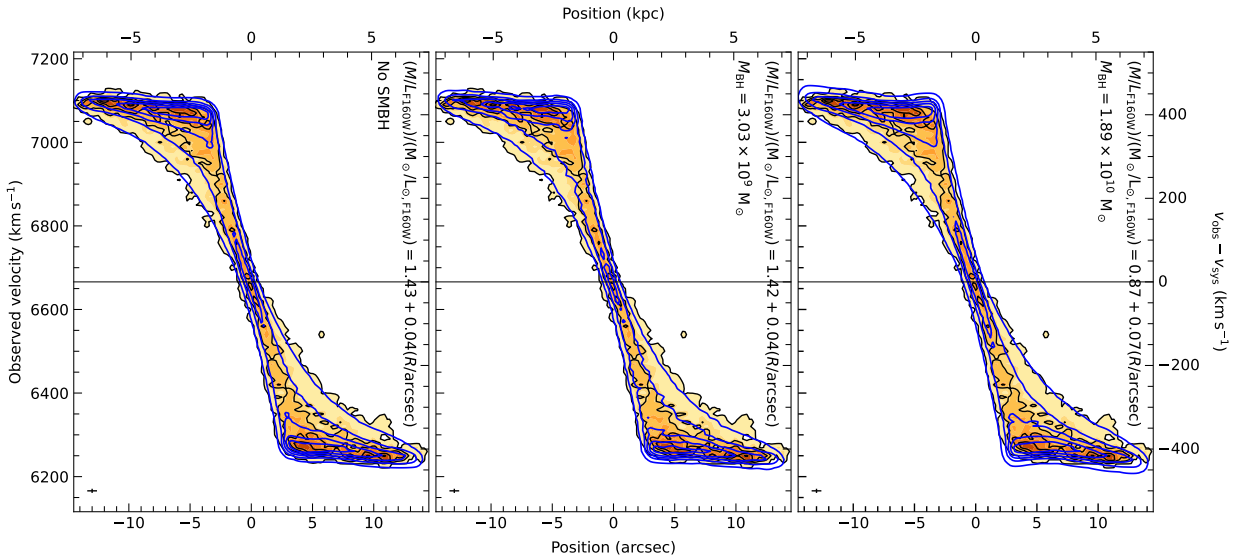


Figure 3.15: As Fig. 2.6, but for NGC 5208.

The fits of the first two panels of Fig. 3.15 are almost indistinguishable with near-identical M/L intercepts and gradients, as expected. The third panel showing the overly-massive SMBH provides a noticeably worse fit in the central parts of the galaxy. As expected, the model has a significantly smaller M/L intercept in order to compensate for the over-massive SMBH in the centre, however in order to fit the outer parts of the galaxy this leads to a greater M/L gradient. Whilst this gradient results in a good fit in the middle parts of the galaxy, it is clear that at the outer edges of the galaxy the model starts overshooting and providing a noticeably worse fit. It's however worth noting that despite a ≈ 0.8 dex more massive SMBH, the effects of the larger SMBH are not significantly pronounced due to the incredibly large depression in the centre of the galaxy.

In Fig. 3.16 we can see a comparison between a model with a radially-constant M/L and our best-fit model with a linearly-varying M/L, clearly the later being a far better fit. There is evidence from stellar-population analyses suggesting that the centres of massive ETGs often host bottom-heavy IMFs, which would increase the central stellar M/L and typically imply a radially decreasing M/L profile (e.g. La Barbera et al. 2016; van Dokkum et al. 2017; Ge et al. 2021b), apparently at odds with our result. However, it is important to stress that our M/L is dynamically determined and therefore represents an effective conversion between light and enclosed mass. It can be influenced not only by IMF variations but also

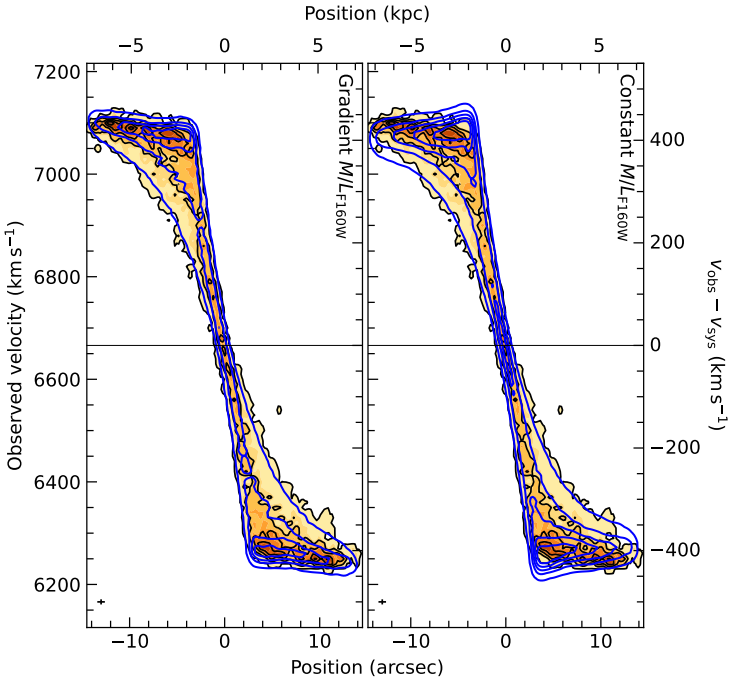


Figure 3.16: As Fig. 2.6, but for but for the best-fitting model with a SMBH and a linearly-varying M/L (left) and best-fitting model with a SMBH and a constant M/L (right), respectively.

by age/metallicity gradients and dust-related systematics in the underlying light model (see Section 2.5.4. Studies that directly infer M/L gradients from dynamical modelling find both positive and negative gradients across ETG samples (Davis & McDermid 2017). We therefore treat the inferred M/L gradient primarily as capturing modest radial changes in the stellar mass distribution, as required by the gas kinematics, rather than as a definitive measurement of the IMF gradient in this system.

Figure 3.17 shows the cumulative mass distribution of NGC 5208, assuming a SMBH at the 3σ upper threshold. The truncation radius of the central depression $R_{\rm hole} = 2.99^{+0.40}_{-0.46}$ arcsec extends far beyond the boundaries of the plot and is far greater than synthesised beam size, indicating that the depression is real. Using the standard definition of the SMBH sphere of influence and our 3σ SMBH mass upper-limit yields a maximal $R_{\rm SoI} \approx 236$ pc (≈ 0.46 arcsec). From Fig. 3.17, $R_{\rm eq} \approx 160$ pc (≈ 0.32 arcsec). Both $R_{\rm SoI}$ and $R_{\rm eq}$ are far smaller than the synthesised beam size, indicating that the SMBH SoI was never probed with our ALMA measurements. In fact only ≈ 21 per cent of the enclosed mass at $R_{\rm beam}$ is due to the SMBH, highlighting the inadequate resolution of the ALMA data. However, due to

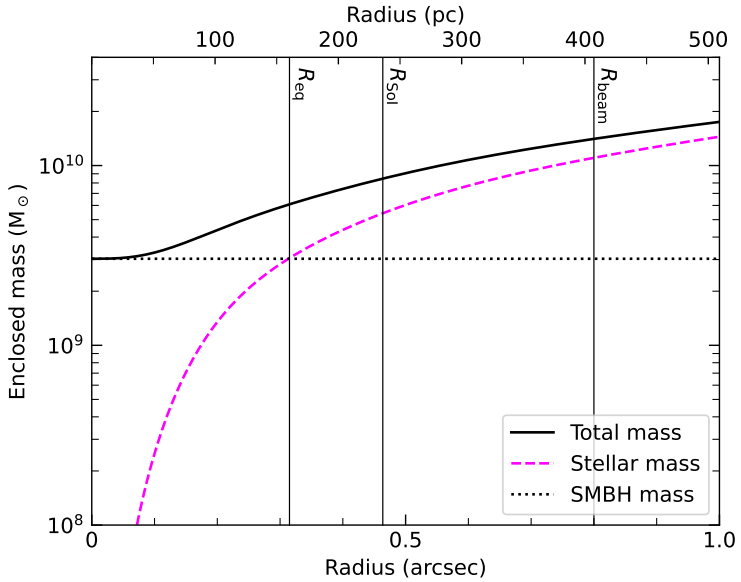


Figure 3.17: As Fig. 2.8, but for NGC 5208 (assuming σ_e = 235 km s^{-1} and our 3σ SMBH mass upper limit).

the enormous size of the hole, only ≈ 5 per cent of the enclosed mass at R_{hole} is due to the SMBH. This is the clear reason why we are unable to see a Keplerian rise of the rotation velocities near the galaxy centre or determine the SMBH mass of NGC 5208. Due to this hole, NGC 5208 is not a good candidate for obtaining higher-resolution data, as it is incredibly unlikely that an improved beam size would yield better constraints on the SMBH mass.

3.4 NGC 0467

3.4.1 Galaxy Properties

NGC 0467 is a S0 lenticular galaxy located at $01^h19^m10\overset{s}{.}13$, $+03°18'03\overset{''}{.}0$ (J2000.0) in the constellation of Pisces. We adopt the distance used in the MASSIVE survey, D = 75.8 Mpc, which is a redshift distance based on radial velocities corrected with a flow model (Ma et al. 2014). At this distance, 1 arcsec corresponds to ≈ 368 pc. According to 2MRS (Crook et al. 2007), NGC 0467 is an isolated system with no major companions within its local environment.

There are no *HST* images of NGC 0467 available. As such, we are unable to inspect the dust lanes or any other complex features of NGC 0467. Instead, in Fig. 3.18, we can see a *Canada-France-Hawaii Telescope* (*CFHT*) Wide-field InfraRed Camera (WIRCam) K_s-band optical image which exhibits a smooth and centrally concentrated stellar light distribution

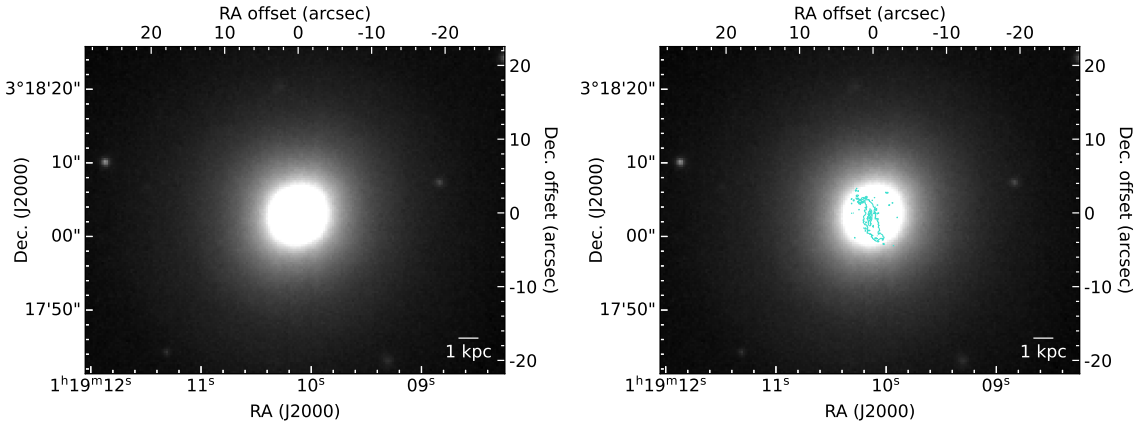


Figure 3.18: Unsharp-masked *CFHT* WIRCam K_s-band image of NGC 0467 (left) overlaid with with the ^{12}CO(2–1) integrated intensity contours (cyan) from our ALMA observations (right).

typical of an early-type system. The galaxy shows a bright, nearly circular core with a steep radial decline in surface brightness and no evidence of spiral features, dust lanes, or other substructure. There are some faint background sources visible in the surrounding field.

NGC 0467 has a moderate molecular gas reservoir, with a total H_2 mass of $(5.87 \pm 1.06) \times 10^8$ $M_\odot$ (Davis et al. 2019). It has an integrated absolute K-band magnitude of -25.76 (Quenneville et al. 2023) corresponding to a total stellar mass of 6.23×10^{11} $M_\odot$, calculated as before.

NGC 0467 does not have a direct SMBH mass measurement, but an estimate can be obtained using the $M_{\rm BH} - \sigma_{\rm e}$ relation of van den Bosch (2016). Assuming $\sigma_{\rm e} = 247$ km s^{-1} (Davis et al. 2019) and the $M_{\rm BH} - \sigma_{\rm e}$ relation of van den Bosch (2016), a SMBH mass of $\approx 6.5 \times 10^8$ $M_\odot$ is expected. Calculating $R_{\rm SoI}$ in the usual manner we get an estimated $R_{\rm SoI} \approx 46$ pc (≈ 0.12 arcsec).

3.4.2 ALMA observations

Observations of the ^{12}CO(2–1) emission line using Band 6 of the 12-m ALMA array were obtained as part of project 2019.1.00657.S (PI: Davis). The properties of the observations are listed in Table 1.2. The NGC 0467 data are compromised of two tracks that were taken on the 2019 October 13 and 2021 July 18, for a total of 48 minutes on source. Baselines span from 15.1 m to 3.7 km, yielding an angular sensitivity of 0.09 arcsec, a maximum recoverable scale of 5.9 arcsec, and a field of view of 24.8 arcsec. Both tracks had four spectral windows

Table 3.9: Parameters of the NGC 0467 continuum image and the detected cleaned continuum source.

Image property	Value
Image (pix)	1024×1024
Image (arcsec)	25.6×25.6
Image size (kpc)	9.4×9.4
Pixel scale (arcsec pix^{-1})	0.025
Pixel scale (pc pix^{-1})	9.2
RMS noise (mJy beam^{-1})	0.02
Synthesised beam (arcsec)	0.11×0.10
Synthesised beam (pc)	40×37
Source property	**Value**
Right ascension (J2000)	$01^{h}19^{m}10\overset{s}{.}1447 \pm 0\overset{s}{.}0004$
Declination (J2000)	$+03°18'02\overset{''}{.}634 \pm 0\overset{''}{.}003$
Integrated flux (μJy)	260 ± 32
Deconvolved size (marcsec)	$(111 \pm 22) \times (32 \pm 17)$
Deconvolved size (pc)	$(41 \pm 8) \times (12 \pm 6)$

with the same setup. One window in each track was used to map the molecular gas and was centred on the redshifted frequency of the ^{12}CO(2–1) line, 227.326512 GHz and 227.348863 respectively. This spectral window, with a bandwidth of 1.875 GHz ($\approx$ 2440 km s^{-1}), was subdivided into 1920 channels of width 977 kHz ($\approx$ 1.27 km s^{-1}). The remaining three spectral windows were used to map the continuum. One of these spectral windows also had a bandwidth of 1.875 GHz ($\approx$ 2440 km s^{-1}) and was subdivided into 1920 channels of width 977 kHz ($\approx$ 1.27 km s^{-1}). The other two spectral windows had a bandwidth of 2 GHz ($\approx$ 2600 km s^{-1}) subdivided into 128 channels of width 16 MHz ($\approx$ 16 km s^{-1}).

Continuum emission

An image of the NGC 0467 continuum was created as usual and cleaned with the CASA task `tclean`. We cleaned to a threshold of 2 times the RMS noise of the dirty continuum, measured away from the source. Using the multi-frequency synthesis mode with Briggs weighting with robust parameter 0.5 we image a continuum with a central frequency of 235.3 GHz (1.27 mm). We detect a central source of continuum emission with an integrated flux density of 260 ± 32 μJy and a peak intensity of 190 ± 14 μJy beam^{-1}. The continuum was then fit using the CASA task `imfit` which reveals a spatially-resolved source with deconvolved FWHM of $(111 \pm 22) \times (32 \pm 17)$ marcsec^2. The continuum image is shown in Fig. 3.19 and its properties are listed in Table 3.9.

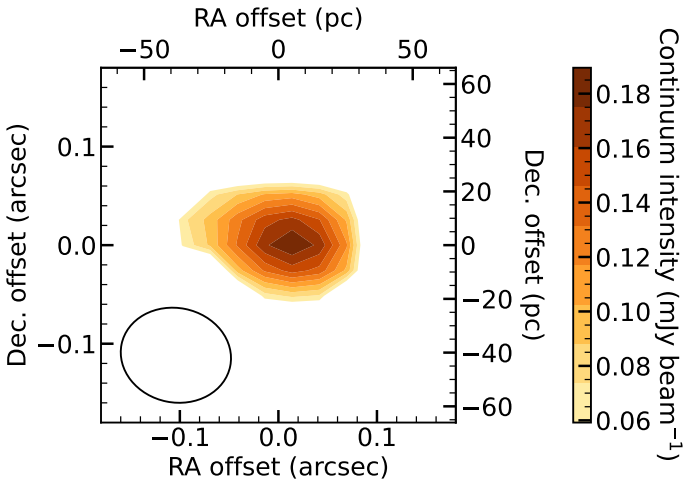


Figure 3.19: Central region (0.36 arcsec × 0.36 arcsec) of the NGC 0467 1.27 mm continuum image. Contours are evenly spaced between the peak intensity of 190 ± 14 μJy beam^{-1} and 3 times the RMS noise. The synthesised beam is shown in the bottom-left corner as a black open ellipse.

Table 3.10: CO data cube properties for NGC 0467.

Image property	Value
Spatial extent (pix)	1024×1024
Spatial extent (arcsec)	25.6×25.6
Spatial extent (kpc)	9.4×9.4
Pixel scale (arcsec pix^{-1})	0.025
Pixel scale (pc pix^{-1})	9.2
Velocity range (km s^{-1})	4920 – 5780
Channel width (km s^{-1})	20
RMS noise (mJy beam^{-1} channel^{-1})	0.22
Number of constraints	69, 048
Synthesised beam (arcsec)	0.12×0.10
Synthesised beam (pc)	45×38

Line emission

We created the cube in the usual manner, first subtracting the continuum using the CASA task `uvcontsub`, and then by cleaning the line emission to a threshold of 3 times the RMS noise of the channels free of emission using the CASA `tclean` task. We image the emission using the typical Briggs weighting with a robust parameter of 0.5. We adopted a channel width of 20 km s^{-1} in order to help us resolve some of the lower signal-to-noise and poorly defined outer regions of the molecular gas. The resulting data cube has a synthesised beam of 0.12 arcsec × 0.10 arcsec (45×38 pc^2) with a RMS noise of 0.22 mJy beam^{-1} channel^{-1}, and its properties are summarised in Table 3.10.

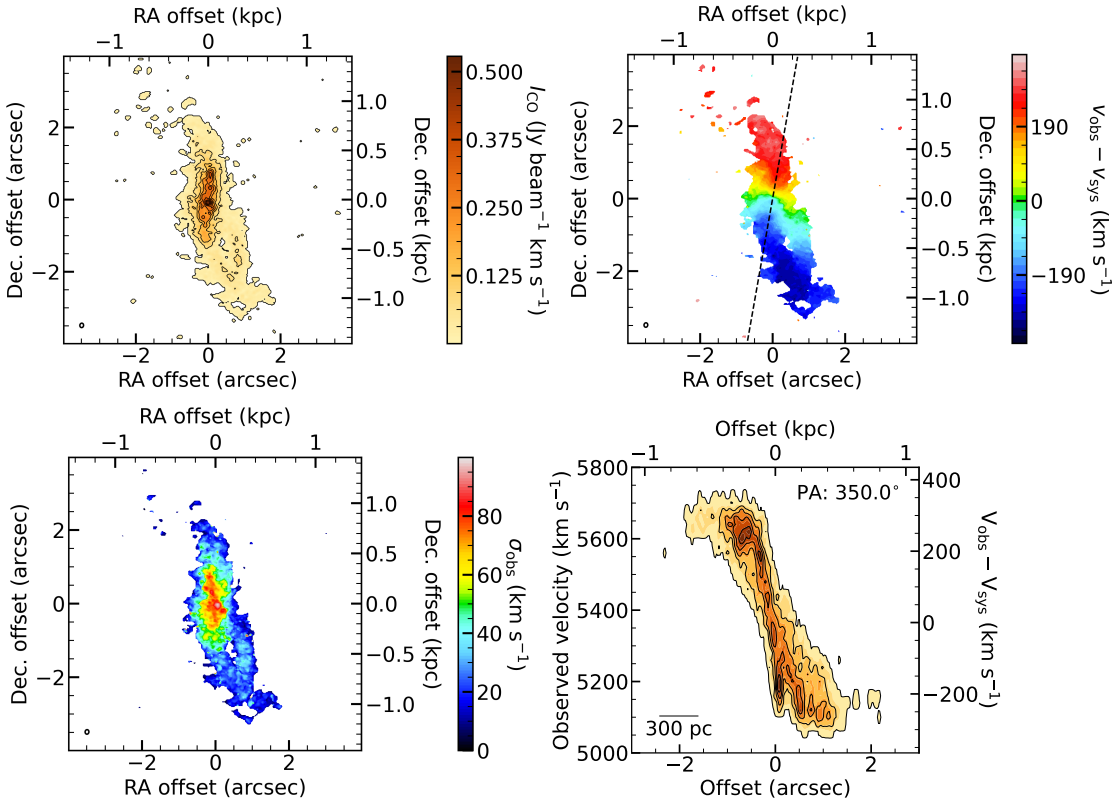


Figure 3.20: As Fig. 2.2 but for NGC 0467.

The moment map mask was created as usual, by clipping the smoothed data cube to a threshold of 5 times the RMS. As shown in Fig. 3.20 we clearly detect an asymmetric disc of molecular gas, about ≈ 6 arcsec across. The first-moment map suggests the presence of a position angle warp in the outer edges of the galaxy, however the centre of the galaxy does not seem to exhibit strong signs of a warp. The gas has a centralised region of higher velocity dispersion (≈ 60 – 90 km s^{-1}) extending around ≈ 2 arcsec across. The rest of the gas appears to be dynamically cold (< 30 km s^{-1}). The molecular gas extends within R_{SoI} all the way to the centre of the galaxy making it a a good candidate for the dynamical modelling of a SMBH mass. However, the lack of a high-resolution optical image means that we may not be able to accurately model the region within R_{SoI} despite the high-resolution ALMA data. We also created a kinematic PVD by taking a 5-pixel wide cut through the masked data cube along the position angle of 350.°0, determined by eye, which represents the position angle in the central parts of the galaxy. The PVD in Fig. 3.20 shows a clear enhancement of velocities on the blue-shifted side of the galaxy, possibly as a result of a SMBH.

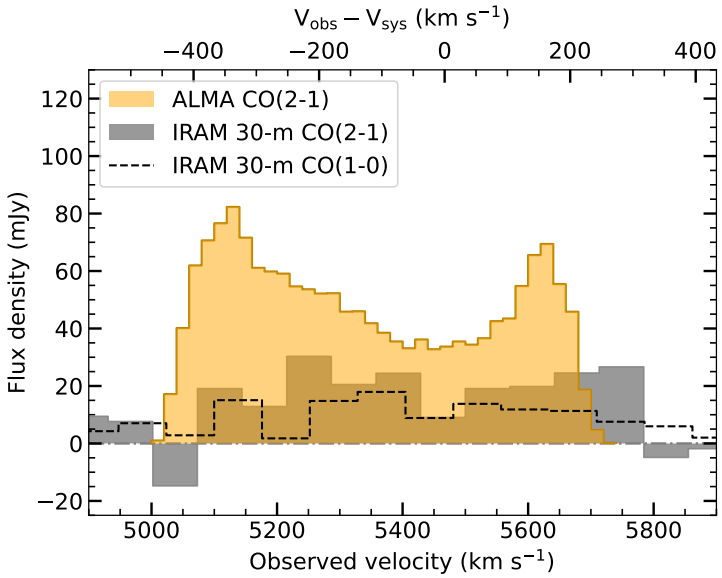


Figure 3.21: ^{12}CO(2–1) integrated spectrum of NGC 0467 derived from our ALMA data (orange shading), overlaid on the IRAM 30-m telescope ^{12}CO(2–1) (grey shading) and ^{12}CO(1–0) (black dashed line) observations of Davis et al. (2015). The ALMA aperture is a 8 arcsec × 8 arcsec ($\approx 2940 \times 2940$ pc^2) region centred on the galaxy centre, that includes all detected emission.

In Fig. 3.21 we can see the integrated ^{12}CO(2–1) spectrum of NGC 0467 with the classic double-horn shape of a rotating disc. This spectrum was extracted from a 8 arcsec × 8 arcsec ($\approx$ 2940 × 2940 pc^2) region around the centre with an integrated FWZI flux density of 33.3 ± 1.5 Jy km s^{-1}. Figure 3.21 also shows the integrated spectrum of the ^{12}CO(2–1) (grey shading) and ^{12}CO(1–0) (black dashed line) lines obtained from the IRAM single-dish 30-m telescope observations reported by Davis et al. (2015). It is clear that both 30-m ^{12}CO(2–1) and ^{12}CO(1–0) spectra do not effectively capture the double-horned profile seen with ALMA, despite the source lying well within the single-dish primary beams. It is unclear why this is the case, however it could be in part due to the coarser spectral sampling of the single-dish observations or a pointing/centering offset.

3.4.3 CO modelling

Model parameters

As mentioned in Section 3.4.1, there are no *HST* images of NGC 0467 available in any band. As such, we are forced to rely on a *CFHT* image to conduct our MGE modelling. The *CFHT* image has a pixel scale of 0.3 arcsec pix^{-1} compared to, for example, the 1.0 arcsec pix^{-1} pixel scale of a 2MASS image. Whilst the *CFHT* image offers a great improvement in

resolution compared to 2MASS, the pixel scale is still ≈ 3 times larger than the typical pixel scale of a *HST* image. Given that the expected $R_{\rm SoI}$ of NGC 0467 is ≈ 0.12 arcsec, the inner component of our MGE will not be resolved within the SoI and as such this makes obtaining a SMBH mass difficult, despite the adequate molecular gas distribution quality. Nevertheless, we attempt the modelling with the *CFHT* image.

The *CFHT* image used for the MGE model is a small K_s-band cutout extracted from a fully reduced WIRCam mosaic, previously used in Quenneville et al. (2023). Starting from raw WIRCam exposures, the data are first detrended using the IDL Interpretor of WIRCam Images ('I'iwi) processing pipeline, which flags saturated pixels, masks known bad pixels, as well as performs some initial sky subtraction. These detrended exposures are then passed to the WIRwolf image stacking pipeline (Gwyn 2014) which uses SWarp (Bertin et al. 2002) to stack and then resample the individual frames onto a common 0.3 arcsec pix^{-1} grid. The final image is an Image Reduction and Analysis Facility (IRAF) cutout of the resulting WIRwolf stack, with dimensions 273 × 273 pixels^2 (81 × 81 arcsec^2).

Typically WIRwolf also performs a photometric calibration against 2MASS stars before the resampling, however given that we are using a cutout of the parent mosaic, this information is not present in the image header. Instead, we perform our own photometric calibration of the image, in two steps. Firstly, we perform a stellar photometric calibration by identifying a single bright, unsaturated star in the image that has high-quality photometry in all three 2MASS bands (JHK_s; `ph_qual` keyword in the 2MASS Point Source Catalog listed as "AAA", indicating scan signal-to-noise ratios of ≥ 10 in all three bands). We use this star's catalogued 2MASS K_s-band magnitude of 12.622 mag as the reference "true" magnitude. We then measure the instrumental flux of the star in the *CFHT* image within a circular aperture with a radius of 10 pixels (3.0 arcsec) and subtract from this the local background, as measured in a concentric annulus extending from 15 to 20 pixels in radius i.e. from 4.5 to 6.0 arcsec from the center of the star. Using this background-subtracted flux F_{CFHT} and the the exposure time $t_{\rm exp}$ we compute the instrumental magnitude $m_{\rm inst} = -2.5\log_{10}(F_{CFHT}/t_{\rm exp})$. From this we get a zero-point of 20.50 mag in the Vega magnitude system, calculated as $ZP = m_{K_s} - m_{\rm inst}$.

However, given that there is only a single high-quality star within the cutout image, this zero point can still be sensitive to details like aperture size, local background subtraction

and other random errors. Given this, we perform a second step of validating the calibration by matching the radial surface-brightness profile in our *CFHT* image to a corresponding 2MASS K_s-band image. We first obtained a 2MASS K_s-band image of NGC 0467 from the All-Sky Extended Source Catalog. We then background subtracted this image using a sky level of 440.6 counts, measured in the outer region of the image which is clearly free of any galaxies and stars. We determined the galactic centre by selecting the central and brightest pixel of the *CFHT* image and mapped this to the 2MASS frame, such that both images share the same centre in world coordinates. Around this common centre we constructed circular annuli in increments of 1 arcsec for both images, and measured the median count per pixel in each annulus for both images. This yielded one-dimensional radial intensity profiles $I(r)$ for both images, sampled at the same set of radii.

We then converted these radial profiles to surface brightness profiles $\mu(r)$ in units of mag arcsec^{-2}. In the case of the *CFHT* image we compute the surface brightness using the star-based zero-point determined in the previous step and a flux calculated by taking the pixel counts, turning them into a count rate using the exposure time and then dividing by the pixel area to get a flux per arcsec^2. We use a similar procedure for the 2MASS profile, instead using the zero-point from the image header (`MAGZP` keyword) and the 2MASS pixel scale. To avoid PSF-dominated differences and central resolution issues at very small radii and low signal-to-noise effects at large radii, we restricted the comparison to the range $5 \leq r \leq 25$ arcsec. In this interval the offset between the surface brightnesses of the *CFHT* and the 2MASS images is approximately constant with an average $\langle \Delta\mu \rangle = -0.08 \pm 0.03$ mag (*CFHT* slightly brighter than 2MASS). We therefore applied this small correction to the star-based zero-point, adopting a final *CFHT* K_s zero-point of 20.57 mag.

As for the *HST* images used before, we parametrise the PSF by fitting a circularised MGE model to an image of the *CFHT* PSF, obtained from background stars. We obtain the stellar light distribution of NGC 0467 as usual, using an MGE model to fit the *CFHT* image. We convert this stellar light distribution in an analogous manner to before, however this time in the Vega magnitude system. We adopt the zero-point as calculated above, a Solar absolute magnitude in the 2MASS K_s-band of 3.27 mag (Willmer 2018), and a galactic extinction of 0.010 mag, calculated from the dust maps of Schlafly & Finkbeiner

Table 3.11: Parameters of the deconvolved best-fitting MGE components of our model of NGC 0467.

$I'_{\odot}$ ($L_{\odot,K_s}$ pc^{-2}) (1)	σ' (arcsec) (2)	q' (3)
153617	0.250	0.941
9723	0.960	0.941
4239	1.681	0.941
3009	2.963	0.941
2000	6.078	0.953
717	17.486	0.961

Notes. Deconvolved MGE components. (1) Central surface brightness of Gaussian component. (2) Standard deviation of Gaussian component. (3) Axial ratio of Gaussian component.

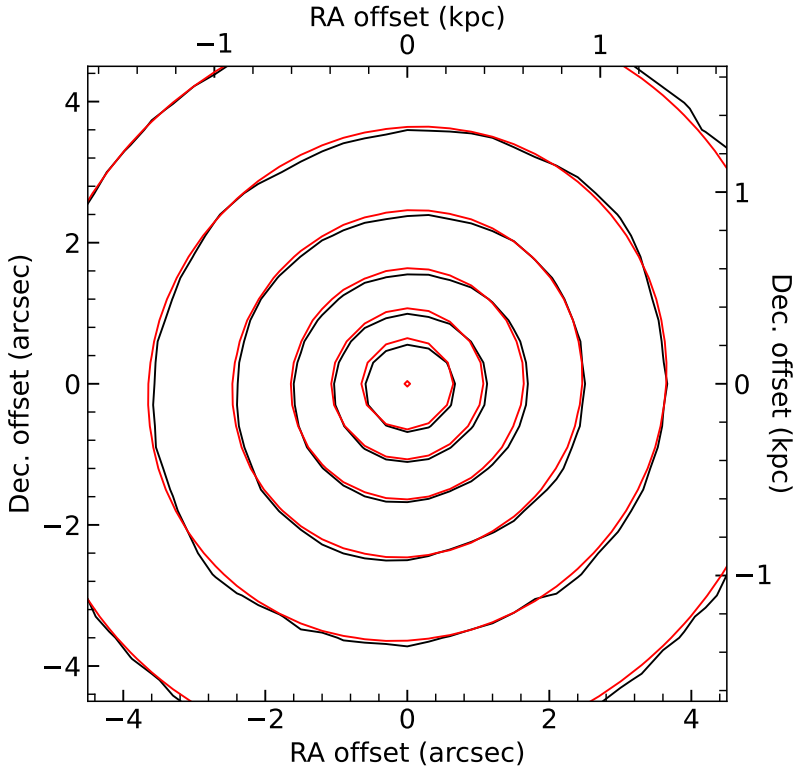


Figure 3.22: *CFHT* WIRCam K_s-band image of NGC 0467 (black contours), overlaid with our best-fitting MGE model (red contours).

(2011) taken from the NASA/IPAC Infrared Science Archive[1]. The resulting deconvolved best-fitting MGE components are listed in Table 3.11. As shown in Fig. 3.22 the resulting MGE is provides a good fit to the central region of the image.

Due to the unusual shape of the molecular gas disc in NGC 0467, we model the gas distribution using SkySampler. We sample the clean components using 5×10^6 particles.

[1] https://irsa.ipac.caltech.edu/applications/DUST/

We have also chosen to include a position angle warp in our model using the `linear` class of the `warp_funcs` module of `kinms_fitter`. This creates a warp that is linear with radius and optionally also flattens after some radius. Therefore, instead of a radially constant position angle, the position angle intercept i.e. the position angle at the centre of the galaxy, position angle warp and position angle cutoff are the three free parameters of the model. Due to these additional position angle parameters we have opted to fix the central position to that of the continuum emission, similarly to NGC 1387 and NGC 0665, in order to reduce the dimensionality of the model.

When modelling the entire extent of the galaxy, the SMBH mass remained poorly constrained, similarly to the case of NGC 0997. This is similarly likely to the relatively small amount of flux within $R_{\rm SoI}$ compared to that of the entire galaxy. We thus restricted the modelling to a 3 arcsec $\times$ 3 arcsec central area, where the effects of the SMBH mass are the largest.

Results

The final MCMC chain had 200, 000 steps. The best-fitting model parameters are shown in Table 3.12. Figure 3.23 shows the posterior probability distribution of each non-nuisance parameter, which appears to suggests that there is a dark object at the centre of NGC 0467, with a best-fitting mass of $2.39^{+1.56}_{-1.32} \times 10^8$ M$_\odot$ (3σ confidence level). The best-fitting M/L in the K_s-band is $0.44^{+0.12}_{-0.06}$ M$_\odot$/L$_{\odot,K_s}$. While the corner plot shows a well-defined posterior for the SMBH mass indicating a detection, we must inspect this result carefuly given the sub-optimal optical image. The results presented here are a "work in progress" and it is clear that the dynamical modelling of NGC 0467 necessitates further work in order to investigate whether our SMBH mass constraint is fully stable and whether the MGE model derived from the *CFHT* image is reliable. It is precisely because of this that we have opted to include our NGC 0467 results among SMBH mass upper limits of this chapter, as opposed to the robust SMBH mass determinations of Chapter 2. However, we highlight that our results indicate a detection nonetheless and not an upper limit.

Firstly, Fig. 3.23 suggests the presence of a warp, yielding a position angle profile of PA $= 324.^\circ2^{+15.0}_{-19.6} + 34.^\circ5^{+32.6}_{-19.4}(R/\text{arcsec})$ up to a cutoff radius of $R_{\rm cutoff} = 0.90^{+0.72}_{-0.27}$. However,

Table 3.12: Best-fitting model parameters of NGC 0467 and associated uncertainties.

Parameter	Prior			Best fit	1σ uncertainty	3σ uncertainty
Mass model						
$\log(M_{\rm BH}/{\rm M}_\odot)$	7	$\rightarrow$	11	8.38	$-0.10, +0.09$	$-0.35, +0.22$
Stellar M/L_{K_s} ($\rm M_\odot/L_{\odot,K_s}$)	0.0	$\rightarrow$	5.0	0.44	$-0.02, +0.03$	$-0.06, +0.12$
Molecular gas disc						
Velocity dispersion (km s^{-1})	0.0	$\rightarrow$	100.0	71.4	± 3.7	$-9.6, +10.7$
Integrated intensity (Jy km s^{-1})	0.0	$\rightarrow$	50.0	17.4	± 0.6	$-1.7, +1.8$
Nuisance parameters						
Inclination (degree)	50.0	$\rightarrow$	90.0	65.6	$-4.0, +5.2$	$-14.3, +8.4$
Position angle intercept (degree)	-180.0	$\rightarrow$	180.0	-35.8	$-6.8, +6.5$	$-19.6, +15.0$
Position angle gradient (degree)	0.0	$\rightarrow$	100.0	34.5	$-8.8, +10.5$	$-19.4, +32.6$
Position angle cutoff (arcsec)	0.0	$\rightarrow$	2.0	0.90	$-0.11, +0.16$	$-0.27, +0.72$
Systemic velocity (km s^{-1})	5000	$\rightarrow$	5600	5374.5	$-3.8, +4.3$	$-10.6, +11.6$

Note. The centre position is fixed to that of the unresolved continuum source, $01^{\rm h}19^{\rm m}10\overset{\rm s}{.}1447$, $+03°18'02\overset{''}{.}634$ (J2000.0).

it is clear that the confidence intervals on the $\rm PA_{intercept}$ and $\rm PA_{gradient}$ are incredibly broad and, as can be seen in Fig. 3.23, strongly degenerate with one another. Models with larger gradients can be compensated by shifting the inner PA such that the effective PA, where the majority of the flux which constrains the model lies, remains similar. It is clear from the data that a twist is present, however the detailed radial dependence of the position angle is weakly constrained. Similarly, when looking at the cutoff radius we can see that it is strongly correlated with the $\rm PA_{intercept}$ and strongly anti-correlated with the $\rm PA_{gradient}$. A cube with a steeper gradient and a smaller $R_{\rm cutoff}$ can resemble a cube with a shallower gradient extending to larger radii. These results simply confirm the presence of a warp but do not uniquely determine how this twist should be assigned between the slope, intercept, and cutoff radius. It is clear that the dynamical modelling of NGC 0467 would benefit from testing additional PA warp freedom, for example through a tilted-ring PA model, in order to determine if the PA truly flattens out, and if so, at what radius.

In Fig. 3.23 we can also see a very strong correlation between inclination and $\rm PA_{intercept}$ and a very strong anti-correlation between inclination and $\rm PA_{gradient}$. It is expected that inclination and PA are correlated in some way as they both describe the geometry of the molecular gas disc. Changing the inclination not only changes the amplitude of the line-of-sight velocities (through $\sin i$) but also the angular placement of those velocities,

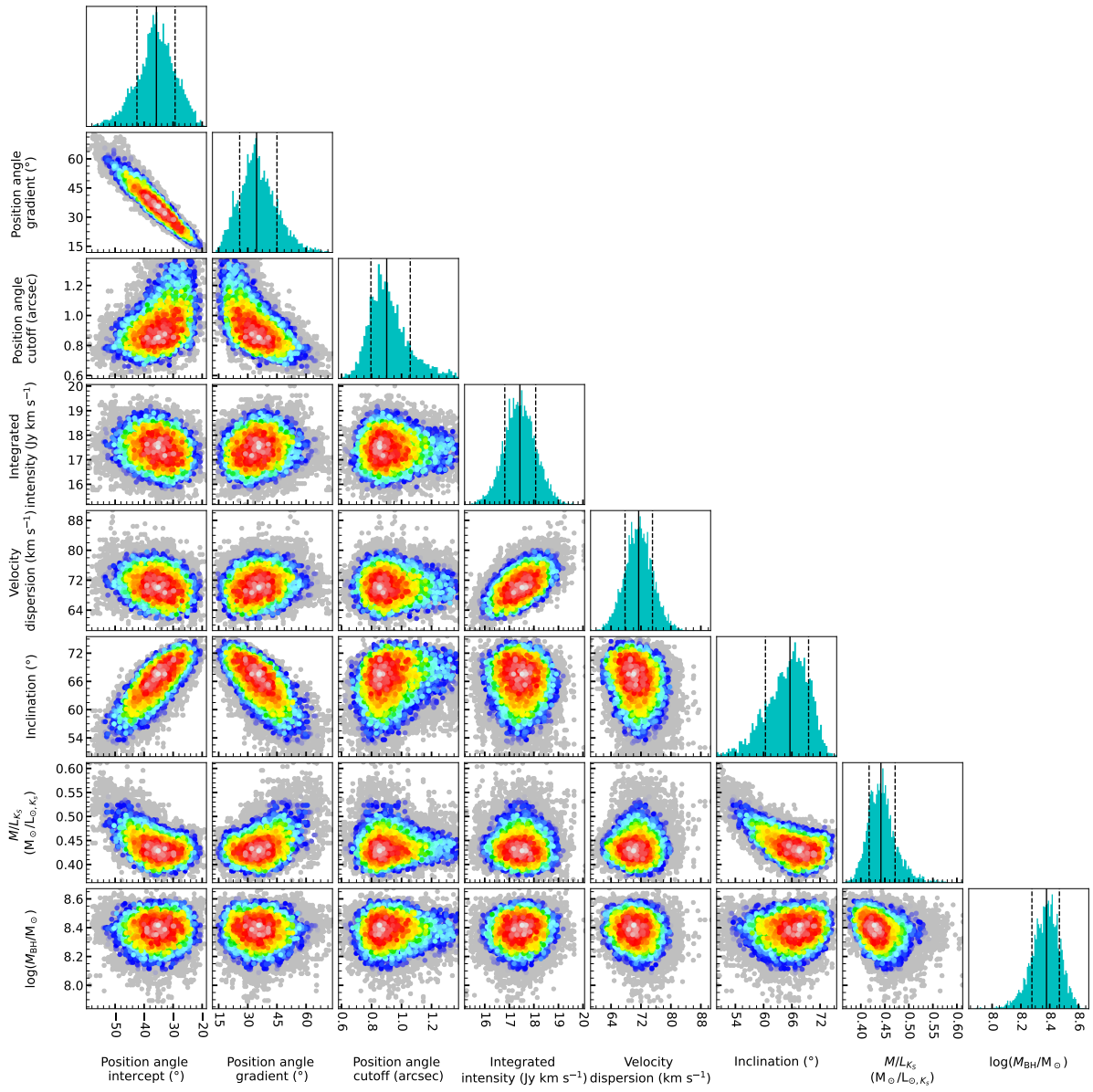


Figure 3.23: As Fig. 2.5, but for the best-fitting model for NGC 0467.

which themselves are described by the PA. The effect of this position angle and inclination dependence is intensified in the presence of a warp, where ultimately four parameters ($PA_{intercept}$, $PA_{gradient}$, R_{cutoff} and i) determine the disc geometry. It is likely that these issues are exacerbated by the fact that we are modelling only the inner 3 arcsec × 3 arcsec region of the galaxy, removing the information about the outer regions of the galaxy. These outer regions contribute significantly to the constraint of the molecular disc inclination as well as the determination of a stable R_{cutoff}. An approach that is likely to yield better results would be one where a two-step modelling approach, as in NGC 0997 or NGC 1387, is employed. In the

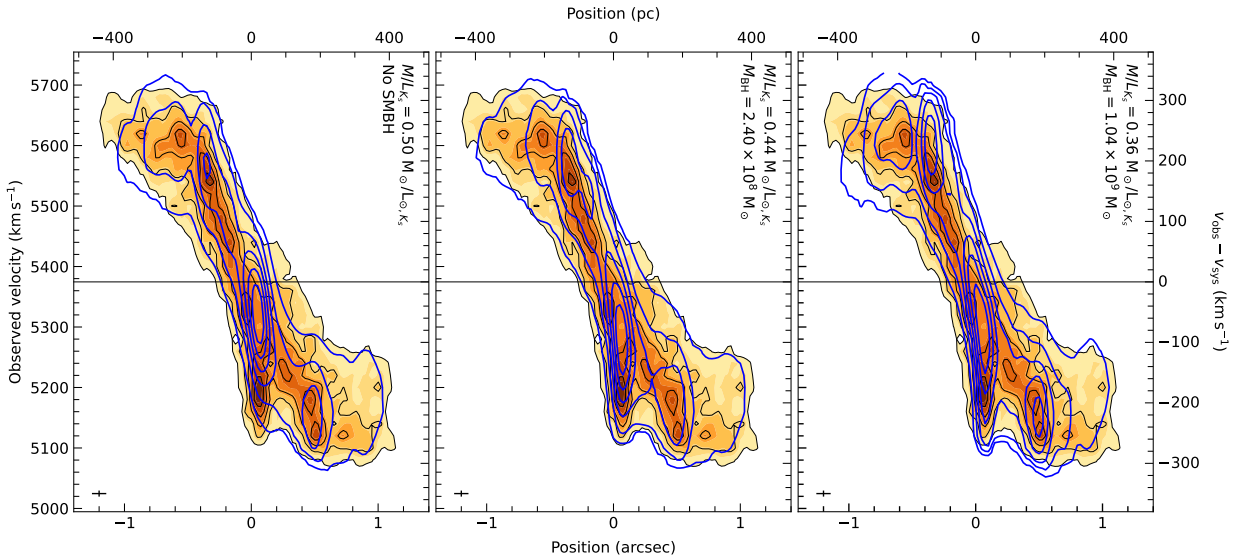


Figure 3.24: As Fig. 2.6, but for NGC 0467.

first step we would model the entire extent of the galaxy, obtaining a more-robust constraint on inclination and the PA profile. In the second step we would then fix these parameters from those of the previous modelling step (or use them as informative priors as in Section 2.6.3) whilst modelling only the central parts of the galaxy most affected by the SMBH. The prior determination of the innermost PA and inclination would also potentially enable us to focus on the central-most area of the galaxy which appears largely non-warped. The modelling of this region could simplify the model and eliminate some of the uncertainties.

In Fig. 3.24 we show our best-fit model, a model with no SMBH and a model with an overly-massive SMBH (≈ 0.7 dex larger than the best fit), where all other parameters are allowed to vary, overlaid over the kinematic major-axis PVD of the data. As can be seen the first panel, the model with no SMBH mass cannot capture the velocity enhancement seen on the blue-shifted side of the PVD despite the increased M/L, providing an overall poor fit. Similarly, the third panel with the overly massive SMBH overshoots the central velocities of the PVD as well as some of the velocities at larger radii, despite the smaller M/L. It is clear that the best-fitting model clearly fits the data best. However, it is also apparent that there is some complexity in the molecular gas distribution that is not fully captured by even the best-fitting model, such as the somewhat ill-fitting internal contours on the red-shifted side of the PVD. This mismatch of contours is likely due to the issues with the PA profile.

Table 3.13: χ^2 of the models discussed.

Model (1)	$\chi^2_{\rm red}$ (2)	k (3)	BIC (4)
Model with no SMBH and PA warp	3.94	8	824
Model with best-fitting SMBH and PA warp	3.76	9	800
Model with overly-massive SMBH and PA warp	3.96	9	839
Model with best-fitting SMBH and constant PA	3.95	7	814

Notes. (1) Model. (2) Reduced χ^2 statistic. (3) Number of free parameters. (4) Bayesian information criterion.

As discussed in Section 2.5.4, we can judge the goodness-of-fit of the model against the data through the use of BIC or the $\chi^2_{\rm red}$ statistic (since the model with no SMBH is nested within the model with a SMBH present). The results for the three models from Fig. 3.24 can be seen in Table 3.13. The model with the best-fitting SMBH mass clearly has the smallest $\chi^2_{\rm red}$ and smallest BIC. The difference in BIC between the best-fitting model and both other models is $\Delta_{\rm BIC} > 10$, which, following the interpretation of Kass & Raftery (1995), constitutes very strong evidence in favour of the best-fitting model. Nevertheless, the $\chi^2_{\rm red} = 3.76$ value of the best-fitting model is somewhat larger than expected and highlights that there are some difficulties in fitting the NGC 0467 data.

In order to test the presence of a PA warp further we created a model with a constant PA, also restricting the modelling to the same 3 arcsec × 3 arcsec central area as with the other models. We find a best-fitting SMBH mass of $2.19^{+1.88}_{-1.57} \times 10^8$ $M_\odot$, a best-fitting $M/L_{K_s} = 0.43^{+0.07}_{-0.06}$ $M_\odot/L_{\odot,K_s}$ and a best-fitting PA of $351\overset{\circ}{.}3^{+3.0}_{-3.8}$. This model yields a very poor $\chi^2_{\rm red} = 3.95$, comparable to the model with no SMBH, and despite the fewer free parameters, also a comparably worse BIC of 814. Since the $\Delta_{\rm BIC} > 10$ between the model with and without a PA warp, it is clear that the PA warp is statistically meaningful in the creating of a better model. However, we also see that the SMBH mass and M/L remain almost unchanged, indicating that the PA warp does not dominate the area close to the SMBH SoI. All of this taken together makes NGC 0467 an ideal candidate for a follow-up survey in which we could obtain high-resolution *HST* optical images, as it appears that, with the right MGE model and with careful modelling, a robust SMBH mass measurement is likely achievable.

Using the best-fitting SMBH for the model with a PA warp yields an $R_{\rm SoI}$ of ≈ 17 pc (≈ 0.05 arcsec), calculated in the usual manner. This is smaller than our $R_{\rm beam}$ meaning that

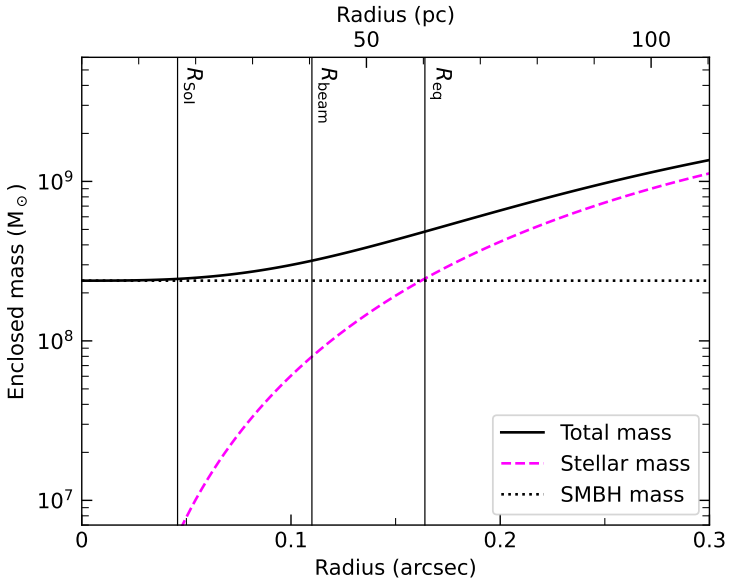


Figure 3.25: As Fig. 2.8, but for NGC 0467 (assuming $\sigma_e = 247$ km s^{-1} and our best-fitting SMBH mass).

our data did not resolve the SoI. Nevertheless, a SMBH mass determination is still possible when the SoI is not resolved. As can be seen in Fig. 3.25, $R_{eq} \approx 60$ pc (0.16 arcsec), meaning that the beam resolves the radius of equal mass contribution, which itself is another measure of the SMBH sphere of influence. In fact, ≈ 75 per cent of the mass at R_{beam} is due to the SMBH mass, which is why a SMBH mass determination is possible in NGC 0467.

The combination of complex molecular gas structure and the absence of a high resolution near-infrared *HST* image for NGC 0467 introduces significant modelling uncertainties. However, it is clear that NGC 0467 is a strong candidate for a robust SMBH mass determination. Targeted follow-up *HST* observations and more detailed modelling work would be valuable in improving the robustness of the SMBH mass measurement.

3.5 NGC 7550

3.5.1 Galaxy Properties

NGC 7550 is an E-S0 lenticular galaxy located at $23^h15^m16\overset{s}{.}01$, $+18°57'42\overset{''}{.}5$ (J2000.0) in the constellation of Pegasus. We adopt the distance used in the MASSIVE survey, $D = 72.7$ Mpc (Ma et al. 2014), obtained through surface brightness fluctuations. At this

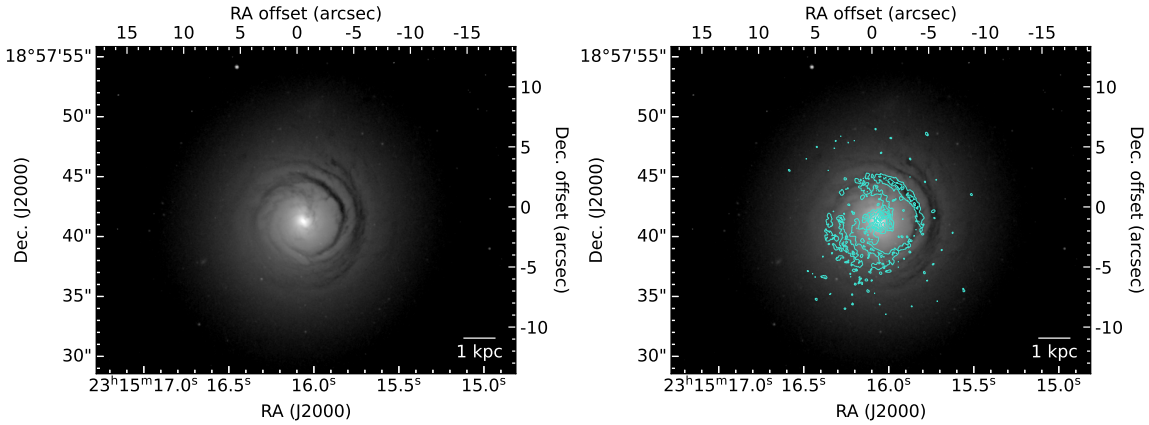


Figure 3.26: Unsharp-masked *HST* Advanced Camera for Surveys (ACS) F606W filter (V-band) image of NGC 7550 (left), overlaid with the ^{12}CO(2–1) integrated intensity contours (cyan) from our ALMA observation (right).

distance, 1 arcsec corresponds to ≈ 353 pc. NGC 7550 is in a group of 3 galaxies (according to 2MRS; Crook et al. 2007), of which it is the brightest.

HST images reveal a prominent and spiral-like dust disc on all sides of the galactic centre and an unobscured nucleus (Fig. 3.26). NGC 7550 has a moderate molecular gas reservoir, with a total H_2 mass of $(7.03 \pm 0.75) \times 10^8$ $M_\odot$ (Davis et al. 2019) and a SFR of 0.86 $M_\odot$ yr^{-1} (Mould et al. 2012). It has an integrated absolute K-band magnitude of −25.43, corresponding to a total stellar mass of 4.47×10^{11} $M_\odot$ (Veale et al. 2017b), calculated as before.

NGC 7550 does not have a direct SMBH mass measurement, but an estimate can be obtained using the $M_{BH} - \sigma_e$ relation of van den Bosch (2016). Assuming σ_e = 224 km s^{-1} (Davis et al. 2019) and the $M_{BH} - \sigma_e$ relation of van den Bosch (2016), a SMBH mass of $\approx 3.8 \times 10^8$ $M_\odot$ is expected, yielding $R_{SoI} \approx 33$ pc (≈ 0.09 arcsec).

3.5.2 ALMA observations

Observations of the ^{12}CO(2–1) emission line using Band 6 of the 12-m ALMA array were obtained as part of project 2019.1.00657.S (PI: Davis). The properties of the observations are listed in Table 1.2. The NGC 7550 data are compromised of three tracks, one of which was taken on 2019 October 3, with the other two taken on 2021 July 2024, for a total of 84 minutes on source. Baselines span from 15.1 m to 5.2 km, yielding angular sensitivity of 0.06 arcsec, a maximum recoverable scale of 4.6 arcsec, and a field of view of 24.8 arcsec. All three tracks had the same setup comprised of four spectral windows. One window in

Table 3.14: Parameters of the NGC 7550 continuum image and the detected cleaned continuum source.

Image property	Value
Image (pix)	864×864
Image (arcsec)	25.9×25.9
Image size (kpc)	9.1×9.1
Pixel scale (arcsec pix^{-1})	0.03
Pixel scale (pc pix^{-1})	10.6
RMS noise (mJy beam^{-1})	0.02
Synthesised beam (arcsec)	0.10×0.08
Synthesised beam (pc)	36×29
Source property	**Value**
Right ascension (J2000)	$23^{h}15^{m}16\overset{s}{.}06380 \pm 0\overset{s}{.}00001$
Declination (J2000)	$+18°57'41\overset{''}{.}2737 \pm 0\overset{''}{.}0003$
Integrated flux (mJy)	4.32 ± 0.05
Deconvolved size (marcsec)	$(47 \pm 2) \times (30 \pm 4)$
Deconvolved size (pc)	$(166 \pm 6) \times (106 \pm 13)$

each track was used to map the molecular gas and was centred on the redshifted frequencies of the ^{12}CO(2–1) line, 227.554768 GHz, 227.577118 GHz and 227.575114 GHz. This spectral window, with a bandwidth of 1.875 GHz ($\approx$ 2440 km s^{-1}), was subdivided into 1920 channels of width 977 kHz ($\approx$ 1.27 km s^{-1}). The remaining three spectral windows were used to map the continuum. One of these spectral windows also had a bandwidth of 1.875 GHz ($\approx$ 2440 km s^{-1}) and was subdivided into 1920 channels of width 977 kHz ($\approx$ 1.27 km s^{-1}). The other two spectral windows had a bandwidth of 2 GHz ($\approx$ 2600 km s^{-1}), subdivided into 128 channels of width 16 MHz ($\approx$ 16 km s^{-1}).

Continuum emission

An image of the NGC 7550 continuum was created as usual and cleaned with the CASA task `tclean`. We cleaned to a threshold of 3 times the RMS noise of the dirty continuum. Using the multi-frequency synthesis mode with Briggs weighting with robust parameter 0.5 we image a continuum with a central frequency of 235.5 GHz (1.27 mm). We detect a central source of continuum emission with an integrated flux density of 4.32 ± 0.05 mJy and a peak intensity of 3.61 ± 0.03 mJy beam^{-1}. The continuum was then fit using the CASA task `imfit` which reveals a spatially-resolved source with deconvolved FWHM of $(47 \pm 2) \times (30 \pm 4)$ marcsec^2. The continuum image is shown in Fig. 3.27 and its properties are listed in Table 3.14.

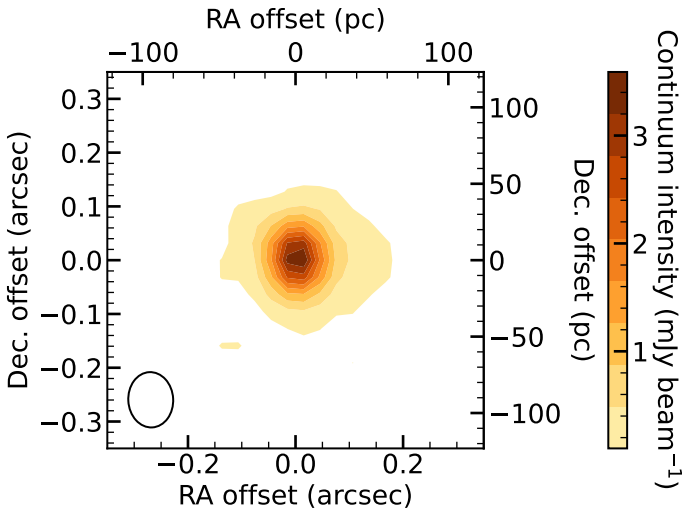


Figure 3.27: Central region (0.7 arcsec × 0.7 arcsec) of the NGC 7550 1.27 mm continuum image. Contours are evenly spaced between the peak intensity of 3.61 ± 0.03 mJy beam^{-1} and 5 times the RMS noise. The synthesised beam is shown in the bottom-left corner as a black open ellipse.

Line emission

The data cube was created as ususal, using the CASA task `uvcontsub` to subtract the continuum after which we use the `tclean` task to clean the line emission to a threshold of 3 times the RMS noise of the line-free channels of the dirty cube. We adopted a Briggs weighting with a robust parameter of 2.0. As will be discussed later, kinematic modelling of NGC 7550 SMBH is not viable, and therefore we are not bound by the need to resolve the SoI. Rather we choose the natural weighting in order to prioritise signal-to-noise. We also adopted a channel width of 20 km s^{-1} partly because we struggled with sufficient signal-to-noise even with a natural weighting. The resulting data cube has a synthesised beam of 0.15 arcsec × 0.12 arcsec (53 × 41 pc^2) with an RMS noise of 0.37 mJy beam^{-1} channel^{-1}. Its properties are summarised in Table 3.15.

The moment maps were created as before, using the typical boxcar kernel in both directions and with a mask created by clipping the smoothed data cube to a threshold of 4 times the RMS noise and then applied to the unsmoothed primary beam corrected data cube. We also created a kinematic PVD by taking a 5-pixel wide cut through the masked data cube along the position angle of 215.°4, determined using PAFIT. The resulting moment maps and PVD are shown in Fig. 3.28. We detect a disc of molecular gas, about ≈ 9 arcsec across, coincident with and slightly smaller than the dust disc (see Fig. 3.26). As can be seen in

Table 3.15: CO data cube properties for NGC 7550.

Image property	Value
Spatial extent (pix)	720×720
Spatial extent (arcsec)	28.8×28.8
Spatial extent (kpc)	10.2×10.2
Pixel scale (arcsec pix^{-1})	0.04
Pixel scale (pc pix^{-1})	14.1
Velocity range (km s^{-1})	4600 – 5780
Channel width (km s^{-1})	20
RMS noise (mJy beam^{-1} channel^{-1})	0.37
Number of constraints	80, 428
Synthesised beam (arcsec)	0.15×0.12
Synthesised beam (pc)	53×41

Fig. 3.28 the gas has an unusual distribution with a dense central region about ≈ 3 arcsec across with regions of higher velocity dispersion gas ($40 - 80$ km s^{-1}) surrounded by two distinct arms of dynamically settled gas. There is a small localised clump of gas ≈ 1 arcsec from the centre of the galaxy, as determined by the position of the continuum emission, where the gas velocity dispersion reaches ≈ 175 km s^{-1}. The gas disc also appears to exhibit a position angle warp. Whilst the molecular gas distribution extends towards the centre of the galaxy, and no discernible holes are visible, the complex nature of the gas does not make it a good candidate for a robust SMBH mass detection. Particularly, the centre of the galaxy where the black hole is to be expected has a significantly different position angle orientation than the rest of the gas. All of these factors make the successful modelling of a SMBH mass unlikely.

In Fig. 3.29 we can see the integrated ^{12}CO(2–1) spectrum of NGC 7550 which exhibits a roughly Gaussian shape. The lack of a double horned profile confirms that the gas is disturbed and is unlikely to yield good modelling results. The spectrum is extracted from a 11 arcsec $\times$ 11 arcsec ($\approx 3900 \times 3900$ pc^2) region around the centre with an integrated FWZI flux density of 40.4 ± 3.9 Jy km s^{-1}. Figure 3.29 also shows the integrated spectrum of the ^{12}CO(2–1) (grey shading) and ^{12}CO(1–0) (black dashed line) lines obtained from the IRAM single-dish 30-m telescope observations reported by Davis et al. (2015). None of the three plotted spectra exhibit the double-horned shape of a regularly rotating disc, once again confirming that the modelling of NGC 7550 is unlikely to be successful.

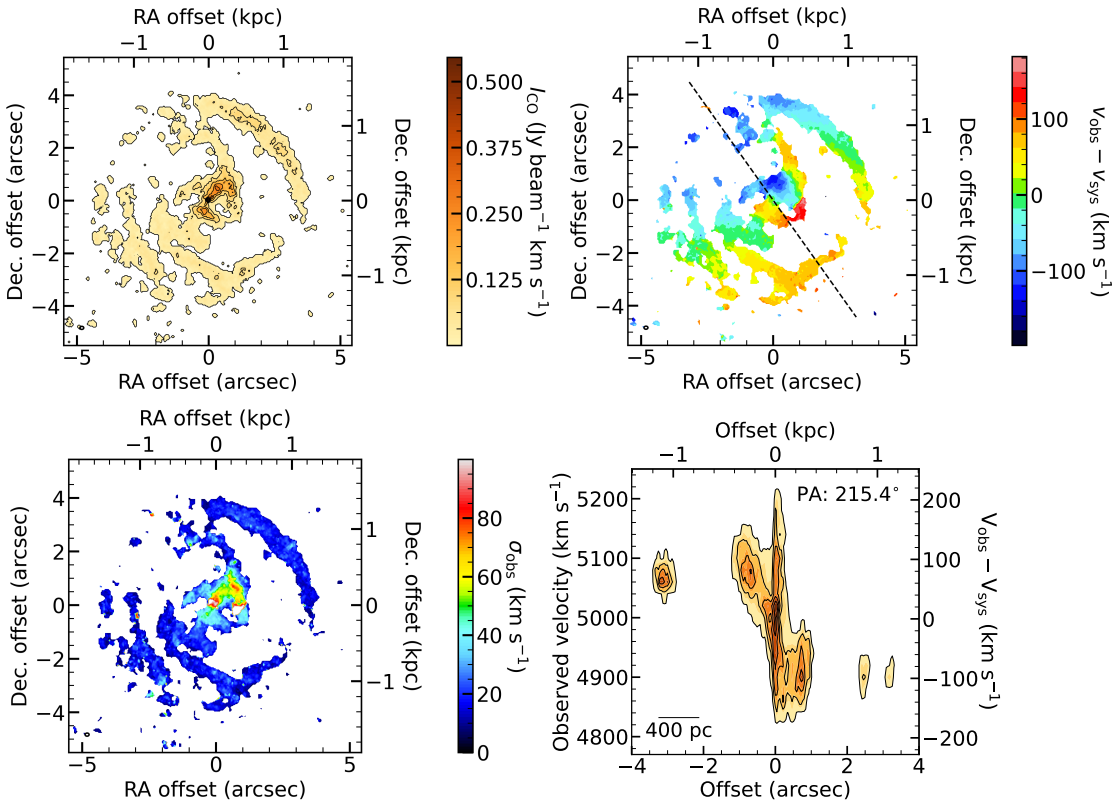


Figure 3.28: As Fig. 2.29 but for NGC 7550.

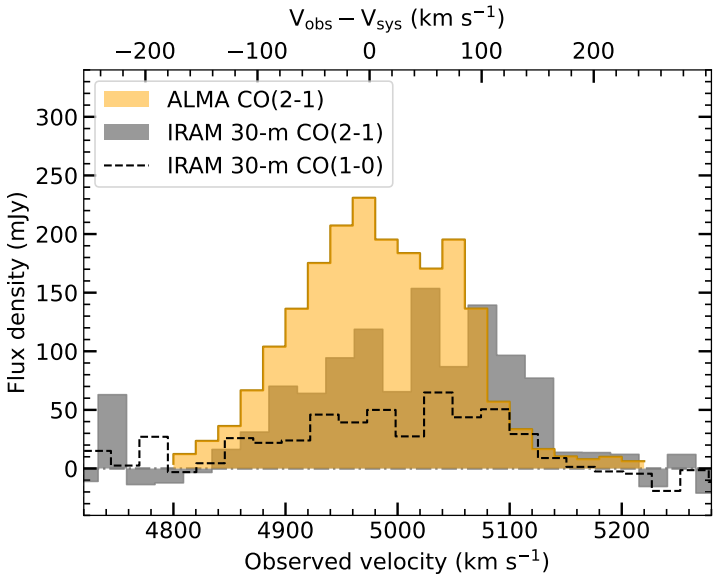


Figure 3.29: ^{12}CO(2–1) integrated spectrum of NGC 7550 derived from our ALMA data (orange shading), overlaid on the IRAM 30-m telescope ^{12}CO(2–1) (grey shading) and ^{12}CO(1–0) (black dashed line) observations of Davis et al. (2015). The ALMA aperture is a 11 arcsec × 11 arcsec ($\approx 3900 \times 3900$ pc^2) region centred on the galaxy centre, that includes all detected emission.

Table 3.16: Parameters of the deconvolved best-fitting MGE components of our model of NGC 7550.

$I'_{\odot}$ ($L_{\odot,F606W}$ pc^{-2}) (1)	σ' (arcsec) (2)	q' (3)
18143	0.052	0.990
7375	0.256	0.990
3401	0.588	0.990
2672	1.364	0.990
810	3.112	0.881
532	8.706	0.990

Notes. Deconvolved MGE components. (1) Central surface brightness of Gaussian component. (2) Standard deviation of Gaussian component. (3) Axial ratio of Gaussian component.

3.5.3 CO modelling

Due to the complex shape of the molecular gas disc in NGC 7550 we opted to model the gas distribution using SkySampler. We sampled the clean components using 5×10^6 particles.

We obtain a stellar light distribution for NGC 7550 as usual, using an MGE model of a *HST* Advanced Camera for Surveys (ACS) F606W filter (V-band) image (GO-14840; PI: Bellini) with a total exposure time of 696 s. We covert this stellar light distribution into luminosities in the AB magnitude system by adopting a zero-point of 26.49 mag (Stark et al. 2025), a Solar absolute magnitude of 4.72 mag (Willmer 2018) for the F606W filter and a galactic extinction of 0.338 mag from NED (Schlafly & Finkbeiner 2011).

Shown in Fig. 3.30 is the MGE model for NGC 7550. There is clearly significant dust extinction in the *HST* image, which is to be expected given that the F606W filter does not trace near-infrared light. Unfortunately, the F606W filter image is the reddest available. Nevertheless, we mask the most prominent dust lanes to the north-west of the nucleus to reduce their impact. The resulting MGE model appears to be a good fit, especially at the small radii that matter the most for a robust SMBH mass determination.

All attempts at modelling the SMBH mass in NGC 7550 were unsuccessful. We explored a range of modelling configurations, including fixing the dynamical centre to that of the continuum emission, fixing the inclination to the value determined by ellipse-fitting the dust lanes of the *HST* image, allowing for a position angle warp and restricting the fit to the inner 1.5 arcsec $\times$ 1.5 arcsec region. In practice we tested these choices both individually and in combination, but in every case the fits failed to converge to a stable solution. This

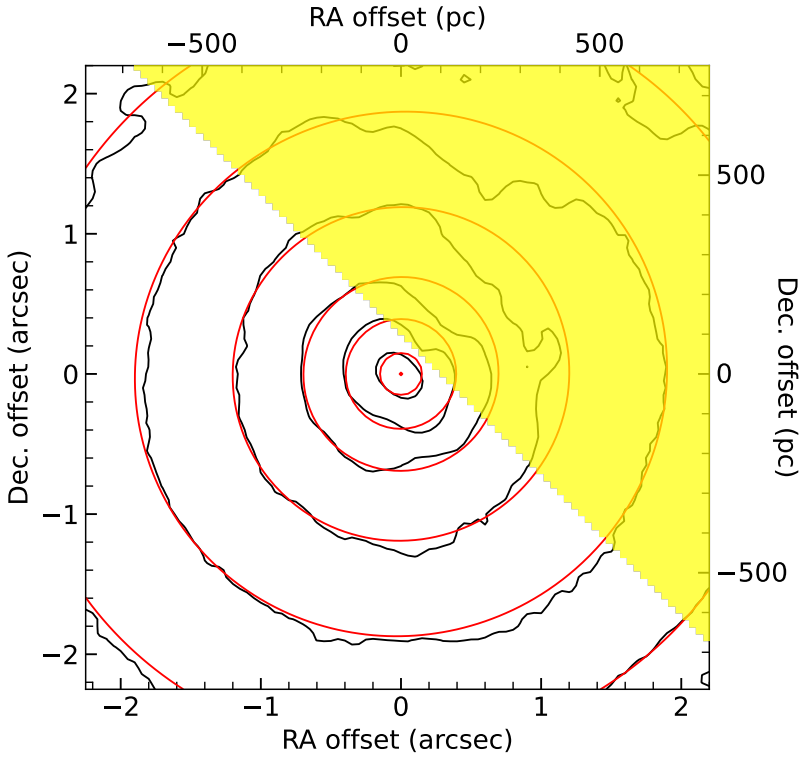


Figure 3.30: *HST* ACS F606W filter image of NGC 7550 (black contours), overlaid with our best-fitting MGE model (red contours). The north-western side of the image is masked (yellow shading), to exclude the most obviously dust-obscured pixels.

is likely because, as can be seen in Fig. 3.28, NGC 7550 exhibits significant non-circular motions, thereby violating the central assumption of our framework that the gas must reside in a thin, dynamically cold disc undergoing approximately circular rotation.

We therefore exclude this galaxy from our quantitative SMBH analysis and treat it instead as an instructive example of the limitations of molecular gas dynamical modelling when the molecular gas disc is significantly unsettled.

3.6 Conclusions

In this chapter we have presented high resolution ALMA observations of the ^{12}CO(2–1) line in four MASSIVE Survey galaxies: NGC 0665, NGC 5208, NGC 0467 and NGC 7550. Where possible, we also presented the molecular gas dynamical measurements of their SMBH masses. The galaxies have a range of molecular gas morphologies, allowing us to

assess when molecular gas dynamical modelling can yield robust SMBH masses, thereby assessing the limitations of the molecular gas method as a whole.

In Section 3.2 we found that NGC 0665 has a clumpy, spiral-like and approximately regularly rotating gas disc with a spatial extent of ≈ 8 arcsec (≈ 2.4 kpc) in radius and a central hole of radius ≈ 1.7 arcsec (≈ 510 pc), much larger than the predicted $R_{\rm SoI}$. This prevents us from detecting any Keplerian rise of the rotational velocities at small radii and from determining a SMBH mass. Using SkySampler to model the cube using the observed gas distribution itself, an MGE model derived from a *HST* WFC3 F110W filter image, assuming a constant M/L and a fixed position angle of 117°, we infer a SMBH mass upper limit of $< 2.7 \times 10^9$ $\mathrm{M}_\odot$ at the 1σ (68 per cent) confidence level, $< 6.1 \times 10^9$ $\mathrm{M}_\odot$ at the 3σ (99.7 per cent) confidence level and a stellar F110W filter M/L of $1.93^{+1.45}_{-0.57}$ $\mathrm{M}_\odot/\mathrm{L}_{\odot,\mathrm{F110W}}$.

In Section 3.3 we found that NGC 5208 has a regularly rotating gas disc with a spatial extent of ≈ 26 arcsec (≈ 13.2 kpc). NGC 5208 has a prominent depression in its centre of radius ≈ 3 arcsec (≈ 1.5 kpc) which prevents us from determining a SMBH mass. Using an axisymmetric exponential surface density profile with an inner truncation, an MGE model derived from a *HST* WFC3 F160W filter image and assuming a linearly-varying M/L, we infer a SMBH mass upper limit of $< 3.03 \times 10^9$ $\mathrm{M}_\odot$ at the 3σ confidence level and a best-fitting M/L in the F160W filter represented by $(M/L_{\mathrm{F160W}})\,/\left(\mathrm{M}_\odot/\mathrm{L}_{\odot,\mathrm{F160W}}\right) = 1.42^{+0.08}_{-0.09} - 0.04^{+0.01}_{-0.01}\ (R/\mathrm{arcsec})$.

In Section 3.4 we found that NGC 0467 has an approximately regularly rotating gas disc with a spatial extent of ≈ 6 arcsec (≈ 2.2 kpc). NGC 0467 has no central hole, making it an ideal candidate for SMBH mass determination. However, there is no *HST* image available of NGC 0467, making the determination of the stellar contribution to the gravitational potential difficult. Nevertheless we attempt modelling using a *CFHT* WIRCam K_s-band image instead. Using SkySampler to model the cube using the observed gas distribution itself, an MGE model of the *CFHT* image, assuming a constant M/L, allowing for a linear position angle warp and restricting modelling to a 3 arcsec × 3 arcsec central area we infer a SMBH mass of $2.39^{+1.56}_{-1.32} \times 10^8$ $\mathrm{M}_\odot$ and a best-fitting M/L in the K_s-band of $0.44^{+0.12}_{-0.06}$ $\mathrm{M}_\odot/\mathrm{L}_{\odot,K_s}$. The modelling of NGC 0467 confirms a presence of a position angle warp, however the position angle parameters and inclination have very broad confidence intervals, suggesting

that the twist is not uniquely determined and NGC 0467 would benefit from additional testing of PA warp freedom. In addition to this, there is some complexity in the molecular gas distribution that we have struggled to match with the best-fitting model, which is reflected in the somewhat large $\chi_{\rm red}$ = 3.76 for the best-fit model. It is clear that whilst we have formally obtained a SMBH mass constraint for NGC 0467, some further investigation is required, making NGC 0467 an ideal candidate for a follow-up study, particularly with the aim of obtaining near-infrared *HST* images.

In Section 3.5 we found that NGC 7550 has an irregular molecular gas distribution with a spatial extent of ≈ 9 arcsec (3.2 kpc). The gas has a dense central region, with high velocity dispersion clumps, surrounded by two arms of dynamically settled gas. The gas also appears to exhibit a position angle warp. The complex nature of the gas does not make it a viable candidate for a SMBH mass detection.

Taken together, these results highlight the primary limitations of molecular-gas-based SMBH mass measurements. While cold molecular gas is detected in a substantial fraction of nearby massive galaxies, only a subset host circumnuclear discs that are sufficiently regular, centrally concentrated and dynamically cold to yield robust SMBH mass constraints. Large central holes, strong non-axisymmetric motions or disturbed gas morphologies can preclude meaningful measurements even when high spatial resolution data is available. Nevertheless, when incorporated using appropriate statistical treatments, SMBH mass upper limits derived from such systems provide valuable constraints on black hole – galaxy scaling relations and play an important role in defining viable target selection criteria for future studies.

Two things fill the mind with ever new and increasing admiration and awe, the more often and steadily we reflect upon them: the starry heavens above me and the moral law within me.

— Immanuel Kant's *Critique of Practical Reason*

4 CO Tully-Fisher relation

Contents

4.1 Introduction 160
4.2 Data 163
4.2.1 CO data 163
4.2.2 Optical data 169
4.2.3 Velocity widths 169
4.2.4 Photometry 172
4.2.5 Inclinations 173
4.3 Results 178
4.3.1 Data sub-samples 178
4.3.2 Tully-Fisher relation 179
4.3.3 Galaxy morphology 181
4.4 Discussion 187
4.4.1 Literature comparisons 187
4.4.2 Galaxy morphology 189
4.4.3 Scatter 192
4.5 Conclusions 193

4.1 Introduction

Scaling relations between the luminosity, mass and kinematics of galaxies are central to our understanding of galaxy formation and evolution. Among these, the Tully-Fisher relation (TFR; Tully & Fisher 1977) remains one of the most fundamental, linking a galaxy's

rotational velocity and luminosity. As the rotation velocity traces the enclosed dynamical mass of a galaxy while the luminosity traces its stellar mass, the relation provides insights into the distribution of baryons and dark matter within galaxies (e.g. Zwaan et al. 1995; McGaugh & de Blok 1998; McGaugh et al. 2000), it constrains the stellar M/L (e.g. Bell & de Jong 2001) and it serves as a test of galaxy formation and cosmological models (e.g. van den Bosch 2000; Yang et al. 2003; Trachternach et al. 2009; McGaugh 2012; Ponomareva et al. 2017). In addition, the TFR can be used as a distance indicator, extending the cosmic distance ladder beyond the local Universe (e.g. Pierce & Tully 1988; Sakai et al. 2000; Springob et al. 2007). Indeed, by comparing the absolute magnitude of a galaxy expected from the TFR with its observed apparent magnitude, the distance to the galaxy can be estimated independently of its redshift.

Traditionally, the TFR has been derived for late-type, gas-rich galaxies using emission from the hyperfine transition of atomic hydrogen (H I) at 21 cm (e.g. Tully & Pierce 2000; Verheijen 2001; Meyer et al. 2008; Ponomareva et al. 2021). However, direct atomic hydrogen detections of individual galaxies within large-area untargeted surveys are rare beyond the nearby Universe (Giovanelli et al. 2005). Recently, targeted deep observations have been able to obtain a single detection at $z = 0.376$ (Fernández et al. 2016; although this result has been recenly called into question by Heywood et al. 2024), six detections at $0.38 < z < 0.5$ (Xi et al. 2024) and eleven detections at $z > 0.25$ with the highest at $z = 0.3841$ (Jarvis et al. 2025). In exceptional cases H I can be detected at $z \approx 0.7$ but only through the use of strong gravitational lensing (Lawrie et al. 2025). A previously claimed strongly lensed H I detection at $z \approx 1.3$ (Chakraborty & Roy 2022) was subsequently challenged by Deane et al. (2024), highlighting the difficulty of H I detections at such redshifts. H I is also problematic when attempting to probe the TFR of ETGs. Indeed, extended atomic gas is less frequent in ETGs (e.g. Young et al. 2014, 2018), and when present it is often kinematically disturbed (e.g. Williams et al. 2010; Serra et al. 2012). When extended regularly rotating H I discs are present, an ETG TFR can be defined, but samples remain small (e.g. den Heijer et al. 2015).

When comparing TFR differences across galaxy morphological types, it is crucial that the same velocity tracer is used for all sample galaxies, as different velocity tracers will likely introduce different systematic biases (e.g. Williams et al. 2010). Thus, the use of CO as

an alternative kinematic tracer in TFR studies has grown considerably in recent years (e.g. Davis et al. 2011a, 2015; Tiley et al. 2016b; Topal et al. 2018). CO is observed across the full Hubble sequence with large surveys mapping CO in a substantial fraction of nearby spirals [e.g. Berkeley-Illinois-Maryland Association Survey of Nearby Galaxies (BIMA SONG); Helfer et al. 2003, Extragalactic Database for Galaxy Evolution and Calar Alto Legacy Integral Field Area Survey (EDGE-CALIFA); Utomo et al. 2017, Extended CO Legacy Database for GASS (xCOLD GASS); Saintonge et al. 2017, CO Multi-line Imaging of Nearby Galaxies (COMING); Sorai et al. 2019] and targeted studies demonstrating routine CO detections in $\approx 20\%$ of ETGs (e.g. ATLAS3D; Young et al. 2011, MASSIVE; Ma et al. 2014). Moreover, contrary to H I, CO is observable across a wide range of galaxy environments, from brightest cluster galaxies (where H I is often depleted due to environmental processes such as ram-pressure stripping and tidal interactions; e.g. Rose et al. 2019; Dunne et al. 2021) to isolated field galaxies (e.g. Young et al. 2011; Davis et al. 2011b). In addition, CO remains detectable up to $z \approx 6$, with numerous detections at high redshifts (e.g. Carilli & Walter 2013; Novak et al. 2019; Decarli et al. 2022; Kaasinen et al. 2024).

Early studies (e.g. Dickey & Kazes 1992; Schoniger & Sofue 1994) showed that CO line-widths correlate well with rotation velocities in spiral galaxies, often yielding TFRs comparable to those derived using H I. The use of CO as a kinematic tracer to derive a TFR for nearby ETGs was first demonstrated by Davis et al. (2011a). Subsequent studies extended this approach to larger and more diverse galaxy samples in the local Universe (e.g. Tiley et al. 2016b; Topal et al. in prep.), to massive ETGs (Davis et al. 2015) and to galaxies at intermediate redshifts (Topal et al. 2018). These studies collectively demonstrate that CO TFRs yield slopes, zero-points and scatters consistent with those of the classical relations, thus providing a robust alternative to H I for rotation-based scaling relations.

In this work, we use the ALMA observations from the WISDOM project to construct a new CO TFR calibration for the local Universe. The WISDOM sample comprises 96 galaxies (75 of which are detected) observed predominantly in the ^{12}CO(2–1) line with high spatial and spectral resolutions, offering one of the largest galaxy molecular gas datasets to date. ALMA's high spatial resolution allows to measure the emission's extent and to identify and exclude targets with non-circular and/or disturbed motions, whereas its high spectral resolution ensures

precise velocity widths with unambiguous profile shapes. Using methodologies analogous to those of Tiley et al. (2016b) and Topal et al. (2018), we measure the rotation velocities from the integrated CO profiles and derive the luminosities using the near-infrared $W1$ (3.4 μm) and K_s (2.15 μm) bands, which best trace the old stellar populations dominating stellar mass. Alongside the TFRs, we also compile a comprehensive catalogue of CO data products (moment maps, position-velocity diagrams and integrated spectra) for all the WISDOM sample galaxies, to serve as a lasting resource for molecular gas and dynamical studies.

The structure of this chapter is as follows. In Section 4.2 we list and discuss the CO and photometric data used for this study, as well as the measurements and deprojection of our CO velocity widths. In Section 4.3 we present the TFR fits of our parent sample of galaxies and various sub-samples. In particular, we explore the impacts of imposing CO data quality and inclination criteria to create more homogenous sub-samples, and look at TFR differences as a function of galaxy morphology. In Section 4.4 we discuss our results and compare them against literature results. We conclude briefly in Section 4.5. The WISDOM CO data products will be made available in the online appendix of Dominiak et al. (2026b).

4.2 Data

4.2.1 CO data

The parent sample for this study consists of 96 galaxies for which ALMA CO data were obtained as a part of the WISDOM project.

The ^{12}CO(2–1) emission line of 60 galaxies was observed using Band 6 of the 7-m Atacama Compact Array (ACA) as a part of projects 2016.2.00046.S (PI: Bureau), 2019.1.00363.S (PI: Davis), 2022.1.01173.S (PI: Liang) and 2023.1.01084.S (PI: Liang). Those data were calibrated using the CASA package (using the version appropriate for the data depending on the ALMA Cycle; McMullin et al. 2007) and its ALMA pipeline. The imaging steps used CASA version 6.7.2.

For these galaxies we create data cubes in the standard manner. We first remove the continuum emission using the CASA task `uvcontsub`. We then interactively clean the continuum-subtracted data using the `tclean` task to thresholds appropriate for each data

set, typically ≈ 3 times the RMS noise. The data were then imaged using the same `tclean` task and natural weighing (Briggs weighing with a robust parameter of 2), to achieve the best possible emission signal-to-noise ratios. Each cube was initially imaged using 10 km s^{-1} channels, increased in cases of low signal-to-noise ratios. One third (21/60) of these ACA sample galaxies were not detected in ^{12}CO(2–1) (3C296, MCG_-02-36-002, NGC0193, NGC1052, NGC1461, NGC1700, NGC3078, NGC3379, NGC3414, NGC4233, NGC4342, NGC4350, NGC4866, NGC5077, NGC5127, NGC5845, NGC7457, NGC7768, PGC046123, PGC214240 and UGC7115).

The remaining 39 galaxies with ^{12}CO(2–1) detections resulted in 28 cubes with 10 km s^{-1} channels, 8 cubes with 20 km s^{-1} channels and 3 cubes with 30 km s^{-1} channels. The cubes have synthesised beam sizes (full widths at half maximum measured along the kinematic major-axis of the CO emission) ranging from 4.0 to 8.2 arcsec. For all cubes we chose a pixel size ensuring a sampling of 3 – 5 spaxels across the synthesised beam and a spatial extent equal to the 20 per cent primary beam response. The properties of the remaining 39 cubes are summarised in Table 4.1.

In addition to these 39 galaxies with ACA low angular resolution observations, we include another 36 galaxies with 12-m array higher angular resolution observations, all part of previous WISDOM studies (e.g. Davis et al. 2022; Elford et al. 2023). The associated cubes use data obtained as part of the aforementioned projects as well as projects 2013.1.00493.S (PI: Bureau), 2015.1.00419.S (PI: Davis), 2015.1.00466.S (PI: Onishi), 2015.1.00598.S (PI: Bureau), 2016.1.00437.S (PI: Davis), 2016.1.00839.S (PI: Onishi), 2016.1.01553.S (PI: Bureau), 2016.2.00053.S (PI: Liu), 2017.1.00391.S (PI: North), 2017.1.00904.S (PI: Smith) and 2018.1.00397.S (PI: Smith). Most of these (32/36) targeted the ^{12}CO(2–1) line, but a few (4/36; NGC3351, NGC4429, NGC4751 and NGC4826) targeted the ^{12}CO(3–2) line using ALMA Band 7. The majority of these cubes have been used in previous WISDOM studies and therefore there is a variability as to the robust weighting used, cleaning thresholds, and channel widths. Four of the resulting cubes have 2 km s^{-1} channels, 23 cubes 10 km s^{-1} channels and 9 cubes have 10 < width ≤ 20 km s^{-1} channels. These cubes have synthesised beam sizes ranging from 0.03 to 0.84 arcsec. The properties of these 36 high-resolution cubes are also summarised in Table 4.1.

Table 4.1: CO data for the galaxy sample.

Galaxy	Type	Array	Width (km s^{-1})	Beam (arcsec)	CO ref.	v_0 (km s^{-1})	W_{50} (km s^{-1})	$i_{b/a}$ (°)	$i_{\rm dust}$ (°)	$i_{\rm CO}$ (°)	$W_{50}/\sin i$ (km s^{-1})	Sample
(1)	(2)	(3)	(4)	(5)	(6)	(7)	(8)	(9)	(10)	(11)	(12)	(13)
ESO383-G035	Sab	7-m	10	6.41×5.46	TW	2332 ± 1	242.5 ± 2.5	57 ± 3	–	–	289 ± 10	I A B
FRL49	E-S0	12-m	15	0.22×0.16	L22	5886.6 ± 0.5	391.6 ± 1.1	38†	57 ± 12	64 ± 1	435.7 ± 3.9	I A B
IC0843	S0	7-m	20	7.72×6.09	TW	7198 ± 6	783 ± 12	68 ± 4	79 ± 2	–	797 ± 14	I A B
IC1481	Sd	7-m	10	7.64×4.65	TW	5994 ± 2	219.3 ± 4.0	28 ± 20	–	–	467 ± 310	I
IC4329A	S0-a	7-m	30	8.31×4.50	TW	4773 ± 4	498 ± 18	58 ± 3	84 ± 2	–	501 ± 18	I A B
MRK0567	Sc	12-m	15	0.16×0.12	D22	9422.0 ± 0.3	222.2 ± 0.6	26†	19 ± 6	–	683 ± 210	I A
NGC0017	S0-a	7-m	10	7.14×5.52	TW	5699.0 ± 0.2	335.5 ± 0.8	74 ± 2	20 ± 9	–	981 ± 420	I A
NGC0289	SBbc	7-m	10	6.61×4.86	TW	1625.0 ± 0.1	144.0 ± 0.1	43 ± 3	–	–	211 ± 12	I
NGC0383	E-S0	12-m	10	0.18×0.10	Z25	4929.3 ± 0.2	523.2 ± 0.5	35 ± 6	37 ± 6	38 ± 3	850 ± 57	I A B
NGC0404	E-S0	12-m	2	0.05×0.03	D20	-55.7 ± 0.1	26.9 ± 0.1	14 ± 14	16 ± 6	37 ± 2	44.7 ± 2.1	×
NGC0449	SBa	12-m	10	0.85×0.51	D22	4683.7 ± 0.6	233.2 ± 1.6	58 ± 3	70 ± 4	–	248.2 ± 6.5	I A B
NGC0524	S0-a	12-m	10	0.38×0.28	S19	2386.3 ± 0.2	306.0 ± 0.4	13 ± 13	13 ± 8	20 ± 7	895 ± 300	I A
NGC0541	E	7-m	10	6.99×4.66	TW	5319 ± 2	239.8 ± 3.5	50 ± 3	29 ± 10	–	495 ± 160	I A
NGC0612	S0-a	12-m	10	0.21×0.18	R23	8636.7 ± 0.3	790.0 ± 0.8	28 ± 8	79 ± 2	81 ± 1	799.8 ± 2.4	I A B
NGC0708	E	12-m	10	0.09×0.08	N21	4763.3 ± 0.6	354.5 ± 1.9	64 ± 2	73 ± 3	77 ± 3	363.8 ± 4.8	I A B
NGC0863	Sa	7-m	10	7.69×5.38	TW	7715.3 ± 0.3	226.4 ± 0.7	25 ± 10	19 ± 14	–	695 ± 490	I A
NGC1084	Sc	7-m	30	7.74×4.96	TW	1356.0 ± 0.1	206.5 ± 0.1	50 ± 2	67 ± 2	–	224.3 ± 3.3	I A B

Notes. (1) Galaxy name. (2) Galaxy morphological type. (3) Most extended ALMA array used for the CO data cube. (4) Cube channel width. (5) Cube synthesised beam size (full widths at half maximum). (6) Source of CO data. TW: this work; D17: Davis et al. (2017); D18: Davis et al. (2018); D20: Davis et al. (2020); D22: Davis et al. (2022); E23: Elford et al. (2023); L22: Lelli et al. (2022); N21: North et al. (2021); R23: Ruffa et al. (2023); S19: Smith et al. (2019); S21: Smith et al. (2021b); Z25: Zhang et al. (2025a). (7) Integrated spectrum best-fitting central velocity. (8) Integrated spectrum velocity width at 50% of the peak. (9) Inclination derived from galaxy HyperLEDA optical axial ratio. Uncertainties are derived using the optical axial ratio uncertainties listed in HyperLEDA. † indicates galaxies for which K-band axial ratios from 2MASS were used instead (for which there is no listed uncertainty). (10) Inclination derived from ellipse fitting to unsharp-masked optical *HST* images. The ellipse parameters were adjusted by eye and the uncertainties listed bracket the range of inclinations for which the ellipse remains an acceptable visual match. (11) Inclination derived from kinematical modelling of the CO cube in the literature. The uncertainties are the average of the listed upper and lower 3σ uncertainties. (12) Integrated spectrum inclination-corrected velocity width at 50% of peak. The uncertainties are propagated in the standard manner. (13) Sample membership of each galaxy. I: initial sample; A: sub-sample A; B: sub-sample B; ×: excluded galaxies.

Table 4.1: continued.

Galaxy	Type	Array	Width (km s^{-1})	Beam (arcsec)	CO ref.	v_0 (km s^{-1})	W_{50} (km s^{-1})	$i_{b/a}$ (°)	$i_{\rm dust}$ (°)	$i_{\rm CO}$ (°)	$W_{50}/\sin i$ (km s^{-1})	Sample
(1)	(2)	(3)	(4)	(5)	(6)	(7)	(8)	(9)	(10)	(11)	(12)	(13)
NGC1194	S0-a	12-m	20	0.30×0.23	E23	4019 ± 1	408.9 ± 3.1	62 ± 3	81 ± 3	–	414.0 ± 4.7	I A B
NGC1300	Sbc	12-m	10	0.82×0.48	TW	1538.0 ± 0.2	211.8 ± 0.5	61 ± 2	55 ± 4	–	259 ± 13	I A B
NGC1358	S0-a	7-m	20	7.56×4.13	TW	3954 ± 2	189.7 ± 6.4	59 ± 3	46 ± 5	–	264 ± 24	I A B
NGC1387	E-S0	12-m	10	0.42×0.35	D25	1263.6 ± 0.1	143.3 ± 0.1	11 ± 11	16 ± 6	14 ± 1	592 ± 42	I A
NGC1400	E	7-m	10	7.20×4.20	TW	547.9 ± 0.1	426.5 ± 0.2	29 ± 5	27 ± 8	–	939 ± 260	I A
NGC1448	Sc	7-m	20	7.47×5.56	TW	1122.3 ± 0.1	221.2 ± 0.4	89 ± 1	82 ± 2	–	223.4 ± 1.2	I
NGC1493	SBc	7-m	10	9.19×3.92	TW	1028.5 ± 0.1	23.5 ± 0.2	22 ± 7	25 ± 7	–	56 ± 15	×
NGC1497	S0	7-m	10	6.99×6.22	TW	6096.7 ± 0.5	588.8 ± 0.9	65 ± 3	70 ± 4	–	627 ± 16	I A B
NGC1574	E-S0	12-m	10	0.20×0.14	R23	1033.4 ± 0.5	226.4 ± 0.9	24 ± 6	28 ± 4	27 ± 4	499 ± 68	I A
NGC2110	E-S0	12-m	20	0.74×0.43	E23	2395 ± 1	403.4 ± 3.5	24 ± 6	45 ± 3	–	571 ± 30	I A B
NGC2179	S0-a	7-m	10	7.50×4.15	TW	2829.8 ± 0.8	413.6 ± 1.4	45 ± 3	51 ± 3	–	532 ± 23	I A B
NGC2187A	S0-a	7-m	20	7.14×6.43	TW	3919.8 ± 0.4	449.7 ± 0.8	64 ± 4	63 ± 2	–	504.7 ± 9.0	I A B
NGC2911	S0	7-m	10	6.86×5.45	TW	3188 ± 1	521.7 ± 2.7	57 ± 3	–	–	622 ± 21	I A B
NGC2964	Sbc	7-m	10	7.54×6.53	TW	1316.1 ± 0.5	173.4 ± 1.3	43 ± 5	63 ± 2	–	194.6 ± 3.8	I A B
NGC2974	E	7-m	10	6.59×4.59	TW	1807 ± 6	519 ± 15	57 ± 4	60 ± 2	–	600 ± 21	I A B
NGC3021	Sbc	7-m	10	10.47×5.67	TW	1515.2 ± 0.3	273.2 ± 0.6	56 ± 5	63 ± 3	–	306.6 ± 8.2	I A B
NGC3156	S0	7-m	20	6.27×5.45	TW	1310 ± 1	140.9 ± 3.2	64 ± 5	–	–	156.8 ± 7.6	I A B
NGC3169	Sa	12-m	10	0.70×0.51	D22	1223.6 ± 0.2	468.9 ± 0.6	53 ± 6	67 ± 3	–	509 ± 11	I A B
NGC3277	Sab	7-m	10	7.58×6.29	TW	1404.5 ± 0.2	235.4 ± 0.4	42 ± 5	32 ± 6	–	444 ± 74	I A B
NGC3351	Sb	12-m	10	0.29×0.14	E23	790.4 ± 0.2	204.1 ± 0.7	53 ± 4	40 ± 6	–	318 ± 40	I A B
NGC3368	Sab	12-m	2	0.21×0.20	D22	907.0 ± 0.1	205.5 ± 0.1	50 ± 5	50 ± 4	–	268 ± 16	I
NGC3393	SBa	12-m	10	0.56×0.45	L23	3697.9 ± 0.4	227.1 ± 2.4	30 ± 7	40 ± 5	–	353 ± 37	I A B
NGC3607	E-S0	12-m	10	0.60×0.50	D22	1181.8 ± 0.3	537.5 ± 0.5	30 ± 13	51 ± 2	–	692 ± 20	I A B
NGC3810	Sc	7-m	10	7.26×5.00	TW	1002.0 ± 0.1	199.9 ± 0.1	49 ± 3	48 ± 3	–	269 ± 13	I A B
NGC3862	E	12-m	10	0.69×0.53	E23	−110.7 ± 0.6	216.6 ± 1.2	5 ± 10	16 ± 9	–	786 ± 430	I A
NGC4030	Sbc	7-m	10	7.93×4.46	TW	1452.4 ± 0.1	329.4 ± 0.1	46 ± 3	40 ± 4	–	513 ± 43	I A B
NGC4061	E	12-m	10	0.15×0.12	D22	7185.5 ± 0.5	696.3 ± 1.3	32 ± 7	60 ± 2	–	804 ± 16	I A B
NGC4203	E-S0	7-m	20	7.43×6.77	TW	1076 ± 2	351.1 ± 1.3	25 ± 10	30 ± 6	–	702 ± 127	I A B
NGC4212	Sc	7-m	10	7.16×5.66	TW	−74.4 ± 0.3	179.1 ± 0.8	55 ± 3	57 ± 3	–	213.6 ± 7.3	I A B

Table 4.1: continued.

Galaxy	Dist. (Mpc)	Array	Width (km s^{-1})	Beam (arcsec)	CO ref.	v_0 (km s^{-1})	W_{50} (km s^{-1})	$i_{b/a}$ (°)	$i_{\rm dust}$ (°)	$i_{\rm CO}$ (°)	$W_{50}/\sin i$ (km s^{-1})	Sample
(1)	(2)	(3)	(4)	(5)	(6)	(7)	(8)	(9)	(10)	(11)	(12)	(13)
NGC4235	Sa	7-m	10	8.09 × 5.09	TW	2234.2 ± 2.0	246.3 ± 4.5	87 ± 3	82 ± 2	–	248.7 ± 4.7	I A B
NGC4245	S0-a	7-m	10	8.69 × 5.37	TW	880.4 ± 0.3	204.6 ± 0.4	52 ± 3	40 ± 6	–	318 ± 40	I A B
NGC4261	E	12-m	15	0.20 × 0.15	R23	−16 ± 8	864 ± 38	38 ± 4	61 ± 3	61 ± 3	988 ± 52	I A B
NGC4278	E	7-m	20	7.09 × 6.32	TW	629 ± 2	411.9 ± 6.1	13 ± 11	57 ± 3	–	491 ± 18	I A B
NGC4429	S0-a	12-m	10	0.23 × 0.16	D18	1090.7 ± 0.3	455.9 ± 0.5	65 ± 3	65 ± 1	67 ± 1	495.3 ± 3.7	I A B
NGC4435	S0	12-m	10	0.25 × 0.23	D22	786.5 ± 0.1	415.7 ± 0.3	46 ± 4	71 ± 2	–	439.7 ± 5.3	I A B
NGC4438	Sa	12-m	10	0.60 × 0.53	D22	−42.7 ± 0.1	441.6 ± 0.3	67 ± 4	65 ± 4	–	487 ± 16	I A B
NGC4501	Sb	12-m	15	0.69 × 0.59	D22	2265.4 ± 0.3	205.1 ± 0.5	62 ± 3	63 ± 3	–	230.2 ± 6.2	I
NGC4697	E	12-m	10	0.56 × 0.53	D17	1241.1 ± 0.4	432.9 ± 0.7	56 ± 3	76 ± 1	76 ± 1	446.2 ± 2.1	I A B
NGC4826	SABa	12-m	2	0.18 × 0.14	D22	404.2 ± 0.1	234.0 ± 0.1	61 ± 3	64 ± 3	–	260.3 ± 6.6	I A B
NGC4845	SABa	7-m	10	7.50 × 4.54	TW	1095.0 ± 0.1	362.7 ± 0.1	85 ± 2	80 ± 1	–	368.3 ± 1.1	I A B
NGC5064	Sb	12-m	20	0.08 × 0.04	D22	2964.6 ± 0.2	543.3 ± 0.5	60 ± 2	69 ± 2	71 ± 2	574.6 ± 6.9	I A B
NGC5084	S0	12-m	2	0.59 × 0.53	TW	1721 ± 4	535 ± 11	82 ± 2	–	–	540 ± 11	I A B
NGC5273	S0	7-m	10	8.39 × 6.42	TW	1086.3 ± 0.8	123.8 ± 2.3	53 ± 4	26 ± 10	–	282 ± 100	I A
NGC5427	SABc	7-m	10	7.33 × 4.53	TW	2711.8 ± 0.1	123.0 ± 0.2	25 ± 15	26 ± 8	–	281 ± 80	I A
NGC5746	Sb	7-m	10	8.59 × 4.64	TW	1724.6 ± 0.7	183.8 ± 2.8	90	85 ± 2	–	184.5 ± 2.9	×
NGC5765b	SABb	12-m	10	0.39 × 0.27	D22	8081.2 ± 0.2	282.2 ± 0.7	49 ± 8	43 ± 5	–	414 ± 39	I A B
NGC5806	Sb	12-m	10	0.33 × 0.27	D22	1354.1 ± 0.2	345.6 ± 0.6	59 ± 2	59 ± 5	–	403 ± 21	I A B
NGC6500	Sab	7-m	10	7.96 × 6.24	TW	3001.8 ± 0.7	447.5 ± 1.3	38 ± 9	53 ± 3	–	560 ± 22	I A B
NGC6753	Sb	12-m	10	0.21 × 0.10	D22	3148.3 ± 0.1	410.3 ± 0.3	30 ± 7	34 ± 10	–	734 ± 190	I A B
NGC6958	E	12-m	10	0.18 × 0.09	TW	2686.6 ± 0.7	450.3 ± 2.1	40 ± 3	45 ± 6	–	637 ± 67	I A B
NGC7049	S0	7-m	20	7.35 × 4.95	TW	2217.7 ± 0.8	644.4 ± 1.6	52 ± 4	55 ± 3	–	787 ± 29	I A B
NGC7052	E	12-m	15	0.13 × 0.10	S21	4627.1 ± 0.9	701.4 ± 0.5	63 ± 2	73 ± 2	75 ± 1	726.1 ± 3.4	I A B
NGC7172	Sa	12-m	10	0.15 × 0.12	D22	2506.9 ± 0.1	637.6 ± 0.4	50 ± 4	83 ± 1	–	642.4 ± 1.4	I A B
NGC7424	Sc	7-m	10	7.14 × 4.91	TW	931.5 ± 0.5	33.1 ± 1.1	33 ± 4	–	–	60.8 ± 6.8	×
PGC006240	E-S0	7-m	10	7.94 × 5.91	TW	7877 ± 1	345.8 ± 4.0	63 ± 4	28 ± 6	–	737 ± 150	I A
PGC043387	E	12-m	13	0.76 × 0.52	D22	6696.6 ± 0.4	500.3 ± 0.7	45 ± 4	47 ± 5	–	684 ± 56	I A B
UGC1214	S0-a	7-m	30	8.00 × 4.67	TW	5066 ± 3	225.2 ± 8.3	25 ± 10	18 ± 3	–	729 ± 120	I
UGC1395	Sb	7-m	10	7.20 × 4.69	TW	5062.2 ± 0.7	200.0 ± 1.7	55 ± 3	51 ± 5	–	257 ± 18	I A B

Integrated-intensity, luminosity-weighted mean line-of-sight velocity and luminosity-weighted line-of-sight velocity dispersion maps were created for all sample galaxies using the PYMAKEPLOTS package. For the ACA data, we created data cubes with and without primary-beam correction. The cubes without primary-beam correction were then first spatially and spectrally smoothed, using typically a boxcar spatial kernel 1.5 times the width of the synthesised beam and a boxcar spectral kernel 4 times the channel width. These smoothed data cubes were then clipped to a specific threshold (typically 3 – 8 times the RMS noise of the line-free channels) to create a binary mask. These masks were then applied to the unsmoothed primary-beam corrected cubes to create moment maps. Major-axis PVDs were created by taking cuts through the masked primary-beam corrected cubes at kinematic position angles determined by eye, as the position angles of the molecular gas distributions do not always align with the optical position angles. The integrated spectra were constructed by summing, for each velocity channel, the flux density over all spatial pixels within the regions with emission as defined by the aforementioned mask. The noise in each velocity bin is calculated using the same method as Liang et al. (2023), whereby for a given emission channel we apply its PYMAKPLOTS mask to each of the line-free channel of the data cube, sum the flux densities within the masked region, and adopt the RMS of those sums as the integrated flux uncertainty of that channel. An example of the resulting moment maps, PVD and integrated spectrum of an ACA sample galaxy is shown in Fig. 4.1. The top-left panel shows the zeroth-moment (integrated-intensity) map. The blue circle indicates the full-width-at-half-maximum (FWHM) of the primary beam, i.e. the field of view. The red circle indicates the extent where the sensitivity is below 20 per cent of the primary beam gain, indicating the maximal extent of the data cube. The galaxy name is displayed to the left of the moment map. The top-middle panel shows the first-moment (intensity-weighted mean line-of-sight velocity) map, with a line overlaid indicating the assumed kinematic major-axis position angle. The top-right panel shows the second-moment (intensity-weighted line-of-sight velocity dispersion) map. The synthesised beam is shown in the bottom-left corner of each map as an open ellipse. The bottom-middle panel shows the kinematic major-axis position-velocity diagram. A cross, whose vertical line shows the channel width of the cube and whose horizontal line shows the size of the synthesised beam projected along

the kinematic major-axis, is shown in the bottom-left corner of the PVD. The position angle along which the PVD is taken is shown in the upper-right corner of the PVD. The rest of the figures for other galaxies can be viewed in the online appendix of Dominiak et al. (2026b).

For the 12-m data, we primarily had access to data cubes without primary-beam correction. We then followed the same procedure as above, but the binary masks were created from and applied to the same cubes. In addition, the position angle from previous kinematic modelling work was adopted when available. The resulting moment maps, PVDs and integreated spectra of the 12-m sample galaxies are as in Fig. 4.1 and will be available in the online appendix of Dominiak et al. (2026b).

4.2.2 Optical data

To compare the CO and optical extents of the galaxies, in the bottom-right panel of Fig. 4.1 (and in each Figure the online appendix) we also overlay the CO contours of each galaxy in green over a red-band optical image from the Digitized Sky Survey-2 (DSS), obtained from the European Southern Observatory archive[1]. As in the zeroth-moment map, the primary beam is shown as a blue circle and the cube extent is shown as a red circle. The optical D_{25} diameter of the galaxy, representing the diameter of the isophote where the surface brightness is 25 mag arcsec^{-2} in the B-band, is shown as a white dashed ellipse.

4.2.3 Velocity widths

To characterise the rotational velocity of each sample galaxy, we adopt the width of the integrated CO spectrum at 50% of its maximum (W_{50}). As in previous studies, we fit the integrated spectrum and derive W_{50} from the fit rather than measure it directly from the data (e.g. Tiley et al. 2016b; Topal et al. 2018). We use one of two functions to fit each spectrum. When the integrated spectrum has the typical double-horned shape expected of a rotating disc, we use a Gaussian Double Peak function (i.e. a central parabola flanked by two symmetric half-Gaussians equidistant from a central velocity; Eq. A2 of Tiley et al. 2016b). This has been shown to be the most accurate fitting function, minimising potential biases as a function of the amplitude-to-noise ratio of the spectrum, the galaxy inclination

[1] https://archive.eso.org/dss/dss

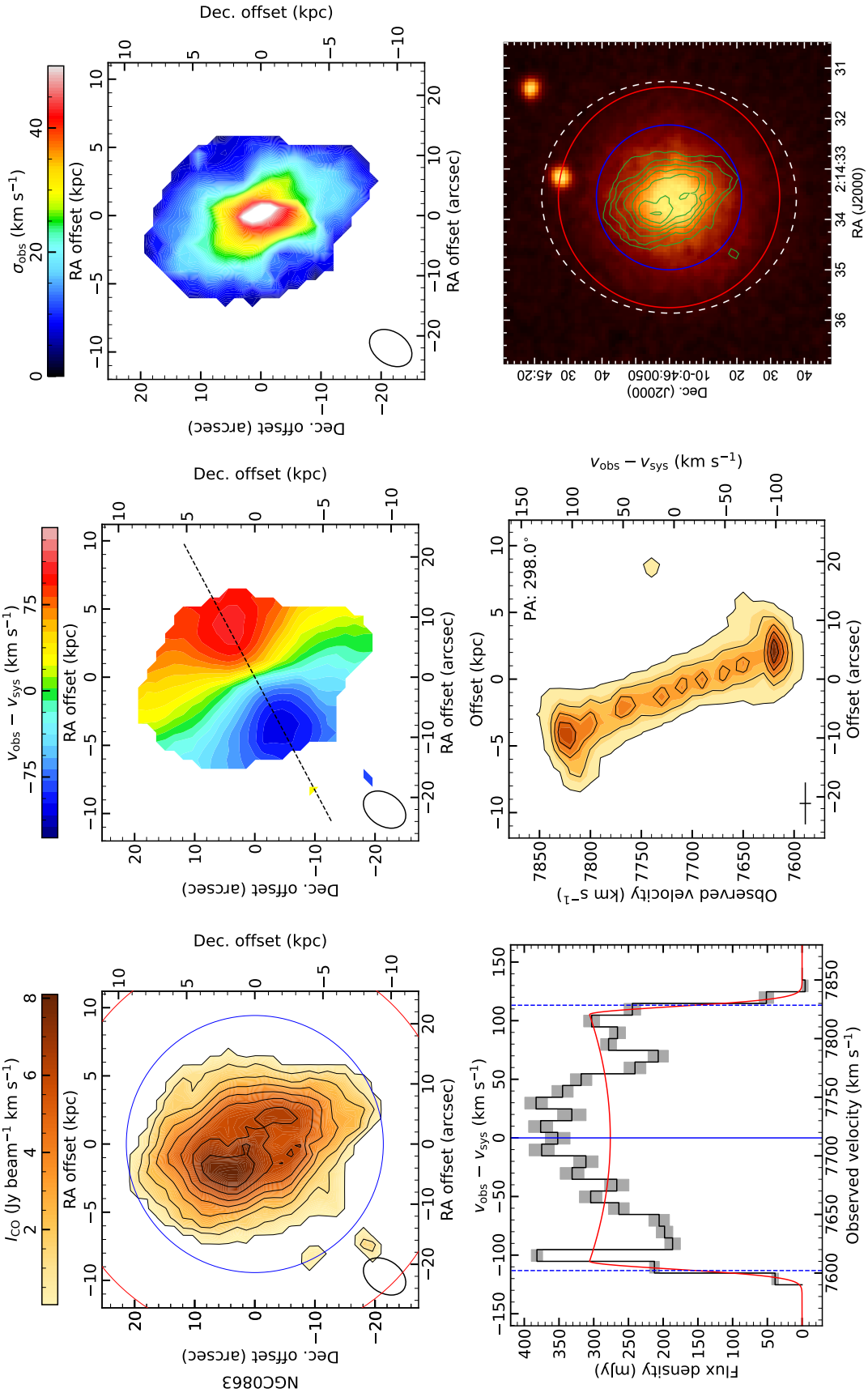


Figure 4.1: Example ^{12}CO(2–1) data products derived from ALMA WISDOM data (see text for details).

and the galaxy rotation velocity (Tiley et al. 2016b). In cases where the spectrum is not double-horned, we use a single Gaussian function. Spectra of that shape are typically observed when a galaxy has an incomplete or spatially limited CO distribution, the inclination of the galaxy is low and/or the galaxy is of a particularly late morphological type (with a solid-body rather than flat rotation curve).

To fit the functions to the integrated spectra, we adopt the Levenberg-Marquardt least-squares minimisation algorithm, using the MPFIT code (Markwardt 2009) implemented as a Python routine in the `astrolibpy`[2] library. The best-fitting parameters are defined as those that minimise the reduced χ^2

$$\chi^2_{\rm red} \equiv \frac{1}{\rm DOF} \sum_i \left(\frac{[F(v_i) - f(v_i)]^2}{\sigma^2_{i,\rm RMS}} \right) \quad , \tag{4.1}$$

where $F(v_i)$ and $f(v_i)$ are the observed and modelled flux density in the $i^{\rm th}$ velocity bin v_i, respectively, DOF the number of degrees of freedom of the fit and $\sigma_{i,\rm RMS}$ the RMS noise of the spectrum in the $i^{\rm th}$ velocity bin. In previous studies $\sigma_{\rm RMS}$ was taken as a constant, defined as the RMS noise in the line-free channels of the cube. However, it is more appropriate to consider the RMS in each velocity bin which we determined as outlined in Section 4.2.1 For each sample galaxy, the best fit overlaid on the integrated spectrum is shown in the online appendix, together with an example in Fig. 4.1, alongside the moment maps and PVD of the galaxy.

To avoid converging to local minima, we run the MPFIT code several times with a variety of initial guesses. For certain integrated spectra, the central parabola of the best-fitting Gaussian Double Peak function has a larger amplitude than that of the half-Gaussians. We allow these profiles as long as $2A_{\rm C}/3 \leq A_{\rm G}$, where $A_{\rm C}$ is the amplitude of the central parabola and $A_{\rm G}$ is the amplitude of the half-Gaussians. If this condition is not met we choose to fit the spectrum with a single Gaussian function irrespective of $\chi^2_{\rm red}$ (see Tiley et al. 2016b; Topal et al. 2018).

The velocity width at 50% of the peak of the Gaussian Double Peak function (W_{50}) can be calculated in an analytical manner as

$$W_{50} = 2(w + \sigma\sqrt{2\ln 2}) \quad , \tag{4.2}$$

[2] https://github.com/segasai/astrolibpy/tree/master

where w is the half-width of the central parabola and σ is the width of the half-Gaussian edges. For a single Gaussian function (i.e. when $w = 0$), this reduces to

$$W_{50} = 2\sqrt{2\ln 2}\sigma \quad . \tag{4.3}$$

The best-fitting W_{50} are listed in Table 4.1. The bottom-left panel of Fig. 4.1 shows the integrated spectrum with statistical uncertainties shown as grey shading. Shown in red is the best-fit function. The solid blue line shows the best-fit central velocity v_0, whilst the dashed blue lines show the width at 50% of the peak W_{50}.

4.2.4 Photometry

In this paper we use two photometric measures as proxies of the luminous masses of galaxies. First, as done in many previous TFR studies, we use the total absolute K-band (2.15 μm) magnitude as a proxy for the bulk of the stellar mass. In particular, we use the `k_m_ext` quantity from the 2MASS (Skrutskie et al. 2006) Extended Source Catalog (XSC), which is the integrated apparent K_s-band magnitude measured within a Kron aperture with an extrapolated surface brightness profile, ensuring the recovery of flux lost as a result of background noise. Despite the near-infrared wavelength, these measurements are nevertheless subject to dust extinction. As such, we calculate the extinction-corrected total absolute K_s-band magnitude as

$$M_{K_s} = m_{K_s} - A_{K_s} - \mu \quad , \tag{4.4}$$

where m_{K_s} is the integrated apparent K_s-band magnitude, A_{K_s} the Galactic extinction in the 2MASS K_s-band calculated from the dust maps of Schlafly & Finkbeiner (2011) taken from the NASA/IPAC Infrared Science Archive[3] and μ is the distance modulus taken as the `modbest` parameter from HyperLEDA[4].

Second, we use the *Wide-Field Infrared Survey Explorer* (*WISE*) Band 1 (3.4 μm) magnitudes ($W1$) as another probe of stellar mass. Specifically, we adopt the `w1gmag` quantity from the AllWISE Source Catalog[5], which is the $W1$ apparent magnitude m_{W1} measured within an elliptical aperture with a size, shape and orientation based on that

[3] https://irsa.ipac.caltech.edu/applications/DUST/
[4] http://atlas.obs-hp.fr/hyperleda/
[5] http://wise2.ipac.caltech.edu/docs/release/allwise/

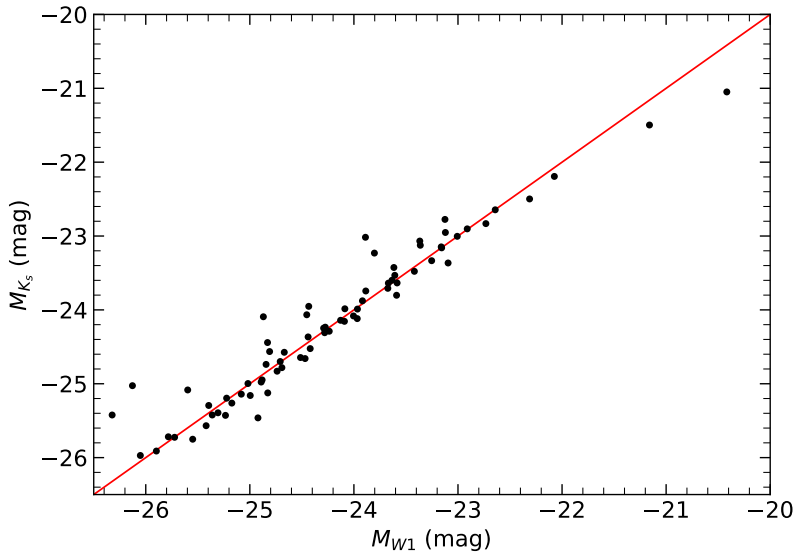


Figure 4.2: Correlation between the total absolute $W1$-band and K_s-band magnitudes of our sample of galaxies. The solid red line shows the 1 : 1 relation.

reported in the 2MASS XSC. We calculate the extinction-corrected total absolute $W1$ magnitudes as in Eq. 4.4, with the extinctions A_{W1} also taken from the NASA/IPAC Infrared Science Archive and the same distance moduli.

The K_s- and $W1$-band apparent magnitudes, as well as the extinctions and the distance moduli, were available for 74 galaxies in our sample, with the exception of NGC0404 which is a nearby low-luminosity dwarf galaxy. The K_s- and $W1$-bands are known to track similar stellar populations and are strongly correlated with one another. We show this correlation in Fig. 4.2, demonstrating that there is no systematic difference between the two measures. The Spearman correlation coefficient is $r_s = 0.97$, in line with Topal et al. (in prep.). The average $K_s - W1$ colour of our sample galaxies (i.e. the average difference between the integrated K_s-band and $W1$-band apparent magnitudes) is ≈ 0.05 mag, with a scatter of ≈ 0.3 mag.

4.2.5 Inclinations

For use in the TFR, the velocity widths obtained in Section 4.2.3 must be deprojected (i.e. corrected for the galaxy inclinations). It is important to use reliable inclination measures, as inclination uncertainties contribute greatly to the deprojected velocity width uncertainties, and reliable inclinations lead to reduced total scatters around the best-fitting TFRs (Davis et al. 2011a). Ideally, we should be using a methodology that directly measures the inclination

Table 4.2: Photometric data for the galaxy sample.

Galaxy	D_{25} (arcsec)	b/a	PA (°)	m_{W1} (mag)	A_{W1} (mag)	m_{K_s} (mag)	A_{K_s} (mag)	μ (mag)	M_{W1} (mag)	M_{K_s} (mag)
(1)	(2)	(3)	(4)	(5)	(6)	(7)	(8)	(9)	(10)	(11)
ESO383-G035	61 ± 7	0.58 ± 0.04	116	8.702 ± 0.005	0.011	9.582 ± 0.017	0.019	32.58 ± 0.49	−23.89 ± 0.50	−23.02 ± 0.51
FRL49	29†	0.80†	160	8.534 ± 0.005	0.012	9.644 ± 0.015	0.020	34.65 ± 0.19	−26.13 ± 0.20	−25.03 ± 0.21
IC0843	64 ± 15	0.49 ± 0.06	135	10.312 ± 0.006	0.003	10.228 ± 0.024	0.005	35.20 ± 0.14	−24.89 ± 0.15	−24.98 ± 0.16
IC1481	43 ± 12	$0.89^{+0.11}_{-0.12}$	45	10.627 ± 0.006	0.015	10.623 ± 0.037	0.024	34.74 ± 0.18	−24.13 ± 0.19	−24.14 ± 0.22
IC4329A	95 ± 7	0.56 ± 0.04	46	7.898 ± 0.005	0.011	8.805 ± 0.013	0.018	34.21 ± 0.23	−26.32 ± 0.24	−25.42 ± 0.24
MRK0567	25†	0.90†	70	10.148 ± 0.006	0.005	10.664 ± 0.029	0.008	35.74 ± 0.11	−25.60 ± 0.12	−25.08 ± 0.14
NGC0017	69 ± 10	0.34 ± 0.02	32	9.825 ± 0.006	0.005	10.074 ± 0.030	0.008	34.63 ± 0.19	−24.81 ± 0.20	−24.56 ± 0.22
NGC0289	203 ± 9	0.74 ± 0.03	132	7.960 ± 0.006	0.004	7.997 ± 0.027	0.006	31.59 ± 0.26	−23.63 ± 0.27	−23.60 ± 0.29
NGC0383	144 ± 10	0.83 ± 0.06	8	8.486 ± 0.007	0.014	8.481 ± 0.023	0.022	34.37 ± 0.21	−25.90 ± 0.22	−25.91 ± 0.23
NGC0404	203 ± 14	$1.00^{+0.00}_{-0.12}$	–	–	–	–	–	–	–	–
NGC0449	41 ± 5	0.56 ± 0.04	78	10.929 ± 0.006	0.006	11.173 ± 0.052	0.018	34.28 ± 0.22	−23.36 ± 0.23	−23.13 ± 0.27
NGC0524	203 ± 19	$1.00^{+0.00}_{-0.09}$	–	7.215 ± 0.006	0.016	7.163 ± 0.012	0.026	32.56 ± 0.03	−25.36 ± 0.04	−25.42 ± 0.04
NGC0541	131 ± 9	0.69 ± 0.03	69	9.453 ± 0.006	0.009	9.295 ± 0.031	0.014	34.44 ± 0.20	−25.00 ± 0.21	−25.16 ± 0.23
NGC0612	89 ± 6	0.89 ± 0.06	160	9.492 ± 0.006	0.004	9.575 ± 0.028	0.006	35.54 ± 0.12	−26.05 ± 0.13	−25.97 ± 0.15
NGC0708	154 ± 14	0.48 ± 0.03	38	8.859 ± 0.008	0.017	8.574 ± 0.026	0.028	33.67 ± 0.41	−24.83 ± 0.42	−25.12 ± 0.44
NGC0863	76 ± 7	0.91 ± 0.06	176	9.738 ± 0.006	0.007	9.540 ± 0.024	0.011	35.28 ± 0.14	−25.55 ± 0.15	−25.75 ± 0.16
NGC1084	203 ± 14	0.66 ± 0.03	40	7.628 ± 0.006	0.005	7.930 ± 0.023	0.008	30.99 ± 0.26	−23.37 ± 0.27	−23.07 ± 0.28
NGC1194	93 ± 9	0.50 ± 0.03	139	9.361 ± 0.005	0.014	9.758 ± 0.029	0.024	33.80 ± 0.27	−24.45 ± 0.28	−24.07 ± 0.30

Notes. (1) Galaxy name. (2) Galaxy diameter at the 25 mag arcsec^{-2} isophote in the B-band from HyperLeda. † indicates galaxies with no measurement, in which case the diameter at the 20 mag arcsec^{-2} isophote in the K_s-band from 2MASS is listed instead (quantity `r_k20fe` of the 2MASS All-Sky Extended Source Catalog). (3) Galaxy axial ratio from HyperLEDA. † indicates galaxies for which the axial ratio of the 3-sigma K_s-band isophote is listed instead (quantity `k_ba` of the 2MASS All-Sky Extended Source Catalog). (4) Position angle of the galaxy major axis at the 25 mag arcsec^{-2} isophote in the B-band from HyperLEDA. (5) Galaxy total apparent $W1$-band Vega magnitude from the AllWISE Source Catalog. (6) $W1$-band extinction from the NASA/IPAC Infrared Science Archive. (7) Galaxy total apparent K_s-band Vega magnitude from the 2MASS All-Sky Extended Source Catalog. (8) K_s-band extinction from the NASA/IPAC Infrared Science Archive. (9) Galaxy mean distance modulus from HyperLEDA. (10) Galaxy extinction-corrected total absolute $W1$-band Vega magnitude. (11) Galaxy extinction-corrected total absolute K_s-band Vega magnitude.

Table 4.2: continued.

Galaxy	D_{25} (arcsec)	b/a	PA (°)	m_{W1} (mag)	A_{W1} (mag)	m_{K_s} (mag)	A_{K_s} (mag)	μ (mag)	M_{W1} (mag)	M_{K_s} (mag)
(1)	(2)	(3)	(4)	(5)	(6)	(7)	(8)	(9)	(10)	(11)
NGC1300	353 ± 24	0.51 ± 0.04	105	7.831 ± 0.008	0.006	7.564 ± 0.047	0.009	30.92 ± 0.32	−23.10 ± 0.33	−23.37 ± 0.37
NGC1358	128 ± 9	0.55 ± 0.04	15	9.033 ± 0.006	0.011	8.948 ± 0.032	0.018	33.76 ± 0.28	−24.74 ± 0.29	−24.83 ± 0.31
NGC1387	169 ± 13	$1.00^{+0.00}_{-0.07}$	–	7.446 ± 0.006	0.002	7.425 ± 0.018	0.004	31.41 ± 0.10	−23.97 ± 0.11	−23.99 ± 0.12
NGC1400	169 ± 8	0.89 ± 0.04	45	7.855 ± 0.006	0.012	7.811 ± 0.018	0.020	32.08 ± 0.09	−24.24 ± 0.10	−24.29 ± 0.11
NGC1448	477 ± 22	0.19 ± 0.01	42	7.517 ± 0.005	0.003	7.660 ± 0.026	0.004	31.40 ± 0.03	−23.89 ± 0.04	−23.74 ± 0.06
NGC1493	208 ± 10	0.93 ± 0.04	93	9.142 ± 0.008	0.002	8.806 ± 0.090	0.003	30.30 ± 1.43	−21.16 ± 1.44	−21.50 ± 1.52
NGC1497	74 ± 7	0.52 ± 0.04	63	9.535 ± 0.006	0.041	9.475 ± 0.028	0.068	34.80 ± 0.17	−25.31 ± 0.18	−25.39 ± 0.20
NGC1574	237 ± 11	0.92 ± 0.04	14	7.033 ± 0.006	0.003	7.109 ± 0.023	0.005	31.47 ± 0.21	−24.44 ± 0.22	−24.37 ± 0.23
NGC2110	109 ± 10	0.92 ± 0.04	175	7.711 ± 0.006	0.071	8.144 ± 0.019	0.116	32.47 ± 0.51	−24.83 ± 0.52	−24.44 ± 0.53
NGC2179	120 ± 8	0.72 ± 0.03	165	9.267 ± 0.006	0.012	9.224 ± 0.027	0.019	32.84 ± 0.43	−23.59 ± 0.44	−23.64 ± 0.46
NGC2187A	213 ± 20	0.48 ± 0.06	75	9.984 ± 0.006	0.018	9.961 ± 0.051	0.029	33.64 ± 0.30	−23.67 ± 0.31	−23.71 ± 0.35
NGC2911	208 ± 14	0.62 ± 0.04	135	8.897 ± 0.009	0.006	8.711 ± 0.033	0.010	33.36 ± 0.34	−24.47 ± 0.35	−24.66 ± 0.37
NGC2964	177 ± 12	0.74 ± 0.05	97	7.781 ± 0.005	0.004	8.355 ± 0.014	0.006	31.58 ± 0.77	−23.80 ± 0.78	−23.23 ± 0.78
NGC2974	213 ± 10	0.62 ± 0.06	44	6.788 ± 0.005	0.010	6.255 ± 0.005	0.017	31.70 ± 0.22	−24.92 ± 0.23	−25.46 ± 0.23
NGC3021	81 ± 13	0.59 ± 0.07	110	8.987 ± 0.006	0.003	9.178 ± 0.015	0.004	32.60 ± 0.04	−23.62 ± 0.05	−23.43 ± 0.06
NGC3156	114 ± 11	0.54 ± 0.06	50	9.663 ± 0.006	0.007	9.548 ± 0.037	0.011	31.73 ± 0.14	−22.07 ± 0.15	−22.19 ± 0.18
NGC3169	262 ± 24	0.62 ± 0.07	49	7.235 ± 0.006	0.006	7.283 ± 0.021	0.010	31.52 ± 0.03	−24.29 ± 0.04	−24.25 ± 0.05
NGC3277	128 ± 9	0.76 ± 0.05	29	9.023 ± 0.006	0.005	8.926 ± 0.017	0.008	31.75 ± 0.71	−22.73 ± 0.72	−22.83 ± 0.73
NGC3351	435 ± 20	0.62 ± 0.06	11	6.742 ± 0.008	0.005	6.665 ± 0.036	0.009	29.99 ± 0.02	−23.25 ± 0.03	−23.33 ± 0.06
NGC3368	499 ± 35	0.66 ± 0.06	5	6.286 ± 0.008	0.005	6.320 ± 0.023	0.008	29.95 ± 0.02	−23.67 ± 0.03	−23.64 ± 0.04
NGC3393	117 ± 8	0.87 ± 0.06	13	8.955 ± 0.006	0.014	9.059 ± 0.039	0.023	33.61 ± 0.30	−24.67 ± 0.31	−24.57 ± 0.34
NGC3607	274 ± 25	0.87 ± 0.10	120	7.082 ± 0.006	0.004	6.994 ± 0.023	0.006	31.77 ± 0.17	−24.69 ± 0.18	−24.78 ± 0.19
NGC3810	199 ± 14	0.68 ± 0.03	29	7.777 ± 0.010	0.008	7.952 ± 0.028	0.014	30.89 ± 0.25	−23.12 ± 0.26	−22.95 ± 0.28
NGC3862	66 ± 17	$1.00^{+0.00}_{-0.01}$	–	9.680 ± 0.007	0.004	9.489 ± 0.035	0.007	34.91 ± 0.17	−25.23 ± 0.18	−25.43 ± 0.21
NGC4030	228 ± 11	0.71 ± 0.03	21	7.221 ± 0.007	0.005	7.330 ± 0.015	0.008	32.06 ± 0.35	−24.84 ± 0.36	−24.74 ± 0.37
NGC4061	55 ± 8	0.85 ± 0.06	1	9.907 ± 0.007	0.007	9.763 ± 0.027	0.011	35.32 ± 0.03	−25.42 ± 0.04	−25.57 ± 0.06
NGC4203	203 ± 9	0.92 ± 0.06	10	7.463 ± 0.008	0.002	7.406 ± 0.014	0.004	30.88 ± 0.18	−23.42 ± 0.19	−23.48 ± 0.19
NGC4212	169 ± 12	0.60 ± 0.04	74	8.021 ± 0.006	0.006	8.375 ± 0.010	0.010	31.14 ± 0.16	−23.13 ± 0.17	−22.78 ± 0.17

Table 4.2: continued.

Galaxy	D_{25} (arcsec)	b/a	PA (°)	m_{W1} (mag)	A_{W1} (mag)	m_{K_s} (mag)	A_{K_s} (mag)	μ (mag)	M_{W1} (mag)	M_{K_s} (mag)
(1)	(2)	(3)	(4)	(5)	(6)	(7)	(8)	(9)	(10)	(11)
NGC4235	262 ± 18	0.20 ± 0.02	49	8.397 ± 0.005	0.004	8.396 ± 0.028	0.006	31.55 ± 0.72	−23.16 ± 0.73	−23.16 ± 0.75
NGC4245	154 ± 11	0.63 ± 0.04	146	8.312 ± 0.006	0.004	8.311 ± 0.019	0.006	30.95 ± 1.04	−22.64 ± 1.05	−22.65 ± 1.06
NGC4261	256 ± 12	0.79 ± 0.04	160	7.350 ± 0.007	0.003	7.263 ± 0.028	0.005	32.52 ± 0.12	−25.17 ± 0.13	−25.26 ± 0.15
NGC4278	173 ± 16	$0.98^{+0.02}_{-0.05}$	23	7.245 ± 0.006	0.006	7.184 ± 0.011	0.009	31.33 ± 0.11	−24.09 ± 0.12	−24.16 ± 0.12
NGC4429	315 ± 15	0.46 ± 0.04	98	6.738 ± 0.006	0.006	6.783 ± 0.023	0.010	30.65 ± 0.41	−23.92 ± 0.42	−23.88 ± 0.43
NGC4435	181 ± 8	0.71 ± 0.05	12	7.506 ± 0.006	0.006	7.297 ± 0.016	0.009	31.09 ± 0.04	−23.59 ± 0.05	−23.80 ± 0.06
NGC4438	547 ± 25	0.44 ± 0.05	27	7.258 ± 0.006	0.005	7.265 ± 0.023	0.009	30.26 ± 0.35	−23.01 ± 0.36	−23.00 ± 0.37
NGC4501	523 ± 36	0.50 ± 0.05	138	6.160 ± 0.008	0.007	6.267 ± 0.017	0.012	30.24 ± 0.02	−24.09 ± 0.03	−23.99 ± 0.04
NGC4697	425 ± 29	0.59 ± 0.04	79	6.442 ± 0.008	0.006	6.367 ± 0.027	0.009	30.44 ± 0.08	−24.00 ± 0.09	−24.08 ± 0.11
NGC4826	628 ± 29	0.51 ± 0.04	114	5.317 ± 0.017	0.008	5.330 ± 0.017	0.013	28.22 ± 0.02	−22.91 ± 0.04	−22.90 ± 0.04
NGC4845	330 ± 15	0.22 ± 0.01	82	7.717 ± 0.005	0.004	7.794 ± 0.023	0.006	31.32 ± 0.33	−23.61 ± 0.34	−23.53 ± 0.35
NGC5064	161 ± 7	0.52 ± 0.02	37	7.967 ± 0.006	0.030	8.014 ± 0.018	0.049	33.16 ± 0.22	−25.22 ± 0.23	−25.20 ± 0.24
NGC5084	600 ± 28	0.25 ± 0.02	80	7.110 ± 0.006	0.022	7.058 ± 0.027	0.036	31.97 ± 0.64	−24.88 ± 0.65	−24.95 ± 0.67
NGC5273	137 ± 10	0.66 ± 0.05	6	8.850 ± 0.007	0.002	8.665 ± 0.024	0.003	31.16 ± 0.12	−22.31 ± 0.13	−22.50 ± 0.14
NGC5427	218 ± 15	0.91 ± 0.08	11	8.614 ± 0.008	0.005	8.590 ± 0.046	0.009	32.89 ± 0.36	−24.28 ± 0.37	−24.31 ± 0.41
NGC5746	435 ± 20	0.15 ± 0.01	172	6.773 ± 0.005	0.008	6.878 ± 0.017	0.012	32.16 ± 0.32	−25.40 ± 0.33	−25.29 ± 0.34
NGC5765b	49 ± 14	0.68 ± 0.09	144	10.429 ± 0.006	0.007	10.455 ± 0.039	0.012	35.44 ± 0.13	−25.02 ± 0.14	−25.00 ± 0.17
NGC5806	181 ± 8	0.54 ± 0.02	172	8.429 ± 0.006	0.010	8.449 ± 0.022	0.016	31.58 ± 0.09	−23.16 ± 0.10	−23.15 ± 0.11
NGC6500	125 ± 17	0.79 ± 0.09	45	9.102 ± 0.007	0.017	9.154 ± 0.029	0.028	33.36 ± 0.34	−24.28 ± 0.35	−24.23 ± 0.37
NGC6753	177 ± 12	0.87 ± 0.06	27	7.450 ± 0.007	0.013	7.523 ± 0.025	0.021	33.22 ± 0.36	−25.78 ± 0.37	−25.72 ± 0.39
NGC6958	147 ± 10	0.78 ± 0.04	93	8.499 ± 0.006	0.009	8.400 ± 0.018	0.014	32.91 ± 0.41	−24.42 ± 0.42	−24.52 ± 0.43
NGC7049	239 ± 17	0.68 ± 0.05	64	7.299 ± 0.007	0.011	7.246 ± 0.022	0.017	32.37 ± 0.20	−25.08 ± 0.21	−25.14 ± 0.22
NGC7052	109 ± 10	0.49 ± 0.03	66	8.560 ± 0.006	0.023	8.574 ± 0.020	0.039	34.26 ± 0.22	−25.72 ± 0.23	−25.73 ± 0.24
NGC7172	151 ± 10	0.66 ± 0.05	104	7.905 ± 0.006	0.005	8.317 ± 0.023	0.008	32.77 ± 0.44	−24.87 ± 0.45	−24.46 ± 0.46
NGC7424	455 ± 31	0.85 ± 0.04	8	9.885 ± 0.009	0.002	9.254 ± 0.066	0.003	30.30 ± 1.41	−20.42 ± 1.42	−21.05 ± 1.48
PGC006240	66 ± 11	0.55 ± 0.05	109	10.606 ± 0.006	0.004	10.617 ± 0.034	0.006	35.31 ± 0.14	−24.71 ± 0.15	−24.70 ± 0.17
PGC043387	50 ± 6	0.72 ± 0.05	150	10.549 ± 0.006	0.002	10.419 ± 0.031	0.004	35.06 ± 0.15	−24.51 ± 0.16	−24.65 ± 0.18
UGC1214	63 ± 7	0.91 ± 0.06	57	9.900 ± 0.006	0.004	10.385 ± 0.030	0.007	34.33 ± 0.21	−24.43 ± 0.22	−23.95 ± 0.24
UGC1395	74 ± 7	0.60 ± 0.04	159	10.396 ± 0.007	0.014	10.254 ± 0.064	0.022	34.35 ± 0.21	−23.97 ± 0.22	−24.12 ± 0.27

of the molecular gas. When available, we thus use inclinations obtained through kinematic modelling of the CO data ($i_{\rm CO}$; Column 11 of Table 4.1). However, the number of galaxies with existing kinematic modelling is rather small.

When no such modelling is available, we attempt to obtain inclination estimates from ellipse fitting to the dust lanes visible in *HST* images ($i_{\rm dust}$; Column 10 of Table 4.1). This method has been shown to yield reliable inclination measures (e.g. Davis et al. 2011a) due to the dust typically being spatially coincident with the molecular gas (e.g. Young et al. 2008; Crocker et al. 2008; Bolatto et al. 2013). Unsharp-masked optical images, preferably in a blue filter for which the dust is more prominent, were thus created and ellipses fit by eye. Figure 4.3 shows representative examples of the ellipse-fitting procedure. In galaxies with a regular dust disc (e.g. NGC 4697), the ellipse parameters are well constrained and the derived inclination is correspondingly precise. In more complex systems, however, the dust may exhibit flocculent or spiral structures (e.g. NGC 4429 and NGC 5995) or be confined to an irregular circumnuclear region (e.g. FRL 49). In such cases, the fitted ellipse is intended to represent the underlying projected geometry of the dust disc rather than individual dust filaments or clumps. Consequently, some degree of judgement is required when defining the best-fitting ellipse, and this subjectivity is reflected in the larger quoted inclination uncertainties for these galaxies. As the dust disc is assumed to be infinitely thin, the inclination is obtained from the usual expression

$$i_{\rm dust} = \cos^{-1}(q) \quad , \tag{4.5}$$

where q is the minor-to-major axis ratio of the best-fitting ellipse. We were able to derive inclinations for the vast majority of our sample galaxies using this method.

When no dust lane is visible in *HST* images, we estimate the galaxy inclination using the axial ratio of the 25 mag arcsec^{-2} B-band isophote taken from HyperLEDA. These axial ratios can be converted into inclinations ($i_{a/b}$) using the standard expression (Holmberg 1958)

$$i_{b/a} = \cos^{-1}\left(\sqrt{\frac{q^2 - q_0^2}{1 - q_0^2}}\right) \quad , \tag{4.6}$$

where q is taken from HyperLEDA and q_0 is the intrinsic axial ratio (when the galaxy is seen edge-on). As q_0 is morphology dependent, we choose $q_0 = 0.34$ for early-type galaxies and

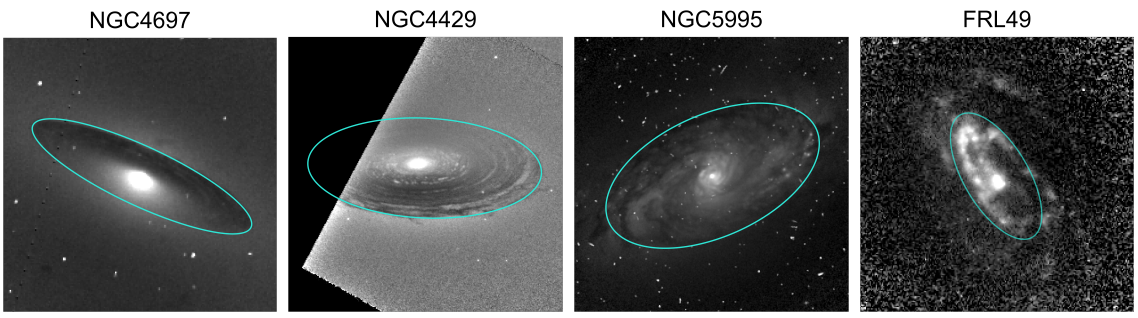


Figure 4.3: Four examples of unsharp-masked images showing dusty discs and spiral structures. Overlaid in cyan are the best-fitting ellipses from which we estimate the dust inclination. From left to right: NGC 4697 with a regular, well-defined dust disc; NGC 4429 with a flocculent dust disc with a clearly identifiable underlying geometry; NGC 5995 with a spiral dust morphology requiring the ellipse to trace the global disc rather than the individual dust lanes; and FRL49 with a compact and asymmetric circumnuclear dust disc where the outer extent of the disc is less clearly defined. These examples illustrate the range of dust morphologies encountered in the sample and the judgement involved when fitting ellipses by eye.

$q_0 = 0.20$ for late-type galaxies, following the methodologies of Davis et al. (2011a) and Tiley et al. (2016b). The galaxy morphological types were also obtained from HyperLEDA and are listed in Table 4.2. Inclinations obtained using this method are listed in Column 9 of Table 4.1.

4.3 Results

4.3.1 Data sub-samples

Of our parent sample of 75 galaxies, one does not have the necessary photometric data available (NGC0404) and three are clear outliers in the sample, two of which have unusually narrow Gaussian-shaped velocity widths (NGC1493 and NGC7424) and one of which has an unusually low velocity width given its very bright absolute magnitude (NGC5746). We refer to the remaining sample of 71 galaxies as the *initial* sample, as it represents the most complete sample of galaxies in this study. However, we can and will impose additional criteria to create more homogenous samples. We explore these below.

Integrated spectral shapes

When studying the CO TFR, we must ensure that the CO emission of each galaxy reaches sufficiently large radii to trace the asymptotically flat region of the galaxy's rotation curve. As the rotational velocity serves as a proxy of the total dynamical mass of the galaxy, any

underestimation of this rotational velocity will result in a systematic bias (and increased scatter) of the TFR relation. However, the integrated spectra of kinematic tracers exhibiting boxy or double-horned shapes likely extend beyond the turnover radii of the rotation curves, and thus reliably probe the outer parts of galaxies (Davis et al. 2011a). As such, in addition to analysing the entire initial sample of galaxies, we will also analyse galaxy subsets which omit all the integrated spectra that do not meet this criterion, i.e. single Gaussian profiles. This eliminates an additional 4 galaxies from our ACA sample and 2 galaxies from our 12-m sample, bringing the total number of sample galaxies to 65. We will refer to this galaxy sub-sample as *sub-sample A*.

Inclinations

Given that the velocities need to deprojected (i.e. corrected for the inclination) for TFR work, the uncertainties of the inclinations translate to (additional) uncertainties in the deprojected velocities. In addition to the restriction based on the shape of the velocity profile discussed above, we therefore create another subset of galaxies by eliminating galaxies whose inclination uncertainties are large, i.e. (face-on) galaxies with low inclinations, specifically galaxies with inclinations $i < 30°$ (e.g. Pierce & Tully 1988; Tiley et al. 2016b). This eliminates 7 more galaxies from our ACA sample and 5 more galaxies from our 12-m data sample, bringing the total number of sample galaxies to 53. We will refer to this galaxy sub-sample, which imposes both the velocity profile shape restriction and the inclination cut-off, as *sub-sample B*.

4.3.2 Tully-Fisher relation

The general form of the Tully-Fisher relation we adopt is

$$M_{W1} = a \left[\log \left(\frac{W_{50}/\sin i}{\mathrm{km\ s^{-1}}} \right) - 2.6 \right] + b \quad , \tag{4.7}$$

where a is the slope of the best-fitting relation, b the zero-point and 2.6 is the pivot point (chosen to reduce the covariance between the slope and the zero-point). We use an analogous form of the relation when considering the K_s-band data.

We fit the TFR with a straight line using the Levenberg-Marquardt least-squares algorithm MPFIT. We first perform a forward fit, which in our case implies that the

deprojected velocity is the independent variable and the absolute magnitude is the dependent variable. This fit formally minimises

$$\chi^2_{\rm for} \equiv \sum_j \frac{1}{\sigma_j^2} \left\{ M_{W1} - \left(a \left[\log \left(\frac{W_{50}/\sin i}{\rm km\ s^{-1}} \right) - 2.6 \right] + b \right) \right\}^2 \quad , \tag{4.8}$$

where the sum is over all sample galaxies and σ_j is the effective uncertainty, defined as

$$\sigma_j^2 \equiv \sigma^2_{M_{W1},j} + a^2 \sigma^2_{\log(W_{50}/\sin i),j} + \sigma^2_{\rm int} \quad , \tag{4.9}$$

where $\sigma_{M_{W1},j}$ and $\sigma_{\log(W_{50}/\sin i),j}$ are the uncertainties of the absolute magnitude and the logarithm of the deprojected velocity of a given galaxy, respectively, and $\sigma_{\rm int}$ quantifies the intrinsic scatter of the relation. In practice, the observational uncertainties do not fully account for the scatter about the TFR, so $\sigma_{\rm int}$ is introduced to account for the variance of the relation not captured by measurement uncertainties. The value of $\sigma_{\rm int}$ is determined by adjusting it until the reduced $\chi^2_{\rm red,for} \equiv \chi^2_{\rm for}/{\rm DOF}$ equals 1. By doing so, we are rescaling the effective uncertainties to match the scatter of the data, in turn ensuring that the uncertainties of the derived slope and zero-point are realistic. Without accounting for this intrinsic scatter, the uncertainties on both would be underestimated.

Given a fit, we can also calculate the total scatter of the relation as

$$\sigma^2_{\rm tot} = \frac{\chi^2_{\rm for}}{\sum_j (1/\sigma_j^2)} \quad . \tag{4.10}$$

This total scatter measures the dispersion of the data around the relation and thus quantifies the quality of the relation.

As the velocity uncertainties are typically (much) larger than the absolute magnitude uncertainties, slopes determined from forward fits are often biased (shallower than the true slopes) and less accurate. In such cases, reverse fits are preferable, where the absolute magnitude is the independent variable and the deprojected velocity is the dependent variable. Such fits minimise

$$\chi^2_{\rm rev} \equiv \sum_j \frac{1}{\zeta_j^2} \left[\log \left(\frac{W_{50}/\sin i}{\rm km\ s^{-1}} \right) - 2.6 - (A\, M_{W1} + B) \right]^2 \quad , \tag{4.11}$$

where A is the slope of the best-fitting relation, B the zero-point and ζ_j the effective uncertainty, defined as

$$\zeta_j^2 \equiv \sigma^2_{\log(W_{50}/\sin i),j} + A^2 \sigma^2_{M_{W1},j} + \zeta^2_{\rm int} \quad , \tag{4.12}$$

where $\zeta_{\rm int}$ is the intrinsic scatter adjusted such that $\chi^2_{\rm red,rev} \equiv \chi^2_{\rm rev}/{\rm DOF} = 1$. The total scatter of the relation is then

$$\zeta^2_{\rm tot} = \frac{\chi^2_{\rm rev}}{\sum_j (1/\zeta^2_j)} \quad . \tag{4.13}$$

The reverse fit parameters can be redefined to enable a direct comparison to the forward fit parameters[6]:

$$a' \equiv \frac{1}{A}, \quad b' \equiv -\frac{B}{A}, \quad \sigma'_{\rm int} \equiv \frac{\zeta_{\rm int}}{A} \quad \sigma'_{\rm tot} \equiv \frac{\zeta_{\rm tot}}{A} \quad . \tag{4.14}$$

The $W1$- and $K_{\rm s}$-band TFRs are shown in Fig. 4.4 for the initial sample, sub-sample A and sub-sample B. Both forward and reverse fits are shown, the latter redefined as above to allow direct comparisons. The benchmark relation of Tully & Pierce (2000) in the local Universe is also shown, with a zero-point calibrated using known Cepheid calibrator galaxies. It is worth noting that Tully & Pierce (2000) use H I as their velocity tracer, although it has been shown that slopes calculated using CO are generally consistent within the uncertainties with (albeit sometimes slightly shallower than) slopes calculated using H I (Tiley et al. 2016b). Comparisons of our fits with literature results are discussed at more length in Section 4.4. The best-fitting parameters of all the fits are listed in Table 4.3.

4.3.3 Galaxy morphology

Separate TFRs were fit for different morphological types, to examine whether galaxy morphology introduces systematic variations in the relation. Previous studies (e.g. Masters et al. 2008; Williams et al. 2010; Davis et al. 2011a; den Heijer et al. 2015) have shown that the TFR can vary systematically with morphology, with ETG TFRs typically offset to fainter magnitudes at a given rotation velocity (see detailed discussion in Section 4.4.2). By constructing morphology-dependent fits, we test whether similar trends are present in our sample and quantify the extent of any systematic difference.

We performed the fits on our initial sample of 71 galaxies. Of these, 20 are classified as ellipticals, 19 as lenticulars and 32 as spirals. We group the lenticulars and ellipticals

[6] Williams et al. (2010) carry out an equivalent derivation, but they list the redefined intrinsic scatter and total scatter as $\sigma'_{\rm int} \equiv A\,\zeta_{\rm int}$ and $\sigma'_{\rm tot} \equiv A\,\zeta_{\rm tot}$. This appears to be a typographical error (see Eq. 4.14 for the correct expressions). Nonetheless, their reported best-fitting scatters appear sensible.

Table 4.3: Best-fitting parameters of the $W1$- and K_s-band CO TFRs.

Sample	Fit	Slope (mag dex^{-1})	Zero-point (mag)	σ_{int} (mag)	σ_{tot} (mag)	Offset (mag)
		WISE $W1$				
Initial	Forward	-3.37 ± 0.42	-24.12 ± 0.09	0.62	0.70	–
	Reverse	-6.42 ± 0.80	-23.97 ± 0.12	0.86	0.96	–
	Fixed (TP00)	-8.78	-23.85 ± 0.16	1.21	1.32	0.20
	Fixed (Ti16)	-7.10	-23.93 ± 0.13	0.95	1.05	0.04
Sub-sample A	Forward	-3.74 ± 0.47	-24.06 ± 0.10	0.63	0.71	–
	Reverse	-6.77 ± 0.84	-23.86 ± 0.13	0.85	0.95	–
	Fixed (TP00)	-8.78	-23.73 ± 0.16	1.13	1.24	0.32
	Fixed (Ti16)	-7.10	-23.84 ± 0.12	0.89	0.99	0.13
Sub-sample B	Forward	-3.75 ± 0.53	-24.09 ± 0.10	0.66	0.72	–
	Reverse	-6.84 ± 0.91	-23.93 ± 0.14	0.89	0.94	–
	Fixed (TP00)	-8.78	-23.83 ± 0.17	1.16	1.21	0.22
	Fixed (Ti16)	-7.10	-23.91 ± 0.14	0.91	0.97	0.06
LTGs	Forward	-3.36 ± 0.63	-24.15 ± 0.12	0.51	0.59	–
	Reverse	-6.18 ± 1.17	-24.36 ± 0.17	0.69	0.79	–
	Common slope	-7.96 ± 1.19	-24.49 ± 0.22	0.96	1.06	–
ETGs	Forward	-3.54 ± 0.76	-24.05 ± 0.17	0.72	0.78	–
	Reverse	-9.43 ± 2.13	-23.19 ± 0.38	1.18	1.28	–
	Common slope	-7.96 ± 1.19	-23.41 ± 0.24	0.96	1.06	–
		2MASS K_s				
Initial	Forward	-3.60 ± 0.38	-24.05 ± 0.08	0.54	0.64	–
	Reverse	-5.75 ± 0.60	-23.94 ± 0.10	0.69	0.79	–
	Fixed (TP00)	-8.78	-23.79 ± 0.15	1.14	1.25	0.26
	Fixed (To18)	-8.43	-23.81 ± 0.14	1.08	1.19	0.50
Sub-sample A	Forward	-4.06 ± 0.42	-23.99 ± 0.08	0.53	0.63	–
	Reverse	-5.98 ± 0.60	-23.86 ± 0.10	0.64	0.75	–
	Fixed (TP00)	-8.78	-23.68 ± 0.14	1.03	1.15	0.37
	Fixed (To18)	-8.43	-23.70 ± 0.14	0.97	1.09	0.61
Sub-sample B	Forward	-4.13 ± 0.46	-24.02 ± 0.09	0.55	0.62	–
	Reverse	-6.01 ± 0.64	-23.91 ± 0.11	0.66	0.73	–
	Fixed (TP00)	-8.78	-23.77 ± 0.15	1.04	1.11	0.28
	Fixed (To18)	-8.43	-23.78 ± 0.15	0.99	1.06	0.53
LTGs	Forward	-3.41 ± 0.62	-24.05 ± 0.11	0.49	0.58	–
	Reverse	-6.08 ± 1.10	-24.24 ± 0.16	0.66	0.76	–
	Common slope	-6.83 ± 0.88	-24.29 ± 0.17	0.76	0.86	–
ETGs	Forward	-3.73 ± 0.67	-24.02 ± 0.15	0.60	0.68	–
	Reverse	-7.52 ± 1.40	-23.47 ± 0.26	0.86	0.96	–
	Common slope	-6.83 ± 0.88	-23.57 ± 0.20	0.76	0.86	–

Notes. All results are derived using a pivot point of 2.6. The slope offsets are measured as ours−theirs.

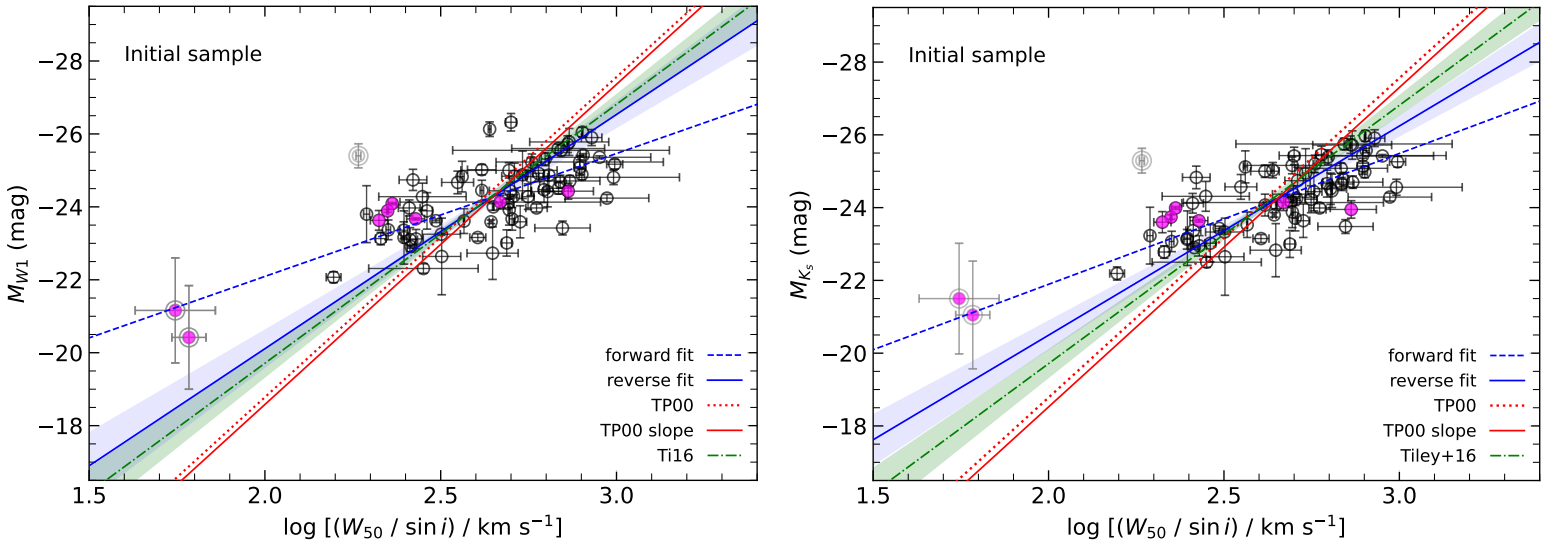


Figure 4.4: CO Tully-Fisher relations. **Top-left:** $W1$-band CO TFR of the initial sample galaxies. The three grey data points marked with a second open circle show the three outliers which are excluded from the initial sample and are not part of the fit. Filled magenta data points indicate galaxies with a single Gaussian profile. **Top-right:** As before, but for the K_s-band CO TFR. **Middle-left:** $W1$-band CO TFR of the sub-sample A galaxies, with single Gaussian profile galaxies removed. Filled orange data points indicate galaxies with inclinations less than 30°. **Middle-right:** As before, but for the K_s-band CO TFR. **Bottom-left:** $W1$-band CO TFR of the sub-sample B galaxies, with single Gaussian profile and face-on ($i < 30°$) galaxies removed. **Bottom-right:** As before, but for the K_s-band CO TFR. The blue dashed and solid lines show the best forward fit and reverse fit, respectively. The blue shaded band indicates the 1σ uncertainty around the best reverse fit. The dotted red line is the K-band TFR of Tully & Pierce (2000). The solid red line shows the reverse fit when the slope is fixed to that of Tully & Pierce (2000). The green dot-dashed line is the $W1$-band TFR of Tiley et al. (2016b); the green shaded band indicates the 1σ uncertainty around their best fit.

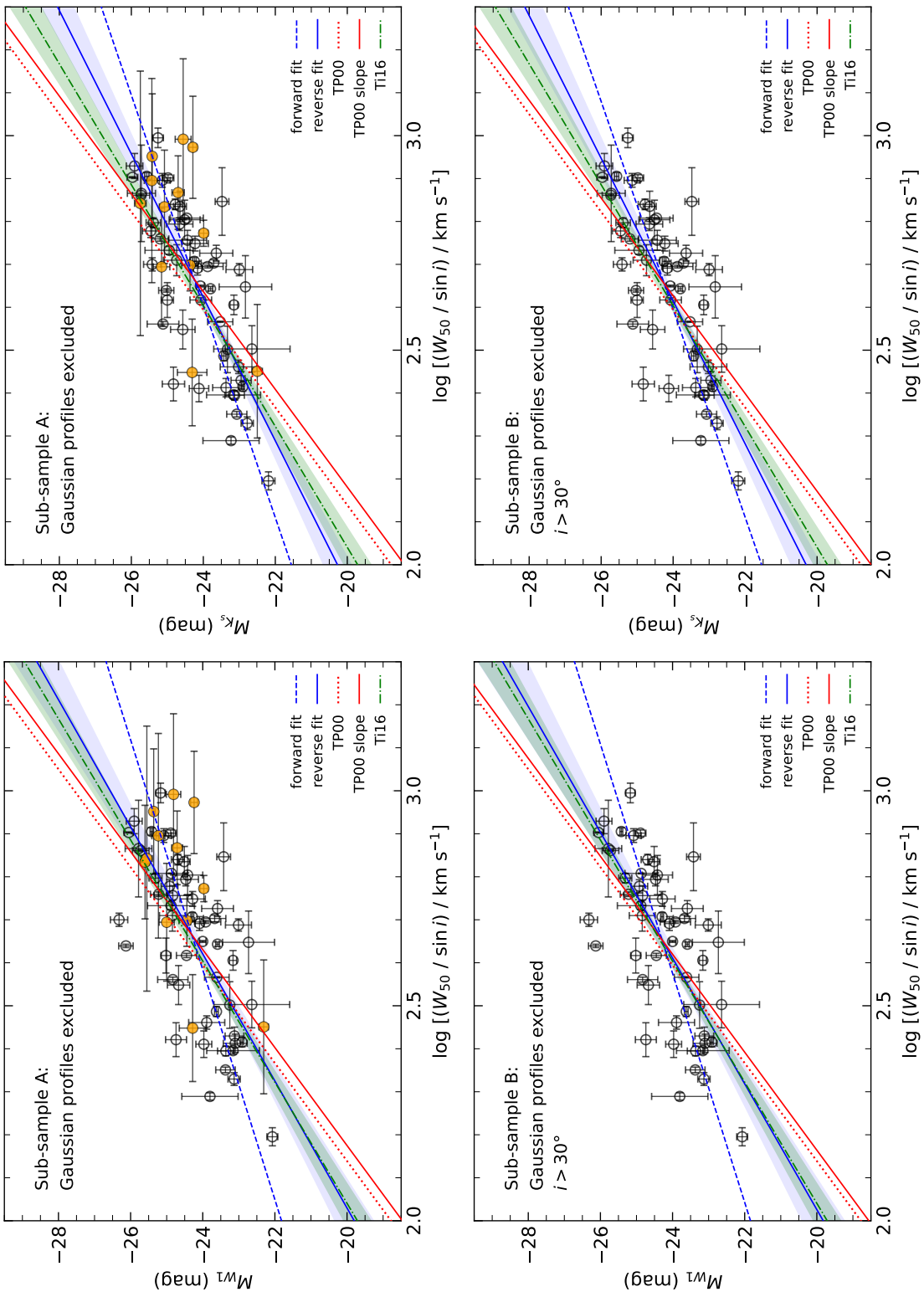


Figure 4.4: continued.

Table 4.4: Best-fitting TFR parameters of literature studies.

Work	Sample	Slope (mag dex^{-1})	Zero-point (mag)	Pivot	Tracer	Measure	Band	Adjusted ZP (mag)
(1)	(2)	(3)	(4)	(5)	(6)	(7)	(8)	(9)
TP00	Spirals	-8.78	-23.17	2.5	H I	W_{20}	K'	-24.05
Wi10	S0s	-9.13 ± 0.87	-23.98 ± 0.20	2.4	stars	$v_{\rm model}$	$K_{\rm s}$	-23.06 ± 0.22
Da11	ETGs	-8.38 ± 0.70	-23.12 ± 0.09	2.6	CO	W_{20}	$K_{\rm s}$	–
Ti16	Spirals	-7.1 ± 0.6	-23.83 ± 0.09	2.58	CO	W_{50}	$W1$	-23.97 ± 0.09
To18	$z \leq 0.3$	-8.4 ± 2.9	-23.47 ± 0.54	2.5	CO	W_{50}	$K_{\rm s}$	-24.31 ± 0.61

Notes. (1) Abbreviation of literature study. TP00: Tully & Pierce (2000); Wi10: Williams et al. (2010); Da11: Davis et al. (2011a); Ti16: Tiley et al. (2016b); To18: Topal et al. (2018). (2) Study sample description. (3) Best-fit TFR slope. (4) Best-fit TFR zero-point. (5) TFR pivot point. (6) Velocity width tracer. (7) Velocity width measure. (8) Photometric band. (9) Zero-point adjusted to our pivot point of 2.6.

together as ETGs, as all ellipticals in our sample have larger than average velocity widths and are thus at larger deprojected velocities than our adopted pivot point. The addition of lenticulars to the ellipticals extends the data over the entire velocity range of the sample, thus offering a more reliable determination of the slope and zero-point of the relation.

The $W1$- and $K_{\rm s}$-band ETG and LTG TFRs are shown in Fig. 4.5. In the same figure we show the best-fitting relations of other studies which are most similar to ours methodologically, yielding the most appropriate benchmarks against which to compare our results. These are Tully & Pierce (2000) and Tiley et al. (2016b) for our LTGs and Williams et al. (2010) and Davis et al. (2011a) for our ETGs. All best-fitting TFRs are listed in Table 4.3.

It is worth highlighting that different studies choose different pivot points for their TFRs, depending on their data (see Eq. 4.7). To ensure a fair comparison, we thus recalculate the zero-points of other studies to our pivot point in the following manner:

$$\begin{aligned} b' &= b + a\,(2.6 - x_0) \quad , \\ \sigma_{b'}^2 &= \sigma_b^2 + \sigma_a^2\,(2.6 - x_0)^2 \quad , \end{aligned} \tag{4.15}$$

where a, b, σ_a and σ_b are the original (literature) slope, zero-point and their respective uncertainties, respectively, x_0 is the original pivot point, b' is the new zero-point and $\sigma_{b'}$ is its uncertainties adjusted to our pivot point of 2.6. The adjusted zero-points of the aforementioned studies are listed in Table 4.4, along with other key information.

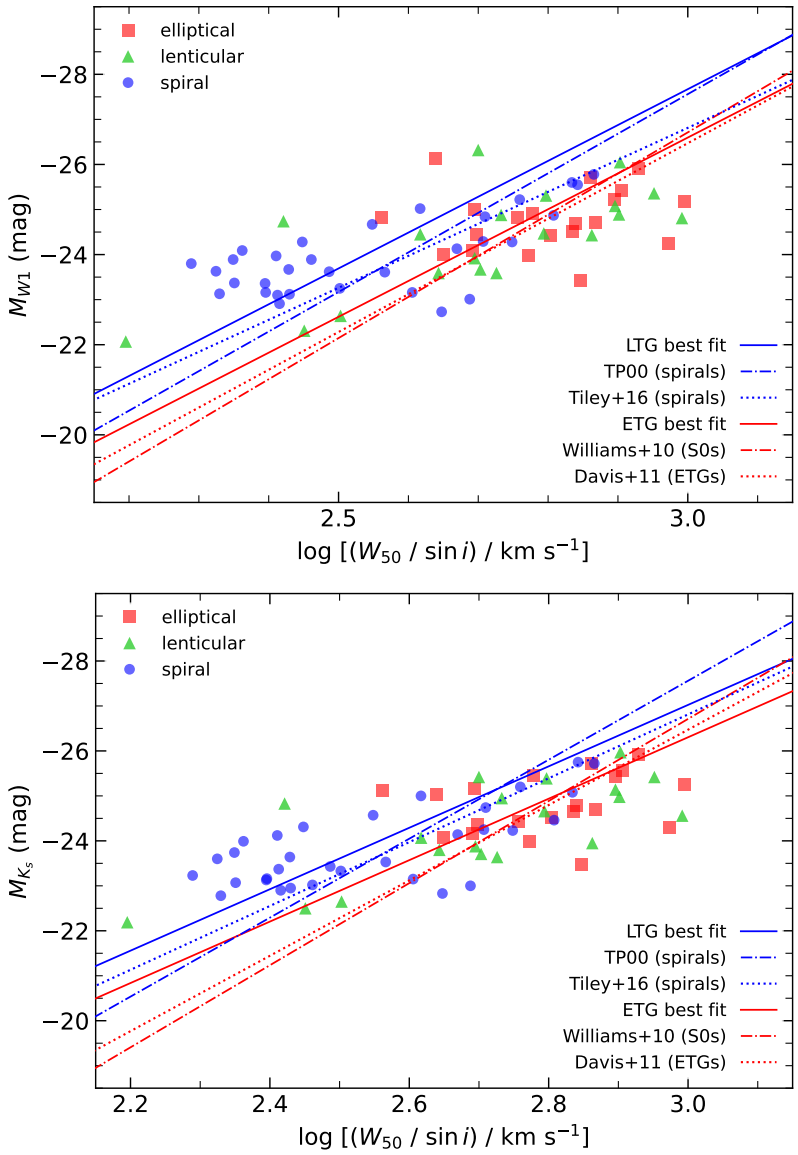


Figure 4.5: As Fig. 4.4, but for galaxies in the initial sample categorised by morphological type. **Top:** $W1$-band CO TFR. **Bottom:** K_s-band CO TFR. Blue circles indicate spirals (LTGs), red squares ellipticals and green triangles lenticulars. Lenticulars and ellipticals together compromise ETGs. The best-fitting TFRs are coloured as the data points, blue lines showing fits for LTGs, red lines for ETGs. Our reverse fits are shown as solid lines. Morphology-dependent TFR fits from the literature are also shown. For LTGs these are Tully & Pierce (2000; blue dash-dotted line) and Tiley et al. (2016b; blue dotted line). For ETGs these are Williams et al. (2010; red dash-dotted line) and Davis et al. (2011a; red dotted line). Error bars have been omitted for clarity.

4.4 Discussion

Given their common use in previous TFR studies, as well as the clearly better fits, we will focus our discussion on the reverse fits.

4.4.1 Literature comparisons

Tiley et al. (2016b)

Tiley et al. (2016b) established the exact method used in this work. Use of the same kinematic tracer and the same velocity width measure (W_{50} of fits to integrated spectra rather than empirical measurements) as us makes this work ideal to compare to our results.

Tiley et al. (2016b) studied the $W1$-band TFR of 207 COLD GASS (Saintonge et al. 2011) galaxies at redshifts $0.025 < z < 0.05$. They found a $W1$-band slope of -7.1 ± 0.6, entirely consistent with the slopes derived for all three of our samples (-6.42 ± 0.80, -6.77 ± 0.84 and -6.84 ± 0.91). To fairly compare zero-points, we carried out fits with the slope set to that of Tiley et al. (2016b), yielding $W1$-band zero-points of -23.93 ± 0.13, -23.84 ± 0.12 and -23.91 ± 0.14, in full agreement with the zero-point of Tiley et al. (2016b; -23.97 ± 0.09 when converted to our pivot point of 2.6).

It is worth noting that 93% of the galaxies in our sample are closer than those of Tiley et al. (2016b), i.e. closer than $z = 0.025$. Taken together, the two studies thus cover the entire extent of the local Universe, and their excellent agreement with one another demonstrates that we have successfully established a robust local benchmark for $W1$-band CO TFRs.

Topal et al. (2018)

Topal et al. (2018) studied the K_s-band TFR of 25 galaxies at redshifts $0.05 < z < 0.3$. All galaxies in our sample, as well as those of Tiley et al. (2016b), are closer than those of Topal et al. (2018). They found a slope of -8.43 ± 2.86 which, partly owing to the large uncertainty, is consistent with the slopes derived for all three of our samples (-5.75 ± 0.60, -5.98 ± 0.60 and -6.01 ± 0.64). To investigate potential zero-point differences, we again carry out fits with the slope fixed, now to that of Topal et al. (2018). Again, our zero-points (-23.81 ± 0.14, -23.70 ± 0.14 and -23.78 ± 0.15) are in broad agreement with that of Topal et al. (2018; -24.31 ± 0.61 when converted to our pivot point of 2.6). These results are in

agreement with those of Topal et al. (2018), who compared their results to those of Tiley et al. (2016b), namely that there does not appear to be any evolution of the K_s-band CO TFR since $z \approx 0.3$. This result is also in line with a growing body of literature results showing relatively stable slope and zero-point of the K-band TFR up to intermediate redshifts (e.g. Conselice et al. 2005; Flores et al. 2006; Tiley et al. 2016a; Tiley et al. 2019).

Notwithstanding the formal consistency, it is worth noting that our measurements favour slopes different from those of Topal et al. (2018). Relative to our uncertainties, a slope as steep as -8.43 is disfavoured at an $\approx 4\sigma$ level, indicating that our data generally favour a much shallower slope. Similarly, our data suggest a zero-point ≈ 0.5 mag fainter than that of Topal et al. (2018) for the same slope, also an $\approx 4\sigma$ offset when judged against our uncertainties. Given that we use the same tracer, velocity width definition, photometric band, pivot point and fitting function as Topal et al. (2018), these differences are not attributable to our choice of methodology. Rather, they likely represent systematic differences emerging from sample differences. This tension, while not significant once Topal et al.'s (2018) larger uncertainties are taken into account, nevertheless motivates further large-scale studies of the K-band CO TFR, particularly to probe whether there could be a potential evolution since intermediate redshift.

Tully & Pierce (2000)

The $W1$-band reverse fits of all three of our samples have slopes shallower than that of Tully & Pierce (2000; -8.78). However, as the samples become more homogenous (from initial sample, to sub-sample A to sub-sample B), their slopes become steeper and more closely approximate that of Tully & Pierce (2000). Nevertheless, the Tully & Pierce (2000) slope is still statistically inconsistent with those of all three of our samples. The slopes of our K_s-band reverse fits are consistently shallower than those of our $W1$-band reverse fits (for all three of our samples), so our K_s-band slopes depart even more from the K'-band fits of Tully & Pierce (2000). It is however worth noting that Tully & Pierce (2000) do not list the uncertainty of their slope, making a direct comparison difficult. This tension with the slope of Tully & Pierce (2000) is not unique to our analysis. Using CO velocity widths and

near-infrared photometry, Tiley et al. (2016b) also reported a slope shallower than that of Tully & Pierce (2000), albeit slightly less shallow than the one derived here.

To compare the zero-points of our TFRs to that of Tully & Pierce (2000), we again carried out reverse fits with the slope fixed, now to that of Tully & Pierce (2000). All three of our $W1$-band samples have zero-points (-23.85 ± 0.16, -23.73 ± 0.16 and -23.83 ± 0.17) which are not in agreement with that of Tully & Pierce (2000; -24.05 when converted to our pivot point of 2.6). Likewise, all three of our K_s-band samples have zero-points (-23.79 ± 0.15, -23.68 ± 0.14 and -23.77 ± 0.15) which are not in agreement with that of Tully & Pierce (2000). However, Tully & Pierce (2000) again do not list the uncertainty of their zero-point, so it is hard to gauge how significant those disagreements are. One possible reason for this relates to the choice of kinematic tracer. The Tully & Pierce (2000) TFR is built from H I integrated spectra of late-type spirals. H I almost always reaches well into the flat parts of the rotation curves, whereas CO can be centrally concentrated. When CO does not extend beyond the turnover radius of a rotation curve, the velocity width will be underestimated, leading to possibly shifted intercepts.

4.4.2 Galaxy morphology

As mentioned in Section 4.3.3, it is essential to look at the morphological breakdown of our galaxy samples. Indeed, a comparison of TFRs between LTGs and ETGs can provide valuable insight into the connection between stellar populations, M/L and the dynamical evolution of galactic discs. For example, an offset between the TFRs of spiral and S0 galaxies could indicate a passive fading of spirals into lenticulars following a cessation of star formation (Bedregal et al. 2006). However, the constancy of the near-infrared TFR across redshifts (see Section 4.4.1) would imply that the high-redshift spiral progenitors of current S0 galaxies lie on the same luminosity–velocity relation as local spirals. In other words, for a given rotation velocity, their near-infrared luminosities were approximately as bright as those of spirals today. A simple model of passive fading would require this fading to occur on such a short timescale that a change in the S0/spiral fraction should be noticeable, but this is observationally ruled out (e.g. Fasano et al. 2000; Wilman et al. 2009). This motivates alternative interpretations in which mass distribution differences instead drive

the spiral-S0 galaxy offset, such as a more concentrated mass distribution in S0 galaxies (Williams et al. 2010). Thus, the degree to which the TFR changes (or not) across Hubble types constrains the mechanisms by which galaxies quench star formation and transform morphologically. Additionally, systematic variations between morphological types within the LTG population itself are well-established. Earlier-type spirals (Sa – Sb) typically possess larger bulge fractions, redder colours and higher M/L than late-type (Sc – Sd) systems, producing measurable differences of both TFR slope and zero-point (e.g. Pierce & Tully 1988; Masters et al. 2008). These variations indicate that the TFR can also be sensitive to the detailed star-formation history and structural composition of galactic discs.

Previous observational studies seem to collectively suggest that ETG TFRs are truly offset from spiral TFRs in the K-band, but the magnitude of the offset varies. Bedregal et al. (2006) analysed S0 galaxies using stellar kinematics and found that they are 0.8 – 1.2 mag fainter than spirals at a given velocity. De Rijcke et al. (2007) reported a comparable offset of $\approx$ 1.2 mag, whilst Davis et al. (2011a) reported an offset of 0.98 $\pm$ 0.22 mag between their ETG CO TFR and a spiral CO TFR established using the linewidths of Chung et al. (2009). In contrast, den Heijer et al. (2015) reported a smaller offset of 0.5 – 0.7 mag when looking at ETGs with extended, regular H I discs measured at large radii. Whether this offset persists when the relation is expressed in terms of stellar or baryonic mass rather than luminosity is less clear. Williams et al. (2010) report $\approx$ 0.2 dex offsets for both the stellar and dynamical mass TFRs and conclude that the offset for the baryonic relation is likely even larger. This suggests that S0s are systematically smaller and/or more concentrated than spirals and therefore spirals may undergo a systematic contraction as they transform into lenticulars. On the other hand den Heijer et al. (2015) find no significant offset between their baryonic ETG TFR and the baryonic spiral TFR of Noordermeer & Verheijen (2007). These works suggest that whilst some of the apparent offset may arise from differences of the stellar populations and/or photometric bandpasses, there are fundamental structural and/or dynamical differences between morphological types.

Nevertheless, when comparing the TFRs of different morphological samples, it is essential to use consistent kinematic tracers. The use of different velocity measures, e.g. H I integrated spectrum line widths for spirals and stellar or molecular gas rotation

curves for ETGs, can introduce systematic biases that mimic intrinsic luminosity offsets. Williams et al. (2010) showed that when circular velocities are derived homogeneously for both ETGs and LTGs, the two TFRs are offset by a more modest 0.53 ± 0.15 mag, albeit in a statistically significant manner.

Most past works that probed the morphological dependence of the TFR used the K-band, so we will begin our discussion by considering our K_s-band results. Our LTG slope of -6.08 ± 1.10 is consistent with our ETG slope of -7.52 ± 1.40. Our LTG zero-point of -24.24 ± 0.16 is 0.77 ± 0.31 mag brighter than our ETG zero-point of -23.47 ± 0.26, which is statistically significant.

As the TFR slopes are consistent within the uncertainties, we can obtain a more robust zero-point offset by constraining both slopes to be equal. We do so by following the methodology of Williams et al. (2010) and simultaneously reverse fitting two straight lines, of the usual form for the LTGs and the following form for ETGs:

$$\log\left(\frac{W_{50}/\sin i}{\mathrm{km\ s^{-1}}}\right) = A\,M_{W1} + B + \Delta + 2.6 \quad , \tag{4.16}$$

where Δ represents the reverse zero-point offset between the two relations. This offset can then be converted back to a forward-equivalent offset $\delta \equiv -\Delta/A$. Using this method, we derive a common slope of -6.83 ± 0.88, a LTG zero-point of -24.29 ± 0.17 and an ETG zero-point offset of 0.72 ± 0.04 mag toward fainter magnitudes. This is in agreement with our previous estimate, but is a far more robust estimate with smaller uncertainties.

Considering the $W1$-band, we derive a LTG slope of -6.18 ± 1.17 and an ETG slope of -9.43 ± 2.13. Whilst these slopes differ from each other somewhat more than in the K_s-band, they are still just statistically consistent. Our $W1$-band LTG zero-point of -24.36 ± 0.17 is 1.17 ± 0.42 mag brighter than the ETG zero-point of -23.19 ± 0.38, which is statistically significant. As the slopes of the two relations are in rough agreement, we again perform a common-slope fit to our $W1$-band data. Using this method, we derive a common slope of -7.96 ± 1.19, a LTG zero-point of -24.49 ± 0.22 and an ETG zero-point offset of 1.07 ± 0.04 mag toward fainter magnitudes.

Both of our $W1$- and K_s-band offsets are consistent within their uncertainties with the offsets derived by Bedregal et al. (2006), De Rijcke et al. (2007) and Davis et al. (2011a).

This result is somewhat surprising, as Williams et al. (2010) suggested that a significant driver behind these observed offsets could be systematic effects due to different tracers and/or methodologies (but this cannot be the case for our result).

4.4.3 Scatter

As shown in Table 4.3, the reverse $W1$-band CO TFR of our initial sample has an intrinsic scatter of $\sigma_{\rm int} = 0.86$, somewhat higher than expected when compared to Davis et al. (2011a; $\sigma_{\rm int} = 0.36$) and Tiley et al. (2016b; $\sigma_{\rm int} = 0.73$). The reverse $K_{\rm s}$-band initial sample CO TFR has an intrinsic scatter of $\sigma_{\rm int} = 0.69$, smaller than our $W1$-band scatter but still rather large.

One explanation for this large scatter may be our choice of inclination measure. Very few of our sample galaxies have inclinations derived from kinematic modelling, which is the gold standard for inclinations. As shown by Davis et al. (2011a), the intrinsic scatter of the TFR derived using dust inclinations only is $\sigma_{\rm int} = 0.66$, almost double that of the TFR derived using inclination measures dominated by interferometric measurements ($\sigma_{\rm int} = 0.36$).

It also appears that the scatter is morphology-dependent. Previous studies have typically focused on a particular morphology, such as ETGs (e.g. Davis et al. 2011a) or spirals (e.g. Tiley et al. 2016b). When dividing our sample galaxies by morphological types, the LTGs have a notably smaller scatter in both bands ($\sigma_{\rm int} = 0.69$ in $W1$ and 0.66 in $K_{\rm s}$) compared to ETGs ($\sigma_{\rm int} = 1.18$ in $W1$ and 0.86 in $K_{\rm s}$). A potential reason for the larger scatter in ETGs is that they tend to have more truncated CO distributions, leading to more biased velocity widths and thus higher scatter. Therefore, when all galaxies are combined together into a single sample, ETGs drive the resulting scatter. Furthermore, by construction we expect our ETG sample to have a larger scatter, as it consists of both elliptical and lenticular galaxies.

It is also worth noting that the intrinsic scatter does not decrease as the galaxy sample is made more homogeneous (i.e. from the initial sample to sub-sample A to sub-sample B), in either band ($\sigma_{\rm int} = 0.86$, 0.85 and 0.89, respectively, in the $W1$-band and $\sigma_{\rm int} = 0.69$, 0.64 and 0.66, respectively, in the $K_{\rm s}$-band). As sub-sample A excludes galaxies with single Gaussian CO integrated spectra, this suggests that profile shape is not the main driver of the scatter. It may also suggest that the molecular gas of some galaxies with double-horned profiles does not reach beyond the turnover radii of the rotation curves. As sub-sample B

additionally excludes galaxies with inclinations $i < 30°$, this also suggests that our dust-based inclinations are precise enough that excluding face-on galaxies does not significantly decrease the intrinsic scatter of the relation. In turn, this suggests that reliable inclinations matter more than inclination cuts, and the imposition of inclination cuts should be more carefully considered in studies where reliable inclinations are available.

4.5 Conclusions

In this chapter we have presented a new CO TFR calibration for the local Universe ($z \lesssim 0.03$), based on a sample of galaxies observed by the WISDOM Project. Using this sample we probed the $W1$- and K_s-band CO TFRs of an initial sample of 71 galaxies, a sub-sample of 65 galaxies with double-horned integrated spectra and a sub-sample of 53 relatively edge-on galaxies. The main results are as follows.

1. The best-fitting reverse $W1$- and K_s-band CO TFRs of our initial sample are
   $M_{W1} = (-6.42 \pm 0.80) \left[\log\left(\frac{W_{50}/\sin i}{\mathrm{km\ s^{-1}}}\right) - 2.6\right] + (-23.97 \pm 0.12)$
   and
   $M_{K_s} = (-5.75 \pm 0.61) \left[\log\left(\frac{W_{50}/\sin i}{\mathrm{km\ s^{-1}}}\right) - 2.6\right] + (-23.94 \pm 0.10)$.
   This provides one of the largest homogeneous local CO TFR calibration to date, establishing a robust benchmark against which future CO TFR studies can be compared.

2. The slopes and zero-points of the best-fitting CO TFRs of our sub-samples that exclude galaxies with single Gaussian profiles and low inclinations are statistically consistent with those of the initial sample. Excluding these galaxies does not substantively decrease the intrinsic scatters of the relations. This suggests that the dominant sources of scatter could be linked to CO radial extent, morphology or intrinsic diversity in galaxy structure.

3. Our results are in excellent agreement with the work of Tiley et al. (2016b), who used the same methodology and kinematic tracer. Taken together, the two studies cover the entire extent of the local Universe and establish a robust local benchmark for the $W1$-band CO TFR. The agreement indicates that CO velocity widths yield a stable

local TFR calibration when analysed with a consistent methodology, strengthening the case for CO as a reliable alternative to H I.

4. Our results are in broad agreement with those of Topal et al. (2018) and indicate no significant evolution of either the zero-point or slope of the CO TFR since $z = 0.3$. Nevertheless, further studies with larger high-redshift CO samples are required to determine whether this apparent lack of evolution reflects genuine stability in the CO TFR or is a consequence of the large uncertainties in the current samples.

5. Our best-fitting CO TFRs are in tension with other studies such as that of Tully & Pierce (2000), suggesting a significantly shallower TFR slope. However, due to the use of different kinematic tracers, analysis methods and sample galaxy morphologies, we cannot assign these differences to specific astrophysical phenomena rather than methodological differences. This highlights that apparent differences between published TFR slopes cannot be interpreted as stemming from physical differences unless methodological differences are taken into account.

6. Due to the morphological variety of our sample galaxies, we constructed a LTG CO TFR for 33 spiral galaxies and an ETG CO TFR for 20 elliptical and 19 lenticular galaxies. By simultaneously fitting the two galaxy samples with a common slope, we infer that ETGs are 0.72 ± 0.04 mag fainter at K_s-band and 1.07 ± 0.04 mag fainter at $W1$-band than LTGs of the same rotation velocity. This offset is broadly consistent with other literature results. This persistent offset demonstrates that even when a homogeneous kinematic tracer is used, ETGs and LTGs do not occupy a common TFR. The offset therefore cannot be explained solely by differences between velocity tracers, implying that the separation between the two galaxy populations is likely due to systematics arising from sample selection or intrinsic differences in stellar populations, mass distributions or formation histories.

7. We have generated and included a comprehensive catalogue of WISDOM CO data products for use in future molecular gas studies. This catalogue provides a homogeneous set of CO kinematic products that can be used to support future studies of molecular gas dynamics beyond the specific TFR calibration presented here.

This is true happiness: to have no ambition and to work like a horse as if you had every ambition. To live far from men, not to need them and yet to love them. To have the stars above, the land to your left and the sea to your right and to realize of a sudden that in your heart, life has accomplished its final miracle: it has become a fairy tale.

— Nikos Kazantzakis's *Zorba the Greek*

5 Conclusions

Contents

5.1 $M_{BH} - \sigma_e$ relation 196
5.1.1 Our results 196
5.1.2 Molecular gas $M_{BH} - \sigma_e$ relation 196
5.1.3 MASSIVE Survey galaxies 201
5.1.4 Systematic biases in SMBH mass measurements and their impact on $M_{BH} - \sigma_e$ relation 203
5.2 Summary 209
5.3 Future work 210
5.3.1 Expanding the molecular gas SMBH mass sample 211
5.3.2 CO Tully-Fisher relation 218

This chapter places the results of this thesis in the context of the $M_{BH} - \sigma_e$ relation. We compare the SMBH mass measurements presented here to the relation, investigate the behaviour of the relation at the high-mass end and construct a $M_{BH} - \sigma_e$ relation based exclusively on molecular gas SMBH masses. We also assess how the systematic differences between SMBH mass measurement techniques might impact the relation. Finally, we summarise this thesis and propose future work.

5.1 M_{BH} – σ_e relation

5.1.1 Our results

As discussed in Chapter 1, SMBH mass measurements are often considered in the wider context of how correlations of SMBH mass with other host galaxy properties inform our understanding of galaxy formation and co-evolution. Figure 5.1 compares the SMBH mass measurements presented in this thesis (blue data points) to the $M_{BH} - \sigma_e$ relation of van den Bosch (2016; black solid line). The figure also shows the SMBH mass measurements used to define the van den Bosch (2016) relation (grey data points), together with all the other molecular gas SMBH mass measurements reported in the literature to date (red data points; see Table 5.1). We highlight that the relation of van den Bosch (2016) was determined prior to the publication of most molecular gas SMBH masses, with only 3 included in the fit (NGC 1097, Onishi et al. 2015; NGC 1332, Barth et al. 2016; NGC 3665, Onishi et al. 2017).

All five SMBH masses presented in this thesis lie within the 1σ scatter of the relationship. Two lie modestly above the relation, two lie below it and one is fully consistent with the best-fitting relation within the uncertainties. Taken together, these results indicate that the SMBH masses derived in this work using the molecular gas method are broadly consistent with the established $M_{BH} - \sigma_e$ relation.

In addition to these detections, our sample includes SMBH mass upper limits derived for galaxies with unfavourable molecular gas distributions. The NGC 5208 upper limit excludes the presence of a strongly over-massive SMBH in this galaxy, while the upper limit for NGC 0665 lies above the 3σ scatter of the relation and therefore does not provide strong constraining information.

5.1.2 Molecular gas M_{BH} – σ_e relation

A primary goal of this thesis was to increase the number of molecular gas SMBH mass measurements. To date, there are 27 SMBH masses and 1 SMBH mass upper limit which have been obtained through molecular gas kinematics (see Table 5.1). This thesis adds 5 more SMBH masses and 2 more upper limits, bringing the total to 32 masses and 3 upper limits. The 7 SMBH mass constraints derived in this thesis constitute a

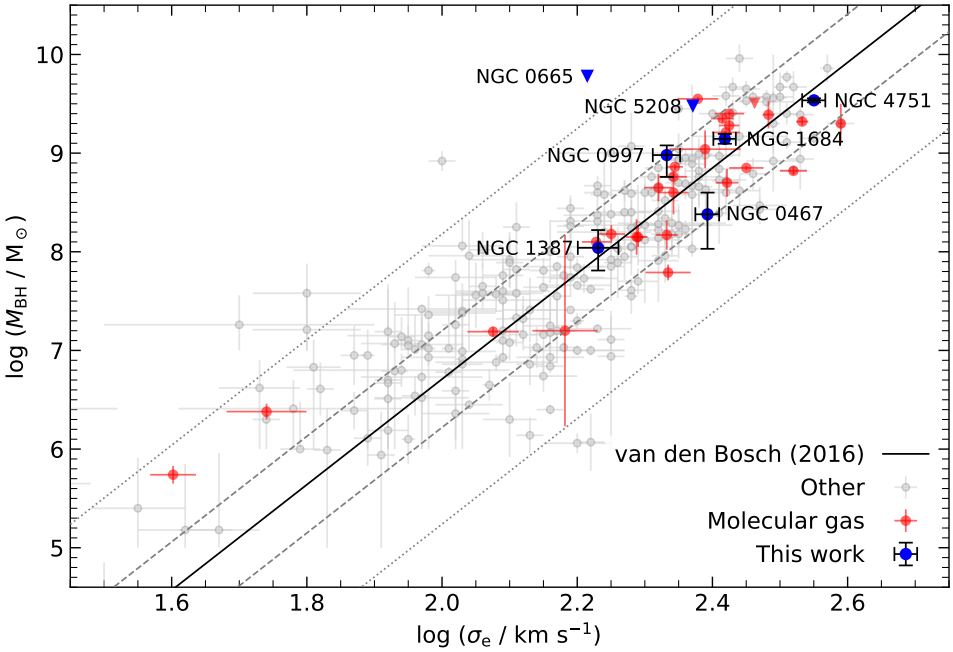


Figure 5.1: Black hole mass – stellar velocity dispersion relation obtained from stellar kinematic, ionised-gas kinematic, maser kinematic and AGN reverberation mapping SMBH mass measurements (grey data points), as reported by van den Bosch (2016). Red data points show measurements obtained from molecular gas kinematics, while the SMBH mass measurements presented in this thesis are shown in blue. Error bars denote 1σ uncertainties. The solid black line shows the best-fitting relation of van den Bosch (2016), while the dashed and dotted grey lines show the 1σ and 3σ scatter of that relation, respectively.

$\approx$ 25 per cent increase of the number of targets studied in the field of molecular gas SMBH mass measurements. The broader aim of this work is to demonstrate that molecular gas dynamics is a high-quality, robust and broadly applicable way of deriving SMBH masses. With a sample size that now surpasses the number of maser measurements in the literature (27; see Section 1 for more detail), the molecular gas method has now reached a level of maturity that allows for a statistically meaningful population-level analysis. In particular, the method has now yielded a sample of SMBH measurements large enough that molecular gas-only $M_{\rm BH} - \sigma_{\rm e}$ correlations can be studied.

Given that the measurement sample contains upper limits, we adopt the Bayesian linear regression framework implemented in `linmix` (Kelly 2007) to pursue this. Unlike standard least-squares or χ^2 minimisation methods, `linmix` allows for "censored" data points to contribute statistically meaningful information to the fit and it treats such data by

Table 5.1: Molecular gas SMBH mass measurements.

Galaxy	Type	σ_e (km s^{-1})	$\log(M_{BH}/M_\odot)$	Sample	Reference
(1)	(2)	(3)	(4)	(5)	(6)
Fairall 49	E-S0	–	8.20 ± 0.28	W	Lelli et al. (2022)
NGC 0315	E	341 ± 7	9.32 ± 0.05	(M)	Boizelle et al. (2021)
NGC 0383	E-S0	239 ± 16	9.55 ± 0.02	W(M)	North et al. (2019), Zhang et al. (2025a)
NGC 0384	E	221 ± 6	8.86 ± 0.03	–	Cohn et al. (2024)
NGC 0404	E-S0	40 ± 3	5.74 ± 0.09	W	Davis et al. (2020)
NGC 0467	S0	247 ± 10	8.38 ± 0.29	M	Dominiak et al. (in prep), Sec. 3.4
NGC 0524	S0-a	220 ± 11	8.60 ± 0.22	W	Smith et al. (2019)
NGC 0612	S0-a	290 ± 31	< 9.51	W	Ruffa et al. (2023)
NGC 0665	S0	164 ± 10	< 9.79	M	Dominiak et al. (in prep), Sec. 3.2
NGC 0997	E	215 ± 10	8.98 ± 0.22	M	Dominiak et al. (2024), Sec. 2.4
NGC 1097	SBb	195 ± 4	8.15 ± 0.10	–	Onishi et al. (2015)
NGC 1275	S0	245 ± 28	9.04 ± 0.19	–	Nagai et al. (2019)
NGC 1332	E-S0	331 ± 15	8.82 ± 0.04	–	Barth et al. (2016)
NGC 1380	S0	215 ± 8	8.17 ± 0.15	–	Kabasares et al. (2022)
NGC 1387	E-S0	170 ± 12	8.04 ± 0.21	W	Dominiak et al. (2026a), Sec. 2.6
NGC 1574	E-S0	216 ± 16	7.79 ± 0.08	W	Ruffa et al. (2023), Zhang et al. (2025b)
NGC 1684	E	262 ± 10	9.15 ± 0.05	M	Dominiak et al. (2024), Sec. 2.3
NGC 3258	E	260 ± 10	9.35 ± 0.04	–	Boizelle et al. (2019)
NGC 3504	Sab	119 ± 10	7.19 ± 0.05	–	Nguyen et al. (2020)
NGC 3557	E	282 ± 16	8.85 ± 0.02	–	Ruffa et al. (2019)
NGC 3593	S0-a	55 ± 7	6.38 ± 0.08	–	Nguyen et al. (2022)
NGC 3665	S0	219 ± 10	8.76 ± 0.03	W	Onishi et al. (2017)
NGC 4261	E	263 ± 12	9.21 ± 0.01	W	Ruffa et al. (2023)
NGC 4429	S0-a	178 ± 8	8.18 ± 0.09	W	Davis et al. (2018)
NGC 4526	S0	209 ± 10	8.65 ± 0.14	W	Davis et al. (2013b)
NGC 4697	E	169 ± 8	8.10 ± 0.02	W	Davis et al. (2017)
NGC 4751	E-S0	355 ± 14	9.54 ± 0.02	W	Dominiak et al. (2025), Sec. 2.5
NGC 4786	E	264 ± 10	8.70 ± 0.14	–	Kabasares et al. (2024)
NGC 5193	E	194 ± 7	8.15 ± 0.18	–	Kabasares et al. (2024)
NGC 5208	S0	235 ± 10	< 9.48	M	Dominiak et al. (in prep), Sec. 3.3
NGC 6861	E-S0	389 ± 3	9.30 ± 0.20	–	Kabasares et al. (2022)
NGC 7052	E	266 ± 13	9.40 ± 0.02	W(M)	Smith et al. (2021b)
NGC 7469	Sa	152 ± 16	7.20 ± 0.97	–	Nguyen et al. (2021)
PGC 11179	S0	266 ± 9	9.28 ± 0.09	–	Cohn et al. (2023)
UGC 2698	E	304 ± 6	9.39 ± 0.14	–	Cohn et al. (2021)

Notes. (1) Galaxy name. (2) Morphological type. (3) Stellar velocity dispersion measured within the half-light radius, with 1σ uncertainties. For MASSIVE galaxies, where uncertainties are not provided, we assume 10 km s^{-1}. (4) SMBH mass, with 1σ uncertainties. Upper limits are listed as the 3σ upper limits. (5) Sample membership of each galaxy: M = MASSIVE Survey, W = WISDOM project. Letters in parentheses denote galaxies that are part of a study but whose SMBH masses were not obtained by said study: NGC 0383 and NGC 7052 are MASSIVE Survey galaxies whose SMBH masses were derived as a part of the WISDOM project, whilst NGC 0315 is a MASSIVE Survey galaxy whose SMBH mass was derived by another group. (6) SMBH mass measurement reference.

marginalising over the values below the reported upper limits of the dependent variable. In addition, `linmix` accounts for measurement uncertainties in both variables and explicitly models the intrinsic scatter of the underlying relation.

The best-fitting $M_{\rm BH} - \sigma_{\rm e}$ relation derived using only molecular gas measurements is

$$\log\left(\frac{M_{\rm BH}}{\rm M_\odot}\right) = (4.07 \pm 0.36) \log\left(\frac{\sigma_{\rm e}}{200\ {\rm km\ s^{-1}}}\right) + (8.45 \pm 0.07) \quad , \tag{5.1}$$

with an intrinsic scatter of 0.35 ± 0.06 dex and a total scatter of 0.42 dex. This relation is obtained using the full molecular gas SMBH mass sample, including upper limits. Excluding upper limits, a slope of 4.07 ± 0.35, an intercept of 8.45 ± 0.07, an intrinsic scatter of 0.35 ± 0.06 dex and a total scatter of 0.42 dex are obtained instead, entirely consistent with the results taking into account upper limits, thus suggesting that the upper limits are consistent with the general relation. Figure 5.2 shows the two $M_{\rm BH} - \sigma_{\rm e}$ relations obtained using molecular gas only.

In their work, using the same `linmix` fitting method and a sample of 72 SMBHs, McConnell & Ma (2013) derived an intercept of 8.31 ± 0.06, somewhat different from ours, but not in a highly statistically significant manner. They also derived a slope of 5.67 ± 0.33, which is significantly steeper than our slope ($\approx 3.3\sigma$ difference). However, assessing the sample of CO SMBH masses, it is clear that both NGC 0404 and NGC 3593 are galaxies with very small stellar velocity dispersions and SMBH masses and lie in a regime not yet well-probed by CO SMBH mass measurements. Excluding these two measurements from our sample yields

$$\log\left(\frac{M_{\rm BH}}{\rm M_\odot}\right) = (4.59 \pm 0.67) \log\left(\frac{\sigma_{\rm e}}{200\ {\rm km\ s^{-1}}}\right) + (8.40 \pm 0.09) \quad , \tag{5.2}$$

with an intrinsic scatter of 0.35 ± 0.06 dex and a total scatter of 0.44 dex. This new intercept is entirely consistent with that of McConnell & Ma (2013), whilst the new slope is significantly steeper and is now consistent with that of McConnell & Ma (2013) at the $\approx 1.3\sigma$ level. Given the differences of sample composition and kinematic tracer, this level of disagreement does not indicate a statistically significant discrepancy. Lastly, McConnell & Ma (2013) reported an intrinsic scatter of 0.40 ± 0.04 dex, similar to ours. We note, however, that the exclusion of the low-SMBH mass galaxies significantly increases the

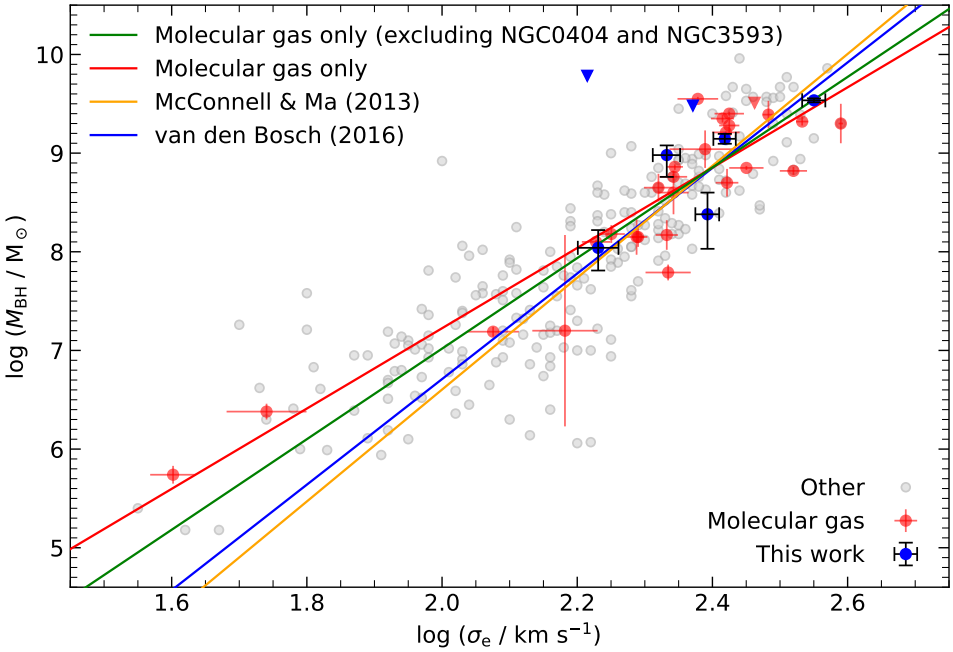


Figure 5.2: Black hole mass – stellar velocity dispersion relation obtained using molecular gas measurements only (red solid line), molecular gas measurements only excluding NGC 0404 and NGC 3593 (green solid line) and from all methods (orange solid line, McConnell & Ma 2013; blue solid line, van den Bosch 2016). Red data points show measurements obtained from molecular gas kinematics (Table 5.1), while the SMBH mass measurements presented in this thesis are shown in blue. Grey data points show SMBH mass measurements from other tracers (van den Bosch 2016). Error bars denote 1σ uncertainties, have been removed from non-molecular gas literature measurements for clarity, but have been retained for molecular gas measurements (including those from this thesis).

uncertainty of the slope, which at least partially explains why our new slope is in agreement with that of McConnell & Ma (2013). This highlights a long-standing need to populate the 10^6 – 10^8 $M_\odot$ SMBH mass range with additional CO-derived mass measurements, to adequately constrain the slope and assess possible systematic differences between SMBH masses determined through CO kinematics and other methods.

Using the `linmix` method, but with an expanded sample of 230 SMBH masses (28 of which are upper limits), van den Bosch (2016) reported an intercept of 8.32 ± 0.04, fully consistent with the intercept of our sample excluding NGC 0404 and NGC 3593, and a slope of 5.35 ± 0.23, also fully consistent with the slope of the same sample. van den Bosch (2016) reported an scatter of 0.49 ± 0.03 dex, larger than ours and to be expected given their substantially larger and heterogeneous sample.

5.1.3 MASSIVE Survey galaxies

As noted by others (e.g. Lauer et al. 2007; McConnell et al. 2011; Thomas et al. 2016; North et al. 2019), some very massive galaxies host SMBHs that lie at the upper edge of the scatter of the $M_{\rm BH} - \sigma_{\rm e}$ relation, among the so-called "over-massive" SMBH population. The apparent overmassiveness of some SMBHs in the most massive ETGs may be partly physical and partly observational. Physically, massive ETGs are expected to grow significantly through dry galaxy mergers, which can increase SMBH mass through the coalescence of their central black holes. Following such mergers, the resulting SMBH binary can also eject stars from the galactic nucleus, producing a depleted stellar core. Since dry mergers can increase $M_{\rm BH}$ without producing a correspondingly large increase in $\sigma_{\rm e}$, repeated dry mergers can move galaxies upward relative to the mean $M_{\rm BH} - \sigma_{\rm e}$ relation. At the same time, the observed high-mass end is affected by selection biases. Dynamical SMBH surveys preferentially target galaxies with large predicted spheres of influence, thereby favouring systems expected to host overmassive SMBHs at fixed $\sigma_{\rm e}$. Larger and more homogeneous samples are therefore needed to determine whether the high-mass offset reflects a genuine consequence of SMBH – host galaxy co-evolution or selection effects.

As discussed in Chapter 1, only 12 of the $\approx$ 100 galaxies of the MASSIVE sample currently have a SMBH mass measurement. These SMBH masses are listed in Table 5.2, together with the results of this thesis which contribute three new SMBH mass measurements and two additional upper limits for MASSIVE galaxies. Although the total number of MASSIVE SMBH measurements remains modest, the three new mass determinations presented here constitute again a 25 per cent increase of the number of SMBH masses available for this extreme galaxy population. When the upper limits are also considered, the total number of dynamical constraints on SMBH masses in MASSIVE galaxies increases by $\approx$ 40 per cent, considerably improving the sampling of the high-mass end of the $M_{\rm BH} - \sigma_{\rm e}$ relation.

Fig. 5.3 shows the distribution of SMBH masses of the MASSIVE sample galaxies relative to other SMBH mass measurements from the literature. The majority (10) of galaxies lie within the 1σ scatter of the best-fitting $M_{\rm BH} - \sigma_{\rm e}$ relation, four galaxies host SMBHs that are significantly above the relation (NGC 383, NGC 1600, NGC 3842 and NGC 4889) and only one galaxy is below the relation (NGC 0467). The median absolute residual

Table 5.2: SMBH mass measurements of galaxies of the MASSIVE Survey sample.

Galaxy	σ_e (km s^{-1})	$\log(M_{BH}/M_\odot)$	Method	Reference
(1)	(2)	(3)	(4)	(5)
NGC 0315	341 ± 7	$9.48^{+0.04}_{-0.05}$	Stars	Pilawa et al. (2025)
NGC 0383	239 ± 16	9.55 ± 0.02	CO	Zhang et al. (2025a)
NGC 0467	247 ± 10	$8.38^{+0.22}_{-0.35}$	CO	Section 3.4
NGC 0665	164 ± 10	< 9.79	CO	Section 3.2
NGC 0997	215 ± 10	$8.98^{+0.10}_{-0.22}$	CO	Section 2.4, Dominiak et al. (2024)
NGC 1453	272 ± 10	9.46 ± 0.06	Stars	Liepold et al. (2020)
NGC 1600	293 ± 10	10.06 ± 0.45	Stars	Thomas et al. (2016)
NGC 1684	262 ± 10	9.15 ± 0.05	CO	Section 2.3, Dominiak et al. (2024)
NGC 2693	296 ± 10	$9.23^{+0.09}_{-0.12}$	Stars	Pilawa et al. (2022)
NGC 3842	270 ± 10	$9.99^{+0.12}_{-0.13}$	Stars	McConnell et al. (2012)
NGC 4472	300 ± 7	$9.40^{+0.05}_{-0.02}$ †	Stars	Rusli et al. (2013)
NGC 4486	324 ± 10	9.54 ± 0.10	Gas	Walsh et al. (2013)
NGC 4649	385 ± 10	$9.65^{+0.09}_{-0.11}$	Stars	Shen & Gebhardt (2010)
NGC 4889	347 ± 10	$10.32^{+0.25}_{-0.62}$	Stars	McConnell et al. (2012)
NGC 5208	235 ± 10	< 9.48	CO	Section 3.3
NGC 7052	266 ± 13	$9.40^{+0.05}_{-0.06}$	CO	Smith et al. (2021b)
NGC 7619	292 ± 5	$9.40^{+0.12}_{-0.06}$ †	Stars	Rusli et al. (2013)

Notes. (1) Galaxy name. (2) Stellar velocity dispersion measured within the half-light radius, with 1σ uncertainties. Where uncertainties are not provided, we assume 10 km s^{-1}. (3) SMBH mass, with 1σ uncertainties. Upper limits are listed as the 3σ upper limits. (4) Method of SMBH mass determination. (5) Reference.

between these SMBH masses and the van den Bosch (2016) relation (where residual is defined as $\Delta \log M_{BH} = \log M_{BH,obs} - \log M_{BH,pred}$, where $\log M_{BH,obs}$ is the observed and $\log M_{BH,pred}$ is the predicted SMBH mass) is 0.29 dex when including the 4 galaxies that lie significantly above the relation and 0.09 dex without them (both results are excluding the upper limits). Even among the galaxies that lie within the scatter, most are systematically above the relation. However, it is worth noting that both median absolute residuals are smaller than the scatter of the relation ($\varepsilon = 0.49 \pm 0.03$ dex). As such, the current MASSIVE SMBH mass sample does not provide statistically significant evidence for a systematic offset from the canonical $M_{BH} - \sigma_e$ relation.

These results suggest that the over-massive SMBHs previously reported in some massive ETGs may in fact be fairly uncommon ($\lesssim$ 30 per cent; 4/15). While there is an indication that massive ETGs may, on average, lie slightly above the mean $M_{BH} - \sigma_e$ relation, any such

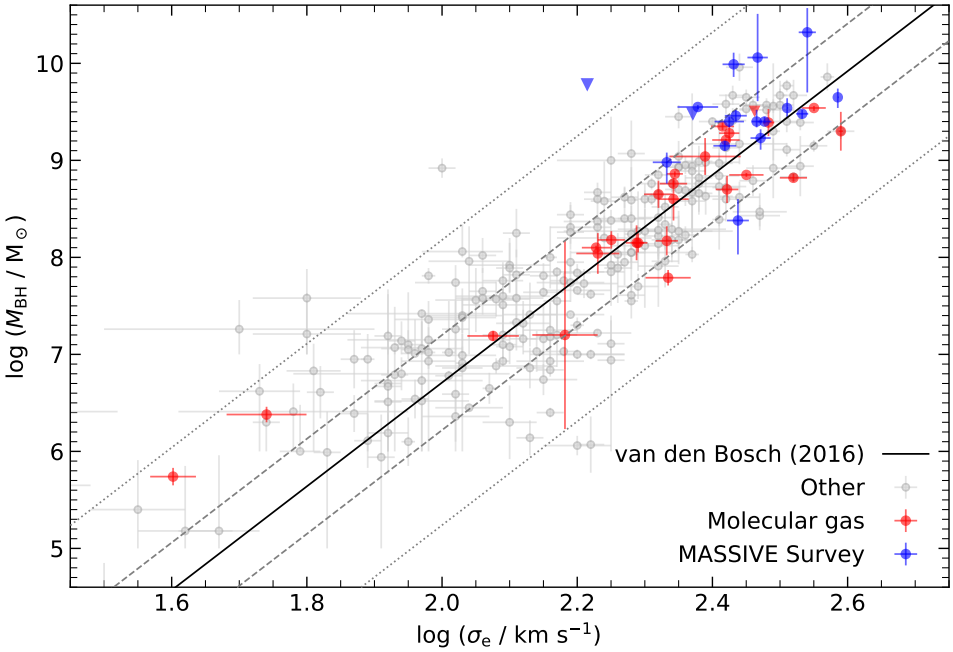


Figure 5.3: Black hole mass – stellar velocity dispersion relation obtained from stellar kinematic, ionised-gas kinematic, maser kinematic and AGN reverberation mapping SMBH mass measurements (grey data points), as reported by van den Bosch (2016). Red data points show measurements obtained from molecular gas kinematics, while the SMBH mass measurements of MASSIVE Survey galaxies are shown in blue. Error bars denote 1σ uncertainties. The solid black line shows the best-fitting relation of van den Bosch (2016), while dashed and dotted grey lines show the 1σ and 3σ scatter of that relation, respectively.

trend appears to be less pronounced than previously inferred from smaller samples. Further work by MASSIVE and other groups (e.g. Nguyen et al. 2023), focussing on increasing the number of massive ETGs with direct SMBH mass measurements, will enable a tighter constraint on the prevalence of over-massive SMBHs and improve our understanding of the high-mass end of the $M_{BH} - \sigma_e$ relation.

5.1.4 Systematic biases in SMBH mass measurements and their impact on $M_{BH} - \sigma_e$ relation

As discussed in Chapter 1, the ability to meaningfully study SMBH – host galaxy correlations relies on accurate methods of SMBH mass determination. While a variety of kinematic tracers can be used to probe the SMBH SoI, such as stars, ionised gas and maser discs, different methods tend to work best in different types of targets. Each method also suffers

from distinct systematic weaknesses that might bias the derived SMBH masses and, in turn, affect the form and interpretation of SMBH scaling relations (van den Bosch 2016).

To identify potential inconsistencies between different methods, uncover systematic SMBH mass biases and resolve the uncertainties in SMBH – host galaxy relations, there is an acute need to cross-check SMBH masses obtained using different methods in the same targets. However, such cross-checks have proven to be incredibly challenging due to the limited number of targets suitable for multiple methods of mass determination. To date, the SMBH masses of only 11 targets have been cross-checked between some of the stellar, ionised gas, reverberation mapping and maser methods (see Liang et al. 2023 for a summary). In addition to these, molecular gas has enabled cross-checks in 7 more objects, increasing the number of cross-checked masses by two thirds.

It is commonly stated that ideally all these methods would be cross-checked against maser measurements, which are generally considered the gold standard of SMBH mass determination, to determine the accuracy and potential biases of the methods. However, the rarity of masers and their strong bias towards relatively low-mass active galaxies (with correspondingly light SMBHs) makes the pursuit of such comparisons impossible. In addition, maser discs often have a complicated velocity structure, less extension towards the SMBH and generally few data points sampling the rotation curves. As a result, even if maser masses are the gold standard measurement for individual galaxies, they cannot function as a universal calibrator for the population or effectively anchor the slope or scatter of the $M_{\rm BH} - \sigma_{\rm e}$ relation.

Given these constraints, the most meaningful cross-check strategy that we can employ is instead to compare our ALMA CO dynamical measurements against the most widely applicable method, which is stellar dynamical modelling. Because stellar kinematics can, in principle, be applied to all galaxy types they have served as the backbone of all SMBH – host galaxy relations. While stellar dynamical masses are not free of systematic uncertainties (e.g. modelling assumptions, orbital anisotropy and the treatment of dark matter), they offer the broadest common basis for comparisons across morphology, mass scale and nuclear activity. Consequently, stellar dynamics functions as the natural reference frame in which to interpret potential tracer-dependent offsets and to assess whether any apparent differences in the inferred $M_{\rm BH} - \sigma_{\rm e}$ relation reflect method-dependent systematics.

Aside from the dwarf galaxy NGC 0404, that has a SMBH mass of $< 10^6$ $M_\odot$, there are currently only four galaxies with both a molecular gas and a stellar kinematic SMBH mass measurement: NGC 0524 (Krajnović et al. 2009; Smith et al. 2019), NGC 1332 (Rusli et al. 2011; Barth et al. 2016), NGC 4697 (Schulze & Gebhardt 2011; Davis et al. 2017) and NGC 6861 (Rusli et al. 2013; Kabasares et al. 2022). In this context, we revisit our results for NGC 4751, which is one of the very few galaxies which now, with the work presented in Section 2.5, has both a CO dynamical and stellar dynamical SMBH mass determination. In fact, with the work of Dominiak et al. (2025), NGC 4751 now also has stellar dynamical SMBH mass measurements obtained using two different methods. NGC 4751 provides a valuable addition to the limited set of robust cross-check targets. Figure 5.4 compares the stellar (left panel) and molecular gas (right panel) kinematic measurements of the SMBH masses of these five objects. Whilst on average the molecular mass measurements tend to lie closer to the $M_{\rm BH} - \sigma_{\rm e}$ relation, four of the five galaxies have SMBH masses that are entirely consistent between the two methods (NGC 524, NGC 4751, NGC 4697 and NGC 6861). In addition, closer inspection of these results provides context and demands caution when making such comparisons. Indeed, the masses were determined using a variety of methods, with a variety of assumptions and a variety of data quality.

Krajnović et al. (2009) used Schwarzschild modelling with the assumption of axisymmetry to model NGC 0524. The data have a PSF FWHM of 0.23 arcsec, which is a few times smaller than the SMBH $R_{\rm SoI}$ of 0.6 arcsec (here and throughout we will use the SMBH mass of the respective work when evaluating the SoI). However, as NGC 0524 is face-on, it is challenging to estimate its inclination, as that involves additional assumptions about its intrinsic shape. Nevertheless, the assumed inclination of 20° is similar to that ($i = 20\overset{\circ}{.}6$) derived by Smith et al. (2019). Whilst the angular resolution of the Smith et al. (2019) data ($R_{\rm beam} = 0.3$ arcsec) is comparable to their estimated SoI ($R_{\rm SoI} = 0.31$ arcsec), the molecular gas data of NGC 0524 exhibit a large central hole, determined to have a radius $R_{\rm hole} = 0.52$ arcsec which, coupled with the low inclination angle, is likely responsible for the unusually large confidence intervals of the reported SMBH mass. Nevertheless, the SMBH masses derived using the two methods are consistent with each other within 3σ.

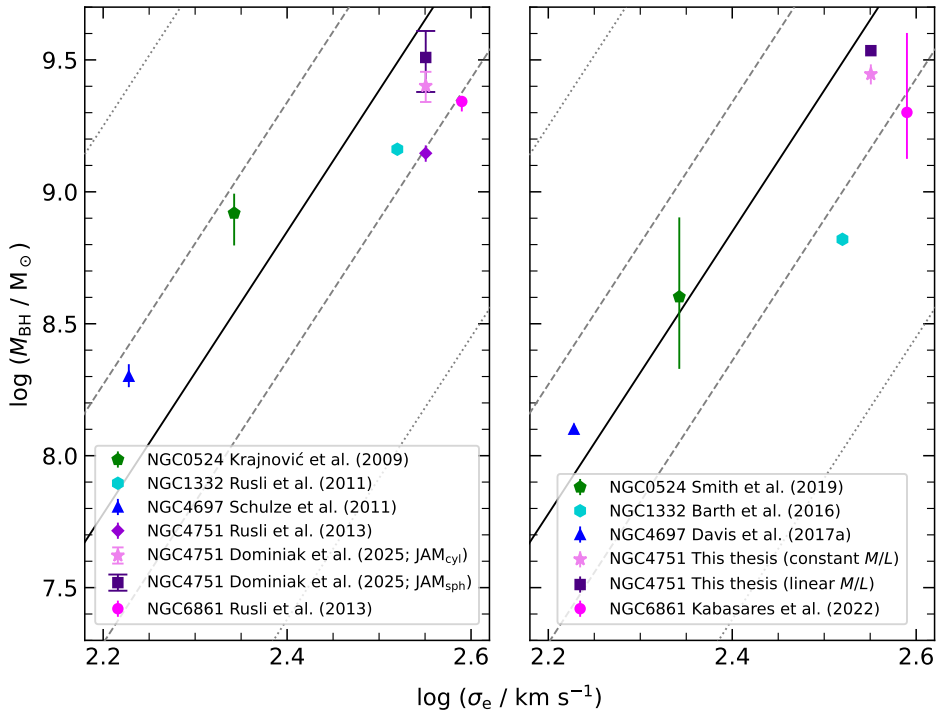


Figure 5.4: Best-fitting SMBH mass – stellar velocity dispersion relation (black line) of van den Bosch (2016), with SMBH masses derived using both stellar kinematics (left) and molecular gas kinematics (right). Dashed and dotted grey lines show the 1σ and 3σ scatter of the relation, respectively. Error bars indicate 3σ confidence level uncertainties for Krajnović et al. (2009) and Smith et al. (2019), 1σ uncertainties otherwise.

NGC 1332 is one of the galaxies for which multiple results disagree with each other. This is particularly surprising as Barth et al. (2016) used the same stellar luminosity profile as Rusli et al. (2011). Rusli et al. (2011) used Schwarzschild modelling with the assumption of axisymmetry, but also assumed an inclination $i = 90°$. The PSF FWHM of the data is 0.14 arcsec whilst $R_{\rm SoI} = 0.38$ arcsec, therefore sufficient resolution of the SoI was achieved. The molecular gas data of Barth et al. (2016) have a geometric mean resolution of 0.044 arcsec, which again more-than-adequately resolves the $R_{\rm SoI}$ of 0.23 arcsec. The data show that NGC 1332 is almost but not exactly edge-on, with an inclination $i = 84.^\circ1$, so that the $i = 90°$ assumption of Rusli et al. (2013) was somewhat inappropriate. However, it is unlikely that such a small change in inclination can lead to a factor of ≈ 2 shift in SMBH mass. We therefore conclude that the SMBH mass discrepancy does not have an easily identifiable dynamical cause.

Schulze & Gebhardt (2011) also modelled NGC 4697 using the Schwarzschild method,

assuming axisymmetry and an inclination $i = 90°$. The $R_{\rm SoI}$ of 0.45 arcsec is fully resolved by the data, whose PSF FWHM is 0.08 arcsec. The molecular gas data of Davis et al. (2017) have a synthesised beam of 0.53 arcsec, which does not formally resolve the $R_{\rm SoI}$ of 0.34 arcsec. The dynamically-determined inclination of 76.°1 suggests that Schulze & Gebhardt's (2011) assumption of $i = 90°$ is severely off. Whilst the results are formally in disagreement with each other, they were also determined assuming different distances. When the Schulze & Gebhardt (2011) result is re-scaled to the distance assumed by Davis et al. (2017), the resultant SMBH mass is 1.6×10^8 $M_\odot$, significantly closer to and consistent with that of Davis et al. (2017) within 3σ (despite the erroneous inclination assumption).

Rusli et al. (2013) used the Schwarzschild method to model NGC 6861, also assuming axisymmetry and an inclination $i = 90°$. The data have a PSF FWHM of 0.38 arcsec, which fully resolves the $R_{\rm SoI}$ of 0.38 arcsec. The molecular gas modelling of Kabasares et al. (2022) yields an inclination $i = 73°$, once again suggesting that the convenient $i = 90°$ assumption in Schwarzschild modelling is incorrect. Despite this, the SMBH masses derived through the two methods are entirely consistent with each other.

As already discussed in Section 2.5.4, NGC 4751 provides a particularly instructive case of tension between stellar and molecular gas SMBH mass measurements. Rusli et al. (2013) obtained a stellar kinematic SMBH mass using the Schwarzschild method, also assuming axisymmetry and an inclination of 90°. The data used have a PSF FWHM of 0.22 arcsec, formally resolving the RSoI of $\approx$ 0.35 arcsec. However, the analysis of the same stellar kinematic data using the JAM method (Dominiak et al. 2025) yields a mass inconsistent with and $\approx 2\times$ larger than Rusli et al.'s. The molecular gas modelling presented in Section 2.5 yields a mass consistent with the one obtained using JAM and similarly inconsistent with the result of Rusli et al. (2013). In addition to having a consistent mass, the CO and JAM results derive similar inclinations ($i = 72°$ for JAM and $i = 78.7°$ for CO).

Despite no clear trend with respect to the $M_{\rm BH} - \sigma_{\rm e}$ relation, Fig. 5.5 suggests that molecular gas kinematics yields systematically lower SMBH mass estimates than stellar kinematics. It is hard to establish whether stellar kinematic modelling overestimates the masses or molecular gas modelling underestimates the masses, but molecular gas modelling is generally considered to be a lot simpler. The main assumption underlying molecular

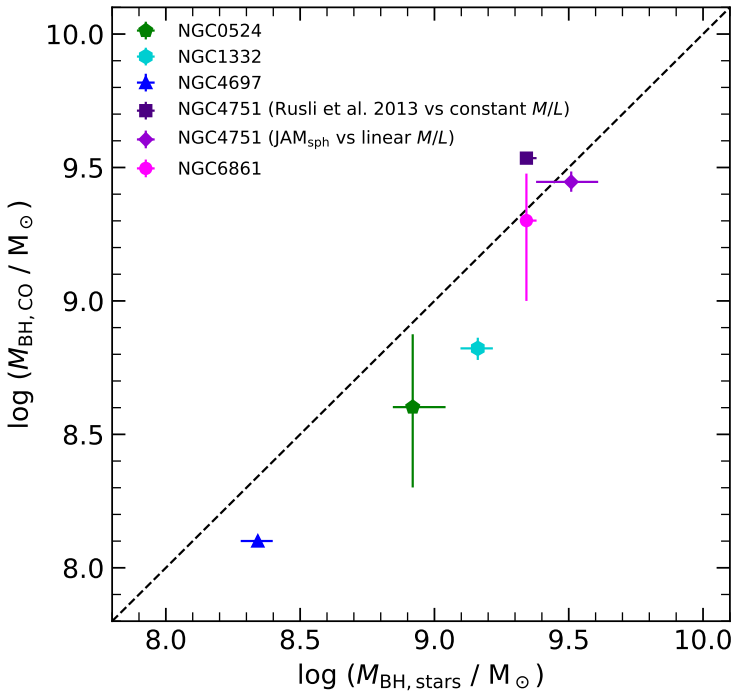


Figure 5.5: Cross comparison of SMBH masses derived using stellar kinematics and molecular gas. For clarity we have only included two data points for NGC 4751, representing the two extremes. One data point compares the least massive stellar kinematic mass estimate (Rusli et al. 2013) and our most massive molecular gas mass estimate (our model with a constant M/L); the other compares the most massive stellar kinematic mass estimate (model of Dominiak et al. 2025 assuming $\mathrm{JAM_{sph}}$) and our least massive molecular gas mass estimate (our model with a linearly-varying M/L). All data points comparing any other two methods would lie between those two. Error bars are as in Fig. 5.4.

gas modelling is the presence of circular motions, which can be easily verified from the data themselves. Subsequently, the modelling is relatively straightforward and has considerable flexibility for implementing position angle and/or inclination warps. Both JAM and Schwarzschild modelling cannot rely on the simple assumption that the tracer population lies in a simple thin disc and they have to fit for the velocity anisotropy of the stars. However, the stars, unlike gas, have the advantage of being unaffected by non-gravitational forces such as inflows, outflows and shocks. Both molecular gas and stellar methods can easily model radial M/L gradients. Overall, more cross-checks are needed to reach a conclusion on the reliability and possible biases of different SMBH mass determination methods.

5.2 Summary

This thesis focused on using cold molecular gas observations to probe different physical scales within galaxies. First focusing on the central regions of galaxies, Chapter 2 started with a description of the methodology of obtaining SMBH masses using molecular gas modelling. It then moved on to present the measurements of SMBH masses in four galaxies. Chapter 3 continued the work of molecular gas modelling, but this time focused on presenting unpublished work, predominantly in galaxies whose data were not conducive to the inference of robust SMBH masses. Instead, it presents the SMBH mass upper limits for two galaxies, a tentative SMBH mass which is recommended for a follow-up study and one target in which modelling was entirely untenable. We then moved on to looking at larger scale galactic features, where Chapter 4 presented a new CO TFR calibration for the local Universe, based on a sample of 71 galaxies. This research has consolidated and extended our knowledge of galactic evolution in the following ways:

- Each of the SMBH masses determined in this thesis using molecular gas dynamics is consistent within 1σ with the $M_{\rm BH} - \sigma_{\rm e}$ relation of van den Bosch (2016), across the full mass range probed. This demonstrates that molecular gas SMBH mass measurements are fully consistent with the expected results based on $M_{\rm BH} - \sigma_{\rm e}$ relations determined largely without the inclusion of molecular gas masses.

- While molecular gas dynamics offer a promising avenue for expanding the sample of direct SMBH mass measurements, this thesis shows that there are some limitations to the method. Although molecular gas is detected in a meaningful fraction of nearby galaxies ($\approx$ 20 per cent), only a subset of those will host the regularly rotating circumnuclear discs suitable for robust measurements (e.g. ones without major central holes/depressions or without significant non-axisymmetric motions). This thesis presents successful measurements, upper limits and untenable cases as a realistic assessment of the real applicability of the method.

- As the field of molecular gas SMBH mass measurements continues to mature, this thesis highlights the increasing importance of carefully quantifying systematic uncertainties

and assessing how modelling assumptions propagate into inferred SMBH masses. In particular, robust measurements require either sufficiently high angular resolution to resolve the SMBH SoI, thereby minimising degeneracies with the stellar mass distribution, or, in cases where the SoI is only marginally resolved, improved treatment of dust attenuation and stellar population variations in the construction of stellar mass models. Addressing these systematics will be essential for obtaining future accurate SMBH masses.

- The expanded molecular gas SMBH sample presented in this thesis enables the construction of a statistically meaningful CO-only $M_{\rm BH} - \sigma_{\rm e}$ relation, which is fully consistent in slope and intercept with literature relations derived using other dynamical tracers. This suggests that molecular gas SMBH masses do not introduce systematic offsets in this fundamental scaling relation.

- The inclusion of new molecular gas SMBH masses and upper limits for MASSIVE Survey galaxies reveals that, while a subset of massive ETGs host genuinely over-massive SMBHs, the majority lie within the scatter of the canonical $M_{\rm BH} - \sigma_{\rm e}$ relation with modestly positive residuals. This suggests that extremely over-massive SMBHs are less common than previously inferred.

- On galactic scales, this thesis establishes a robust local benchmark for the $W1$-band CO TFR relation using a sample of 71 galaxies. The results demonstrate that CO provides a reliable kinematic tracer for TFR studies across a broad range of galaxy types.

- Finally, this work identifies a systematic difference between the CO TFRs of ETGs and LTGs, potentially reflecting underlying structural or dynamical differences between these populations.

5.3 Future work

This thesis has demonstrated that ALMA CO kinematics can be used to probe galaxies on both nuclear and galactic scales. Despite the clear success of the method, this thesis also

highlights some of the limitations in the field. In this section we will explore the questions that are yet to be answered and highlight directions for future work.

5.3.1 Expanding the molecular gas SMBH mass sample

As demonstrated in this thesis and in previous work, molecular gas provides a reliable and comparatively straightforward tracer for determining SMBH masses across a range of galaxy types. As discussed in Section 5.1.2, molecular gas methods have been used to determine the SMBH masses of 34 targets to date, which remains a relatively small sample compared to those obtained using other techniques (e.g. 92 stellar and 104 ionised gas SMBH masses in van den Bosch 2016). Expanding the molecular gas SMBH mass sample is therefore of clear scientific value, particularly if future observations are targeted toward regimes that are currently under-represented. In the following subsections we outline several such regimes where additional molecular gas SMBH mass measurements would provide the greatest leverage.

High-mass SMBHs

This thesis has presented three new SMBH mass measurements and two SMBH mass upper limits for galaxies in the MASSIVE Survey, probing the high-mass end of the $M_{\rm BH} - \sigma_{\rm e}$ relation. Although this regime is highly informative for understanding SMBH – host galaxy co-evolution, it remains sparsely populated by SMBH mass measurements.

At present, constraints at the high-mass end are dominated by a small number of giant ellipticals and brightest cluster galaxies (e.g. McConnell & Ma 2013; Saglia et al. 2016). These systems are precisely those in which galaxy assembly is expected to be governed primarily by dissipationless (dry) merging and by SMBHs coalescing, rather than by secular gas accretion. As a result, different observational outcomes at the high-mass end of the relation carry distinct implications for our understanding of galaxy assembly.

If future studies were to confirm that a substantial fraction of massive ETGs host SMBHs that lie significantly above the extrapolated $M_{\rm BH} - \sigma_{\rm e}$ relation, this would support a picture in which SMBHs continue growing even in gas-poor environments after the bulge velocity dispersions have been largely saturated. In such a scenario, dry mergers would increase SMBH mass through coalescence while producing only modest changes in $\sigma_{\rm e}$, naturally

leading to an upward offset or increased scatter at the massive end. This outcome would support galaxy assembly models where late SMBH growth is dominated by hierarchical merging. Conversely, if an expanded high-mass SMBH sample was to show that even the most massive galaxies follow the $M_{\rm BH} - \sigma_{\rm e}$ extrapolated from lower mass galaxies, this would suggest that either SMBH growth and bulge growth remain coupled even in largely dissipationless regimes, or that subsequent dynamical processes act to preserve the relation despite complex merger histories.

There is a clear need to extend molecular gas SMBH mass measurements beyond the MASSIVE Survey in order to resolve these issues. MASSIVE is a volume-limited survey selected using a stellar mass and K-band magnitude threshold, and it is likely that additional suitable targets exist outside its formal boundaries. Davis et al. (2015) selected a pilot sample of 15 MASSIVE galaxies with indications of potential molecular gas content, such as prominent dust lanes in *HST* imaging or strong 22 μm emission. Of the 15 targets, 10 were detected in CO. Four of these CO detected systems have been modelled in this thesis (NGC 0665, NGC 0997, NGC 1684 and NGC 5208) and they likely represent some of the most favourable high-mass targets within the MASSIVE sample. While further suitable systems may still be identified within MASSIVE, these results indicate that a comprehensive exploration of the high-mass end of the $M_{\rm BH} - \sigma_{\rm e}$ relation will require extending molecular gas SMBH surveys to massive ETGs beyond the MASSIVE Survey.

Low-mass SMBHs

As discussed in Section 5.1.2 the vast majority of molecular gas SMBH mass measurements currently lie in the $\approx 10^8 - 10^{9.5}$ M$_\odot$ range, with only five galaxies which lie below $< 10^8$ M$_\odot$. It is also evident that the overall slope of the $M_{\rm BH} - \sigma_{\rm e}$ relation determined using molecular gas measurements only remains uncertain and is affected by the small number of data points in the low-mass range. In particular, if the two low SMBH mass measurements of NGC 0404 and NGC 3593 are representative of the underlying population rather than statistical outliers, this would imply that the molecular gas only $M_{\rm BH} - \sigma_{\rm e}$ relation departs from relations derived using other (heterogeneous) samples, potentially indicating tracer dependent systematics

(McConnell & Ma 2013; van den Bosch 2016). Robustly testing this possibility requires substantially expanding the CO SMBH mass sample at low masses.

From a physical perspective, the low-mass regime is particularly important because it may encode information about SMBH seeding, early growth and the role of secular processes and nuclear star formation in shaping SMBH – host galaxy relations. If a systematic offset or change in slope is confirmed at low masses, this could indicate that SMBH growth in small galaxies is less tightly regulated by the bulge potential, or that different growth channels dominate compared to massive ETGs.

The key observational challenge in the low-mass regime is that small galaxies have small SMBHs which in turn have small SoIs. While it is possible to probe these small SoIs using ALMA, the longest baseline configurations required are not available in each Cycle and, taking into consideration atmospheric conditions, are available for only a few days each year. As such, obtaining the volume of measurements necessary to constrain this low-mass end is challenging. Nevertheless, recent studies demonstrate that progress is feasible. Davis et al. (2020) achieved an excellent resolution of ≈ 0.8 pc and measured a SMBH mass of 5.5×10^5 $M_\odot$ in the dwarf galaxy NGC 0404. Similarly, the Measuring Black Holes Below the Milky Way mass galaxies (MBHBM*) project has obtained SMBH mass measurements of 1.6×10^7 $M_\odot$ in NGC 3504 (Nguyen et al. 2020) and 2.4×10^6 $M_\odot$ in NGC 3595 (Nguyen et al. 2022). These examples illustrate that targeted, high-resolution ALMA observations of nearby low-mass galaxies can yield decisive SMBH mass constraints. Future work should prioritise the nearest low-mass systems with compact, bright nuclear CO discs in order to anchor the low-mass end of the $M_{\rm BH} - \sigma_{\rm e}$ relation and determine whether molecular gas SMBH masses exhibit systematic offsets in this regime.

Spiral galaxies

Spiral galaxies represent a critical but comparatively under-explored regime for molecular gas SMBH mass measurements. While the majority of existing CO SMBH masses have been obtained in ETGs, it is spiral galaxies that dominate the local Universe in number (Conselice 2006). Spiral galaxies span a wide range of bulge properties, from classical bulges formed during violent mergers to pseudo-bulges formed through secular evolution

(e.g. Kormendy & Kennicutt 2004). Therefore, increasing the number of SMBH mass measurements in spirals is essential, as it allows us to test how SMBH scaling relations are linked to bulge properties and galaxy structure.

If SMBHs in spirals hosting classical bulges were found to follow the same $M_{\rm BH} - \sigma_{\rm e}$ relation as ETGs, this would support a picture in which SMBH mass is primarily regulated by the depth of the central gravitational potential, largely independent of galaxy morphology. Conversely, if spirals (particularly those hosting pseudo-bulges) systematically deviate from the relation, this would imply that secular processes such as bar-driven inflows, nuclear rings and episodic gas accretion play a more prominent role in SMBH growth than violent mergers. Such a result would favour models in which SMBH growth in discs is stochastic and less tightly coupled to bulge formation than in massive ETGs.

Observationally, spiral galaxies present opportunities and challenges for molecular gas SMBH mass measurements. On one hand, spirals typically host abundant molecular gas reservoirs increasing the likelihood of detecting CO. On the other, spirals often exhibit complex gas morphologies such as bars, spiral arms, rings and other non-circular motions which violate the assumptions of an axisymmetric disc when modelling. Additionally, the presence of dust and ongoing star formation can complicate the construction of accurate stellar mass models needed to estimate the stellar contribution to the gravitational potential.

However, it is clear the molecular gas modelling can be successful in spiral galaxies, as has been shown in NGC 1097 (Onishi et al. 2015), NGC 3504 (Nguyen et al. 2020) and NGC 7469 (Nguyen et al. 2021). In fact, 35 of the 75 WISDOM Project galaxies tabulated in Chapter 4 are spiral galaxies, and of these $\approx$ 15 appear to have regularly rotating circumnuclear discs which could be fit for SMBH modelling or for follow-up high resolution ALMA observations.

By systematically expanding CO SMBH mass measurements to spiral galaxies, we can test whether SMBH scaling relations depend primarily on bulge structure, secular evolution or global galaxy properties. Such studies will be crucial for establishing whether the apparent differences between ETGs and LTGs reflect genuine physical differences in SMBH growth or arise from heterogeneous measurement techniques and sample selection effects.

High-redshift SMBH masses

Conventional methods of SMBH mass determination, which rely on resolving the SoI, have rarely been used in determining SMBH masses beyond the local Universe. The majority of reliable SMBH mass determinations at high redshifts have relied on reverberation mapping techniques. These methods seem to suggest the presence of over-massive SMBHs at $z > 2$ compared to local SMBH mass scaling relations (e.g. Targett et al. 2012; Stone et al. 2024). However, as discussed in Chapter 1, reverberation mapping relies on the highly uncertain calibration of the form factor based on local scaling relations. Additionally reverberation mapping methods require active SMBHs and are thus biased towards the most luminous quasars. Measuring high-redshift SMBHs directly from dynamical methods would substantially reduce the bias and better constrain the evolution of SMBH mass – host galaxy scaling relations across cosmic time.

Recently it has been proposed that strong gravitational lensing can be used as a means of magnifying the luminosity and extending the angular size of a lensed object, thereby enabling the observation of high-redshift galaxies. The gas kinematics of several highly magnified galaxies have already been mapped to unprecedented, sub-kpc physical resolutions which are comparable to the SoIs of SMBHs that are of the order of $\approx 10^9$ $M_\odot$ (e.g. Rizzo et al. 2020; Rizzo et al. 2021; Gururajan, G. et al. 2022). In fact, Hezaveh (2014) showed that the inner 50 pc could be detected in up to 20 per cent of strongly lensed galaxies allowing the measurement of $\gtrsim 10^8$ $M_\odot$ SMBHs using ALMA. Therefore, the gas kinematics of strongly lensed galaxies observed with ALMA are a promising avenue for determining a statistically significant sample of dynamical SMBH mass measurements beyond the local Universe.

Cross-checking SMBH masses

A crucial step toward improving the reliability of SMBH scaling relations is to increase the number of galaxies for which SMBH masses are measured using multiple independent techniques, thereby probing method-dependent offsets and systematic uncertainties. As discussed in this thesis, the traditional approach of cross-checking molecular gas SMBH masses against maser measurements is severely limited in practice, owing to the rarity of maser systems and the frequent coexistence of masers with disturbed or irregular CO

kinematics (Liang et al. 2023). As a result, maser vs. molecular gas comparisons are unlikely to yield a statistically meaningful calibration sample.

In practice, the most impactful cross-check strategy is one which expands the sample of galaxies with both stellar dynamical and molecular gas SMBH mass measurements. At present, only six galaxies provide such direct cross-checks, highlighting the need for a deliberate effort aimed at identifying additional suitable targets. Although selecting galaxies which are suitable for robust modelling with multiple methods is challenging, recent work suggests that this approach is feasible with careful target selection. As an example, a recent WISDOM-led ALMA ACA programme (Project `2022.1.01173.S`) targeted nine galaxies with existing SMBH mass measurements obtained using other techniques. These targets were selected based on either prior single-dish CO detections or the presence of dust structures in *HST* imaging, which are often associated with molecular gas reservoirs. CO emission was detected in all nine galaxies, six of which exhibit kinematic properties indicative of regularly rotating circumnuclear discs that are suitable for high-resolution follow-up studies enabling detailed molecular gas dynamical modelling.

Building on such pilot studies, future work should pursue a systematic stellar vs. molecular gas cross-check programme, focusing on nearby galaxies with large predicted spheres of influence and regular gas kinematics. Expanding this cross-check sample will be essential for quantifying tracer-dependent systematics and establishing a robust uncertainty budget for SMBH – host galaxy scaling relations.

Galactic environment

There has been growing evidence that scaling relations, including $M_{\rm BH} - \sigma_{\rm e}$, may depend on galaxy environment. In particular, McGee (2013) showed that central galaxies follow a steeper $M_{\rm BH} - \sigma_{\rm e}$ relation than satellite galaxies, and that this separation persists even when restricting the sample to ETGs and when removing known brightest cluster galaxies (BCGs). These results motivate treating environment as a potentially non-negligible parameter in SMBH demographics, rather than assuming a universal scaling relation independent of the halo (e.g. McGee 2013; Shankar et al. 2016).

It has long been suggested that the richest environments preferentially host SMBHs that are over-massive relative to their σ_e particularly among BCGs and other central galaxies (e.g. Lauer et al. 2007; McConnell et al. 2012; Thomas et al. 2016). Such an offset could arise in a variety of ways. Firstly, interaction and merger rates depend on local galaxy density and on the availability of bound companions. Therefore, galaxies in groups and clusters have enhanced opportunities for close encounters and mergers compared to isolated field galaxies (e.g. Patton et al. 2000; Lotz et al. 2011). Since mergers can deliver gas to the nuclear regions through gravitational torques and increase SMBH mass through subsequent merging of central SMBHs, elevated interaction rates naturally accelerate SMBH growth in dense environments (e.g. Barnes & Hernquist 1992; Volonteri et al. 2003).

Secondly, according to ΛCDM models, galaxies form and reside in the centres of dark matter haloes. Groups and clusters grow by accreting other smaller haloes with the most massive galaxy typically occupying the halo centre. Satellite galaxies lose their angular momentum through dynamical friction and are gradually drawn toward the halo centre, depositing their stars and, in some cases, their central black holes into the central galaxy (Binney & Tremaine 2008). These dissipationless (dry) mergers efficiently grow the stellar mass and size of the central galaxy together with its SMBH without significant increases to σ_e. It is for this reason that BCGs often populate the high-mass end of the $M_{BH} - \sigma_e$ relation. Conversely, the same environmental processes can act in the opposite sense for satellite galaxies, suppressing their cold gas supply required for secular SMBH growth. Satellites which orbit a more massive halo are subject to ram-pressure stripping and tidal interactions which can remove gas reservoirs, thereby quenching star formation and no longer fueling nuclear activity. Even when the cold gas is not stripped immediately, fresh accretion can halt in satellites once they fall into a group or cluster (e.g. Peng et al. 2015). These effects provide a natural explanation for why satellite galaxies may host systematically smaller SMBHs than central galaxies at fixed stellar velocity dispersion, consistent with the environmental separation reported by McGee (2013).

Environment is also expected to affect the presence, morphology and dynamical regularity of cold molecular gas, which directly impacts the feasibility and selection of CO SMBH mass measurements. The same ram-pressure stripping and tidal interactions that affects the cold

molecular gas that fuels the growth of satellite galaxies also impedes our ability to observe it. Even if some surveys have shown that molecular gas is commonly detected in ETGs across a range of environments, its kinematic structure seems to depend on environment (e.g. Davis et al. 2011b; Young et al. 2011). In clusters, molecular gas discs are more likely to be compact, disturbed or misaligned with the stellar body, reflecting environmental processing and external gas acquisition histories (e.g. Davis et al. 2013a; Brown et al. 2021). Such effects can reduce the fraction of galaxies that host dynamically cold, regularly rotating nuclear discs suitable for precise SMBH mass modelling.

As a result, environmental trends in SMBH scaling relations may arise not only from genuine differences in SMBH growth histories, but also from environment-dependent selection effects. Therefore, distinguishing between these observational selection effects and true astrophysical differences requires joint studies of SMBH masses and molecular gas properties across a variety of galactic environments.

5.3.2 CO Tully-Fisher relation

Scaling relations provide a powerful framework for linking observable galaxy properties to the physical processes that govern galaxy formation and evolution, but their interpretation depends greatly on measurement homogeneity and a clear understanding of selection effects. As demonstrated in this thesis, CO observations offer a homogeneous kinematic tracer that can be applied consistently across galaxy morphology, spatial scale and, in principle, across cosmic time, enabling the same data to be used to measure SMBH masses and to probe intermediate-scale galaxy dynamics through the TFR. In this context, TFR studies should be viewed as a natural extension of the molecular gas SMBH programme, rather than as a separate line of investigation.

Although CO TFR studies remain limited in number, it is already clear that the use of CO as a tracer enables informative analyses of rotation-based scaling relations. Future progress on the CO TFR will require both methodological refinement and targeted observational programmes, particularly with regard to velocity definitions, tracer-dependent systematics and sample selection, the details of which we outline below.

Velocity width measures

A practical limitation in comparing rotation-based scaling relations, such as the TFR, across different samples is that rotation velocity is not a uniquely defined observable. Depending on data quality and kinematic tracer, studies variously adopt the maximum observed rotational velocity of the galaxy ($v_{\rm max}$), the asymptotic rotation velocity of the outer flat part of the rotation curve ($v_{\rm flat}$), the rotation velocity at a fixed physical or scaled radius, or integrated line-width measures corrected for inclination (W_{20} or W_{50}). In addition, integrated line widths themselves may be measured directly from observed spectra or inferred from parametric fits, as was done in Chapter 4. While such 1D measures are often necessary for unresolved data, interferometric CO observations provide full 3D data cubes, allowing the rotation field to be analysed without reducing the data to a single integrated profile and avoiding the associated loss of spatial information.

Future work would therefore benefit from a systematic simulation-based study to quantify how different velocity definitions compare when applied to the same underlying galaxy kinematics. For example, synthetic CO data cubes generated with KinMS could be analysed to recover rotation velocities using multiple approaches, including (i) velocities derived from best-fitting integrated W_{50} measurements, (ii) rotation velocities measured at the outermost detected CO radius, (iii) $v_{\rm flat}$ values inferred from the flat portion of the rotation curve where present and (iv) $v_{\rm max}$ values obtained by fitting the full data cube with a parametric rotation model (e.g. an arctan profile). Quantifying systematic differences between these measures would enable the definition of more robust and reproducible velocity metrics for future CO TFR studies. Such a comparison would also clarify whether the typically limited radial extent of CO emission in some galaxies implies that CO rotational velocities preferentially trace the baryon-dominated inner regions or approach the flat part of the rotation curve set by the dark matter halo.

Early- and late-type TFRs

As shown in Chapter 4, even when using a homogeneous kinematic tracer such as CO, a systematic offset of $\sim 0.8 - 1.1$ mag persists between the TFRs of ETGs and LTGs. This contrasts with some previous studies that reported reduced offsets when adopting a single

tracer for both populations (Williams et al. 2010), indicating that the magnitude and, to some extent, origin of the offset remains uncertain. Resolving this discrepancy is important because a genuine offset informs us about galaxy formation and structural evolution.

Several factors may contribute to differences between ETG and LTG TFRs. ETGs typically have higher bulge fractions and a more centrally concentrated baryon distributions, which can alter the relationship between rotation velocity and total baryonic or stellar mass (e.g. Cappellari et al. 2013; Cappellari 2016). Additionally, differences in stellar populations and M/L, particularly in quenched systems, can result in shifts in the TFR (e.g. Bell & de Jong 2001). ETGs also often exhibit a combination of rotational and pressure support, such that the gas velocity dispersion or asymmetric drift may reduce the observed rotation speed relative to late-type, disc-dominated systems (e.g. Cappellari et al. 2007). In such a case, the offset would reflect intrinsic differences in mass distribution and orbital structure that arise from distinct formation pathways, such as mergers and quenching, rather than measurement systematics.

An additional and potentially important consideration is the radial extent of the molecular gas. In many ETGs CO discs are compact and may not fully trace the outer gravitational potential where the rotation curve flattens. If the CO rotation velocities in ETGs only sample the baryon-dominated inner regions, this could lead to a systematic underestimation of the rotation velocity used in TFR analyses. Combining CO observations with H I kinematics, where available, would be particularly informative, as H I typically extends to larger radii and better traces the dark matter halo. Such a study would help determine whether the observed ETG offset reflects intrinsic differences in mass distribution and formation history, or instead arises because different tracers probe different regions of the gravitational potential.

High-redshift CO TFR

As discussed in Chapter 4, the current sample of galaxies used to determine a CO TFR at high redshift remains very limited (25 galaxies; Topal et al. 2018). As a result, the inferred slope and intercept of the high-redshift CO TFR have large uncertainties. Although the relation of Topal et al. (2018) is formally consistent with our local CO TFR within these uncertainties, the best-fitting parameters differ substantially. The slope reported by Topal et al. (2018) is disfavoured by our measurements at the $\sim 4\sigma$ level and the intercept is offset

by $\sim$ 0.5 mag, also corresponding to a $\sim 4\sigma$ difference relative to our result. Whether this apparent discrepancy reflects genuine physical evolution or is driven by small-number statistics and selection effects remains unclear.

Investigating this potential offset is therefore an important goal for future work. Evolution over cosmic time in optical band TFRs, particularly in the B-band, has been reported in several studies and is generally attributed to higher star formation rates and younger stellar populations at earlier times, which boost luminosities at fixed rotation velocity (e.g. Vogt et al. 1996; Bamford et al. 2006; Miller et al. 2011). Such evolution is less expected in the near-infrared K_s- and $W1$-bands which trace older stellar populations and more closely reflect stellar mass rather than recent star formation. Consequently, a significant offset in a near-infrared CO TFR would be difficult to explain through stellar population effects alone.

High-redshift discs are known to be more turbulent than their local counterparts with pressure support from random motions contributing significantly to the overall dynamical balance (e.g. Förster Schreiber et al. 2009; Wisnioski et al. 2015). In such a case, the observed rotation velocity would underestimate the true circular velocity of the potential, producing an apparent offset in rotation-based scaling relations (e.g. Burkert et al. 2010; Übler et al. 2017). Many high-redshift galaxies may also not yet host fully settled and extended rotation curves, meaning that the rotation velocity inferred from CO kinematics may not reflect the final equilibrium state of the galaxy (e.g. Genzel et al. 2017). Alternatively, the offset could arise from selection effects rather than intrinsic evolution. High-redshift CO samples preferentially target compact, gas-rich systems in which molecular gas traces only the inner, baryon-dominated regions of the galaxy (e.g. Tacconi et al. 2013; Übler et al. 2017). If CO does not extend to radii where the rotation curve flattens, the resulting velocity measurements may not be directly comparable to those obtained in local galaxies, leading to an apparent shift in the TFR even in the absence of true physical evolution.

Future work will require significantly expanding the high-redshift CO TFR sample using a homogeneous tracer and a consistent velocity definition across redshift and morphology. By analysing local and distant galaxies with the same CO methodology, it will be possible to disentangle true evolutionary effects from observational biases. Establishing whether

the CO TFR evolves with redshift would provide a powerful constraint on the evolution of baryon assembly, angular momentum retention and disc settling.

Bibliography

Alatalo K., et al., 2013, MNRAS, 432, 1796

Alatalo K., et al., 2015, ApJ, 798, 31

Andreani P., Carpenter J., Diaz-Trigo M., Hibbard J., Nyman L., Remijan T., Tatematsu K., 2016, ALMA Cycle 4 Proposer's Guide and Capabilities, ALMA Doc. 4.2 v1.0, https://almascience.nrao.edu/documents-and-tools/cycle4/alma-proposers-guide

Athanassoula E., 1992, MNRAS, 259, 345

Athanassoula E., 2005, MNRAS, 358, 1477

Atkinson J. W., et al., 2005, MNRAS, 359, 504

Bamford S. P., Aragón-Salamanca A., Milvang-Jensen B., 2006, MNRAS, 366, 308

Barnes J. E., Hernquist L., 1992, ARA&A, 30, 705

Barth A. J., Sarzi M., Ho L. C., Rix H.-W., Shields J. C., Filippenko A. V., Rudnick G., Sargent W. L. W., 2001, in Knapen J. H., Beckman J. E., Shlosman I., Mahoney T. J., eds, Astronomical Society of the Pacific Conference Series Vol. 249, The Central Kiloparsec of Starbursts and AGN: The La Palma Connection. p. 370

Barth A. J., Boizelle B. D., Darling J., Baker A. J., Buote D. A., Ho L. C., Walsh J. L., 2016, ApJ, 822, L28

Bedregal A. G., Aragón-Salamanca A., Merrifield M. R., 2006, MNRAS, 373, 1125

Behroozi P. S., Wechsler R. H., Conroy C., 2013, ApJ, 770, 57

Beifiori A., Sarzi M., Corsini E. M., Dalla Bontà E., Pizzella A., Coccato L., Bertola F., 2009, ApJ, 692, 856

Bell E. F., de Jong R. S., 2001, ApJ, 550, 212

Benson A. J., Bower R. G., Frenk C. S., Lacey C. G., Baugh C. M., Cole S., 2003, ApJ, 599, 38

Bentz M. C., et al., 2010, ApJ, 716, 993

Bentz M. C., et al., 2013, ApJ, 767, 149

Bertin E., Mellier Y., Radovich M., Missonnier G., Didelon P., Morin B., 2002, in Bohlender D. A., Durand D., Handley T. H., eds, Astronomical Society of the Pacific Conference Series Vol. 281, Astronomical Data Analysis Software and Systems XI. p. 228

Bigiel F., Leroy A., Walter F., Brinks E., de Blok W. J. G., Madore B., Thornley M. D., 2008, AJ, 136, 2846

Binney J., Tremaine S., 2008, Galactic Dynamics: Second Edition

Birnboim Y., Dekel A., 2003, MNRAS, 345, 349

Bittner A., et al., 2020, A&A, 643, A65

Blakeslee J. P., et al., 2009, ApJ, 694, 556

Blandford R. D., McKee C. F., 1982, ApJ, 255, 419

Blumenthal G. R., Faber S. M., Primack J. R., Rees M. J., 1984, Nature, 311, 517

Boizelle B. D., Barth A. J., Walsh J. L., Buote D. A., Baker A. J., Darling J., Ho L. C., 2019, ApJ, 881, 10

Boizelle B. D., et al., 2021, ApJ, 908, 19

Bolatto A. D., Wolfire M., Leroy A. K., 2013, ARA&A, 51, 207

van den Bosch F. C., 2000, ApJ, 530, 177

van den Bosch R. C. E., 2016, ApJ, 831, 134

van den Bosch R. C. E., de Zeeuw P. T., 2010, MNRAS, 401, 1770

van den Bosch R. C. E., van de Ven G., 2009, MNRAS, 398, 1117

van den Bosch R. C. E., van de Ven G., Verolme E. K., Cappellari M., de Zeeuw P. T., 2008, MNRAS, 385, 647

van den Bosch R. C. E., Greene J. E., Braatz J. A., Constantin A., Kuo C.-Y., 2016, ApJ, 819, 11

Brook C. B., et al., 2011, MNRAS, 415, 1051

Brown T., et al., 2021, ApJS, 257, 21

Burkert A., et al., 2010, ApJ, 725, 2324

Campbell L. A., et al., 2014, MNRAS, 443, 1231

Cantiello M., Blakeslee J. P., 2023 (arXiv:2307.03116)

Cappellari M., 2002, MNRAS, 333, 400

Cappellari M., 2008, MNRAS, 390, 71

Cappellari M., 2013, ApJL, 778, L2

Cappellari M., 2016, ARA&A, 54, 597–665

Cappellari M., 2020, MNRAS, 494, 4819

Cappellari M., et al., 2007, MNRAS, 379, 418

Cappellari M., Neumayer N., Reunanen J., Van Der Werf P. P., De Zeeuw P. T., Rix H.-W., 2009, MNRAS, 394, 660

Cappellari M., et al., 2013, MNRAS, 432, 1709

Carilli C. L., Walter F., 2013, ARA&A, 51, 105

Chakraborty A., Roy N., 2022, MNRAS, 519, 4074

Choi W., et al., 2023, MNRAS, 522, 4078

Choi W., et al., 2024, MNRAS, 531, 4045

Chung E. J., Rhee M.-H., Kim H., Yun M. S., Heyer M., Young J. S., 2009, ApJS, 184, 199

Cohn J. H., et al., 2021, ApJ, 919, 77

Cohn J. H., et al., 2023, ApJ, 958, 186

Cohn J. H., et al., 2024, ApJ, 975, 179

Collin S., Kawaguchi T., Peterson B. M., Vestergaard M., 2006, A&A, 456, 75

Combes F., 2001, in Aretxaga I., Kunth D., Mújica R., eds, Advanced Lectures on the Starburst-AGN. p. 223

Conselice C. J., 2006, MNRAS, 373, 1389

Conselice C. J., Bundy K., Ellis R. S., Brichmann J., Vogt N. P., Phillips A. C., 2005, ApJ, 628, 160

Courteau S., Dutton A. A., van den Bosch F. C., MacArthur L. A., Dekel A., McIntosh D. H., Dale D. A., 2007, ApJ, 671, 203

Courteau S., et al., 2014, RMP, 86, 47–119

Cretton N., de Zeeuw P. T., van der Marel R. P., Rix H.-W., 1999, ApJS, 124, 383

Crocker A. F., Bureau M., Young L. M., Combes F., 2008, MNRAS, 386, 1811

Crook A. C., Huchra J. P., Martimbeau N., Masters K. L., Jarrett T., Macri L. M., 2007, ApJ, 655, 790

Croton D. J., et al., 2006, MNRAS, 365, 11

Dalla Bontà E., Ferrarese L., Corsini E. M., Miralda-Escudé J., Coccato L., Sarzi M., Pizzella A., Beifiori A., 2009, ApJ, 690, 537

Dame T. M., 2011, preprint, (arXiv:1101.1499)

Davidson J. R., et al., 2024, ApJ, 972, 127

Davis T. A., 2014, MNRAS, 443, 911

Davis T. A., McDermid R. M., 2017, MNRAS, 464, 453

Davis T. A., et al., 2011a, MNRAS, 414, 968

Davis T. A., et al., 2011b, MNRAS, 417, 882

Davis T. A., et al., 2013a, MNRAS, 429, 534

Davis T. A., Bureau M., Cappellari M., Sarzi M., Blitz L., 2013b, Nature, 494, 328

Davis T. A., Greene J., Ma C.-P., Pandya V., Blakeslee J. P., McConnell N., Thomas J., 2015, MNRAS, 455, 214

Davis T. A., Bureau M., Onishi K., Cappellari M., Iguchi S., Sarzi M., 2017, MNRAS, 468, 4675

Davis T. A., et al., 2018, MNRAS, 473, 3818

Davis T. A., Greene J. E., Ma C.-P., Blakeslee J. P., Dawson J. M., Pandya V., Veale M., Zabel N., 2019, MNRAS, 486, 1404

Davis T. A., et al., 2020, MNRAS, 496, 4061

Davis T. A., et al., 2022, MNRAS, 512, 1522

De Rijcke S., Zeilinger W. W., Hau G. K. T., Prugniel P., Dejonghe H., 2007, ApJ, 659, 1172

Deane R. P., Blecher T., Obreschkow D., Heywood I., 2024, MNRAS, 535, L70

Decarli R., et al., 2022, A&A, 662, A60

Dekel A., Birnboim Y., 2006, MNRAS, 368, 2

Dekel A., Silk J., 1986, ApJ, 303, 39

Dickey J. M., Kazes I., 1992, ApJ, 393, 530

Dietrich M., et al., 1993, ApJ, 408, 416

van Dokkum P., Conroy C., Villaume A., Brodie J., Romanowsky A. J., 2017, ApJ, 841, 68

Dominiak P., Bureau M., Davis T. A., Ma C.-P., Greene J. E., Gu M., 2024, MNRAS, 529, 1597

Dominiak P., et al., 2025, MNRAS, 542, 2039

Dominiak P., et al., 2026a, MNRAS, 548, stag546

Dominiak P., et al., 2026b, MNRAS, submitted

Drehmer D. A., Storchi-Bergmann T., Ferrari F., Cappellari M., Riffel R. A., 2015, MNRAS, 450, 128

Dressler A., 1984, ApJ, 286, 97

Dressler A., Richstone D. O., 1988, ApJ, 324, 701

Dunne D. A., Webb T. M. A., Noble A., Lidman C., Shipley H., Muzzin A., Wilson G., Yee H. K. C., 2021, ApJL, 909, L29

Dutton A. A., van den Bosch F. C., Dekel A., Courteau S., 2007, ApJ, 654, 27

Dutton A. A., Conroy C., van den Bosch F. C., Prada F., More S., 2010, MNRAS, 407, 2

D'Onofrio M., Marziani P., Chiosi C., 2021, FSPAS, 8

Elford J. S., et al., 2023, MNRAS, 528, 319

Ellison S. L., Viswanathan A., Patton D. R., Bottrell C., McConnachie A. W., Gwyn S., Cuillandre J.-C., 2019, MNRAS, 487, 2491

Emsellem E., Monnet G., Bacon R., 1994, A&A, 285, 723

Emsellem E., et al., 2007, MNRAS, 379, 401

Emsellem E., et al., 2011, MNRAS, 414, 888

Ene I., et al., 2018, MNRAS, 479, 2810

Ene I., Ma C.-P., McConnell N. J., Walsh J. L., Kempski P., Greene J. E., Thomas J., Blakeslee J. P., 2019, ApJ, 878, 57

Ene I., Ma C.-P., Walsh J. L., Greene J. E., Thomas J., Blakeslee J. P., 2020, ApJ, 891, 65

Fabian A. C., 2012, ARA&A, 50, 455

Falcke H., Körding E., Markoff S., 2004, A&A, 414, 895

Fall S. M., Efstathiou G., 1980, MNRAS, 193, 189

Fasano G., Poggianti B. M., Couch W. J., Bettoni D., Kjærgaard P., Moles M., 2000, ApJ, 542, 673

Fernández X., et al., 2016, ApJL, 824, L1

Ferrarese L., 2002, ApJ, 578, 90

Ferrarese L., Ford H., 2005, SSR, 116, 523

Ferrarese L., Merritt D., 2000, ApJL, 539, L9

Ferrarese L., Ford H. C., Jaffe W., 1996, ApJ, 470, 444

Fitzpatrick E. L., 1999, PASP, 111, 63

Flores H., Hammer F., Puech M., Amram P., Balkowski C., 2006, A&A, 455, 107

Förster Schreiber N. M., et al., 2009, ApJ, 706, 1364

Gao F., et al., 2016, ApJ, 834, 52

Ge J., Mao S., Lu Y., Cappellari M., Long R. J., Yan R., 2021a, MNRAS, 507, 2488

Ge J., Mao S., Lu Y., Cappellari M., Long R. J., Yan R., 2021b, MNRAS, 507, 2488

Gebhardt K., Thomas J., 2009, ApJ, 700, 1690

Gebhardt K., et al., 2000, ApJL, 539, L13

Gebhardt K., et al., 2003, ApJ, 583, 92

Gebhardt K., Adams J., Richstone D., Lauer T. R., Faber S. M., Gültekin K., Murphy J., Tremaine S., 2011, ApJ, 729, 119

Genzel R., et al., 2017, Nature, 543, 397

Gerhard O. E., Binney J. J., 1996, MNRAS, 279, 993

Giovanelli R., et al., 2005, AJ, 130, 2598

Glover S. C. O., Clark P. C., 2012, MNRAS, 421, 116

Goulding A. D., et al., 2016, ApJ, 826, 167

Goullaud C. F., Jensen J. B., Blakeslee J. P., Ma C.-P., Greene J. E., Thomas J., 2018, ApJ, 856, 11

Greenhill L. J., Jiang D. R., Moran J. M., Reid M. J., Lo K. Y., Claussen M. J., 1995, ApJ, 440, 619

Greenhill L. J., et al., 2003, ApJ, 590, 162

Gu M., Greene J. E., Newman A. B., Kreisch C., Quenneville M. E., Ma C.-P., Blakeslee J. P., 2022, ApJ, 932, 103

Gültekin K., et al., 2009, ApJ, 698, 198

Gururajan, G. et al., 2022, A&A, 663, A22

Gwyn S. D. J., 2014, in Manset N., Forshay P., eds, Astronomical Society of the Pacific Conference Series Vol. 485, Astronomical Data Analysis Software and Systems XXIII. p. 387

Harms R. J., et al., 1994, ApJL, 435, L35

Harrison C. M., 2017, Nature Astronomy, 1, 0165

Harrison C. M., Costa T., Tadhunter C. N., Flütsch A., Kakkad D., Perna M., Vietri G., 2018, Nature Astronomy, 2, 198–205

den Heijer M., et al., 2015, A&A, 581, A98

Helfer T. T., Thornley M. D., Regan M. W., Wong T., Sheth K., Vogel S. N., Blitz L., Bock D. C.-J., 2003, ApJS, 145, 259

Herrnstein J. R., Moran J. M., Greenhill L. J., Trotter A. S., 2005, ApJ, 629, 719

Heywood I., et al., 2024, MNRAS, 534, 76

Hezaveh Y. D., 2014, ApJL, 791, L41

Hollenbach D., Salpeter E. E., 1971, ApJ, 163, 155

Holmberg E., 1958, Meddelanden fran Lunds Astronomiska Observatorium Serie II, 136, 1

Hopkins P. F., Hernquist L., Cox T. J., Di Matteo T., Robertson B., Springel V., 2006, ApJS, 163, 1

Hopkins P. F., Hernquist L., Cox T. J., Kereš D., 2008, ApJS, 175, 356

Hopkins P. F., Cox T. J., Younger J. D., Hernquist L., 2009, ApJ, 691, 1168

Hopkins P. F., Torrey P., Faucher-Giguère C.-A., Quataert E., Murray N., 2016, MNRAS, 458, 816

Huang S., Ho L. C., Peng C. Y., Li Z.-Y., Barth A. J., 2013, ApJL, 768, L28

Humphreys E. M. L., Reid M. J., Moran J. M., Greenhill L. J., Argon A. L., 2013, ApJ, 775, 13

Iodice E., et al., 2019, A&A, 623, A1

Jarvis M. J., et al., 2025, MNRAS, 544, 193

Jeans J. H., 1915, MNRAS, 76, 70

Jeans J. H., 1922, MNRAS, 82, 122

Jensen J. B., et al., 2021, ApJS, 255, 21

Jorsater S., van Moorsel G. A., 1995, AJ, 110, 2037

Kaasinen M., et al., 2024, A&A, 684, A33

Kabasares K. M., et al., 2022, ApJ, 934, 162

Kabasares K. M., et al., 2024, ApJ, 966, 132

Kaspi S., Smith P. S., Netzer H., Maoz D., Jannuzi B. T., Giveon U., 2000, ApJ, 533, 631

Kass R. E., Raftery A. E., 1995, JASA, 90, 773

Kelly B. C., 2007, ApJ, 665, 1489

Kennicutt Jr. R. C., 1998, ARA&A, 36, 189

Kennicutt R. C., Evans N. J., 2012, ARA&A, 50, 531

Kereš D., Katz N., Weinberg D. H., Davé R., 2005, MNRAS, 363, 2

King A., 2003, ApJL, 596, L27

King A., Pounds K., 2015, ARA&A, 53, 115

Kormendy J., 1988, ApJ, 325, 128

Kormendy J., Ho L. C., 2013, ARA&A, 51, 511

Kormendy J., Kennicutt Jr. R. C., 2004, ARA&A, 42, 603

Kormendy J., Richstone D., 1995, ARA&A, 33, 581

Kormendy J., Fisher D. B., Cornell M. E., Bender R., 2009, ApJS, 182, 216

Kormendy J., Bender R., Cornell M. E., 2011, Nature, 469, 374

Krajnović D., McDermid R. M., Cappellari M., Davies R. L., 2009, MNRAS, 399, 1839

Krist J. E., Hook R. N., Stoehr F., 2011, in Proc. SPIE, 8127, 81270J.

Krumholz M. R., 2014, Phys. Rep., 539, 49

Krumholz M. R., Klein R. I., McKee C. F., Offner S. S. R., Cunningham A. J., 2009, Science, 323, 754

Kuo C. Y., et al., 2011, ApJ, 727, 20

La Barbera F., Vazdekis A., Ferreras I., Pasquali A., Cappellari M., Martín-Navarro I., Schönebeck F., Falcón-Barroso J., 2016, MNRAS, 457, 1468

Lauer T. R., et al., 1995, AJ, 110, 2622

Lauer T. R., et al., 2007, ApJ, 662, 808

Lawrie G., Deane R., Blecher T., Obreschkow D., Heywood I., Ranchod S., 2025, (arXiv:2511.01715)

Leaman R., et al., 2019, MNRAS, 488, 3904

Lelli F., McGaugh S. S., Schombert J. M., 2016, AJ, 152, 157

Lelli F., Davis T. A., Bureau M., Cappellari M., Liu L., Ruffa I., Smith M. D., Williams T. G., 2022, MNRAS, 516, 4066

Leroy A. K., Walter F., Brinks E., Bigiel F., de Blok W. J. G., Madore B., Thornley M. D., 2008, AJ, 136, 2782

Leroy A. K., et al., 2022, ApJ, 927, 149

Liang F.-H., et al., 2023, MNRAS, 527, 9343

Liang F.-H., et al., 2026, MNRAS, 547, stag221

Liepold C. M., Quenneville M. E., Ma C.-P., Walsh J. L., McConnell N. J., Greene J. E., Blakeslee J. P., 2020, ApJ, 891, 4

Liepold E. R., Ma C.-P., Walsh J. L., 2023, ApJL, 945, L35

Liu L., Bureau M., Blitz L., Davis T. A., Onishi K., Smith M., North E., Iguchi S., 2021, MNRAS, 505, 4048

Liu L., et al., 2025, MNRAS, 541, 3081

Lotz J. M., Jonsson P., Cox T. J., Croton D., Primack J. R., Somerville R. S., Stewart K., 2011, ApJ, 742, 103

Lu A., et al., 2022, MNRAS, 514, 5035

Lu A., et al., 2025, MNRAS, 540, 71

Lynden-Bell D., 1967, MNRAS, 136, 101

Ma C.-P., Greene J. E., McConnell N., Janish R., Blakeslee J. P., Thomas J., Murphy J. D., 2014, ApJ, 795, 158

Macchetto F., Marconi A., Axon D. J., Capetti A., Sparks W., Crane P., 1997, ApJ, 489, 579

Magorrian J., et al., 1998, AJ, 115, 2285

Marconi A., Hunt L. K., 2003, ApJL, 589, L21

Marconi A., Risaliti G., Gilli R., Hunt L. K., Maiolino R., Salvati M., 2004, MNRAS, 351, 169

van der Marel R. P., van den Bosch F. C., 1998, AJ, 116, 2220

Markwardt C. B., 2009, in Bohlender D. A., Durand D., Dowler P., eds, Astronomical Society of the Pacific Conference Series Vol. 411, Astronomical Data Analysis Software and Systems XVIII. p. 251 (arXiv:0902.2850)

Masters K. L., Springob C. M., Huchra J. P., 2008, AJ, 135, 1738

McConnell N. J., Ma C.-P., 2013, ApJ, 764, 184

McConnell N. J., Ma C.-P., Gebhardt K., Wright S. A., Murphy J. D., Lauer T. R., Graham J. R., Richstone D. O., 2011, Nature, 480, 215

McConnell N. J., Ma C.-P., Murphy J. D., Gebhardt K., Lauer T. R., Graham J. R., Wright S. A., Richstone D. O., 2012, ApJ, 756, 179

McGaugh S. S., 2012, AJ, 143, 40

McGaugh S. S., de Blok W. J. G., 1998, ApJ, 499, 41

McGaugh S. S., Schombert J. M., Bothun G. D., de Blok W. J. G., 2000, ApJL, 533, L99

McGee S. L., 2013, MNRAS, 436, 2708

McMullin J. P., Waters B., Schiebel D., Young W., Golap K., 2007, in ASP Conf. Ser. Vol. 376, Astronomical Data Analysis Software and Systems XVI. p. 127

McNamara B. R., Nulsen P. E. J., 2007, ARA&A, 45, 117

McQuinn K. B. W., et al., 2021, ApJ, 918, 23

Mehrgan K., Thomas J., Saglia R., Mazzalay X., Erwin P., Bender R., Kluge M., Fabricius M., 2019, ApJ, 887, 195

Merloni A., Körding E., Heinz S., Markoff S., Di Matteo T., Falcke H., 2006, New Astron., 11, 567

Meyer M. J., Zwaan M. A., Webster R. L., Schneider S., Staveley-Smith L., 2008, MNRAS, 391, 1712

Mihos J. C., Hernquist L., 1994, ApJL, 431, L9

Mihos J. C., Hernquist L., 1996, ApJ, 464, 641

Miller S. H., Bundy K., Sullivan M., Ellis R. S., Treu T., 2011, ApJ, 741, 115

Mitzkus M., Cappellari M., Walcher C. J., 2017, MNRAS, 464, 4789

Miyoshi M., Moran J., Herrnstein J., Greenhill L., Nakai N., Diamond P., Inoue M., 1995, Nature, 373, 127

Mo H. J., Mao S., White S. D. M., 1998, MNRAS, 295, 319

Mo H., van den Bosch F. C., White S., 2010, Galaxy Formation and Evolution

Morganti R., Oosterloo T., Oonk J. B. R., Frieswijk W., Tadhunter C., 2015, A&A, 580, A1

Mould J., et al., 2012, ApJS, 203, 14

Naab T., Ostriker J. P., 2017, ARA&A, 55, 59

Naab T., Johansson P. H., Ostriker J. P., 2009, ApJL, 699, L178

Nagai H., et al., 2019, ApJ, 883, 193

Napolitano N. R., et al., 2022, A&A, 657, A94

Neufeld D. A., Maloney P. R., 1995, ApJL, 447, L17

Neumayer N., 2010, PASA, 27, 449

Nguyen D. D., et al., 2020, ApJ, 892, 68

Nguyen D. D., et al., 2021, MNRAS, 504, 4123

Nguyen D. D., et al., 2022, MNRAS, 509, 2920

Nguyen D. D., Cappellari M., Pereira-Santaella M., 2023, MNRAS, 526, 3548

Noordermeer E., Verheijen M. A. W., 2007, MNRAS, 381, 1463

North E. V., et al., 2019, MNRAS, 490, 319

North E. V., et al., 2021, MNRAS, 503, 5179

Novak M., et al., 2019, ApJ, 881, 63

Onishi K., Iguchi S., Sheth K., Kohno K., 2015, ApJ, 806, 39

Onishi K., Iguchi S., Davis T. A., Bureau M., Cappellari M., Sarzi M., Blitz L., 2017, MNRAS, 468, 4663

Onken C. A., Peterson B. M., 2002, ApJ, 572, 746

Pandya V., et al., 2017, ApJ, 837

Patton D. R., Carlberg R. G., Marzke R. O., Pritchet C. J., da Costa L. N., Pellegrini P. S., 2000, ApJ, 536, 153

Peebles P. J. E., 1972, ApJ, 178, 371

Peng Y.-j., et al., 2010, ApJ, 721, 193

Peng Y., Maiolino R., Cochrane R., 2015, Nature, 521, 192

Pesce D. W., Braatz J. A., Condon J. J., Gao F., Henkel C., Litzinger E., Lo K. Y., Reid M. J., 2015, ApJ, 810, 65

Pesce D. W., et al., 2020, ApJL, 891, L1

Peterson B. M., Wandel A., 1999, ApJL, 521, L95

Peterson B. M., et al., 1991, ApJ, 368, 119

Peterson B. M., et al., 2004, ApJ, 613, 682

Pierce M. J., Tully R. B., 1988, ApJ, 330, 579

Pilawa J. D., Liepold C. M., Andrade S. C. D., Walsh J. L., Ma C.-P., Quenneville M. E., Greene J. E., Blakeslee J. P., 2022, ApJ, 928, 178

Pilawa J., Liepold E. R., Ma C.-P., 2024, ApJ, 966, 205

Pilawa J., Liepold E. R., Ma C.-P., Walsh J. L., Greene J. E., 2025, ApJ, 989, 98

Pizzella A., Corsini E. M., Dalla Bontà E., Sarzi M., Coccato L., Bertola F., 2005, ApJ, 631, 785

Ponomareva A. A., Verheijen M. A. W., Papastergis E., Bosma A., Peletier R. F., 2017, MNRAS, 474, 4366

Ponomareva A. A., et al., 2021, MNRAS, 508, 1195

Quenneville M. E., Liepold C. M., Ma C.-P., 2022, ApJ, 926, 30

Quenneville M. E., Blakeslee J. P., Ma C.-P., Greene J. E., Gwyn S. D. J., Ciccone S., Nyiri B., 2023, MNRAS, 527, 249

Riess A. G., et al., 2024, ApJ, 977, 120

Rizzo F., Vegetti S., Powell D., Fraternali F., McKean J. P., Stacey H. R., White S. D. M., 2020, Nature, 584, 201

Rizzo F., Vegetti S., Fraternali F., Stacey H. R., Powell D., 2021, MNRAS, 507, 3952

Rose T., et al., 2019, MNRAS, 489, 349

Ruffa I., Davis T. A., 2024, Galaxies, 12

Ruffa I., et al., 2019, MNRAS, 489, 3739

Ruffa I., et al., 2023, MNRAS, 522, 6170

Rusli S. P., Thomas J., Erwin P., Saglia R. P., Nowak N., Bender R., 2011, MNRAS, 410, 1223

Rusli S. P., et al., 2013, AJ, 146, 45

Rybicki G. B., 1987, in de Zeeuw P. T., ed., IAU Symposium Vol. 127, Structure and Dynamics of Elliptical Galaxies. D. Reidel, Dordrecht, p. 397

Saglia R. P., et al., 2016, ApJ, 818, 47

Sahu N., Graham A. W., Davis B. L., 2019, ApJ, 876, 155

Sahu K. C., Anderson J., Baggett S., 2021, WFC3 Data Handbook, v5.0, https://hst-docs.stsci.edu/wfc3dhb

Saintonge A., et al., 2011, MNRAS, 415, 32

Saintonge A., et al., 2017, ApJS, 233, 22

Sakai S., et al., 2000, ApJ, 529, 698

Sarzi M., Rix H.-W., Shields J. C., Rudnick G., Ho L. C., McIntosh D. H., Filippenko A. V., Sargent W. L. W., 2001, ApJ, 550, 65

Scharwächter J., McGregor P. J., Dopita M. A., Beck T. L., 2013, MNRAS, 429, 2315

Schlafly E. F., Finkbeiner D. P., 2011, ApJ, 737, 103

Schoniger F., Sofue Y., 1994, A&A, 283, 21

Schultheis M., Sormani M. C., Gadotti D. A., 2025, A&AR, 33, 7

Schulze A., Gebhardt K., 2011, ApJ, 729, 21

Schwarzschild M., 1979, ApJ, 232, 236

Schwarzschild M., 1993, ApJ, 409, 563

Scott N., et al., 2009, MNRAS, 398, 1835

Serra P., et al., 2012, MNRAS, 422, 1835

Shankar F., et al., 2016, MNRAS, 460, 3119

Shankar F., et al., 2019, MNRAS, 485, 1278

Shen Y., 2013, BASI, 41, 61

Shen J., Gebhardt K., 2010, ApJ, 711, 484

Shlosman I., Frank J., Begelman M. C., 1989, Nature, 338, 45

Silge J. D., Gebhardt K., 2003, AJ, 125, 2809

Silk J., Rees M. J., 1998, A&A, 331, L1

Simon D. A., Cappellari M., Hartke J., 2023, MNRAS, 527, 2341

Siopis C., et al., 2009, ApJ, 693, 946

Skrutskie M. F., et al., 2006, AJ, 131, 1163

Smith M. D., et al., 2019, MNRAS, 485, 4359

Smith M. D., et al., 2021a, MNRAS, 500, 1933

Smith M. D., et al., 2021b, MNRAS, 503, 5984

Somerville R. S., Davé R., 2015, ARA&A, 53, 51

Sorai K., et al., 2019, PASJ, 71, S14

Springel V., et al., 2005, Nature, 435, 629

Springob C. M., Masters K. L., Haynes M. P., Giovanelli R., Marinoni C., 2007, ApJS, 172, 599

Stark D. V., et al., 2025, ACS Instrument Handbook v25.0, https://hst-docs.stsci.edu/acsihb

Stone M. A., Lyu J., Rieke G. H., Alberts S., Hainline K. N., 2024, ApJ, 964, 90

Strateva I., et al., 2001, AJ, 122, 1861

Tacconi L. J., et al., 2013, ApJ, 768, 74

Targett T. A., Dunlop J. S., McLure R. J., 2012, MNRAS, 420, 3621

Thater S., Krajnović D., Cappellari M., Davis T. A., de Zeeuw P. T., McDermid R. M., Sarzi M., 2019, A&A, 625, A62

Thomas J., Ma C.-P., McConnell N. J., Greene J. E., Blakeslee J. P., Janish R., 2016, Nature, 532, 340

Tiley A. L., et al., 2016a, MNRAS, 460, 103

Tiley A. L., Bureau M., Saintonge A., Topal S., Davis T. A., Torii K., 2016b, MNRAS, 461, 3494

Tiley A. L., et al., 2019, MNRAS, 482, 2166

Tonry J. L., 1984, ApJL, 283, L27

Tonry J. L., 1987, ApJ, 322, 632

Toomre A., Toomre J., 1972, ApJ, 178, 623

Topal S., Bureau M., Tiley A. L., Davis T. A., Torii K., 2018, MNRAS, 479, 3319

Trachternach C., de Blok, W. J. G. McGaugh, S. S. van der Hulst, J. M. Dettmar, R.-J. 2009, A&A, 505, 577

Tremaine S., et al., 2002, ApJ, 574, 740

Tully R. B., Fisher J. R., 1977, A&A, 54, 661

Tully R. B., Pierce M. J., 2000, ApJ, 533, 744

Übler H., et al., 2017, ApJ, 842, 121

Utomo D., et al., 2017, ApJ, 849, 26

Veale M., et al., 2017a, MNRAS, 464, 356

Veale M., Ma C.-P., Greene J. E., Thomas J., Blakeslee J. P., McConnell N., Walsh J. L., Ito J., 2017b, MNRAS, 471, 1428

Veale M., Ma C.-P., Greene J. E., Thomas J., Blakeslee J. P., Walsh J. L., Ito J., 2018, MNRAS, 473, 5446

Veilleux S., Cecil G., Bland-Hawthorn J., 2005, ARA&A, 43, 769

Verheijen M. A. W., 2001, ApJ, 563, 694

Vestergaard M., Peterson B. M., 2006, ApJ, 641, 689

Viaene S., Sarzi M., Baes M., Fritz J., Puerari I., 2017, MNRAS, 472, 1286

Visser R., van Dishoeck E. F., Black J. H., 2009, A&A, 503, 323

Vogt N. P., Forbes D. A., Phillips A. C., Gronwall C., Faber S. M., Illingworth G. D., Koo D. C., 1996, ApJL, 465, L15

Voit G. M., Donahue M., O'Shea B. W., Bryan G. L., Sun M., Werner N., 2015, ApJL, 803, L21

Volonteri M., Haardt F., Madau P., 2003, ApJ, 582, 559

Wada K., Fukushige R., Izumi T., Tomisaka K., 2018, ApJ, 852, 88

Walsh J. L., Barth A. J., Ho L. C., Sarzi M., 2013, ApJ, 770, 86

Wandel A., Peterson B. M., Malkan M. A., 1999, ApJ, 526, 579

Wegner G., et al., 2003, AJ, 126, 2268

White S. D. M., Frenk C. S., 1991, ApJ, 379, 52

White S. D. M., Rees M. J., 1978, MNRAS, 183, 341

Williams M. J., Bureau M., Cappellari M., 2010, MNRAS, 409, 1330

Williams T. G., et al., 2023, MNRAS, 525, 4270

Willmer C. N. A., 2018, ApJSS, 236, 47

Wilman D. J., Oemler A., Mulchaey J. S., McGee S. L., Balogh M. L., Bower R. G., 2009, ApJ, 692, 298

Wisnioski E., et al., 2015, ApJ, 799, 209

Woo J.-H., et al., 2010, ApJ, 716, 269

Xi H., Peng B., Staveley-Smith L., For B.-Q., Liu B., Ding D., 2024, ApJS, 274, 18

Yang X., Mo H. J., van den Bosch F. C., 2003, MNRAS, 339, 1057

Young L. M., Bureau M., Cappellari M., 2008, ApJ, 676, 317

Young L. M., et al., 2011, MNRAS, 414, 940

Young L. M., et al., 2014, MNRAS, 444, 3408

Young L. M., Serra P., Krajnović D., Duc P.-A., 2018, MNRAS, 477, 2741

Yu Q., Tremaine S., 2002, MNRAS, 335, 965

Zhang H., et al., 2024, MNRAS, 530, 3240

Zhang H., et al., 2025a, MNRAS, 537, 520

Zhang H., Bureau M., Ruffa I., Davis T. A., Dominiak P., Elford J. S., Lelli F., Williams T. G., 2025b, MNRAS, 541, 2540

Zhao W., et al., 2018, ApJ, 854, 124

Zwaan M. A., van der Hulst J. M., de Blok W. J. G., McGaugh S. S., 1995, MNRAS, 273, L35